THE UNIVERSITY *of* EDINBURGH

The viscosity of fayalite melt at high pressure and the evolution of the Iceland mantle plume

Holly Spice

Thesis submitted for the degree of Doctor of Philosophy

School of Physics and Geosciences

The University of Edinburgh

2016

Abstract

Part 1

The viscosity of silicate melts is a fundamental physical property that determines the mobility and transport behaviour of magma on the surface and in planetary interiors. The viscosity of liquid fayalite (Fe_2SiO_4), the Fe-rich end-member of the abundant upper mantle mineral olivine, was determined up to 9.2 GPa and 1850 °C using *in situ* falling sphere viscometry and X-ray radiography imaging. The viscosity of liquid fayalite was found to decrease with pressure both along the melting curve and an isotherm, with temperature having very little influence on viscosity at high pressure. This work is the first to determine the viscosity of a highly depolymerized silicate melt at high pressure as only recent advances in experimental techniques have allowed the difficulties associated with studying depolymerized liquids at high pressure to be overcome. The results are in contrast with previous studies on moderately depolymerized silicate melts such as diopside and peridotite which found viscosity to initially increase with pressure. In accordance with recent *in situ* structural measurements on liquid fayalite, the viscosity decrease is likely a result of the increase in Fe-O coordination with pressure. The results show that the behaviour of silicate melts at depth is strongly dependent on the melt structure and composition.

Part 2

The magnitude of the thermal anomaly at hotspot locations has a fundamental influence on the dynamics of mantle melting and therefore has an important role in shaping the surface of our planet. The North Atlantic Igneous Province (NAIP) is the surface expression of a major mantle plume and is unique in the fact that it has a complete magmatic history. The highest $^{3}He/^{4}He$ volcanic rocks on Earth are found in the early NAIP picrites of West Greenland and Baffin Island and high $^{3}He/^{4}He$ rocks are still erupted on Iceland today. However, the relationship between $^{3}He/^{4}He$ and mantle plumes has remained enigmatic. The main aim of this work is to use the ideal opportunity provided by the NAIP to investigate the relationship between temperature, mantle melting dynamics and helium isotopes within a mantle plume.

The magmatic temperatures of a suite of picrites and primitive basalts spanning the spatial and temporal range of the NAIP was determined using traditional olivine-melt thermometry, a forward mantle melting model and the newly developed Al-in-olivine thermometer. This study is the first to provide a detailed petrologic approach to investigating the mantle temperature of the NAIP throughout its magmatic history and is the first to compare all three techniques in detail. The Al-in-olivine thermometer was found to be the most robust proxy for mantle temperature. The early stage of volcanic activity in the NAIP is associated with the arrival of the ancestral Iceland plume head and resulted in a uniform temperature anomaly with Al-in-olivine temperatures 250-300℃ above that of ambient MORB across an area 2000 km in diameter. In addition, the temperature of the plume is shown to have been subject to large temperature fluctuations on a timescale of 10^{7} years and is currently increasing, which has had profound effects on the melting dynamics and bathymetry of the North Atlantic region.

Using existing and new $^{3}He/^{4}He$ measurements, no clear relationship between $^{3}He/^{4}He$ and temperature is observable. However, it is noted that the maximum $^{3}He/^{4}He$ of primitive basalts from the NAIP has decreased through time. These relationships are explicable if the high $^{3}He/^{4}He$ reservoir is located in either the core or the core-mantle boundary (CMB), from which helium diffuses into the lower mantle. The high $^{3}He/^{4}He$ signature is incorporated into a plume when it breaks away from the base of the mantle and over the lifetime of the plume, the

$^{3}He/^{4}He$ source is gradually depleted. The temperature of the plume can vary independently in responses to heat flow at the CMB, which is in turn related to changes in mantle convection. Global plate tectonics and mantle processes are therefore intricately linked with melting dynamics at hotspot locations.

Author's Declaration

I declare that this thesis has been composed solely by myself and that it has not been submitted, either in whole or in part, in any previous application for a degree. Except where otherwise acknowledged, the work presented is entirely my own.

Holly Spice

2015

Acknowledgments

I would like to take this opportunity to thank the many people who have helped me during my PhD. In particular I thank Prof. Godfrey Fitton and Dr. Linda Kirstein for their excellent supervision, dedication to my project and for their constant support and encouragement. I thank my colleagues from the Centre for Science at Extreme Conditions Dr. James Drewitt, Dr. Benjamin Cochain, Dr. Chrystele Sanloup and Charlotte de Grouchy for their assistance with experiments at the APS. I thank the instrument scientist Dr. Yoshio Kono for his invaluable work and expertise during the experimental beamtime. I thank Ana Carracedo Plumed of SUERC for carrying out the helium isotope measurements.

I also thank the numerous technical and research staff at the University of Edinburgh for their much needed help and assistance. In particular, I thank Dr. Chris Hayward for his assistance with EPMA analysis, Mike Hall for producing polished thin sections, Dr. Nic Odling for carrying out XRF analysis, and Dr. John Craven for his assistance with the SEM and much needed advice. I am greatly indebted to Dr. Tom Barraclough and Jen Brooke for their willingness to carry heavy rocks around in the field, your assistance was greatly appreciated! I also thank Prof. Brian Upton, Dr. Findlay Stuart, Prof. Thor Thordarson and Björn Hardarson for providing samples. Thanks also must go to Dr. John Faithfull for sending me in the direction of the Mull picrites and to James Westland for showing me around the field area.

I thank the Engineering and Physical Sciences Research Council (EPSRC) for providing financial support for my project.

Last but by no means least, I would like to thank my family and friends for their love, support and encouragement. Firstly, to Jen for keeping me sane during the final few months of my write up. Secondly, a general shout out to all the yummicks who have made the past seven years in Edinburgh a total blast. Finally, to my family and in particular, my parents and sister Robyn who have always supported me in everything I do, and it is to them I dedicate this work.

Contents

Author's Declaration iv

Acknowledgments v

Table of Contents vi

I The viscosity of liquid fayalite at high pressure 1

1 Introduction 2
1.1 The viscosity of silicate melts 2
1.2 Background and previous work 4

2 Methods 7
2.1 Sample choice 7
2.2 High P-T techniques 8
2.2.1 The Paris-Edinburgh Press 8
2.2.2 Synchrotron X-ray source 10
2.2.3 Beamline set-up at 16-BM-B 11
2.2.4 Pressure determination 12
2.3 Viscosity experiments 13
2.3.1 Density determination at high-P-T 15

3 Results 17
3.1 Viscosity results 17
3.2 Sample analysis 23
3.2.1 Experimental errors 26

4 Discussion 28
4.1 Pressure and silicate melt viscosity 28
4.2 Temperature and silicate melt viscosity 32
4.3 Geological implications 33
4.4 Suggested further work 35

5 Conclusions 36

II The evolution of the Iceland mantle plume 38

1 Introduction 39
1.1 Background . . . 39
1.1.1 Mantle melting and the role of temperature . . . 39
1.1.2 Mantle plumes . . . 39
Plume theory . . . 40
Mantle plumes and helium isotopes . . . 41
1.1.3 Alternative theories . . . 43
1.1.4 Mantle melting and temperature . . . 44
1.1.5 Project aims and motivation . . . 46
1.2 The North Atlantic Igneous Province . . . 47
1.2.1 The NAIP and the mantle plume model . . . 48
1.2.2 History and geology of the NAIP . . . 50
1.2.3 West Greenland . . . 52
1.2.4 Baffin Island . . . 53
1.2.5 The British Tertiary Igneous Province . . . 53
Skye . . . 57
Rum . . . 59
Mull . . . 59
1.2.6 Iceland . . . 61
1.3 The geochemical composition of the North Atlantic Mantle . . . 65
1.3.1 The Iceland mantle source . . . 65
1.3.2 The early NAIP mantle . . . 71
1.3.3 Location of the high $^{3}He/^{4}He$ reservoir . . . 76
1.4 Chapter outline . . . 77

2 Field geology, petrology and geochemistry 79
2.1 Introduction . . . 79
2.2 Sampling . . . 79
2.2.1 Sample ages . . . 81
2.3 Field geology . . . 82
2.3.1 Skye . . . 82
2.3.2 Rum . . . 83
2.3.3 Mull . . . 84
2.4 Petrology . . . 86
2.4.1 Skye . . . 86
2.4.2 Rum . . . 87
2.4.3 Mull . . . 87
2.4.4 Iceland neovolcanic zones . . . 88
2.4.5 Iceland Tertiary . . . 88
2.5 Whole-rock compositions . . . 91
2.5.1 Major elements . . . 91
2.5.2 Trace elements . . . 93

2.6 Mineral chemistry . . . 98
2.6.1 Skye . . . 98
2.6.2 Mull . . . 99
2.6.3 Rum . . . 100
2.6.4 Iceland . . . 101
2.6.5 Baffin Island and West Greenland . . . 103
2.6.6 The magma system and origin of high-Mg olivines . . . 104
2.6.7 Cr-spinel chemistry . . . 107
2.7 Summary . . . 108

3 Thermometry 110
3.1 Introduction . . . 110
3.2 Olivine-melt Fe-Mg thermometry . . . 111
3.2.1 Introduction . . . 111
Roeder and Emslie thermometer . . . 112
Other olivine-melt thermometers . . . 114
3.2.2 Application of olivine-melt thermometry to the NAIP . . . 116
Primary melt composition . . . 116
Oxidation state . . . 119
Pressure and K_D(Fe-Mg)$^{ol-liq}$ . . . 119
Temperature calculation . . . 123
Crystallization temperatures and comparison to MORB . . . 131
3.2.3 Discussion . . . 133
Choice of K_D(Fe-Mg)$^{ol-liq}$ . . . 133
Oxygen fugacity . . . 134
Sample choice . . . 134
Most primitive olivine composition . . . 135
Clinopyroxene fractionation . . . 136
PRIMELT3 . . . 137
3.3 Al-in-olivine thermometry . . . 142
3.3.1 Introduction . . . 142
3.3.2 Results . . . 145
Al_2O_3 content of olivine . . . 145
Temperatures . . . 148
Comparison to MORB . . . 154
Location of the early plume centre . . . 157
3.4 Comparison of thermometry techniques . . . 159
3.5 Summary . . . 163

4 NAIP melting dynamics and helium isotopes 165
4.1 Introduction . . . 165
4.2 Temperature of the NAIP mantle through time . . . 166
4.2.1 Bathymetry of the North Atlantic . . . 166
4.2.2 Geochemistry . . . 174

4.2.3 Summary 174
4.3 Helium isotopes 175
4.3.1 Helium isotope results 176
4.3.2 Interpretation of helium isotope data 179
4.4 Synthesis 181
4.4.1 NAIP helium isotopes and temperature 181
4.4.2 Mantle plumes and origin of the high $^{3}He/^{4}He$ reservoir . . 184

5 Conclusions and future work 192
5.1 Conclusions 192
5.2 Further work 195

Refences 196

Appendix A Viscosity results 229

Appendix B Analytical set-ups 230
B.1 Whole-rock major and trace element analysis: (XRF) spectrometry 230
B.2 Mineral compositions: EPMA 232
B.3 Helium isotopes 234

Appendix C Sample list and locations 236

Appendix D Whole-rock compositions 238
D.1 Major elements 238
D.2 Trace elements 238

Appendix E Olivine compositions 240
E.1 Olivine core compositions 240
E.2 Olivine rim compositions 247
E.3 Olivine matrix compositions 249

Appendix F Spinel compositions 250

Appendix G Olivine-melt thermometery primary melt compositions 253

Appendix H Al-in-olivine thermometery results 255

Part I

The viscosity of liquid fayalite at high pressure

1 Introduction

1.1 The viscosity of silicate melts

Viscosity is a very important physical property of silicate melts. On the Earth's surface, it dictates the style of volcanic eruptions. Low viscosity magma produces effusive eruptions while viscous magmas (particularly in combination with volatiles) result in explosive eruptions that can have a devastating impact on human activity. Beneath the surface, the viscosity of silicate melts is a key parameter because it controls the transport properties of magma in the mantle.

The rocky inner planets were formed by gradual accretion of the fine material comprising the protoplanetary disk orbiting our sun at the beginning of the Solar System (Chambers, 2004). It is widely accepted that the gravitational and kinetic energy gained as a result of accretion was enough for extensive melting of planetary mantles to occur. These molten outer layers are known as magma oceans. Current models estimate that the base of Earth's magma ocean was around 700-1200 km, or 25-40 GPa (Fiquet et al., 2008). The magma oceans played a key role in the formation of the rocky planets. On Earth for example, the segregation of siderophile elements from the silicate mantle into the metallic core likely occurred in the magma ocean (Ringwood, 1966; Davies, 1985).Viscosity would have been a critical variable influencing the dynamics and processes occurring in terrestrial magma oceans. It is thought that the silicate mantle solidified via the crystallization and settling of minerals from the liquid. Crystal settling (Solomatov and Stevenson, 1993) and other processes such as cumulate overturn (Elkins-Tanton et al., 2003) are more efficient in a lower viscosity liquid. Convection has a strong dependency on viscosity, and so the viscosity of silicate melts would have been an important control on convection dynamics in the magma oceans and hence, the thermal evolution of the planets (Ghosh and Karki, 2011). Viscosity has a crucial control on the diffusion of chemical elements within magma and would have

influenced chemical reactions between silicates and core-forming metallic liquids at the base of the magma ocean (Ghosh and Karki, 2011). Thus, determining the viscosity of silicate liquids at depth is integral to our understanding of the formation of the rocky planets.

Viscosity is a complex function of melt composition, structure and temperature. However, despite its importance, the viscosity of silicate melts is still poorly constrained over the mantle pressure-temperature regime due to experimental difficulties associated with obtaining the high temperatures and pressures necessary to melt and analyse silicate minerals under mantle conditions. Previous experimental studies have been restricted to relatively low pressures (typically $<$5 GPa, equivalent to a depth of 180 km in the Earth, with very few studies reaching higher pressures, and none above 13 GPa) and polymerized liquids that have high viscosities. Only a handful of studies have attempted to measure the viscosity of more depolymerized silicate liquids with compositions relevant to those that would have been present in the magma oceans of the terrestrial planets e.g. peridotite (Liebske et al., 2005) and diopside (Reid et al., 2003). Many studies (Kushiro, 1976; Kushiro et al., 1976; Kushiro, 1977; Suzuki et al., 2002, 2005, 2011) have found that the viscosity of silicate melts initially decreases with increasing pressure. This has often been attributed to a structural change in the liquid at high pressure and was first suggested by Waff (1975). However, the lack of *in situ* structural data on silicate melts has meant that the matter has remained an issue of contention in the literature.

The work presented in this chapter investigates the viscosity of fayalite melt at pressures up to 9 GPa. Fayalite (Fe_2SiO_4) is the iron-rich end member of the abundant upper mantle mineral olivine ($(Mg,Fe)_2SiO_4$), and is composed of isolated silica tetrahedra linked by Fe^{2+} in six-fold coordination, and so is as depolymerized as possible for a silicate melt. This work represents the first study to determine the viscosity of such a depolymerized melt, as their extremely low viscosities present significant experimental challenges that have only recently been overcome with new experimental techniques utilizing ultrafast X-ray imaging. This work is also significant as it is one of the first studies to present viscosity data for a melt for which the structure at high pressure has been determined *in situ* and will allow the relationship between the melt structure and viscosity at high pressure to be investigated.

The work presented in this chapter has been successfully published in the peer reviewed journal Geochimica et Cosmochimica Acta (Spice et al., 2015).

1.2 Background and previous work

A summary of previous experimental studies on the viscosity of silicate melts is shown in Figure 1.1. The degree of polymerization in crystalline silicates is often expressed by the ratio of non-bridging oxygens to tetrahedrally coordinated cations (NBO/T). As indicated in Figure 1.1, the degree of polymerization in the silicate strongly influences the viscosity of the melt. The most polymerized silicates (e.g. albite and jadeite) have liquid viscosities at least several orders of magnitude higher than the more depolymerized silicates (e.g. diopside and peridotite).

Early studies focussed on highly polymerized melts with NBO/T=0. Kushiro (1976) was the first to measure the viscosity of a silicate liquid at pressures above 1 GPa, in which the viscosity of jadeite ($NaAlSi_2O_6$) melt was determined using the falling sphere method in a piston cylinder apparatus. At constant temperature, the viscosity was found to decrease by more than a factor of 10 between ambient pressure and 2.4 GPa. In a similar study, Kushiro et al. (1976) found the viscosities of both andesite and basalt melt to decrease with increasing pressure along their respective liquidii. Kushiro hypothesised that the viscosity decrease must result from a change in the melt structures at high pressure, and argued that the findings supported the theory of Waff (1975), who had suggested that the Al^{3+} cation in a silicate melt will transform from four to six-fold coordination by oxygen at high pressures, similar to the transformation in crystalline silicates. Waff (1975) predicted that this would result in a decrease in viscosity of the melt. Aluminium is a network former in aluminosilicates, therefore structural transformations disrupt the structural network, resulting in the melt becoming more depolymerized, and hence, less viscous.

In order to investigate the role of Al in silicate liquid viscosity, Kushiro (1976) measured the viscosity of a melt with a composition of $Na_2Si_3O_7$, similar to jadeite, but without Al. The viscosity was found to decrease by a factor of 3

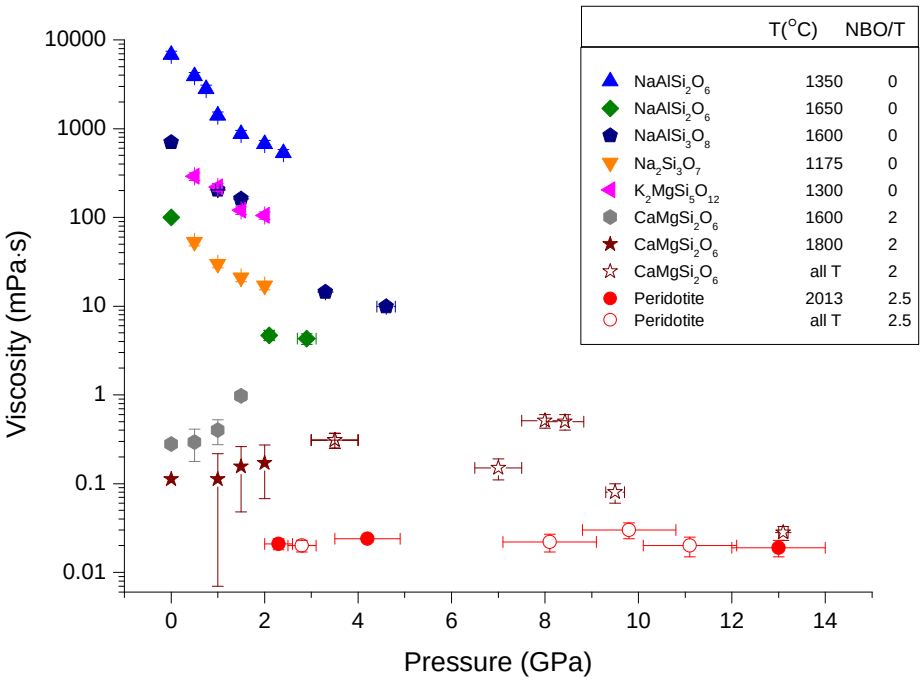

Figure 1.1: A summary of experimental studies on the viscosity of silicate melts at high pressure. The NBO/T (at ambient pressure) and temperature is also given for each composition. Blue triangles: jadeite at 1350 °C (Kushiro, 1976); green diamonds: jadeite at 1650 °C (Suzuki et al., 2011); navy pentagons: albite at 1600 °C, first 3 points from Brearley et al. (1986), points at 3.3 and 4.6 GPa from Suzuki et al. (2002); orange triangles: $Na_2Si_3O_7$ at 1175 °C (Kushiro, 1976); magenta triangles: $K_2MgSi_5O_{12}$ at 1300 °C (Kushiro, 1977); grey hexagons: diopside at 1600 °C (Brearley et al., 1986); stars: diopside at 1800 °C (Taniguchi, 1992), highest pressure point from Reid et al. (2003) at 1730 ± 100 °C; red circles: peridotite at 2013 °C (Liebske et al., 2005).

between atmospheric pressure and 2 GPa, whereas, the viscosity of jadeite melt decreased by a factor of 10 over the same pressure range. Kushiro (1977) then measured the viscosity of $K_2MgSi_5O_{12}$ melt and found it to decrease by a factor of 3 between 0.5 GPa and 2 GPa. Kushiro suggested that this could be a result of the K^+, Mg^{2+} or Si^{4+} cations undergoing coordination changes. On the basis of these results, it is possible that Al plays a dominant role in the large viscosity decrease of jadeite, however, it is not the only constituent or factor that may influence the melt structure, and hence, the viscosity at depth.

Several studies have since focussed on more depolymerized melts. Brearley et al. (1986) and Taniguchi (1992) measured the viscosity of liquid diopside ($CaMgSi_2O_6$,

NBO/T=2), which at the time was the most depolymerized silicate liquid to have been studied. Both studies found the viscosity of diopside melt to increase with pressure, however, the highest pressure reached in the experiments was 2 GPa. As a result, it has often been assumed that other depolymerized silicate melts will behave in the same way, and that they will not display the same 'anomalous' viscosity decrease at depth that is observed in some polymerized silicate melts. However, later work has revealed a more complex behaviour in depolymerized melts at higher pressures. Studies of diopside (Reid et al., 2003) and peridotite (Liebske et al., 2005) found the viscosity of the melts to initially increase with pressure, but decrease above ∼9-10 GPa. A recent theoretical study simulating the behaviour of liquid $MgSiO_3$ at depth found a viscosity decrease similar to that reported in polymerized melts, with the viscosity reaching a minimum value near 5 GPa, and then increasing further upon compression (Karki and Stixrude, 2010) due to the reduction in free volume of the liquid. The results from these studies suggest that it is not appropriate to make assumptions about the behaviour of a silicate melt at depth based on the properties of other melts. As will be demonstrated later in the chapter, the viscosity of melts at depth must be considered on an individual basis and is strongly dependent on the melt structure and composition.

2 Methods

The best method for determining the viscosity of liquid silicates at high pressure is the *in situ* falling sphere viscometry technique using X-ray radiography (e.g. Reid et al., 2003; Liebske et al., 2005; Kono et al., 2013). The method uses a sphere of greater density than the sample, which falls through the sample upon melting. Using high energy synchrotron X-ray radiation, the fall of the sphere is imaged as it passes through the liquid. From this, a distance/time curve of the sphere's descent is produced, from which the velocity, and hence viscosity, can be calculated.

2.1 Sample choice

Olivine is estimated to be the most abundant mineral in the upper mantle (∼56% according to the pyrolite model (Ringwood, 1975)) and its melt viscosity at high pressures is therefore highly relevant to the magma ocean theory. It exhibits continuous solid solution between its two end members: forsterite (Mg_2SiO_4) and fayalite (Fe_2SiO_4). Mantle olivine shows little compositional variability, with nearly all ranging from Fo_{89} to Fo_{94} (Deer et al., 1997). However, the melting temperature of forsterite (1890℃ at ambient pressure) is too high to be within the capabilities of the experimental equipment, therefore the Fe-rich end-member fayalite, which has a much lower melting temperature (1205℃ at ambient pressure), was chosen instead.

Natural fayalite purchased from Alfa Aesar was used in the experiments. Table 2.1 shows the average composition of the quenched fayalite melt as obtained by electron microprobe analysis (EPMA). The analyses were performed on a CAMECA SX100 electron microprobe with a 15 kV accelerating voltage and a 1 μm beam, with a current of 30 nA. The sample contains approximately 3.5 wt%

MnO, 0.6 wt% MgO, and trace amounts of CaO.

Table 2.1: Mean composition from 9 analyses on quenched fayalite melt as obtained by EPMA. Data is given in oxide wt% along with the standard deviation (δ).

oxide	**wt %**	δ
SiO_2	29.82	0.81
FeO	65.52	0.98
MgO	0.61	0.18
CaO	0.031	0.026
MnO	3.47	0.55

2.2 High P-T techniques

2.2.1 The Paris-Edinburgh Press

High pressure (P) and temperature (T) experiments were conducted with a VX-3 Paris-Edinburgh (PE) press (Figure 2.1). The PE press can compress a large sample volume of 100 mm^3 up to 10 GPa. The VX model has been specifically designed for X-ray studies and has only two support pillars, helping to avoid unwanted scattering of the beam by the sample. Cup-shaped tungsten carbide alloy anvils designed by Yamada et al. (2011) were used to generate high pressures using a double-stage hydraulic pump. The cup diameter was 12 mm, with a bottom diameter of 3 mm, as shown in Figure 2.1.

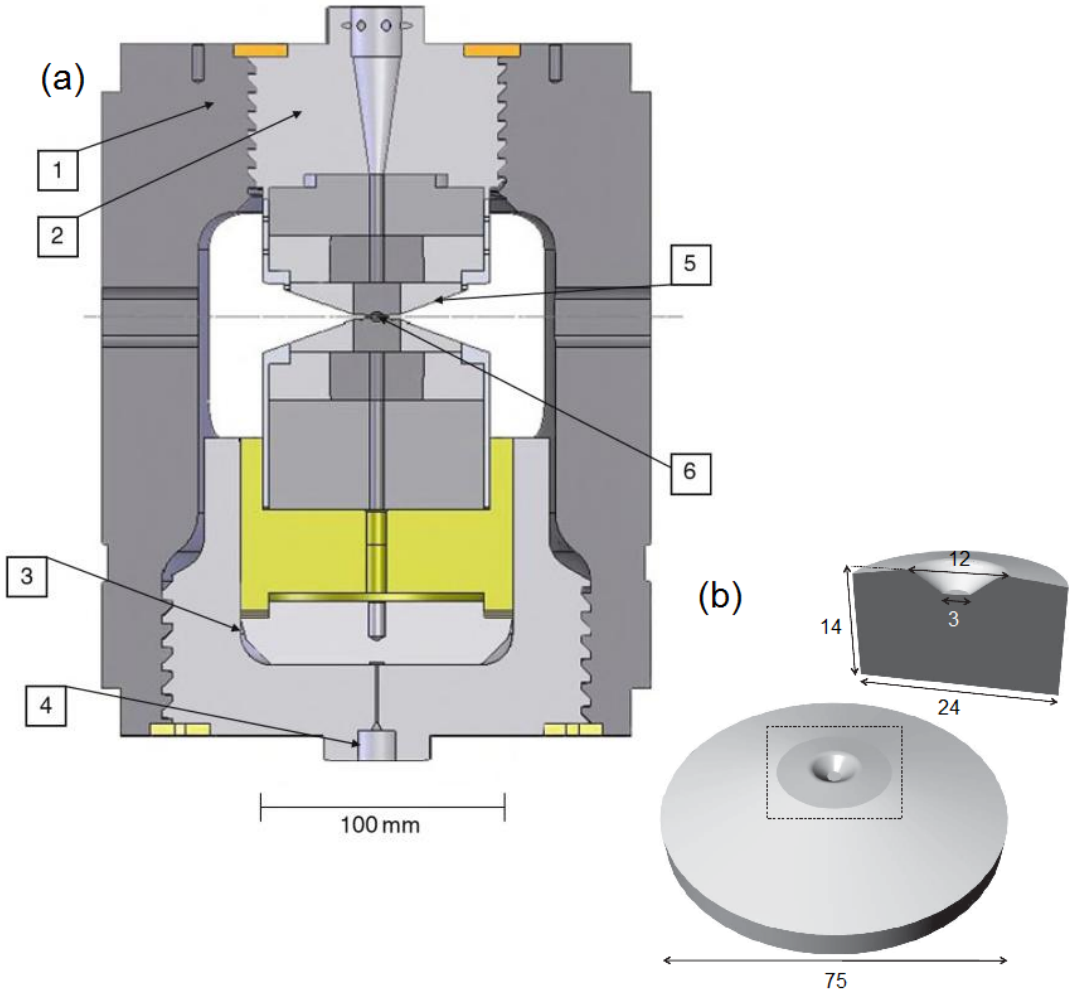

Figure 2.1: (a) Schematic diagram of the Paris-Edinburgh press VX-3 model (McMahon, 2012). (1) Hardened steel main frame; (2) breech; (3) piston; (4) hydraulic fluid inlet; (5) tungsten carbide anvils; (6) sample chamber. (b) Tungsten-carbide anvil used during the experiments (Yamada et al., 2011), dimensions are given in mm.

The sample was placed in a cell assembly between the two anvils. The cell assembly (Figure 2.2) was designed by Sakamaki et al. (2012) to allow X-rays a large vertical access to the sample while limiting the extrusion of cell materials, even at high P-T conditions. The outer pressure media consisted of ZrO_2 caps and a ring-shaped boron epoxy gasket (boron:epoxy = 4:1 by weight) with an outer supporting polycarbonate plastic (Lexan) ring. The gasket and zirconia caps provide good thermal insulation for high-T experiments. An MgO ring 6 mm in diameter is placed between the gasket and a graphite heater to increase

stability of the cell and maintain the anvil gap. The graphite capsule was inserted into an MgO sleeve with MgO caps + a small layer of packed pyrex powder above and below the capsule. This prevented the oxidation of iron and the consequential decomposition of fayalite at high-T. Ta rods and a thin disc of Mo foil were inserted inside the zirconia caps above and below the graphite heater to ensure electrical conductivity. Maximum transparency for X-rays is achieved by the use of low density materials such as boron epoxy and graphite.

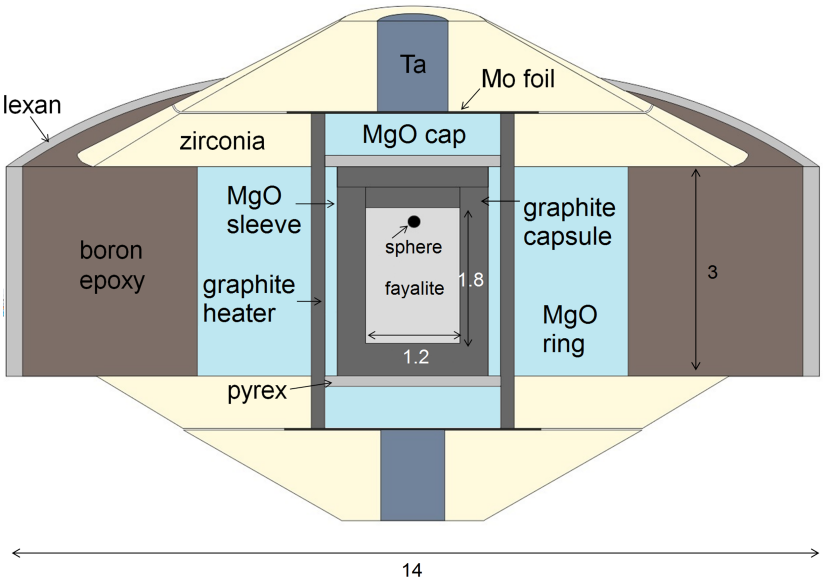

Figure 2.2: Schematic cross section of the cell assembly; adapted from Sakamaki et al. (2012). Dimensions are given in mm.

The cell assembly enabled a sample volume up to 1.8 mm high and 1.2 mm in diameter to be measured, however the X-ray window is limited by the anvil gap at high pressures. For example, the typical anvil gap is approximately 0.7 mm at 7 GPa and 1700 °C (Kono et al., 2014).

2.2.2 Synchrotron X-ray source

The Advanced Photon Source (APS) at the Argonne National Laboratory, Illinois, USA is an example of a third generation synchrotron radiation facility, illustrated in Figure 2.3. Electrons are accelerated by high-voltage alternating electric fields

in a linear accelerator (LINAC) and booster ring until they are travelling at around 99.99% of the speed of light. Bending and focussing magnets are used to maintain the orbital path of the electrons. The electrons are then injected into the 1.1 km circumference storage ring where powerful electromagnets force the electrons to follow a curved trajectory. Synchrotron radiation (at the APS, X-ray radiation) is emitted tangentially to the electron path. Intense focussed beams of high energy X-rays are produced at the experimental beamlines by X-ray optics.

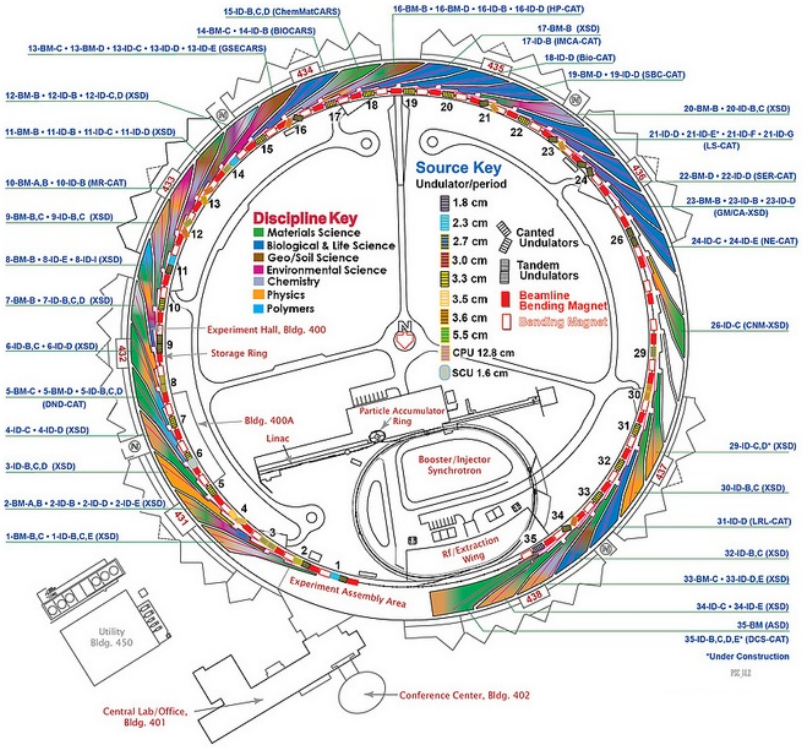

Figure 2.3: The APS at the Argonne National Laboratory, Illinois, USA (http://www.aps.anl.gov/).

2.2.3 Beamline set-up at 16-BM-B

The experiments were carried out at the HPCAT (high-pressure collaborative access team) 16-BM-B beamline at the APS. 16-BM-B is a bending magnet beamline providing white X-rays (5-120 keV) with high brightness (Sakamaki et al.,

2012). Figure 2.4 shows the experimental set-up at 16-BM-B. The beamline is capable of white beam X-ray diffraction and radiography experiments using the VX-3 PE press. X-rays scattered by a sample are collimated with a 0.1 mm gap collimator 80 mm downstream of the sample and a 0.1 mm receiving slit 400 mm further down upon arrival at the detector. The scattered X-rays are detected using a Ge solid state detector (Ge-SSD) mounted on a large Huber rotating stage allowing precise control of the 2θ angle from 2° to 39.5° (Kono et al., 2014). To photograph and measure the sample or sphere dimensions, a charged coupled device (CCD) camera was used. To avoid interference with X-ray diffraction measurements, the camera can be moved vertically in and out of the beam. A high-speed video camera (Photron FASTCAM SA3) is located at the downstream side of the Ge-SSD. The camera has a high frame rate capable of >1000 frames per second (fps) and is therefore highly useful for experiments where the sample viscosity is very low.

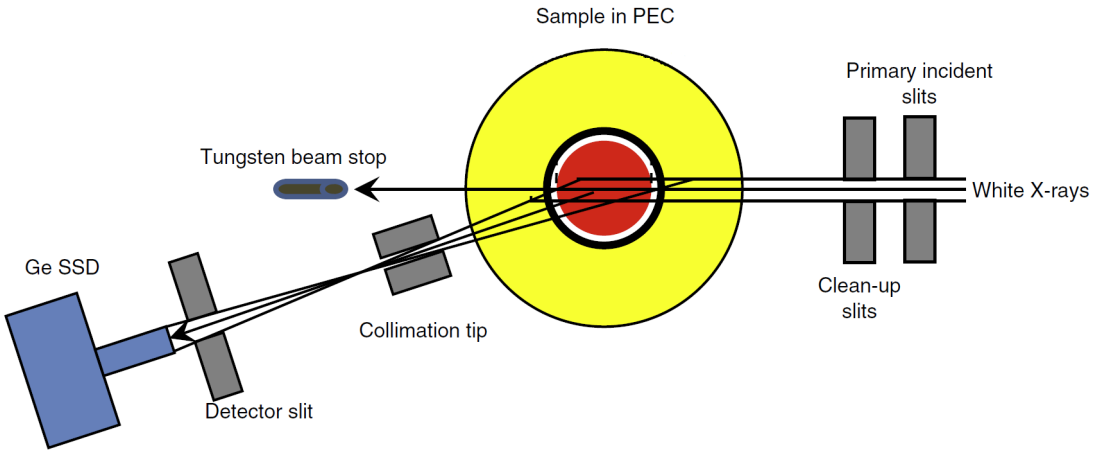

Figure 2.4: A schematic diagram of the X-ray diffraction set-up at HPCAT 16-BM-B beamline (Kono et al., 2014).

2.2.4 Pressure determination

The MgO ring in the cell assembly is used as a pressure standard using the equation of state and calibration reported by Kono et al. (2010). X-ray diffraction measurements were collected for the MgO ring, and the pressure was determined

from the Bragg diffraction peak positions, which are a function of lattice plane spacing (d) and unit cell volume given by:

$$2dsin\theta = n\lambda \tag{2.1}$$

where θ is the scattering angle. The unit cell volume decreases with increasing pressure, but increases with increasing temperature. The calibration determined by Kono et al. (2010) takes into account these competing effects, therefore it is important to precisely determine the temperature when measuring pressure. The temperature of the sample in the PE press cell assembly was determined from the calibration measurements reported by Kono et al. (2014) using a W5%Re-W26%Re thermocouple. The uncertainty in the pressure determination is estimated to be around ± 0.2 GPa. However, a pressure gradient exists between the 1.2 mm distance between the centre of the sample and the outer edge of the MgO ring. Further measurements by Kono et al. (2014) found that a linear relationship in pressure difference is observed above 1000 °C. This can be expressed by $P_{sample} - P_{ring} = 7.7 - T \times 8.3 \times 10^{-4}$ where T is the temperature in °C and is accounted for in the quoted pressure values. Within the sample capsule itself, the pressure gradient was found to be negligible (Kono et al., 2014).

2.3 Viscosity experiments

Falling sphere viscometry experiments were carried out on the HPCAT 16-BM-B beamline. Powdered fayalite was packed inside the graphite capsule and a rhenium sphere was placed on top of the sample. Rhenium was chosen due to its high density contrast with silicate melts, and because there was no reaction with the sample under reducing conditions. It was important to pack a thin layer of fayalite powder above the sphere to prevent it making contact with the graphite cap as this inhibits the fall. In some of the experiments, a second rhenium sphere was placed in the middle of the sample to indicate the commencement of melting as it was not possible to view the top sphere at high pressure due to the reduced anvil gap. Once the cell was loaded into the PE press, images of the capsule were taken using the high resolution CCD camera (Prosilica GC1380, resolution: 0.954 μm/pixel) to check the positioning of the sphere and to measure its radius.

The pressure was then raised at room temperature using a double-stage hydraulic pump. Temperature was then raised slowly by electrical heating to approximately 100 °C below the liquidus. At this point, pressure was determined by collecting X-ray diffraction data on the MgO ring. After calculating the pressure, the sample was rapidly heated to a super-liquidus set-point temperature, typically 50−100 °C above the melting point..

Upon melting, the rhenium sphere descended through the sample. The viscosity of liquid fayalite is extremely low, resulting in very fast falling times of the sphere (often <250 ms), therefore a high-speed video camera (Photron FASTCAM SA3, resolution: 5.92 ± 0.01 μm/pixel) was used to collect images of the falling spheres at a rate of 250 fps. The large density difference, and hence X-ray absorption coefficients between the rhenium sphere and the sample, allows for clear X-ray radiography imaging of the sphere's descent through the capsule. The imaged descent path of the sphere was used to calculate a distance/time plot using the Tracker plug-in in Java-based image processing software, ImageJ.

The velocity of the sphere is calculated from the distance/time plot. The viscosity η of the liquid is then calculated using Stokes' law:

$$\eta = \frac{2gr_s^2(\rho_s - \rho_l)W}{9vE} \tag{2.2}$$

where r_s is the radius of the sphere, ρ_s and ρ_l are the densities of the sphere and the liquid, respectively, at a given pressure and temperature, and g=9.803 ms^{-2} is the acceleration due to gravity. W and E are correction factors that account for the wall and end-effects of a finite cylindrical container (Faxén, 1922) of radius r_c and height h_c given by:

$$W = 1 - 2.104\left(\frac{r_s}{r_c}\right) + 2.09\left(\frac{r_s}{r_c}\right)^3 - 0.95\left(\frac{r_s}{r_c}\right)^5 \tag{2.3}$$

$$E = 1 + 3.3\left(\frac{r_s}{h_c}\right) \tag{2.4}$$

r_s of the rhenium spheres, as determined from X-ray shadowgraph images using

the high resolution CCD camera, ranged between 54-93 μm, where the largest uncertainty was $\pm$ 2 μm.

2.3.1 Density determination at high-*P*-*T*

In order to calculate the viscosity of the liquid using Stokes' Law, the density of both the sphere and the liquid must be known. The density of rhenium is a function of pressure can be calculated using a third-order Birch-Murnaghan equation of state (Birch, 1952):

$$P = \frac{3}{2} \cdot {K_T}^0 \cdot \left\{ \left(\frac{\rho}{\rho_0} \right)^{\frac{7}{3}} - \left(\frac{\rho}{\rho_0} \right)^{\frac{5}{3}} \right\} \cdot \left\{ 1 - \frac{3}{4} \cdot (4 - {K_T}') \cdot \left(\left(\frac{\rho}{\rho_0} \right)^{\frac{2}{3}} - 1 \right) \right\} \quad (2.5)$$

where ρ_0 is the density of the material at atmospheric pressure, ${K_T}^0$ is the isothermal bulk modulus at atmospheric pressure, and ${K_T}'$ is the first pressure derivative of the isothermal bulk modulus. Values of 372 GPa and 4.05 were used for ${K_T}^0$ and ${K_T}'$ respectively, using data from Vohra et al. (1987), and rhenium has a density of 21.0 gcm^{-3} at atmospheric pressure and room temperature (Bauccio, 1993). Thermal expansion of rhenium was accounted for using the equation:

$$\rho = \frac{\rho_0}{1 + \alpha \cdot \Delta T} \quad (2.6)$$

where ρ_0 is the density at a fixed pressure, α is the volumetric thermal expansion coefficient of the material (19.89 x 10^{-6} K^{-1} (Ho and Taylor, 1998)), and ΔT is the change in temperature.

The density of liquid fayalite at high pressure was taken from Sanloup et al. (2013a) who determined the density of liquid fayalite at 1627 °C up to 7.5 GPa (Figure 2.5). For experimental runs not carried out at 1627 °C, thermal expansion was accounted for using a thermal expansion coefficient of 4.8 x 10^{-5} K^{-1} (Agee, 1992).

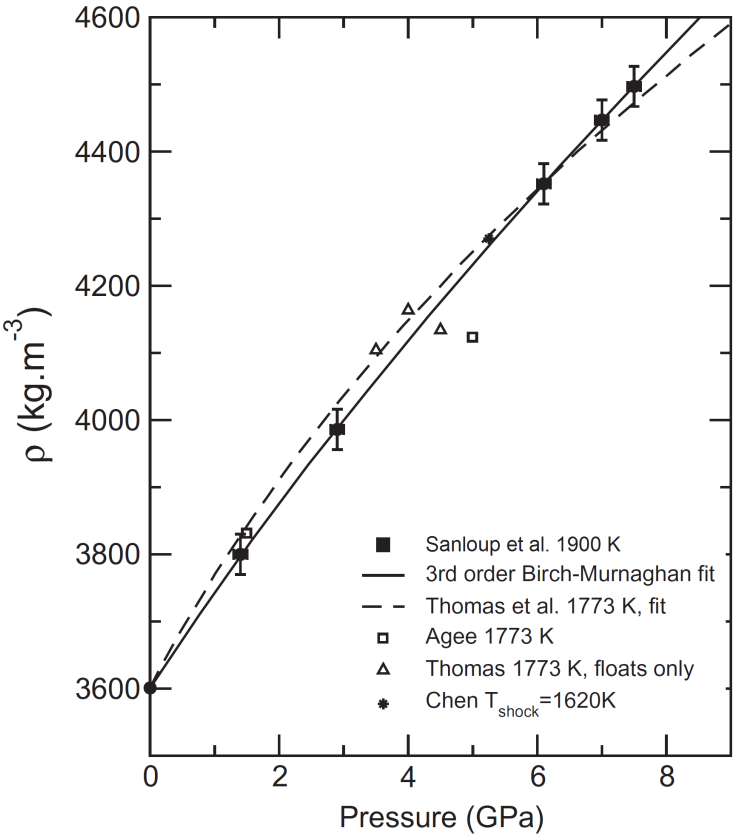

Figure 2.5: A summary of studies that have determined the density of fayalite melt at high-pressure and temperature (Sanloup et al., 2013a).

3 Results

3.1 Viscosity results

The experimental conditions, sphere diameter (d_s), terminal velocity and viscosity results are summarised in Table 3.1. A complete list of each parameter and associated uncertainties used in the viscosity calculation are presented in Appendix A.

Table 3.1: Experimental run conditions, results and uncertainties

Run	P GPa	T °C	d_s μm	v_s mm·s^{-1}	η mPa·s
A5	2.0 ± 0.5	1350 ± 70	173 ± 2	3.7 ± 0.1	52.1 ± 2.8
A10	3.6 ± 0.5	1550 ± 80	171 ± 2	5.1 ± 0.2	38.3 ± 3.7
A12	6.3 ± 0.5	1600 ± 80	185 ± 2	6.4 ± 0.2	34.7 ± 2.7
A8	9.2 ± 0.6	1850 ± 95	185 ± 2	7.2 ± 0.1	31.3 ± 2.7
B17	1.3 ± 0.5	1580 ± 80	183 ± 2	4.0 ± 0.2	51.9 ± 4.0
B14	2.8 ± 0.5	1570 ± 80	155 ± 2	4.0 ± 0.2	42.0 ± 3.7
B11	3.8 ± 0.5	1600 ± 80	133 ± 2	3.2 ± 0.1	41.0 ± 2.8
B7	4.3 ± 0.5	1640 ± 80	108 ± 2	2.3 ± 0.1	41.0 ± 3.6
B13	5.1 ± 0.5	1650 ± 85	173 ± 2	5.3 ± 0.2	37.6 ± 2.3

Prior to the experiments, the sample dimensions were 1.2 mm by 1.8 mm. Runs A5 and A8 were carried out at 2.0 and 9.1 GPa respectively, and the dimensions of the recovered samples were 1.2 mm (width) by 1.6 mm (height) for both samples. These dimensions were therefore used to calculate the wall and end correction parameters for every run. The experiments in Run A were made along the fayalite liquidus. In order to investigate the viscosity pressure dependence, independently of changes in temperature, the experiments in Run B were made as a function of pressure along the 1600 °C isotherm. An example of the calculated distance/time

plot and the X-ray shadowgraph images of the fall of the rhenium sphere from experiment B13 are shown in Figure 3.1. A linear straight line fit to the data indicates that the sphere had reached its terminal velocity prior to reaching the bottom of the capsule, following an initial acceleration. Since the velocity of the falling sphere is constant, it can be assumed that the temperature gradient within the sample capsule is negligible.

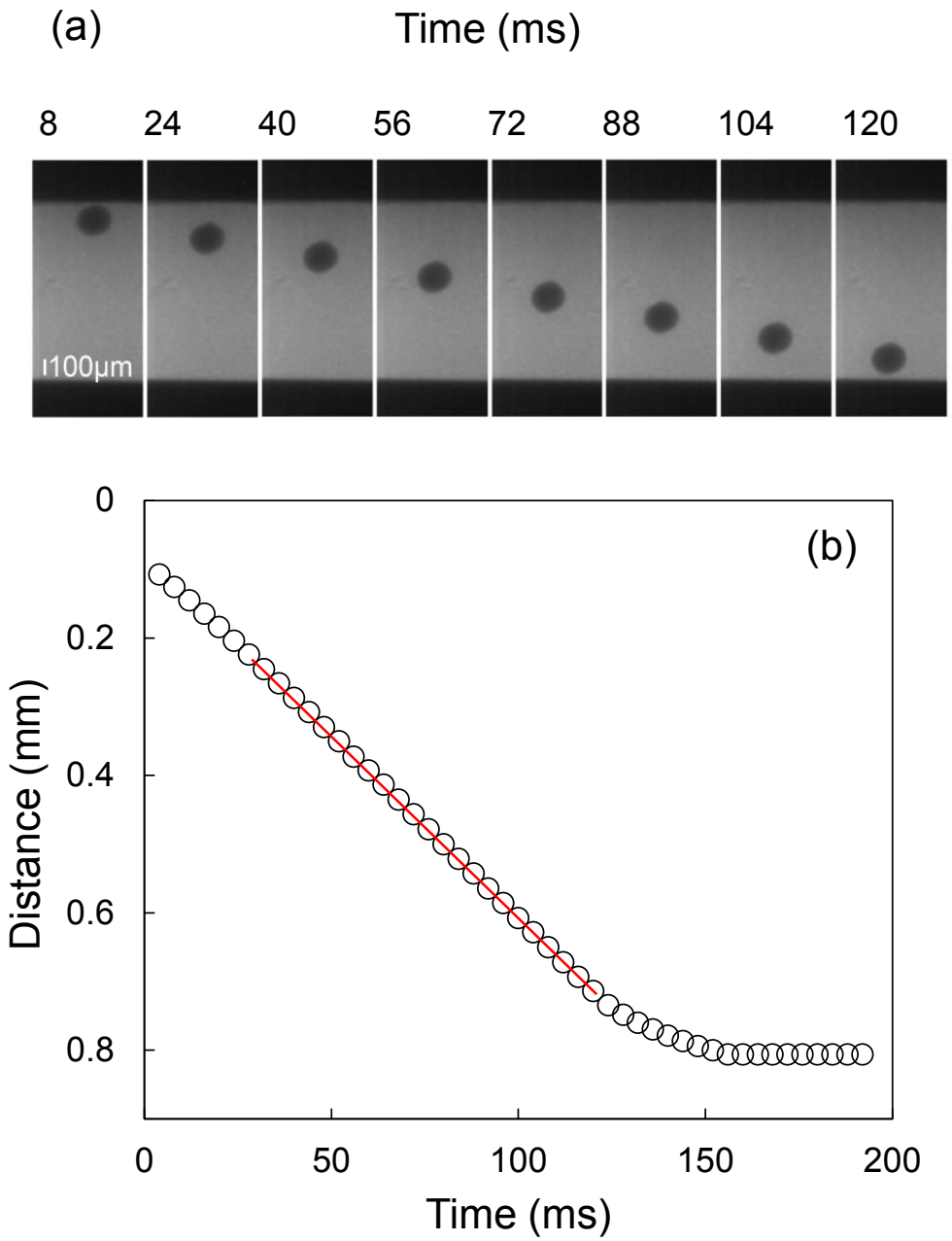

Figure 3.1: (a) A series of X-ray radiography images showing the rhenium sphere (radius 86.5 μm) descent through liquid fayalite at 5.0 GPa and 1650 °C (run B13). Every 4th frame is shown between 8 and 120 ms. (b) The results of the sphere fall analysis for each frame during experiment B13. The straight line fit to the data points indicates that terminal velocity was achieved prior to the sphere reaching the bottom of the capsule.

The velocity/time plot for the rhenium sphere of experiment B13 is shown in Figure 3.2. There is an initial acceleration, followed by a 'velocity plateau' where

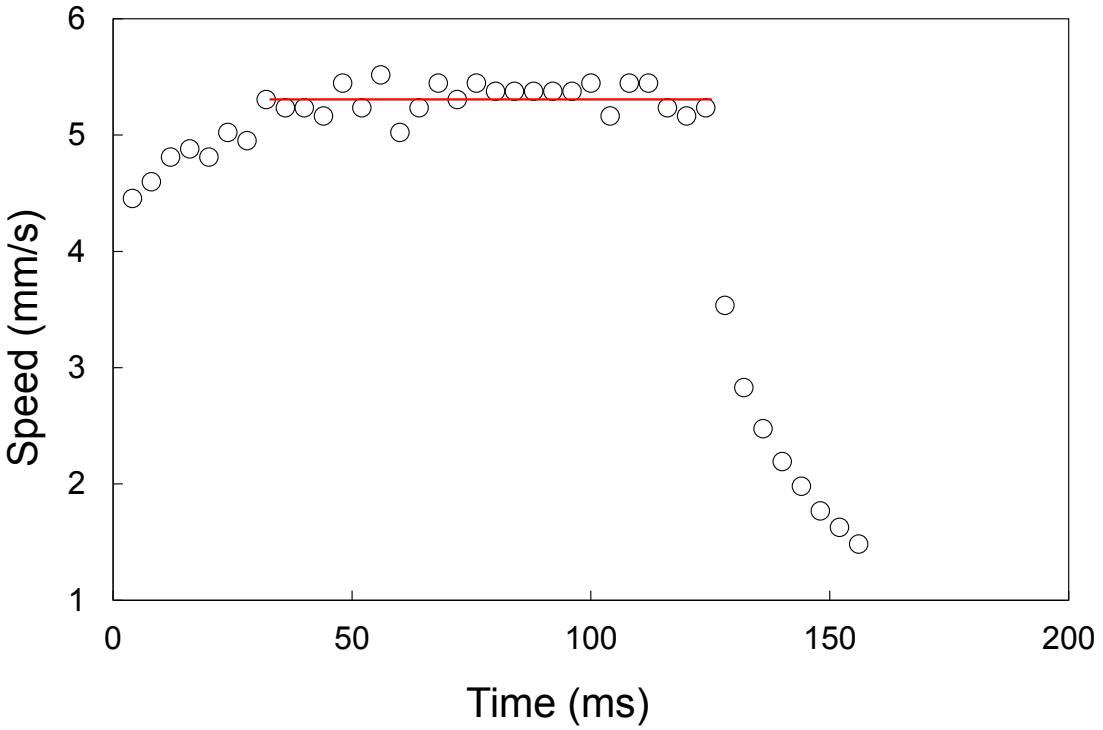

Figure 3.2: The velocity/time plot of the rhenium sphere in experiment B13. Points either side of the red line were deemed to have achieved terminal velocity, which is first reached after 30 ms. The scatter either side of the line is used to determine the error in the sphere velocity. The rapid deceleration at 130 ms occurs as the sphere approaches the bottom of the capsule.

the shape of the graph is flat and the sphere is deemed to have reached its terminal velocity. The error in the velocity determination is taken as the scatter either side of the best fit line shown in Figure 3.2. Recent studies that have measured the viscosity of silicate melts using the falling sphere technique have had few data points on the 'velocity plateau'. For example, Reid et al. (2003) had only five velocity points for their measurement of diopside viscosity at 7.0 GPa. However, the use of the high-speed camera during these measurements meant that the minimum number of points obtained to calculate the velocity was 12 (and most had >20), increasing the reliability of the results.

The viscosity of liquid fayalite was found to decrease along the liquidus (experimental Run A, black points in Figure 3.3) from 76.0 ± 6.7 mPa·s at ambient pressure, 1250 °C (Shiraishi et al., 1978), to 31.3 ± 2.8 mPa·s at 9.2 GPa, 1850 °C. Viscosity decreased rapidly from ambient pressure to around 4 GPa, after which it decreased much more slowly. The P-T conditions of each experiment in Run

A in relation to the Fe_2SiO_4 phase diagram are shown in Figure 3.4. When the uncertainty in the temperature determination is taken into account, the experiments are calculated to have been carried out at a maximum of 100 °C above the melting curve. Experimental Run B was carried out at a constant temperature of 1600±50 °C. The viscosity decreased from 51.9 ± 4.0 mPa·s at 1.3 GPa, to 34.7± 2.7 mPa·s at 6.3 GPa (grey points in Figure 3.3), indicating that pressure was the main cause of the viscosity decrease along the fayalite liquidus. It is noteworthy that the viscosity values measured at 1600 °C are not lower than those measured at lower temperatures. In fact, when the isotherm and liquidus viscosity values are plotted on the same diagram (Figure 3.3), the values all fit on the same trend. This suggests that at high-T, temperature has very little effect on viscosity and that pressure is the main controlling variable.

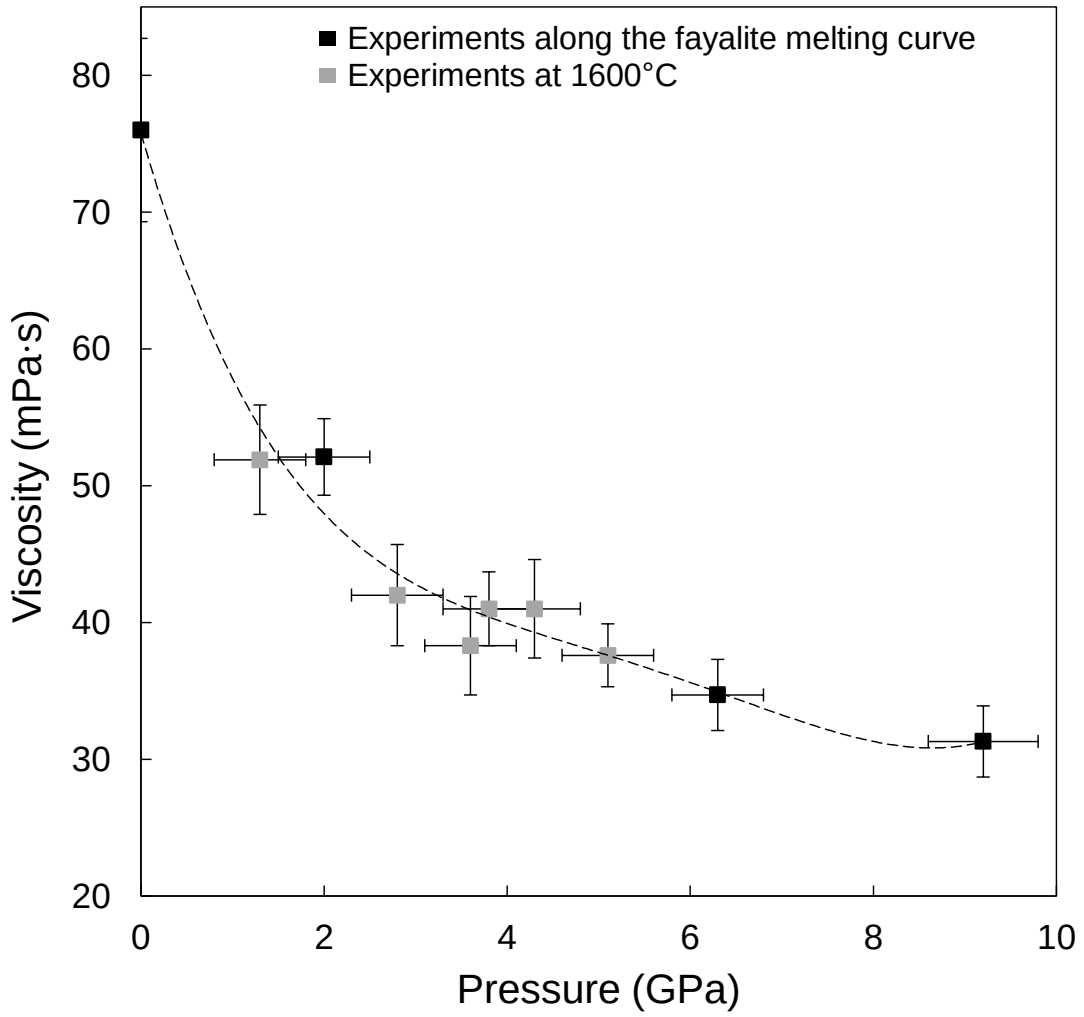

Figure 3.3: The viscosity of liquid fayalite as a function of pressure. The black squares are values obtained along the fayalite liquidus (Run A), with the temperature indicated. The grey squares are values obtained along the 1600 °C isotherm (Run B). The ambient pressure measurement is from Shiraishi et al. (1978) at 1250 °C. The curve was fit to a polynomial function and has an R^2 value of 97.6%.

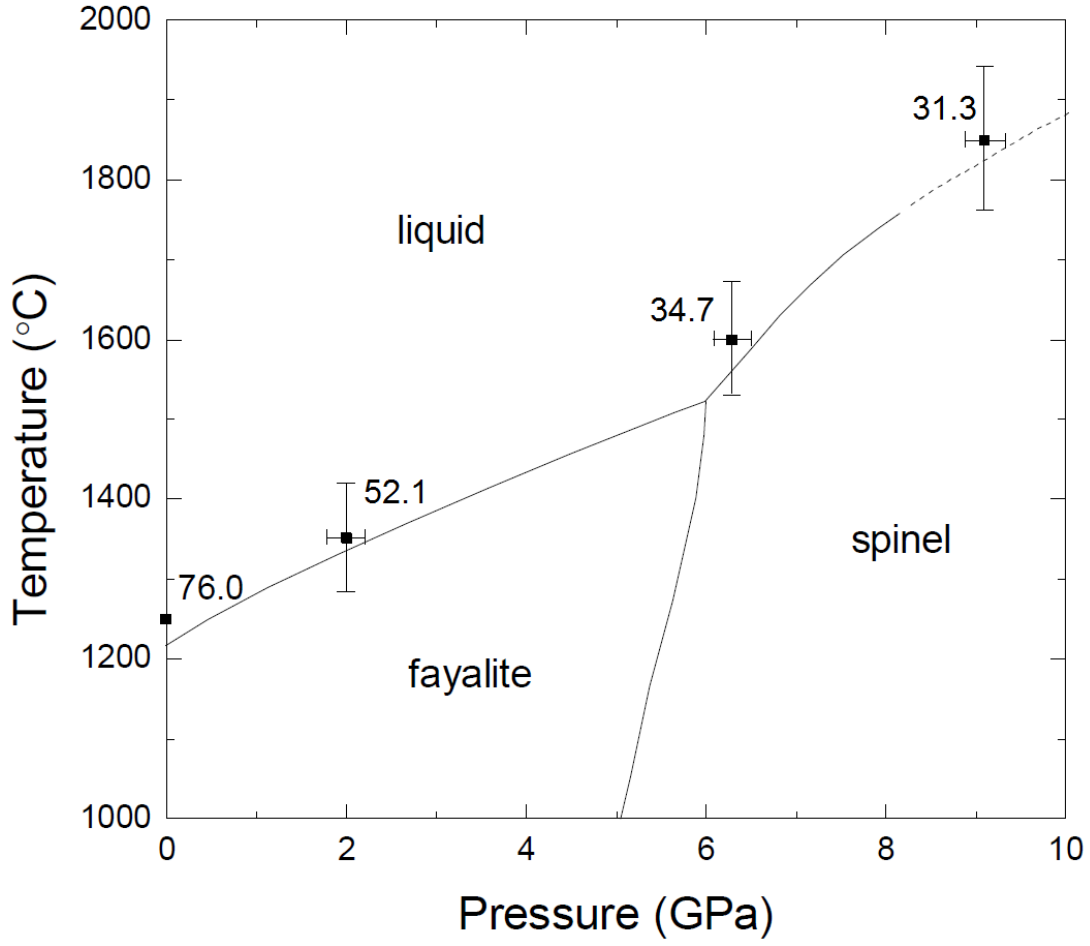

Figure 3.4: The P-T conditions of each run obtained along the fayalite liquidus (Run A) in relation to the Fe_2SiO_4 phase diagram. The viscosity values are shown in mPa·s beside each P-T point.

3.2 Sample analysis

After the experiments, the samples were quenched and recovered for imaging and electron microprobe analysis at EMMAC (The Edinburgh Materials and Micro-Analysis Centre), University of Edinburgh. A Philips XL30CP scanning electron microscope (SEM) was used to image the samples. A back scattered electron (BSE) image of experimental run A5 is shown in Figure 3.5. The composition of the samples was then analysed using a CAMECA SX100 electron microprobe with a 15 kV accelerating voltage and a 1 μm beam, with a current of 30 nA.

The analysis showed the samples were overwhelmingly of fayalite composition. In one of the highest P runs (A12, 6.3 GPa), a very small number of interstitial areas richer in FeO were detected. This was not the case for the other samples (e.g. the example illustrated in Figure 3.5) where only fayalite crystals were detected. While this suggests minor oxidation of the sample with FeO in some of the interstices, it is considered it to be insignificant since Sanloup et al. (2013a), using Mössbauer spectroscopy to quantify the ratio of Fe^{3+} to Fe^{2+} in fayalite after high P-T experiments using the same cell assembly as this study, and found no evidence for the presence of Fe^{3+} within the experimental uncertainty of $\sim$1%.

A Re-Fe alloy of variable thickness was detected on the rim of some of the recovered spheres. For example, the sample shown in Figure 3.5 has a rim of 14 μm and a maximum rim thickness of 40 μm was measured on sample B7. However, it must be concluded that this growth occurred after the fall as no growth in the size of the spheres was detected during the fall within the error of $\pm$ 2 μm. The interaction between the spheres and the sample during the experiments is therefore considered to be negligible.

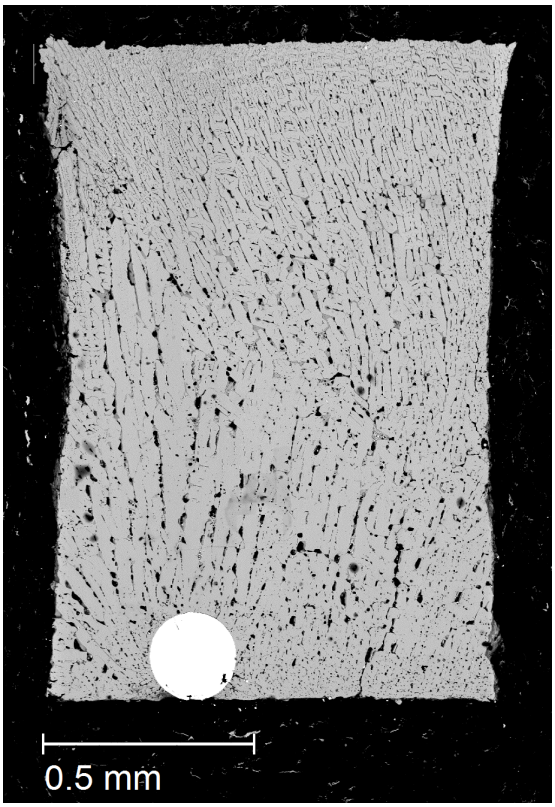

Figure 3.5: A BSE SEM image of experimental run A5. The sample was quenched as 100% fayalite crystals. The rhenium sphere can be seen in the bottom left side of the sample. The dark material surrounding the sample is the graphite capsule.

3.2.1 Experimental errors

Experimental errors arose from several sources. The uncertainty in the pressure and temperature calibrants led to a maximum uncertainty in P and T determination of ± 0.6 GPa and ± 95 °C, respectively. The uncertainty in P and T resulted in an error in the determination of the rhenium sphere and liquid density at high pressure. The largest error in the liquid density due to this was 1.5%, while the largest error in the sphere density was 1.0%. Due to the small sphere size used in our study, the uncertainty in the measurement of the sphere radii also contributes to the overall viscosity uncertainty. The CCD camera set-up had an image resolution of ± 2 μm. (Kono et al., 2014). The error in the sphere size measurement introduced an uncertainty into the wall W and end E correction factors. These were a maximum of 1.3% and 1.2%, respectively. The error in the determination of terminal velocity was taken from the spread of velocity values on the 'velocity plateau'. The standard deviations in terminal velocities ranged from ± 2-6%.

An additional uncertainty may arise if the shape of the sphere deviates from spherical. The actual terminal velocity of an ellipsoid particle may be found by multiplying the measured terminal velocity by a shape factor S. If the ellipsoid is assumed to be a spheroid in which two of the principle diameters are equal (i.e. $a = b \neq c$), then using the method of Kerr and Lister (1991), the shape factor is a function of the single aspect ratio $\gamma = c/a$ and is averaged over all possible orientations using the expression:

$$S = \frac{\gamma^{\frac{1}{3}}}{(\gamma^2 - 1)^{\frac{1}{2}}} \cdot cosh^{-1}\gamma \tag{3.1}$$

The most elliptical sphere had an aspect ratio of c/a = 0.85 (Run B7), which corresponds to a shape factor of 0.998, and thus a 0.2% error in the terminal velocity calculation. In fact, the effect of an elliptical sphere is small even at c/a=0.5, which results in S=0.96 and only a 4% error in terminal velocity. The effect of sphere shape on viscosity in this study is therefore considered to be negligible.

The overall uncertainty in the final viscosity values was determined by standard

error propagation:

$$\Delta\eta = \eta \cdot \sqrt{\frac{2g}{9} \cdot \left(\left(\frac{2\Delta r_s}{r_s} \right)^2 + \left(\frac{\sqrt{(\Delta\rho_s)^2 + (\Delta\rho_l)^2}}{\rho_s - \rho_l} \right)^2 + \left(\frac{\Delta W}{W} \right)^2 + \left(\frac{\Delta E}{E} \right)^2 + \left(\frac{\Delta v}{v} \right)^2 \right)} \tag{3.2}$$

The error in the final viscosity values ranged from 5.4-9.5%. Table 3.2 summarises the relative importance of each variable on the final viscosity value. This was calculated by increasing each variable by 1% in turn. A 1% change in the sphere radius results in the largest viscosity change, whereas a 1% increase of the liquid density has the least impact. A table of the results and errors in full can be found in Appendix A.

Table 3.2: The viscosity change calculated from a 1% increase in each value from Equation 2.2.

variable	$\Delta\eta$ (%)
r_s	2.0
ρ_s	1.5
ρ_l	0.1
W	1.3
E	0.8
v	1.0

4 Discussion

4.1 Pressure and silicate melt viscosity

This work represents the first study to measure the viscosity of a highly depolymerized silicate melt, where NBO/T=4. The most depolymerized silicates studied previously are diopside (Reid et al., 2003) and peridotite (Liebske et al., 2005) with an NBO/T= 2 and 2.5, respectively. In contrast to the results presented here, these studies found viscosity to initially increase with pressure, before decreasing above $\sim$ 9-10 GPa. An initial viscosity decrease has, however, been previously recognised in a variety of polymerized melts including jadeite (Kushiro, 1976), basalt and andesite (Kushiro et al., 1976) and albite (Brearley et al., 1986; Suzuki et al., 2002), as shown in Figure 1.1. In the literature, this observation has often been attributed to an increase in Al^{3+} coordination by oxygen (e.g. Waff, 1975; Kushiro, 1976). There are two reasons that the increase in aluminium-oxygen coordination results in a decrease in melt viscosity (Waff, 1975; Reid et al., 2003; Liebske et al., 2005). First, aluminium is a network former in polymerized silicates. Structural transformations disrupt the structural network, resulting in the melt becoming more depolymerized, and hence, less viscous. Second, higher coordinated cations are characterised by longer, and thus weaker, cation-oxygen bonds, which is thought to lower the activation barriers to self-diffusion, and hence leads to a further reduction in viscosity.

As a result of the viscosity behaviour of polymerized melts, a number of previous studies have focussed on determining the structure of aluminosilicate glass structures at high pressure, specifically looking for changes in aluminium-oxygen coordination. The results were inconclusive. At ambient pressure, Al is in tetrahedral (4-fold) coordination with oxygen. Some studies indeed suggest that higher coordinated aluminium cations are present at relatively moderate pressures. For example, Allwardt et al. (2007) reported the significant presence of 5-fold (with

minor 6-fold) coordinated aluminium in a range of aluminosilicate glasses at 3 GPa, however the relative proportions of the 4-,5- and 6-fold species was highly variable between glasses of different compositions. On the other hand, studies such as that by Poe et al. (2001) found no evidence for significant changes in Al coordination below 6 GPa. Consequently, a number of other explanations have been put forward to explain the anomalous viscosity behaviour of polymerized silicate melts at high pressure. Schmelzer et al. (2005) argued that the decrease in viscosity occurs when the thermal expansion coefficient of the liquid is negative. McMillan and Wilding (2009) favour a 'reactive ion transfer model', whereby the O^{2-} self-diffusivity increases with increasing pressure, resulting in a viscosity decrease. However, a recent theoretical study by Bauchy et al. (2013) attempted to relate viscosity and diffusivity of silicate melts at high pressure and could not find a definitive relationship. The clear discrepancies in the literature, combined with the additional problem that high pressure Si-O and Al-O bond arrangements have been found to return to tetrahedral coordination upon decompression (Williams and Jeanloz, 1988), demonstrates the need for the *in situ* determination of the structure of silicate melts.

It is only recently with the advent of third generation synchrotron radiation sources, which provide extremely brilliant beams, combined with the development of specific high-pressure liquid beamlines such as 16-BM-B at the APS, that it has been possible to measure the structure of liquid silicates *in situ*. Both the high melting temperatures of silicate melts and poor scattering power of the liquids (resulting in a weak signal) had previously prevented the *in situ* measurement of liquid silicate structure at high pressure. In a recent study, (Drewitt et al., 2015) determined the structure of liquid anorthite ($CaAl_2Si_2O_8$) *in situ* up to a pressure of 32.4 GPa, and found a continuous increase in Al coordination by oxygen from ambient pressure, with 5-fold coordinated Al dominating at 15 GPa, and an increasing dominance of 6-fold coordinated Al at higher pressures. The theory of Waff (1975) that an increase in Al coordination by oxygen is responsible for the decrease in viscosity with an increase in pressure in aluminosilicate melts may therefore be correct.

The work presented here is of particular interest because it is one of the first silicate melt viscosity studies for which *in situ* structural data is already available. This is significant because it is one of the first studies that allows the relationship

between liquid structure and physiochemical properties such as viscosity to be investigated. The structure of fayalite melt was determined by Sanloup et al. (2013a) using X-ray diffraction (Figure 4.1). At ambient pressure, the average coordination number (CN) of the Fe-O bond was measured to be 4.8 ± 0.2, and is a result of approximately 60% FeO_4 and 40% FeO_6 structural units (Drewitt et al., 2013). With increasing pressure up to 7.5 GPa, the average CN of the Fe-O bond increases to 7.2 ± 0.3. This is thought to be due to the appearance of 8-fold coordinated Fe, however it is hard to resolve the exact proportions of FeO_x species as the resolution at high pressure is limited.

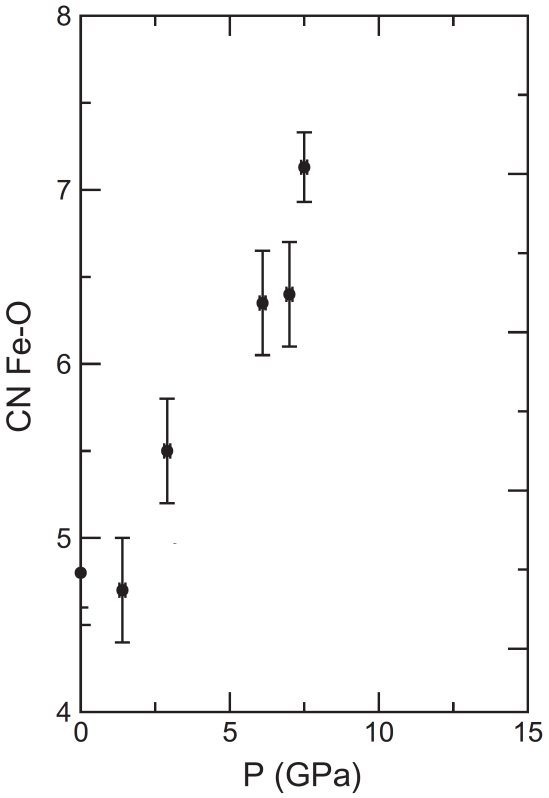

Figure 4.1: The increase in average coordination number of the Fe-O bond in Fe_2SiO_4 liquid with increasing pressure. The average CN increases from 4.8 ± 0.2 at ambient pressure to 7.2 ± 0.3 at 7.5 GPa. These measurements were carried out *in situ* at high pressure by Sanloup et al. (2013a).

The measured decrease in fayalite melt viscosity presented here is likely due to the increase in Fe-O coordination with pressure. It is useful to note the results of Kohara et al. (2004), who used X-ray and neutron diffraction measurements to

show that the Mg_2SiO_4 glass structure network is built by MgO_x polyhedra. If we can assume that the Fe_2SiO_4 melt structure behaves in the same way and is built from FeO_x polyhedra, then an increase in Fe-O coordination number would result in the melt structure becoming more depolymerized, thus resulting in a decrease in viscosity. In addition, the longer bonds required to accommodate more oxygens around the Fe^{2+} cation are weaker, resulting in a further decrease in viscosity.

The results presented here show that liquid fayalite exhibits different behaviour in viscosity at high pressures compared to other moderately depolymerized melts such as diopside and peridotite. It is therefore not appropriate to make assumptions about the viscosity behaviour of a melt at depth based on the properties of other silicates. Instead, the viscosity of silicate melts at high pressure should be considered on an individual basis and is strongly dependent on the melt structure and composition. By comparison with polymerized melts (Figure 1.1), it is clear that the viscosity decrease of fayalite melt is not as great as that observed in polymerized melts. For example, liquid fayalite viscosity decreased by a factor of 2.5 between 0-9 GPa, whereas, liquid jadeite viscosity decreased by a factor of 10 between 0-2.4 GPa (Kushiro, 1976), a much smaller pressure range. Since fayalite melt is already highly depolymerized, structural changes are likely to have a less significant effect on the melt viscosity.

At high P, a silicate melt is expected to reach a densely packed state, after which, there are no further changes in cation coordination (i.e. a viscosity minimum). Viscosity will then increase in response to closer atomic packing. It is likely that the viscosity minimum will vary for silicate melts of different composition. The four- to six-fold Si coordination change occurring between 20-35 GPa (Sato and Funamori, 2010; Sanloup et al., 2013b) measured in SiO_2 glass and basaltic liquid may have an important effect on polymerized melts whose network is largely built of tetrahedrally coordinated Si^{4+} cations, however it may not affect fayalite as Si^{4+} is not a network former in the fayalite crystalline state. However, the influence of the Si-O coordination change on viscosity is still unknown even for the most polymerized silicate melts as viscosity experiments have so far been limited to $<$13 GPa for melts of any composition. Further experimental studies on silicate melts at high pressure are needed in order to fully understand the effects of the various pressure-induced structural changes in relation to melt viscosity.

4.2 Temperature and silicate melt viscosity

The values for viscosity of liquid fayalite measured along the 1600 °C isotherm fall on the same trend as those values measured at lower temperatures along the fayalite liquidus (Figure 3.3). This suggests that at high T, temperature may have very little effect on viscosity and that pressure is the controlling variable. A weak viscosity-T-dependency implies that the liquid is fragile, i.e. it has a non-Arrhenian viscosity behaviour (Figure 4.2). Depolymerized silicate melts have been shown to be fragile liquids at 1 bar (Giordano et al., 2008). The changes that occur at high P, i.e. the increase of Fe-O CN resulting in the further depolymerization of the liquid structure, is likely to reinforce the fragile behaviour of the melt. This effect has been shown for SiO_2 and Na_2O-SiO_2 melts from a computational approach (Barrat et al., 1997; Micoulaut and Bauchy, 2013), whereby the liquid goes from strong to fragile and becomes less viscous as the Si-O CN increases from 4 to 6. Depolymerized silicate melts may therefore show fragile behaviour at high pressure.

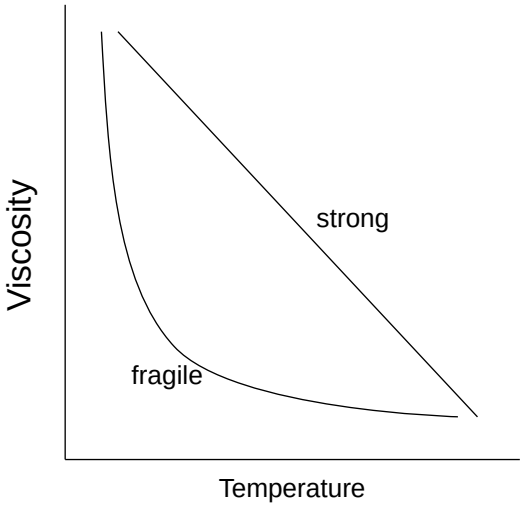

Figure 4.2: An illustrative figure showing the difference between fragile and strong liquids in relation to melt viscosity. A strong liquid exhibits Arrhenian behaviour and its viscosity continues to decrease even at high temperature. In contrast, fragile liquid viscosity is unchanged by increasing temperature at very high T and is considered to be be non-Arrhenian.

4.3 Geological implications

The fayalite viscosity results presented here hold particular significance for FeO-rich planetary magma oceans that existed in reduced environments. The experiments were carried out under reducing conditions and the final sample composition was found to contain $Fe^{3+}/\sum Fe \leq 0.01$ (Sanloup et al., 2013a). The present day Moon and Mars are estimated to have high-mantle iron contents (up to 22 wt% FeO (Cahill et al., 2009; Baratoux et al., 2011)) in a reducing environment (Sato et al., 1973; Herd et al., 2002).

Lacks et al. (2007) carried out molecular dynamics simulations to calculate viscosity along the MgO-SiO_2 join to investigate the effect of composition and pressure on transport properties. At atmospheric pressure, viscosity was found to vary by more than 3 orders of magnitude along the compositional join, however at pressures > 15 GPa, the viscosity varied by less than an order of magnitude over the entire compositional range. If the FeO-SiO_2 system behaves in the same way, then planetary magma oceans viscosities will be particularly sensitive to FeO content at lower pressures. The results presented here suggest that the increase in P along the magma ocean adiabat will favour a decrease in melt viscosity of a FeO-rich magma, and may be most important at upper mantle depths. Additionally, the viscosity decrease may be particularly pronounced in magma oceans with reducing conditions and it is therefore worth considering when modelling processes occurring in planetary magma oceans. For example, the Moon and Mars are Fe-rich bodies, while Mercury is less Fe-rich (Robinson and Taylor, 2001). In addition, before the segregation of the Fe-rich core, the Earth's magma ocean contained far more Fe in than the present-day mantle, and so the results presented here may be directly applicable to the early Earth.

It is important to consider whether the negative pressure effect is present in other compositions. MgO is far more abundant in the Earth's mantle than FeO (McDonough and Sun, 1995) and is a major oxide constituent of mantle minerals such as olivine, pyroxene and perovskite. In addition, Mercury is depleted in Fe compared to the other terrestrial planets, and is highly Mg-rich. Although no *in situ* data on the structural arrangement of the Mg-O bond in silicate liquids is presently available, Mg-O has been shown to undergo pressure- induced coor-

dination changes similar to those observed in the fayalite Fe-O bond in silicate glasses (Wilding et al., 2012). On this basis, it is likely that melts of the Mg-rich end-member of olivine, forsterite, will also initially decrease in viscosity with pressure, as Mg-O is a network former in the Mg_2SiO_4 glass structure (Kohara et al., 2004). It is therefore possible that a decrease in melt viscosity may have been present in the magma oceans on Earth and Mercury at upper mantle depths, as well as those bodies that are more FeO rich. Karki and Stixrude (2010) used first principle molecular dynamics simulations to show that the combined effect of pressure and temperature along a model Earth magma ocean geotherm would lead to an order of magnitude increase in viscosity across the depth of the mantle. The viscosity of fayalite melt decreases by a factor of two between ambient pressure and 9 GPa, and while this is small compared to an order of magnitude increase in viscosity across the entire mantle, it is not insignificant. In addition, it is possible that the viscosity decrease at upper mantle depths could become considerable with the additional influence of MgO-rich melts.

Due to the lack of data on silicate melts at high pressure, assumptions about the viscosity of depolymerized melts at depth have often been made. Solomatov and Stevenson (1993) assumed that the viscosity of depolymerized melts would increase with depth due to closer interatomic spacing. Tonks and Melosh (1990, 1993) assumed no pressure effect on silicate melt viscosity in their global magma ocean model. The results from this study, however, show that depolymerized silicate melts may exhibit a hitherto unexpected decrease in viscosity at depth. Viscosity will have been an important influencing property on the chemical evolution of the early terrestrial bodies due to the fact that convection (Davaille and Jaupart, 1993), crystal settling (Solomatov and Stevenson, 1993), cumulate overturn (Elkins-Tanton et al., 2003), and chemical diffusion (Rubie et al., 2003) are much more efficient in low viscosity melts. In addition, magma oceans with low viscosities will be able to convect faster, which can result in more rapid cooling, although this is also dependent on the rigid lid that can form on the surface of the magma ocean (Davaille and Jaupart, 1993). However, more work is needed to understand the properties of other silicate melts relevant to magma ocean compositions across a larger pressure range. While the existence of a fayalitic magma ocean in a planetary body is unlikely, it is nevertheless important to measure the properties of simple end-member compositions so that we can begin to understand

how different compositional mixtures influence planetary magma viscosities and processes.

4.4 Suggested further work

Simple end-member silicate compositions are very important as it is difficult to resolve the bond arrangements from X-ray diffraction data in liquids such as basalt and peridotite because they have many major element constituents. In order constrain and understand the viscosity behaviour of magmas at depth, further structural and viscosity measurements of other simple end-member compositions relevant to mantle compositions, such as forsterite Mg_2SiO_4, enstatite $MgSiO_3$, ferrosilite $FeSiO_3$ and garnet, are required. By measuring each end-member, it will be possible to identify which constituent(s) are most influential on magma viscosities at depth.

So far, no silicate melt viscosity has been experimentally determined above 13 GPa, so it is unclear whether pressure induced structural changes occurring at higher pressures (such as the Si^{4+} coordination increase from four- to six-fold coordination between 20-35 GPa (Sato and Funamori, 2010; Sanloup et al., 2013b)) will have an impact on viscosity. Therefore, further work at pressures above 13 GPa is required to investigate this, and to better constrain silicate melt properties at high pressures. Experimental measurements are also needed in order to test computational simulation results. For example, molecular dynamics simulations have been used to calculate the viscosity of enstatite liquid at high pressure (Karki and Stixrude, 2010), but no studies have managed to determine liquid enstatite viscosity experimentally. If experimental measurements are found to confirm results calculated from simulations, more confidence can be placed in the model.

5 Conclusions

The viscosity of silicate melts is an important physical property that determines the mobility and transport behaviour of magma and therefore has an important influence on a variety of igneous processes. However, despite its importance, the viscosity of silicate melts is still poorly constrained over the mantle pressure-temperature regime due to experimental difficulties associated with obtaining the high temperatures and pressures necessary to melt and analyse silicate minerals under mantle conditions.

This study presents the first viscosity measurements on a highly depolymerized silicate melt, fayalite (Fe_2SiO_4), which has NBO/T=4. This work is also significant because it is one of the first to investigate the viscosity of a silicate melt for which the structure at high pressure has been determined *in situ*, and so it is possible to investigate the relationship between the viscosity and melt structure at high pressure.

The viscosity of the melt was measured up to 9.2 GPa *in situ* using falling sphere viscometry both along the fayalite liquidus and along an isotherm. The viscosity of fayalite melt was found to decrease by a factor of 2.5 along the liquidus, and the results from experiments carried out along the isotherm suggest that temperature has very little influence on fayalite melt viscosity at high pressure. The viscosity decrease with increasing pressure is likely due to the increase of Fe-O coordination with pressure (Sanloup et al., 2013a). In polymerized melts, the structural transformation of tetrahedrally coordinated cations (such as Al^{3+}) to higher species has often been cited as the cause of the decrease in viscosity with pressure of polymerized silicate melts, however this study is the first to record an initial decrease in viscosity with increasing pressure in a depolymerized silicate melt. Previously, it has often been assumed that the viscosity of depolymerized silicate melts will not decrease at depth. This work shows that this assumption is not appropriate, and that the behaviour of silicate melts at depth should be

considered on an independent basis for melts of varying composition. The viscosity of silicate melts at high pressure will be strongly dependent on the individual melt composition and structure.

Part II

The evolution of the Iceland mantle plume

1 Introduction

1.1 Background

1.1.1 Mantle melting and the role of temperature

Mantle melting is an extremely important process that is fundamental to global magmatism and the formation of the Earth's crust. There are three principal mechanisms that will cause the steady-state mantle to melt: (i) adiabatic decompression of normal mantle; (ii) lowering the temperature of the mantle solidus due to the addition of volatiles; and (iii) anomalous thermal perturbation of the geotherm. Partial melting beneath mid-ocean ridges (MORs) and hotspots is predominantly the result of adiabatic upwelling of the asthenosphere to shallow levels, resulting in the intersection of the mantle geotherm with the mantle solidus. At hotspot locations, this process occurs due to a thermal anomaly. The magnitude of the thermal anomaly is a critical variable that influences the dynamics of mantle melting as well as the volume and composition of the magmatic products. Being able to accurately constrain the mantle temperature at such locations is therefore fundamental to our understanding of mantle melting and its role in shaping the surface of our planet.

1.1.2 Mantle plumes

It is well established that mantle plumes are thermal anomalies in the mantle (e.g. Griffiths and Campbell, 1990; Campbell, 2007). Mantle plumes are here defined as channels of buoyancy driven flow, originating from deep within the mantle or at the core-mantle boundary (CMB). They were first proposed by Wilson (1963) and Morgan (1971) in order to explain time-progressive volcanic chains such as

the Hawaiian-Emperor seamount chain. It is now thought that mantle plumes are responsible for the huge outpourings of predominantly basaltic magmas not linked to normal plate-boundary magmatism that form large igneous provinces (LIPs). After oceanic spreading centres, LIPs represent the most voluminous accumulations of mafic material on the Earth's surface and are therefore an important mechanism for growing the Earth's crust over geological time (Coffin and Eldholm, 1994). LIPs occur on the continents and in the oceans (Figure 1.1) and include continental flood basalts (e.g. the Deccan and Siberian Traps), volcanic passive margins (e.g. parts of the North Atlantic Igneous Province) and oceanic plateaus (e.g. the Ontong Java Plateau and Iceland) (Ernst, 2014).

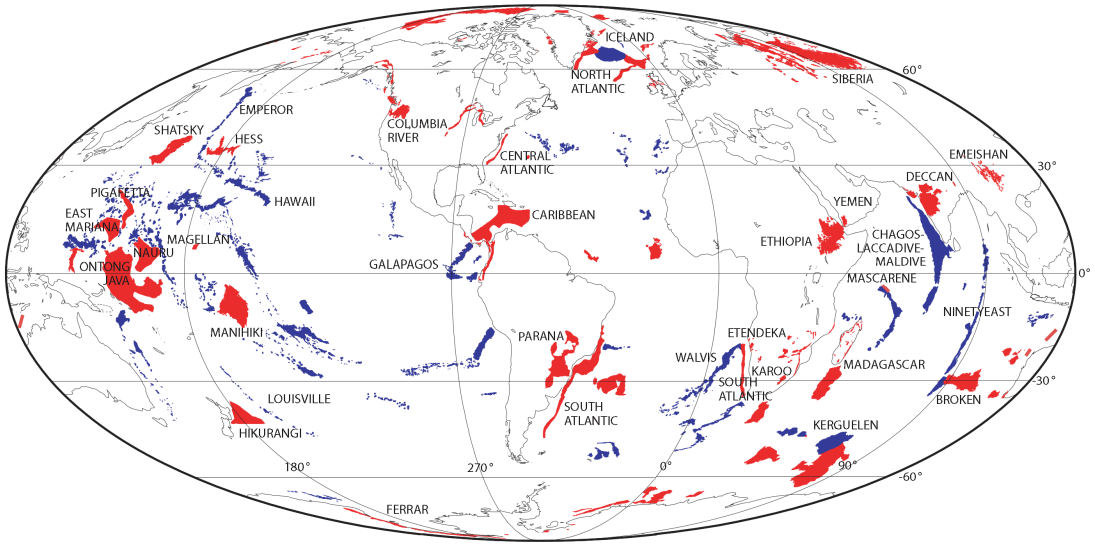

Figure 1.1: Phanerozoic distribution of global LIPs. Red = LIP volcanism related to plume heads, blue = LIP volcanism related to plume tails. From Coffin et al. (2001).

Plume theory

High pressure experiments on iron-nickel alloys show that the core must be several hundred degrees hotter than the overlying mantle (Boehler, 1993). Such a large temperature difference will produce an unstable thermal boundary layer between the core and the mantle, which will heat the overlying mantle and lower its density until it breaks away to form buoyant plumes (Campbell, 2007). Plume theory is supported by dynamo theory, because the Earth's magnetic field requires a

large heat flow from the core (Gubbins et al., 2003) and plumes are the only mechanism by which this can occur efficiently. In order for the heated material in the boundary layer to rise, it must be buoyant enough to overcome the viscosity of the overlying mantle. A new rising plume will develop a large head followed by a narrow tail, which requires less buoyancy to rise when following the existing pathway of the head (Campbell, 2007).

As the plume rises through the mantle, it grows through two mechanisms (Griffiths and Campbell, 1990). Firstly, material from the high temperature, low viscosity tail rises faster than the head which therefore swells to form a characteristic mushroom shape (Figure 1.2). Secondly, the rising plume head continually heats and entrains material from the surrounding mantle and becomes a mix of high temperature tail material and heated surrounding mantle material, and consequently has a lower temperature than the plume tail. When the plume head arrives at the base of the lithosphere, it has an excess temperature of several hundred degrees and quickly flattens out to form a disk (Figure 1.2) covering an area of 2000-2500 km (Campbell, 2007).

Many studies have identified a difference in mantle potential temperature between MOR and LIP settings of 100-300°C using a variety of petrological approaches (Larsen and Pedersen, 2000; Herzberg and O'Hara, 2002; Putirka, 2005; Herzberg et al., 2007; Putirka et al., 2007; Herzberg and Asimow, 2008; Herzberg and Gazel, 2009; Coogan et al., 2014). The anomalously high temperatures can result in dynamic uplift of the lithosphere and, if the hot mantle can upwell to shallow enough levels to undergo decompressional melting, vast outpourings of basaltic magma over an area with a diameter of ∼2000 km. With time, melt becomes focussed into a narrow mantle upwelling in the plume tail that is connected to the plume-head stage of activity by a volcanic chain (Griffiths and Campbell, 1990; Campbell, 2007).

Mantle plumes and helium isotopes

Helium isotope ratios are a useful and sensitive tracer of mantle processes (Hilton and Porcelli, 2003). Helium has two isotopes: ^{3}He, which is primordial, and ^{4}He, which is predominantly produced by radioactive α-particle decay of the ^{238}U,

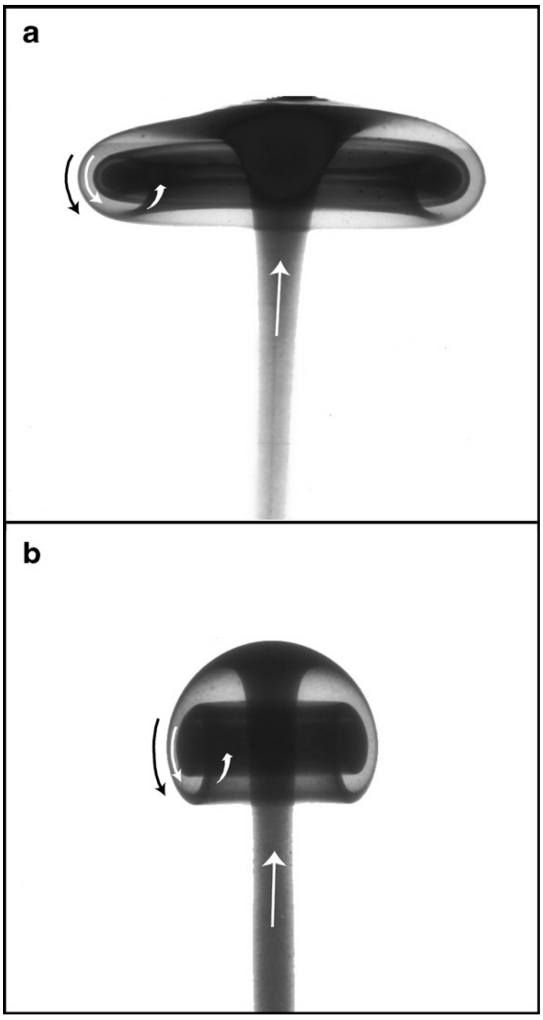

Figure 1.2: Photograph of a laboratory experiment (Griffiths and Campbell, 1990) of a thermal mantle plume (a) after the head flattens out at the base of the lithosphere and (b) part-way through its ascent. White arrows show motion within the plume and the black arrow shows the direction of motion of the surrounding material. The dark colouring indicates hot material from the thermal boundary layer and lighter shades represent cooler entrained material. From Campbell (2007).

^{235}U, ^{232}Th and ^{147}Sm decay series. ^{3}He is not produced in the Earth's mantle, so high ^{3}He/^{4}He values represent a long-lived primordial source (Porcelli and Ballentine, 2002) that has been stored since the Earth's formation. It has long been recognised that a number of plume-related ocean island basalt (OIB) and LIP provinces have higher ^{3}He/^{4}He than that of mid-ocean ridge basalts (MORB) (e.g. Kurz, 1982; Hart et al., 1992; Stuart et al., 2003), which have values of 8 $\pm$ 1 R/R_a, where R=^{3}He/^{4}He and R_a=1.39 x 10^{-6}, the atmospheric value. It is on this basis that many have argued in the past for two-layer mantle convection and

that plumes sample a deep reservoir that has remained undegassed and convectively isolated from the upper mantle MORB source since Earth's formation (e.g. Kurz, 1982; Kellogg and Wasserburg, 1990; O'Nions and Tolstikhin, 1994; Porcelli and Wasserburg, 1995; Gonnermann and Mukhopadhyay, 2007). However, high $^{3}He/^{4}He$ is not ubiquitous in mantle plumes and so called 'low $^{3}He/^{4}He$' plumes have also been identified (e.g. Class et al., 2005).

A number of workers have attempted to characterise the high $^{3}He/^{4}He$ mantle reservoir using trace element and Sr-Nd-Pb-Hf isotope ratios (e.g. Hofmann, 1997; Class and Goldstein, 2005; Starkey et al., 2009) however, these studies have indicated that the compositional range of the high $^{3}He/^{4}He$ source is similar to that of the upper mantle and that the high $^{3}He/^{4}He$ reservoir on Earth does not have a unique composition for any incompatible trace element or isotopic tracer. In addition, recent developments in seismic tomographic imaging provide strong evidence for whole mantle convection. Subducting slabs have been shown to penetrate to well below the 670 km discontinuity (van der Hilst et al., 1997), while low seismic velocities extending to the core-mantle boundary (CMB) have been identified at many hot spot locations (French and Romanowicz, 2015). In summary, the combination of both geochemical and geophysical evidence poses a real problem for the preservation of primordial ^{3}He in the mantle and seems to rule out the possibility of a discrete, isolated mantle reservoir. The source of the high $^{3}He/^{4}He$ reservoir therefore remains enigmatic, and its relationship mantle plumes at hotspot locations is an outstanding problem in geosciences.

1.1.3 Alternative theories

A number of workers have argued that thermal anomalies are not required to explain LIP volcanism. Some suggest that melting of more fusible mantle is responsible for magmatism at LIPs. For example, Foulger and Anderson (2005a) and Foulger et al. (2005b) suggest that melting of highly fertile subducted Iapetus oceanic crust associated with the Caledonian orogeny is responsible for the enhanced melting beneath Iceland. Still others argue that all large continental flood basalt provinces are found on the margins of thick cratonic lithosphere (usually Archean), which focuses strain, and that the subsequent upwelling is

capable of producing large quantities of basaltic magma (King and Anderson, 1995). However, these ideas are contrary to most workers' views on LIPs and many researchers now accept that mantle plumes play an important role in their formation (e.g. White and McKenzie, 1989). Recent work by Herzberg and Gazel (2009) and Coogan et al. (2014) identified the presence of thermal anomalies in the order of several hundred degrees at multiple LIP locations using completely independent methodologies. When this evidence is added to that from seismic tomographic imaging, it seems unlikely that mantle plumes did not play an important role in volcanism at major LIP locations.

1.1.4 Mantle melting and temperature

It is well established that the mantle is highly heterogeneous (Sun and McDonough, 1989) and is likely to consist of blobs or streaks of fertile material in a more depleted matrix (e.g. Hofmann, 1997; Fitton, 2007). Such heterogeneity is sampled at both hotspots (e.g. Hofmann, 1997, 2003; Dasgupta et al., 2010) and MORs (e.g. Dosso et al., 1999; le Roux et al., 2002; Salters and Dick, 2002). Ito and Mahoney (2005a) showed that it is possible to explain many of the differences in isotopic and trace element composition of MORBs and OIBs without the need for OIBs to sample a convectively isolated layer, simply by melting of a heterogeneous mantle source.

Temperature is a fundamental parameter to melting dynamics at MOR and hotspot locations. At fixed lithosphere thickness, it controls the degree of melting and therefore the magma composition. During mantle melting, it is the enriched source components that begin to melt first (Figure 1.3) and some of these are predicted to be almost 100% melted before the depleted matrix even begins to melt significantly. The relative degrees to which each source is sampled (and therefore the composition of the erupted basalt) is dependent on the interplay between mantle temperature and lithosphere thickness. At MORs, the asthenospheric mantle can upwell almost to the surface, resulting in high degrees of melting and efficient sampling of the depleted matrix at normal mantle temperatures. At hotspot locations where there is a thick lithosphere, small temperature anomalies result in efficient sampling of the more fusible enriched source, whereas a large

temperature anomaly will result in the melting of the depleted matrix (Figure 1.3a) and the magma will subsequently appear more 'MORB-like'. Essentially, the higher the temperature, the more depleted the composition of a given magma will be. Where a mantle plume rises beneath a MOR or a very young oceanic plate, temperature will have less of an influence on the incompatible trace element and isotope composition of the melt because the degree of melting will be higher and the depleted mantle source plays a more important role.

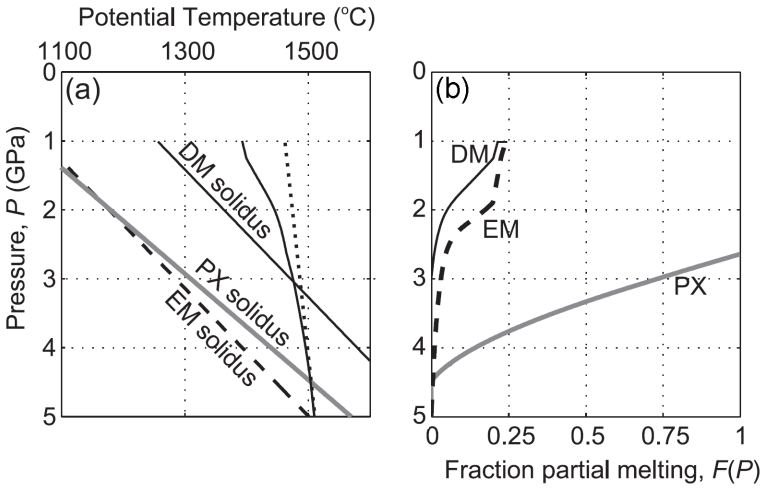

Figure 1.3: (a) Solidi for depleted mantle (DM), which behaves as nominally dry peridotite and is assumed to be most depleted in incompatible trace elements and is isotopically similar to 'DMM' (Hart et al., 1992), and the enriched mantle sources: enriched mantle (EM), which is comparable to adding 0.05 wt% H_2O to DM, is enriched in the most incompatible elements and has isotopic characteristics similar to the proposed 'EM1' or 'EM2' end-members (Hofmann, 1997) and pyroxenite mantle (PX) which represents the compositionally diverse array of mantle lithologies rich in pyroxene with incompatible trace elements similar to MORB and is isotopically similar to 'HIMU' (Hofmann, 1997). The adiabat (dotted line) and predicted temperature profile (black curve) are shown for a potential temperature of 1450 °C. Melting of EM and PX begins at much greater depths compared to DM. (b) Predicted melting fractions as a function of pressure for each lithology. PX melts to 100% quickly at high pressures and will therefore have a dominant influence on the composition of deep, low-degree melts. Modified from Ito and Mahoney (2005a).

As well as having a strong control on the geochemistry of magmas generated at hotspot locations, mantle temperature is crucial to the volume of melt produced (Figure 1.4) both at hotspots and MORs. Raising the mantle temperature increases the degree to which the geotherm oversteps the mantle solidus, resulting in a higher degree of partial melting. Relatively small changes in mantle temperature can lead to a considerable increase in the production of basaltic melt

(White and Lovell, 1997). For example, at an oceanic spreading centre, an increase in mantle potential temperature of as little as 50°C from 1280°C to 1330°C results in a 50% increase in the volume of basaltic crust generated by decompressional melting of the upwelling mantle (White and Lovell, 1997). This would translate to dramatic changes in the bathymetry of the seafloor. Being able to accurately constrain the temperature of the mantle is therefore fundamental to our understanding of the generation of the Earth's crust.

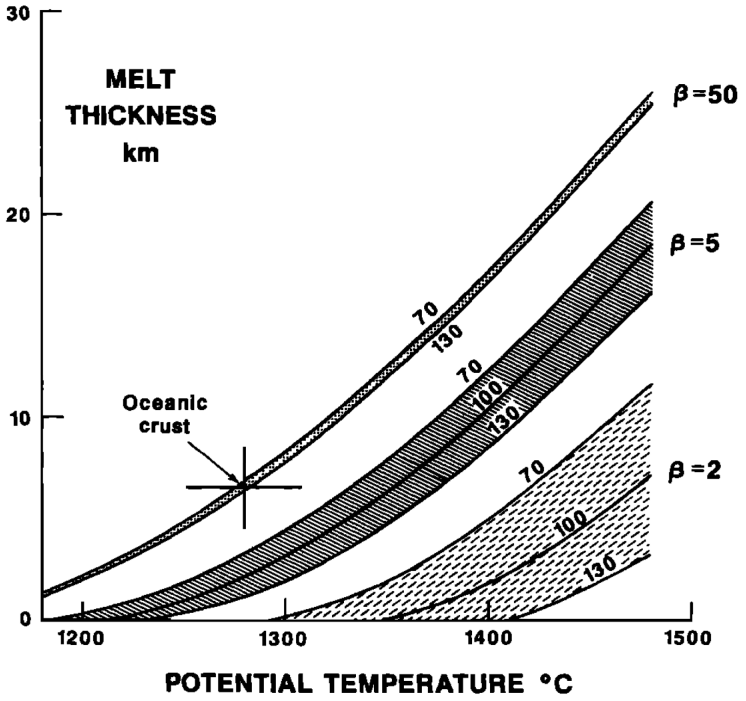

Figure 1.4: Thickness of basaltic melt produced by adiabatic decompression of the asthenospheric mantle over a range of potential temperatures. The importance of mantle temperature is clearly demonstrated whereby relatively small increases result in very large changes in the volume of basaltic crust generated. Curves for initial thickness of the mechanical boundary layer of 70, 100 and 130 km are given, corresponding to lithospheric thicknesses of 87, 118 and 149 km, respectively. Thinning by factors of 2, 5 and 50 are shown. The cross indicates the thickness of oceanic crust at normal mantle temperatures. From White and McKenzie (1989).

1.1.5 Project aims and motivation

The North Atlantic Igneous Province (NAIP) is unique in the fact that it is the surface expression of a major mantle plume with a complete magmatic history.

Present-day magmatism at Iceland represents the plume-tail phase of activity and is connected to the Atlantic Paleogene igneous provinces representing the plume-head phase of activity by a hotspot trail (the Greenland-Iceland-Faeroe Ridge). In addition, the highest $^{3}He/^{4}He$ volcanic rocks on Earth are found in the Paleogene picrites of West Greenland and Baffin Island (Stuart et al., 2003; Starkey et al., 2009) and high $^{3}He/^{4}He$ magmas are still erupted on Iceland today (Kurz et al., 1985; Breddam et al., 2000; Macpherson et al., 2005a). The main aim of this project is to exploit the ideal opportunity provided by the NAIP to investigate the relationship between temperature, mantle melting dynamics, and helium isotopes within a major mantle plume throughout its lifetime. In order to achieve this, a suite of primitive volcanic rocks spanning the spatial and temporal range of the NAIP will be examined. The samples are all Mg-rich, highly primitive igneous rocks and will therefore contain the most information about the mantle temperature. The sample suite includes the high $^{3}He/^{4}He$ picrites from Baffin Island and West Greenland, a suite of picrites from Skye, Rum and Mull, the 13-14 Ma high $^{3}He/^{4}He$ picrites from Iceland, and zero-age picrites and primitive basalts from Iceland. This study is the first to provide a detailed petrologic approach to determining the mantle temperature of the NAIP throughout its magmatic history, from the onset of volcanism between 62 and 61 Ma, through to the present day. To do this, three main approaches for calculating magmatic temperature are used: the traditional technique of olivine-melt thermometry, a forward mantle melting model, and the newly developed Al-in-olivine thermometer. This work is the first to examine all techniques and provide a detailed comparison of the results. The temperature results will then be compared with existing and new $^{3}He/^{4}He$ data in order to gain a better understanding of their relationship within a mantle plume and how they relate to mantle dynamics on a global scale.

1.2 The North Atlantic Igneous Province

The NAIP is one of the most extensively studied LIPs in the world. The province extends from Baffin Island in Eastern Canada, to the British Isles, a pre-drift distance of nearly 2000 km. Estimates of the total volume of magma erupted exceed 6 x 10^{6} km^{3} (Saunders et al., 1997), making the NAIP one of the largest LIPs on Earth. Magmatism began between 62 and 61 Ma (Table 1.1), and has

continued until the present day, with two major phases of volcanism that began at ∼62 and ∼56 Ma, respectively (Saunders et al., 1997). The NAIP comprises the flood basalt provinces of Baffin Island, West Greenland, East Greenland, Faeroe Islands and the British Isles, the extensive offshore seaward dipping reflector series (SDRS) erupted along the east Greenland and northwest Europe continental margins and the Greenland-Iceland-Faeroe ridge (Figure 1.5).

Table 1.1: Onset of Phase 1 magmatism across the NAIP at different locations. Data from [a]Ganerød et al. (2010), [b]Pedersen et al. (2002), [c]Storey et al. (2007).

Location	**Age (Ma)**
West Greenland[a]	61.7 ± 0.5
Baffin Island[b]	62-61.7
British Tertiary Igneous Province[a]	62.6 ± 0.6
East Greenland[c]	59.2 ± 1.4 Ma
Faeroes[a]	60.1 ± 0.6

1.2.1 The NAIP and the mantle plume model

The NAIP conforms to many of the predictions of the mantle plume model (Griffiths and Campbell, 1990; Campbell, 2007). Firstly, it is predicted that plumes consist of a large head, followed by a narrow tail, so that initial volcanism is the most voluminous and erupts over a period of only a few million years, followed by lower eruption rates of narrow volcanic chains which connect the initial flood basalt province to melting in the narrower plume tail. In the North Atlantic, the initial phases of volcanism prior to and during continental separation were the most voluminous and occurred over a narrow time period, with most of Phase 1 and Phase 2 volcanism each lasting only 3-4 million years (Saunders et al., 1997). The Greenland-Iceland-Faeroe Ridge (GIFR) represents the subsequent hotspot trail of the plume tail and connects the flood basalt provinces representing the plume-head stage of activity to the present-day location of the plume beneath Iceland.

The arrival of an anomalously hot plume head in the upper mantle is predicted

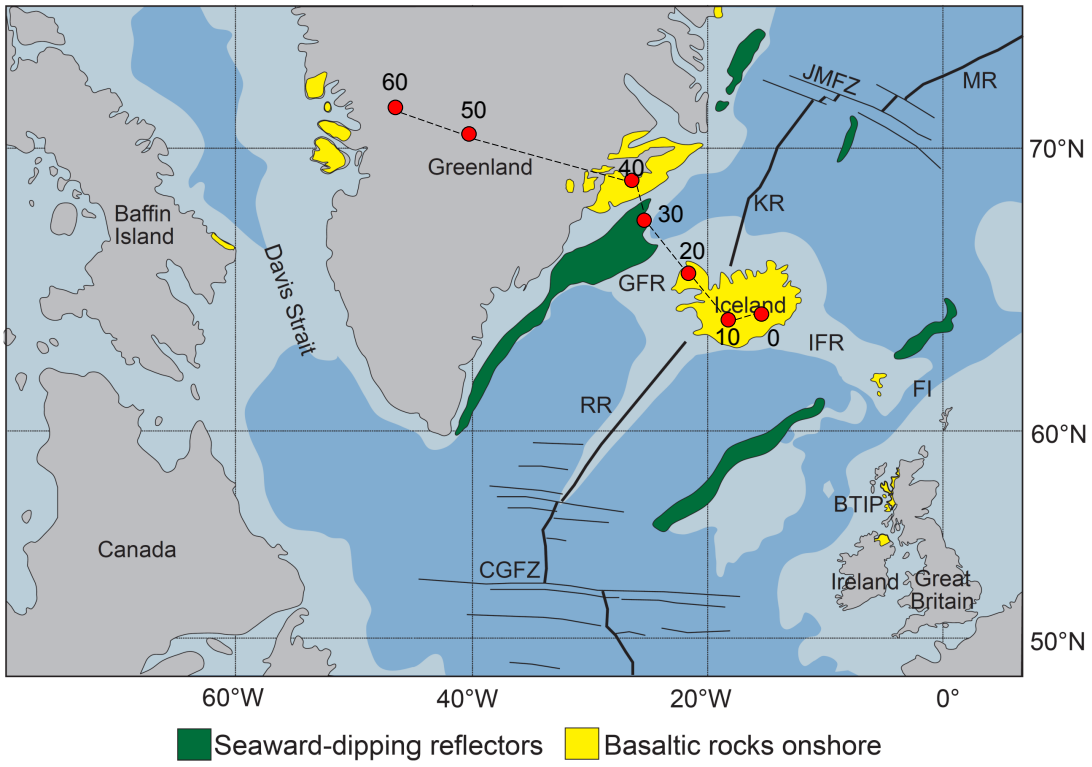

Figure 1.5: Map of the North Atlantic Igneous province and location of onshore and offshore plateau basalts and SDRS. Plume track from 60 Ma to present is shown by the dashed line as calculated by Lawver and Müller (1994). CGFZ = Charlie Gibbs Fracture Zone, RR = Reykjanes Ridge, GFR = Greenland-Faeroes Ridge, IFR = Iceland-Faeroes Ridge, FI = Faeroe Islands, KR = Kolbeinsey Ridge, JMFZ = Jan Mayen Fracture Zone, MR = Mohns Ridge, BTIP = British Tertiary Igneous Province.

to produce domal uplift at the surface (Griffiths and Campbell, 1990; Campbell, 2007). Uplift begins when the top of the plume reaches the upper mantle and is at its maximum when the plume head is at 250 km below the surface. Since this is too deep for extensive melting to occur, the onset of voluminous magmatism is therefore preceded by a period of uplift. For a plume head with an average excess temperature of 100°C, this uplift is estimated to be 1000 ± 500 m close to the plume axis and will decrease away from it (Griffiths and Campbell, 1991a). Evidence for uplift preceding Phase 1 volcanism can be found across the NAIP, for example, around the British Isles, where Upper Cretaceous marine sediments are overlain by Paleocene subaerial flood basalts (Emeleus and Bell, 2005). At other localities across the NAIP, including Northern Ireland (Saunders et al., 2007), East Greenland (Clift and Turner, 1995; Ukstins Peate et al., 2003) and West Greenland (Dam et al., 1998), the uplift is generally estimated to be in the

order of 400 m.

Another prediction of the plume model is that picrites should dominate early products of flood volcanism. Mantle entrainment results in a heterogeneous temperature distribution within the plume head, and the hottest (and hence most buoyant) material from the plume source forms the top of the head (Figure 1.2), and so is the first to ascend to a level where it can melt. This hot Mg-rich material will melt to form picrites, and so if the magmas do not stall and fractionate within the crust, picrites will dominate the early products of flood volcanism, becoming more uncommon as cooler material reaches a level where it can melt. Picrites are predicted to be most abundant near the centre of the plume and decrease towards the margin. In the NAIP, picrites dominate early volcanism in West Greenland and Baffin Island, with high-Mg successions reaching thicknesses of around 1800 m (Larsen and Pedersen, 2000) and 300 m (Francis, 1985) at each location respectively.

1.2.2 History and geology of the NAIP

During the Mesozoic, stretching and thinning of the lithosphere had produced a series of offshore basins in the North Atlantic region (Srivastava and Tapscott, 1986) and these were partly precursors to continental separation. Seafloor spreading began in the North Atlantic at ∼130 Ma, when Iberia separated from Newfoundland (Saunders et al., 1997). Spreading extended northwards into Rockall Trough, and was underway everywhere south of Greenland by 84 Ma. At this time, spreading ceased in the Rockall Trough (Kristoffersen, 1978; Roberts et al., 1981), and by 61 Ma, the axis of break-up had shifted westwards and was propagating northwards between Labrador and Greenland.

Prior to ∼62 Ma, there is little evidence of large-volume volcanic activity in the region, but between ∼62 and 59 Ma (Table 1.1), a massive flare-up of volcanic activity occurred (Phase 1), producing large volumes of picrites, basalts and associated intrusives, in Baffin Island, West Greenland, SE Greenland, East Greenland, the Faeroe Islands and the British Isles, across a a disk-shaped region 2000 km in diameter (Figure 1.6; Saunders et al., 1997). Such a sudden outburst in large-volume volcanism across such a wide area is thought to re-

quire a widespread sudden increase in mantle temperature, and is attributed to the arrival of the mantle plume now situated beneath Iceland (e.g. White and McKenzie, 1989; Saunders et al., 1997). Beneath the pre-existing thin spots, hot mantle could decompress to shallow enough levels to undergo melting (Thompson and Gibson, 1991).

The second main phase of magmatism (Phase 2) followed a brief hiatus in volcanism of up to 3 million years and accompanied continental break-up and the separation of Greenland from NW Europe (Figure 1.6; Saunders et al., 1997). The extent to which the plume influenced continental separation is unclear, but the main axis of seafloor spreading moved to the east of Greenland at ∼56 Ma, soon after the arrival of the plume (Saunders et al., 1997). Magmatism at the initial stages of plate separation during this second phase of volcanism was the most intense observed in the NAIP (Saunders et al., 1997). Flood basalts reaching thicknesses of >5 km were erupted along the East Greenland coast (e.g. Larsen et al., 1989) and at the Faeroe Isles (Waagstein, 1988), while even thicker and more extensive SDRS were erupted offshore along the continental shelves of east Greenland and Norway, and at Rockall (Ritchie and Hitchen, 1996).

Plate tectonic reconstructions (Lawver and Müller, 1994) place the centre of the plume close to the centre of Greenland between 60 and 50 Ma (Figure 1.5 and 1.6), however others have placed it near to the east coast (Brooks, 1973; Brooks and Nielsen, 1982; White and McKenzie, 1989). The plume axis crossed the East Greenland coast at 40-35 Ma (Lawver and Müller, 1994), reaching the Mid-Atlantic Ridge at ∼25 Ma (Vink, 1984). The Greenland-Iceland-Faeroes ridge is a hotspot 'track' and connects Iceland to the Phase 1 and Phase 2 volcanic provinces that represent the plume-head stage of activity. It comprises a broad strip of shallow ocean with thicker-than-average oceanic crust of 20-35 km, the result of high volumes of melt and anomalously hot material uplifting the ocean floor (White and Lovell, 1997; Darbyshire et al., 1998). Since ∼25 Ma, the Mid-Atlantic Ridge has remained locked above the plume axis, and the hot mantle in the core of the plume beneath the spreading axis has led to extensive melting, creating a thick oceanic plateau with Iceland representing the subaerial extent of the plateau. Spreading continued in the Labrador Sea at a reduced rate until ∼36 Ma (Saunders et al., 1997), leaving only one active spreading axis, that rapidly propagated northwards between Norway and Greenland into the Arctic Ocean

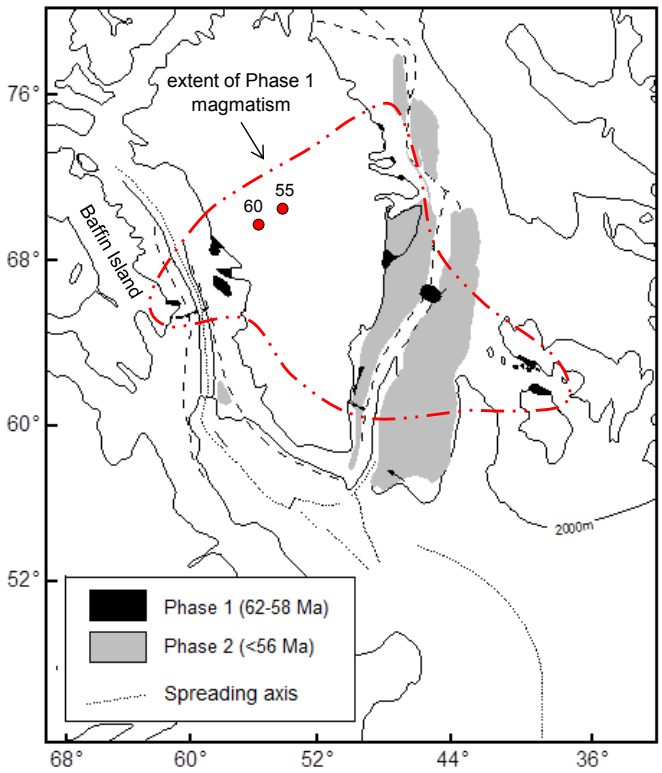

Figure 1.6: Tectonic reconstruction of the North Atlantic Igneous Province at ~61 Ma showing the distribution of Phase 1 and 2 magmatism. The dashed line indicates the extent of Phase 1 magmatism. The circles indicate the calculated locations of the centre of the Iceland plume at 55 and 60 Ma, as calculated by Lawver and Müller (1994). Modified from Saunders et al. (1997).

and remains active today.

1.2.3 West Greenland

Phase 1 volcanism in West Greenland (Figure 1.7) began at 61.7 ± 0.5 Ma (Ganerød et al., 2010) and lasted around one million years (Pedersen et al., 2002). The erupted volcanic pile has an estimated total volume of 68,000 km^3 (Larsen and Pedersen, 2009). It is divided into two parts, a lower part comprising dominantly picrites of around 22,000km^3, and an upper part consisting of basalts (Clarke and Pedersen, 1976). The picrites are formally known as the Vaigat Formation and are very Mg-rich, ranging up to 30 wt% MgO (Larsen and Pedersen, 2000). The lavas were erupted onto Cretaceous and Tertiary sediments of the Nuussuaq Basin, except in the far east where they were erupted directly onto the Precam-

brian basement (Pedersen et al., 1993, 1996, 1998). Five picrite samples with high $^{3}He/^{4}He$ were selected for this study and form part of the Vaigat Formation on Disko Island and the Nuussuaq Peninsula.

1.2.4 Baffin Island

The Baffin Island volcanic rocks outcrop in a narrow fringe running roughly NW-SE along 90 km of coast from Cape Searle southwards (Figure 1.7), and are considered to be stratigraphically equivalent to the West Greenland volcanic sequence (Upton, 1988). They have a much smaller areal extent and thickness than their West Greenland counterparts, comprising a 300 m succession of picrites and an upper part made up of basalt flows, with a total thickness not exceeding 750 m (Francis, 1985). As in West Greenland, they were erupted onto Tertiary sediments and Precambrian basement and their magnetic polarity implies an age of 62.0-61.7 Ma (Pedersen et al., 2002). The West Greenland and Baffin Island volcanic provinces contain an unusually high proportion (30-50% by volume) of picrites compared to other continental flood basalt provinces (Gill et al., 1992). Seven picrite samples from Baffin Island were selected for this study that were collected from Padloping Island, Durban Island and Akpat Point.

1.2.5 The British Tertiary Igneous Province

The British Tertiary Igneous Province (BTIP) is made up of many separate areas of volcanic activity that was most vigorous in the Inner Hebrides and north-west Scotland, but also extended to southern Scotland, northeast Ireland, northeast England and the Outer Hebrides. The volcanic activity took many forms and involved a variety of magmas and eruption styles, and took place from 62.6 $\pm$ 0.6 Ma (Ganerød et al., 2010) to 55.7 $\pm$ 0.1 Ma (Emeleus and Bell, 2005). The remains of extensive accumulations of basaltic lava flows cover large areas of Skye, Mull and northeast Ireland. Central intrusive complexes consisting of peridotite, gabbro, granite and other rock types, occur in a narrow north-south trending zone approximately 40 km wide, from Skye to the Bristol Channel, and at several other places in the northeast Atlantic (e.g. St Kilda). In Scotland, the main cen-

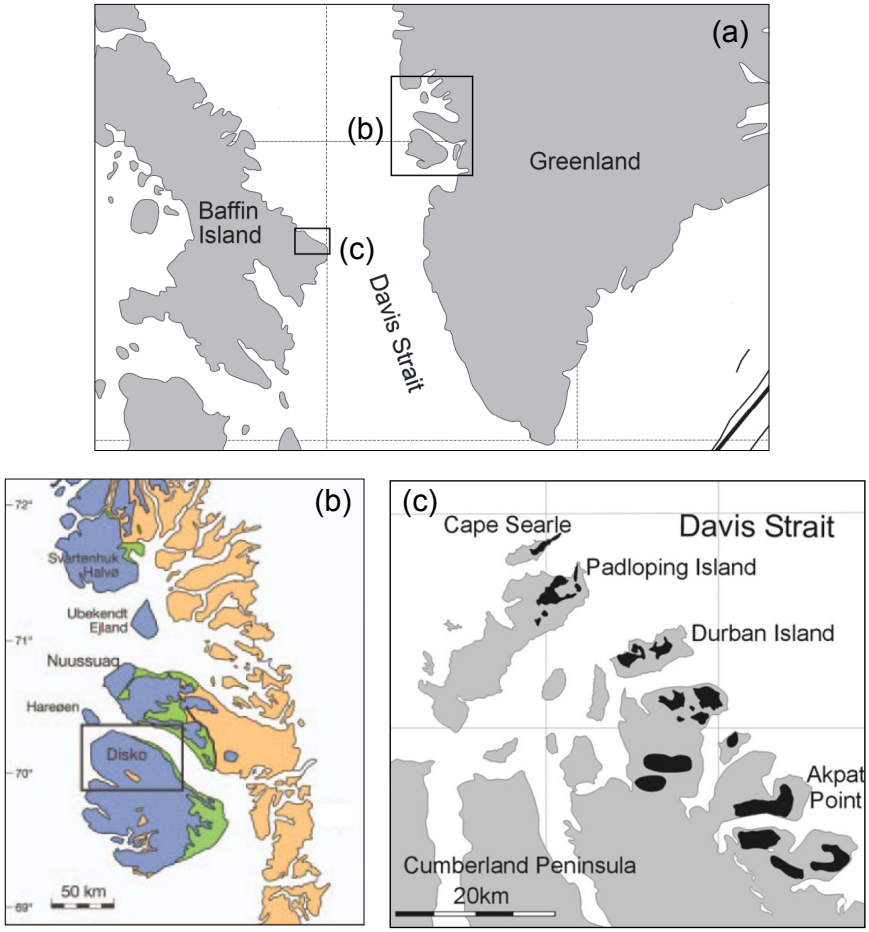

Figure 1.7: Maps showing the location of Phase 1 onshore volcanic rocks in (b) West Greenland and (c) Baffin Island. From Starkey et al. (2009).

tral complexes are found on Skye, Rum, Ardnamurchan, Mull and Arran. Several northwest-southeast trending regional dyke swarms cross the region, reflecting a northeast-southwest extensional stress system (England, 1988), and extend from the Outer Hebrides and northeast Ireland to north Yorkshire, north Wales and parts of central England, intensifying in the vicinity of the central complexes. Figure 1.8 shows the location of the main igneous activity in Scotland and northeast Ireland.

Thinning of the lithosphere during the late Paleozoic and Mesozoic produced a series of major sedimentary basins that trend approximately north-south (Figure 1.9). During the Permian and Triassic, thick sequences of desert and fluvial sandstones accumulated, with a progressive change to marine conditions during

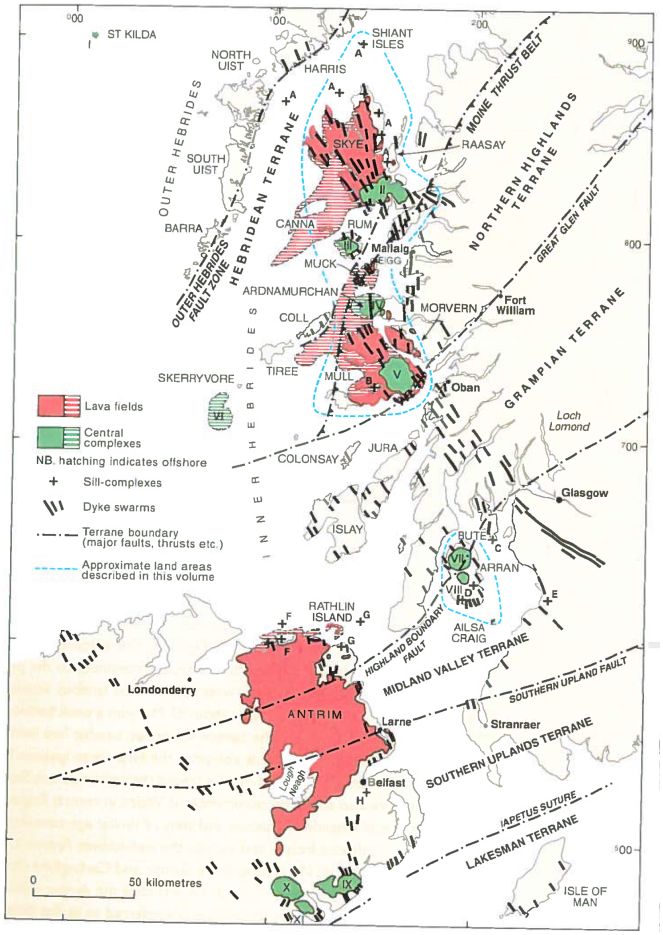

Figure 1.8: Map showing the positions of the Paleogene central complexes, sill complexes, lava fields and dyke swarms in western Scotland and northeast Ireland. From Emeleus and Bell (2005).

the Jurassic, followed by the accumulation of marine sandstones and chalks during the Cretaceous (Emeleus and Bell, 2005). These sedimentary basins had an important structural control on the BTIP, as they appear to have influenced the location of the central complexes, and possibly the accumulation of the lava fields. The central complexes are situated where Mesozoic or older Paleozoic structures cross the north-south trending zone. For example, the Mull Central Complex occurs on the trace of the Great Glen Fault, and the Skye and Rum central complexes are situated close to the Camasunary Fault, a major structure forming part of the boundary of the Inner Hebrides Basin (Emeleus and Bell, 2005).

Rapid regional uplift and resultant erosion between the Late Cretaceous and the early Paleocene gave rise to a land surface on which the first volcanic products

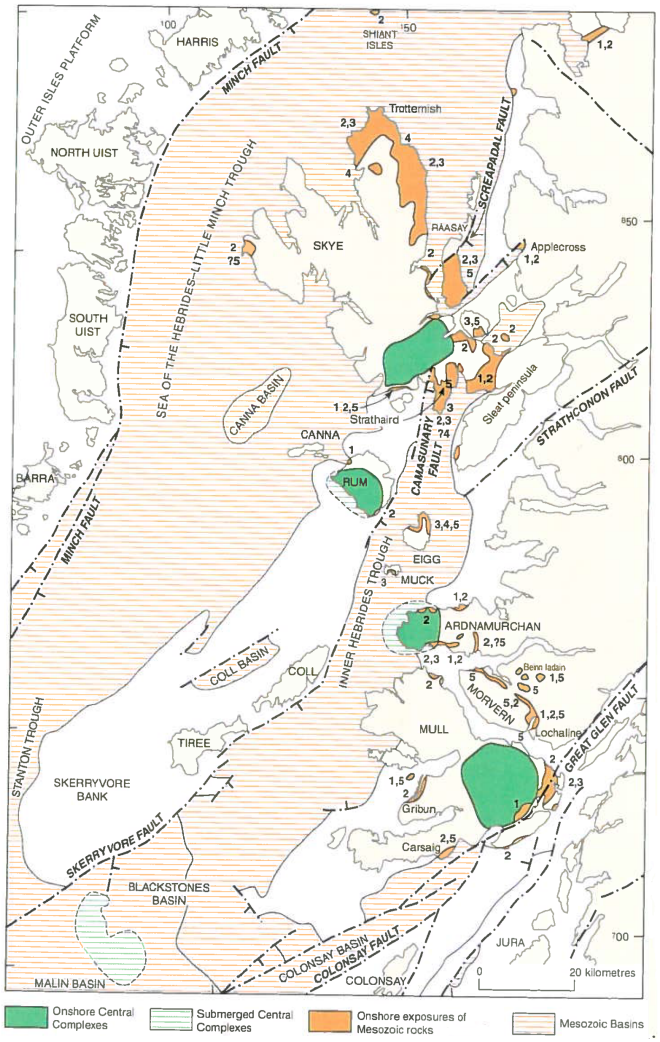

Figure 1.9: Map of the Inner Hebrides showing the position of offshore Mesozoic basins, the locations of Mesozoic rocks onshore and the positions of the Paleogene central complexes. 1 Permo-Triassic; 2 Lower Jurassic, 3 Middle Jurassic, 4, Upper Jurassic; 5 Upper Cretaceous. From Emeleus and Bell (2005).

were erupted. For example, on Mull, the earliest lava flows were erupted onto a land surface of Late Cretaceous marine sediments. The lavas are thick, dominantly basaltic flows that were fed from the multitude of dyke swarms intruding the BTIP, forming fissure eruptions similar to those occurring on present-day Iceland. Today the dyke swarms are seen to intrude almost every volcanic product in the BTIP, and so it is likely that lava eruption continued throughout the duration of magmatic activity.

The central complexes generally postdate the lava fields and represent a funda-

mental change in the character of igneous activity, from the widespread feeders of the dominantly basaltic lava fields, to localised and intense volcanic activity at compositionally diverse central volcanoes, with intrusive rocks ranging in composition from peridotite to gabbro to granite. The central complexes are the eroded remains of the roots of major volcanoes at these centres. Radiometric and paleomagnetic dating indicate that individual lava fields were erupted in little over one million years, and that the life span of individual central complexes may have been equally short (Emeleus and Bell, 2005).

Skye

On Skye, most of the volcanic activity is thought to have occurred in less than 3 million years, although the total duration was ∼7 million years (Chambers and Pringle, 2001). The first volcanic activity on Skye was the eruption of a 1.2-1.7 km thick succession of flood basalts, exposed in the north, west and central areas of Skye (Figure 1.10) over an area of 1500 km^2 (Thompson, 1982; Emeleus, 1991; England, 1994; Williamson and Bell, 1994). The lavas are thought to have been erupted over an interval of less than 1.6 million years (Emeleus and Bell, 2005), beginning at 59.8 ± 0.4 Ma (Ganerød et al., 2010).

Towards the end of the fissure-style flood volcanism, a central intrusive complex developed in which four magmatic centres successively formed as the focus of igneous activity migrated eastward. From oldest to youngest, these are the Cuillin centre, which is dominantly mafic, and the Srath na Creitheach, Western Red Hills and Eastern Red Hills centres, which are dominantly granitic (Emeleus and Bell, 2005). The emplacement of gabbros of the Cuillin Centre are dated at 58.9 ± 0.1 Ma (Hamilton et al., 1998) and intrude the Skye Lava Group. Ages of 58.6 ± 0.3 Ma (Chambers and Pringle, 2001) and 53.5 ± 0.8 Ma (Dickin, 1981) have been reported for granites from the Western Red Hills and Eastern Red Hills centres respectively.

The Cuillin complex represents the deep core of a large basaltic volcano. It has an average diameter of 8 km and the overlying succession comprising the original volcano, estimated to have had a thickness of 2 km (Tibaldi et al., 2011), has been completely removed by erosion. The complex consists of gabbroic and peridotitic

ring-intrusions, some of which exhibit well-developed mineral layering. In general, the intrusions are older around the margin of the centre and progressively young inwards (Emeleus and Bell, 2005). The main intrusions are cut by numerous cone sheets which are in turn cut by northwest trending basaltic dykes. The picrite samples from Skye studied here are a suite of olivine-rich dykes (up to 30 cm wide) that intrude the outer gabbros of the Cuillin central complex (Figure 1.10) and were first described by Drever and Johnston (1958).

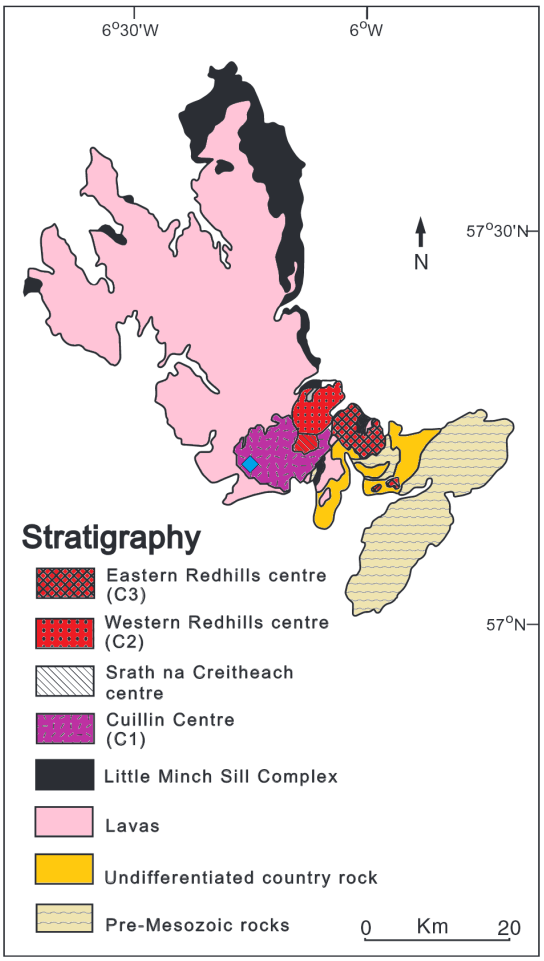

Figure 1.10: Simplified geological map of Skye showing the main divisions of Tertiary igneous rocks. The location of the picrite samples is indicated by the blue marker. Modified from Fowler et al. (2004).

Rum

Rum lies on a ridge of Precambrian rocks that separates two Mesozoic basins, the Sea of the Hebrides and the Inner Hebrides (Figure 1.9). Igneous activity began with the eruption of basaltic lava flows of the Eigg Lava Formation dated at 61.2 ± 0.3 (Ganerød et al., 2010). However, on Rum, these are only exposed as faulted relics associated with Jurassic sediments (Smith, 1985; Emeleus et al., 1996). The Rum Central Complex was emplaced into the thick succession of fluvial sandstones that form the Proterozoic Torridon Group. There were at least three distinct phases of igneous and tectonic activity. Phase 1 was dominated by silicic magmatism, the development of an arcuate system of faults termed the Main Ring Fault (Figure 1.11), and caldera formation (Emeleus and Bell, 2005). Phase 2 marks a change to dominantly basaltic magmatism with the intrusion of cone sheets, northwest-trending dykes, the emplacement of gabbros and layered ultrabasic rocks, and an array of minor intrusions. The intrusions from Phase 2 were emplaced at 60.5 ± 0.2 Ma (Hamilton et al., 1998) and involved large volumes of primitive basaltic magma. Cessation of igneous activity was followed by Phase 3, which was marked by deep subaerial erosion and unroofing of the central complex. The emplacement of the entire central complex occurred over about 1 million years (Emeleus and Bell, 2005), similar to other central complexes in the region. The Rum picrite samples described in this study are two dykes (M9 and R10) from the Phase 2 Eastern and Western Layered intrusions of the Rum Central Complex (Figure 1.11).

Mull

Mull is one of the largest igneous centres within the BTIP. The base of the Mull lava field is dated at 60.6 ± 0.3 Ma (Chambers and Pringle, 2001) and covers an area of 840 km^2 (Figure 1.12), with a present-day thickness of nearly 1000 m. Zeolite mineral compositions suggest that approximately 1000 m has been eroded off the top of the lava pile (Walker, 1971). Fissure eruptions feeding the lava flows eventually gave way to the development of a central volcanic complex. Cross-cutting intrusions within the complex indicate that the igneous activity was concentrated around three centres (Bailey et al., 1924) that gradually shifted

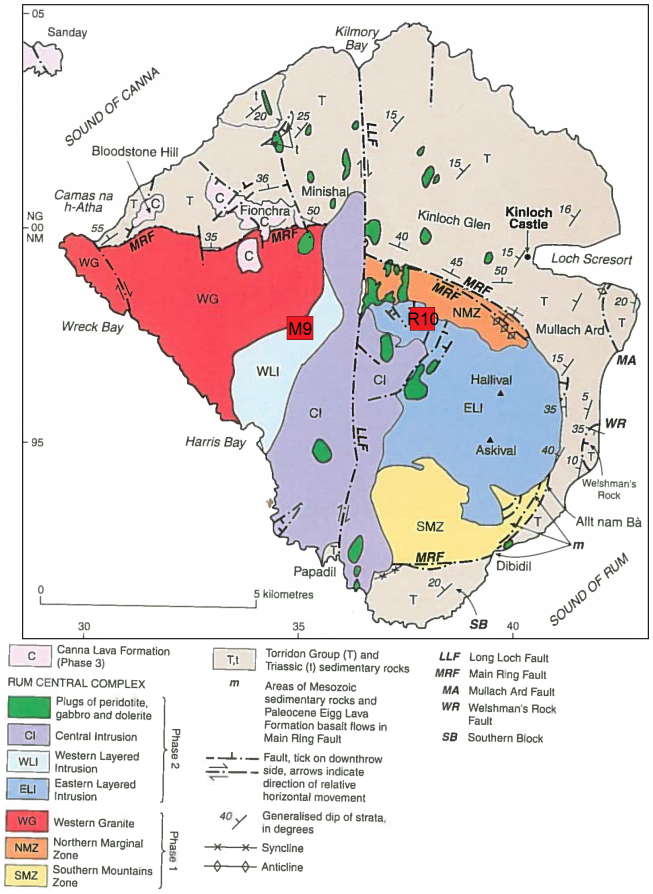

Figure 1.11: A simplified geological map of the Isle of Rum showing the principle divisions of the Rum Central Complex. The Rum picrite locations are indicated with a red marker. Modified from Emeleus and Bell (2005).

northwestwards (Figure 1.12) through time. Centres 1 and 3 are considered to be related to the development of calderas (Emeleus and Bell, 2005). The last intrusion in the central complex is the Loch Ba ring dyke from Centre 3, dated at 58.5 $\pm$ 0.2 Ma (Chambers and Pringle, 2001). Finally, the whole area was cut by the regional northwest-trending dyke swarm. The dykes that cross-cut the Loch Ba ring dyke are dated at 58.12 $\pm$ 0.13 Ma (Chambers and Pringle, 2001). The picrite samples from Mull in this study are a suite of large dyke-like bodies that intrude the Centre 1 complex and Mull plateau lavas in the southeast of the island (Figure 1.12).

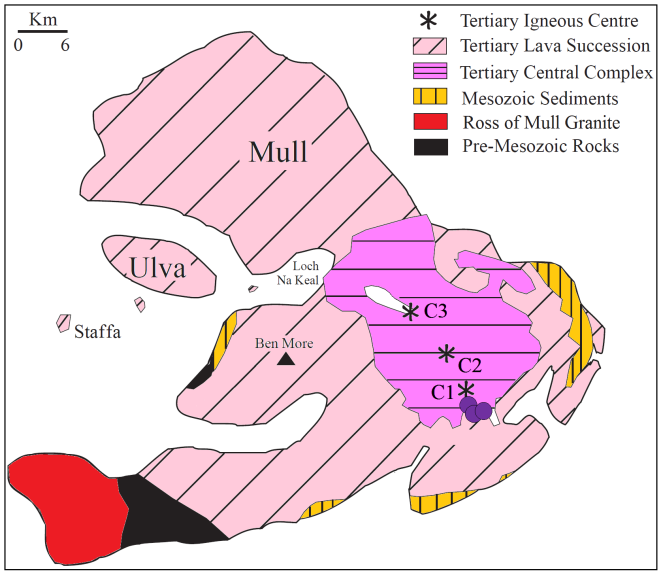

Figure 1.12: A simplified geological map of the Isle of Mull showing the position of the three igneous centres within the central volcano, seen to move northwestwards through time. The locations of the Mull picrites are indicated by the purple markers. Modified from Chambers and Pringle (2001).

1.2.6 Iceland

Iceland represents the only part of the NAIP that remains volcanically active and marks the location of the mantle plume rising beneath the Mid-Atlantic spreading axis (Saunders et al., 1997). It is surrounded by a large basalt plateau and is located at the junction of two major oceanic structures, the Greenland-Iceland-Faeroe Ridge, and the Mid-Atlantic Ridge (Figure 1.13). Iceland is connected to the flood basalt provinces that represent the plume-head stage of volcanic activity via the GIFR hotspot trail. The basalt plateau covers an area of around 350,000 km^2, and is raised more than 3000 m above the surrounding seafloor, with a crustal thickness of 10-40 km (Thordarson, 2007). About 30% of the plateau is above sea level, and the remainder forms the 50-200 km-wide shelf surrounding Iceland. The construction of the plateau is thought to have begun at around 25 Ma (e.g. Kristjansson, 1982), i.e. when the spreading axis became locked over the plume (e.g. Saunders et al., 1997). The spreading axis in Iceland continues to drift northwestwards with respect to the plume, but is periodically recaptured in rift relocation cycles (Hardarson et al., 1997). As a result, the very oldest rocks in Iceland are exposed in the far northwest.

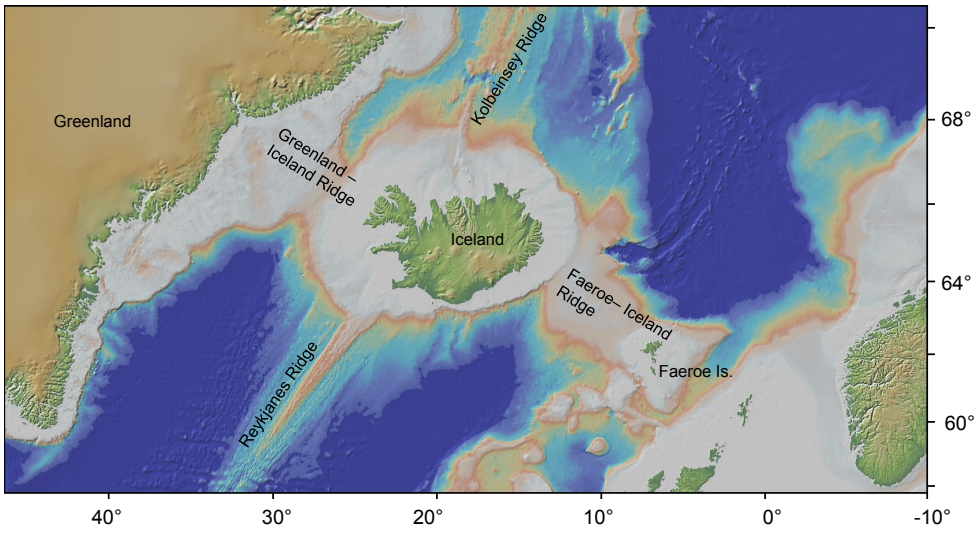

Figure 1.13: Bathymetric map of the North Atlantic region near Iceland. Iceland is an elevated basalt plateau in the middle of the Northeast Atlantic and is located at the junction of the Reykjanes Ridge and Kolbeinsey Ridge segments of the Mid-Atlantic Ridge, and the Greenland-Iceland-Faeroes Ridge, which connects Iceland to the early plume-head flood basalt provinces.

Current volcanic activity in Iceland is found on the neovolcanic zones (<0.7 million years old), 15-50 km wide belts of active faulting and volcanism (e.g. Sæmundsson, 1979; Vink, 1984; Hardarson et al., 1997; Thordarson, 2007). The neovolcanic zones may be divided into two tectonic groups (Sæmundsson, 1979), the axial rift zones and the off-axis (or flank) zones. Figure 1.14 shows the location of the main geological subdivisions, volcanic zones and rift zones in Iceland.

The axial rift zones include the West (WVZ) and North (NVZ) Volcanic Zones, which are joined by the Mid-Iceland Belt (MIB) and may be viewed as extensions of the Mid-Atlantic Ridge, linked by the Reykjanes Volcanic Zone (RVZ) in the south, and the Tjörnes Fracture Zone (TFZ) in the North. They are typified by tholeiitic magmatism with small amounts of silicic and intermediate rocks (Thordarson, 2007), and are characterised by tensional tectonics and active rifting, with both central and fissure eruptions present. The East Volcanic Zone (EVZ) is an axial rift that is in the process of taking over from the WVZ (Thordarson, 2007). The EVZ has formed by southwestwards propagation of volcanism through pre-existing crust and is presently the most active volcanic region in Iceland. It is here that the thickest crust (>40 km) in Iceland is found (e.g. Kaban and Pálmason, 2002), due to its location above the centre of the plume conduit. Tryggvason et al. (1983) and Wolfe et al. (1997) used seismological studies to image a 100-200

km wide cylindrical low velocity zone beneath southeast Iceland, and a regional gravity minimum occurs here also (Eysteinsson and Gunnarsson, 1995).

The flank zones are two active intraplate volcanic belts of mildly alkalic magmatism (Thordarson, 2007), with lower discharge rates than at the main axial rift zones (Jakobsson, 1972). These are the Snæfellsnes Volcanic Belt (SVB) and the Öræfi Volcanic Belt (OVB). These zones have poorly developed extensional features, little evidence of rifting, and their mildly alkalic character is consistent with small-degree melts derived from greater depths than the tholeiites of the axial zones (Saunders et al., 1997).

Rocks older than 0.7 million years are known as the marginal zones and make up more than two-thirds of Iceland (Figure 1.14). The oldest crust is found in the northwest, where basalts up to 16 million years old are found (Hardarson et al., 1997). In eastern Iceland, the oldest crust is ∼13-14 million years old (Watkins and Walker, 1977).

Two groups of Icelandic picrites and primitive basalts are used as part of this study. The first group are from the Tertiary Basalt Formation (Figure 1.14) representing some of the oldest rocks on the island. They include the highest $^{3}He/^{4}He$ volcanic rocks on Iceland (Ellam and Stuart, 2004) with $^{3}He/^{4}He$ up to 37 R/R_a. The second group of samples are from the active neovolcanic zones, with samples from the RVZ, EVZ and NVZ (Figure 1.14).

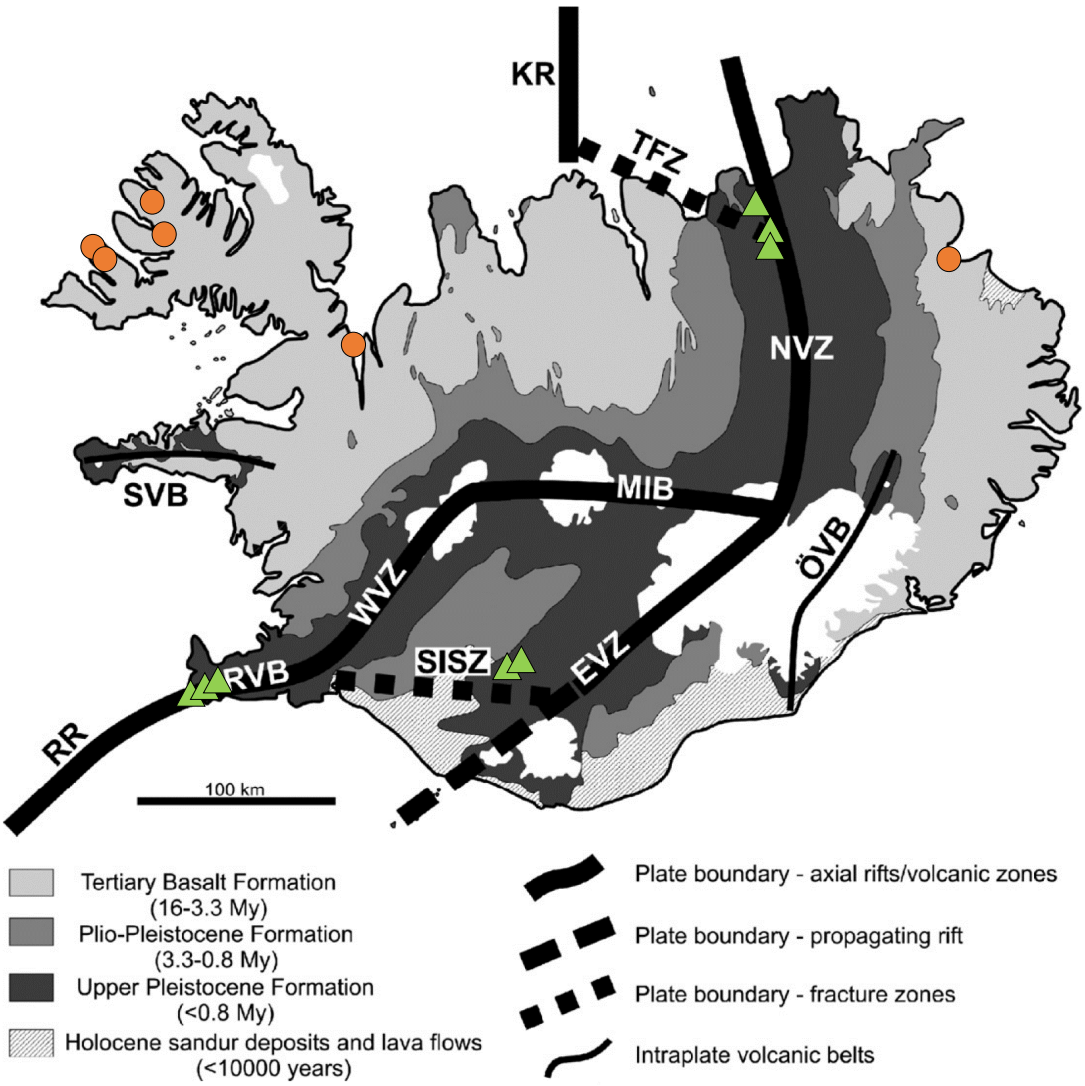

Figure 1.14: A simplified geological map of Iceland, outlining the location of the major geological subdivisions and the main volcanic and fault zones. RR = Reykjanes Ridge, RVB = Reykjanes Volcanic Belt, SISZ = South Iceland Seismic Zone, WVZ = Western Volcanic Zone, EVZ = East Volcanic Zone, MIB = Mid-Iceland Belt, NVZ = North Volcanic Zone, TFZ = Tjörnes Fracture Zone, KR = Kolbeinsey Ridge, ÖVB = Öræfi Volcanic Belt, SVB = Snæfellsnes Volcanic Belt. From Thordarson (2007). The orange and green markers show the locations of the Tertiary and neovolcanic Icelandic samples used in this study, respectively.

1.3 The geochemical composition of the North Atlantic Mantle

1.3.1 The Iceland mantle source

The NAIP mantle has two source end-members: a depleted N-MORB source and an enriched plume source (Fitton et al., 1997, 1998; Chambers and Fitton, 2000). The abundance of Nb relative to Zr and Y can be used to distinguish between the two end-members. Icelandic mantle has $\Delta Nb>0$, whilst N-MORB mantle has $\Delta Nb<0$. ΔNb is defined as:

$\Delta Nb = 1.74 + \log(Nb/Y) - 1.92\log(Zr/Y)$

On a Nb/Y vs Zr/Y diagram (Figure 1.15), the two sources define distinct, parallel arrays. ΔNb is a fundamental source characteristic that is insensitive to the effects of variable degrees of mantle melting, source depletion or subsequent alteration (Fitton, 2007). Contamination with continental crust has little effect on ΔNb because crustal rocks plot on or below the lower bound of the Iceland array. Therefore crustal contamination may only lower ΔNb and cannot make a sample appear enriched (Fitton et al., 1997; Chambers and Pringle, 2001). All Icelandic basalts plot above the $\Delta Nb=0$ line and so represent a clearly distinct source from that of N-MORB.

It has long been recognised from Nd-Sr-Hf-Pb-Os-O isotope systematics that the mantle beneath Iceland is heterogeneous (e.g. Zindler and Frey, 1979; Hemond et al., 1993; Fitton et al., 2003; Thirlwall et al., 2004; Sigmarsson and Steinthórsson, 2007; Debaille et al., 2009; Shorttle and Maclennan, 2011; Koornneef et al., 2012). At least two distinct sources are present: an 'enriched' source with low $^{143}Nd/^{144}Nd$, high $^{87}Sr/^{86}Sr$ preferentially sampled by alkali basalts from the flank zones, and a 'depleted' source with high $^{143}Nd/^{144}Nd$, low $^{87}Sr/^{86}Sr$, preferentially sampled by tholeiitic basalt and picrite from the axial rift zones (Hemond et al., 1993). This distribution can be explained using the model of Ito and Mahoney (2005a), whereby the off-axis flank zones sample deep, small degree melts under conditions where only an enriched, more fusible source can melt. At the axial rift

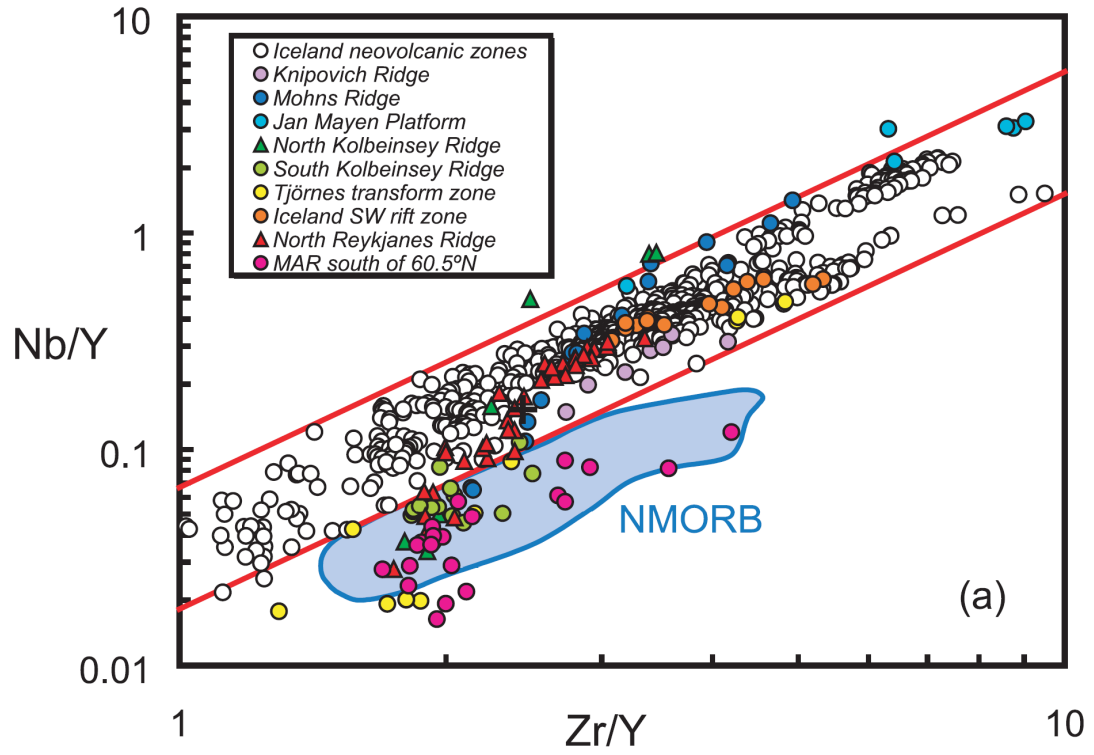

Figure 1.15: Nb/Y and Zr/Y variation for basalts from Iceland and the MAR. The N-MORB field is based on data from the Reykjanes Ridge (south of 61 °N). The parallel lines mark the limits of the Iceland data. From Fitton et al. (2003).

zones, the mantle can upwell to shallower levels than beneath the flank zones, and this, combined with the higher temperatures predicted in the core of the plume (e.g. Wolfe et al., 1997), results in more extensive melting and the sampling of both sources. The mantle upwelling in the plume is therefore heterogeneous, with blobs or streaks of enriched material in a depleted refractory matrix.

He isotope systematics from Iceland indicate the contribution of a primordial ^{3}He-rich source. The distribution of helium isotope ratios from Icelandic basalts is shown in Figure 1.16. Tertiary basalts from the northwest and northeast of Iceland represent some of the oldest rocks on the island, and have ^{3}He/^{4}He up to 37 R/R_a (Ellam and Stuart, 2004). Today, the high ^{3}He/^{4}He anomaly extends across the entire neovolcanic zone. Each volcanic zone has a distinctive ^{3}He/^{4}He isotope signature: 18-26 R/R_a in the EVZ and central Iceland, 12-16 R/R_a in the WVZ and 8-11 R/R_a in the NVZ (Kurz et al., 1985). The fact that the highest ^{3}He/^{4}He ratios from the neovolcanic zones are observed in eastern and central

Iceland is considered to be due to the fact that these areas have the greatest contribution from the plume and is in line with other evidence indicating the location of the plume centre in this area. Breddam et al. (2000) attempted to map out the conduit of the Iceland plume with helium isotopes and reported a 'plateau' of high $^3He/^4He$ ratios ($>20\ R/R_a$) around 100 km in diameter, located in southeast Iceland, and argued that this zone outlines the width of the Iceland plume conduit at depth.

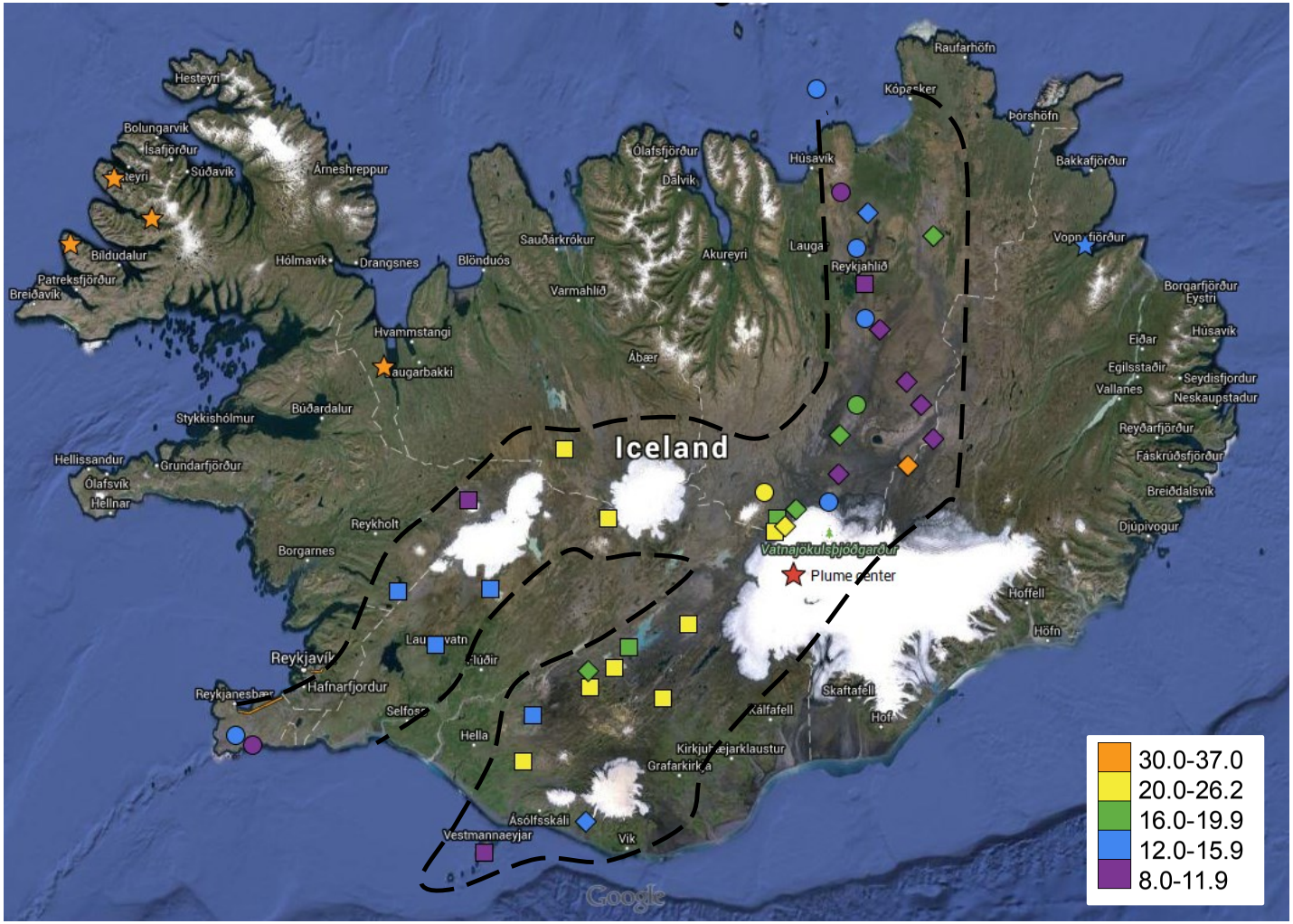

Figure 1.16: Map indicating the distribution of helium isotope ratios from Icelandic basalts. The black dashed line outlines the area of the neovolcanic zone. The red star indicates the location of the plume axis based on crustal thickness data from Kaban and Pálmason (2002). $^3He/^4He$ has been colour coded according to R/R_a values. Squares = data from Kurz et al. (1985), circles = data from Breddam et al. (2000), diamonds = data from Macpherson et al. (2005a). Yellow stars = data from tertiary Iceland basalts from Ellam and Stuart (2004). The one offshore MAR sample from the Tjörnes Fracture Zone is from Macpherson et al. (2005b).

More recent studies have painted a more complicated picture of the distribution of high $^3He/^4He$ ratios in Iceland. Macpherson et al. (2005a) measured $^3He/^4He$ ratios from central Iceland and found a value of 34.3 R/R_a from Vadalda, just north of the Vatnajökull icecap. This value is much higher than the previous highest value from the neovolcanic zones (26.2 R/R_a) and is comparable with the highest values from Tertiary basalts of northwest Iceland, but it has a large error of ± 4 R/R_a. Macpherson et al. (2005a) found that the central Iceland $^3He/^4He$ values generally fell into two categories: (i) MORB-like values from trace element enriched lavas north of Vatnajökull, and (ii) high $^3He/^4He$ values up to 26 R/R_a from trace element depleted rocks found farther from the location of the proposed plume centre. There are however, some exceptions to this rule, and so it appears that high $^3He/^4He$ can be associated with either enriched or depleted mantle, but in Iceland, it is more likely to be associated with the latter. This association is consistent with the observations from high $^3He/^4He$ Tertiary rocks. Here, the high $^3He/^4He$ rocks are associated with high $^{143}Nd/^{144}Nd$, low $^{87}Sr/^{86}Sr$ and therefore represent the depleted source (Ellam and Stuart, 2004). On the other hand, $^3He/^4He$ does not correlate with $^{87}Sr/^{86}Sr$ and $^{143}Nd/^{144}Nd$ in the neovolcanic systems (Condomines et al., 1983), suggesting that $^3He/^4He$ is in fact decoupled from other isotopic tracers.

The high $^3He/^4He$ anomaly extends north of Iceland from the Tjörnes Fracture Zone to the North Kolbeinsey Ridge (Macpherson et al., 2005b). $^3He/^4He$ of basalts does not systematically change along the Kolbeinsey Ridge, but varies between values of 8.3 and 12.6 R/R_a. Slightly higher R/R_a values of up to 13.6 are detected on the Tjörnes Fracture Zone (Macpherson et al., 2005b). The lack of $^3He/^4He$ variation along the Kolbeinsey Ridge was thought to be inconsistent with present active mantle outflow from beneath Iceland, although it may have occurred in the past (Macpherson et al., 2005b). The higher values from the Tjörnes Fracture Zone are thought to mark the northern limit of shallow-level Icelandic mantle outflow. High $^3He/^4He$ values are not detected farther north than the Kolbeinsey Ridge and basalts at 72 °N from the Mohns Ridge have normal mantle R/R_a (Macpherson et al., 2005b).

Along the Reykjanes Ridge, the thermal and geochemical effects of the plume extend far south of Iceland (Figure 1.17). It has long been recognised that there is a systematic geographical variation in incompatible elements along the ridge

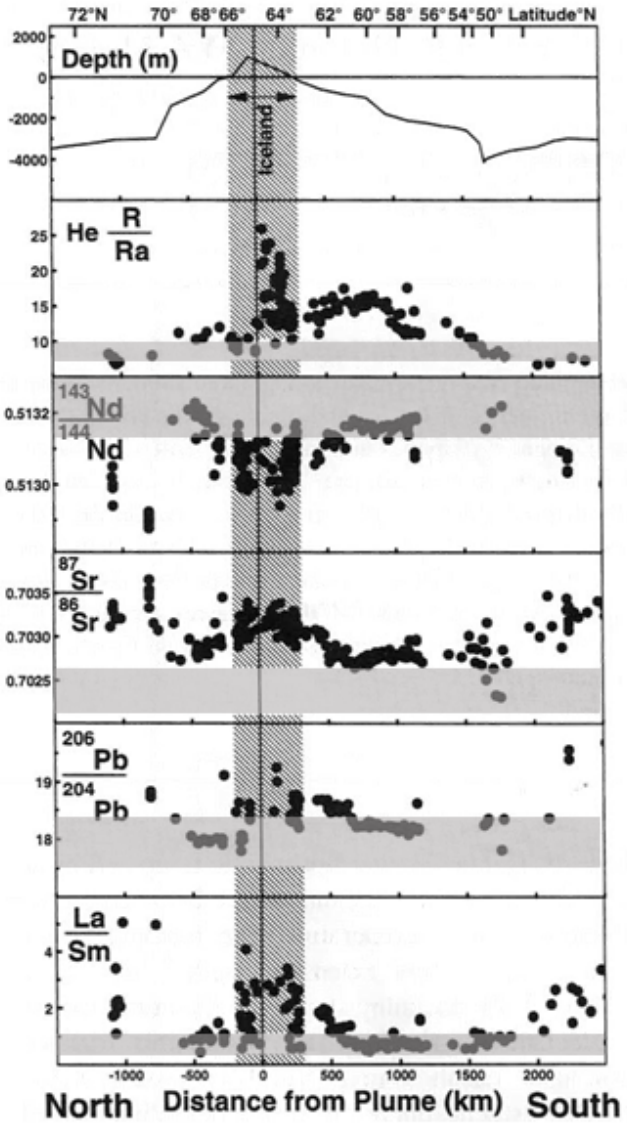

Figure 1.17: Variation in water depth, He, Nd, Sr and Pb isotopes and La/Sm along the Reykjanes Ridge with distance from the centre of the Iceland plume. The vertically shaded area represents the extent of Iceland. The horizontal shaded area represents the range of values found in N-MORB away from the influence of mantle plumes. From Taylor et al. (1997).

(e.g. Schilling, 1973; Murton et al., 2002), and this has been attributed to mixing of the N-MORB and Icelandic mantle source, with the Icelandic contribution increasing towards the centre of the plume. The ΔNb of Reykjanes Ridge basalts is >0 at Iceland and decreases abruptly at 61 °N, where it changes to <0, after which it no longer varies with distance from Iceland. The thermal anomaly, on the other hand, gradually decreases much farther south to 1700 km from the plume

axis (Figure 1.17), as indicated by water depth and major-element compositions of basalt (Klein and Langmuir, 1987; Saunders et al., 1997). Reykjanes Ridge basalts with the Sr-Nd-Pb isotopic signature of the Iceland plume are also recognised up to 2400 km from the plume axis (Taylor et al., 1997), indicating that the compositional effects of the plume extend past the thermal anomaly, although they may represent anomalous blobs of enriched material in the upper mantle.

The $^3He/^4He$ anomaly closely corresponds to the area affected by thermal uplift (Poreda et al., 1986; Taylor et al., 1997), as shown in Figure 1.17. As in Iceland, $^3He/^4He$ appears to be decoupled from all other isotopic systems (Figure 1.17). $^3He/^4He$ increases along the Reykjanes Ridge from around 50 °N to around 59 °N, interpreted to be the result of increasing contribution of plume material towards Iceland. After 61 °N, $^3He/^4He$ decreases towards Iceland. This seems counter-intuitive, but was explained by Hilton et al. (2000) to be the result of eruption under shallow water conditions close to Iceland. This results in low-pressure pre-eruptive degassing of magmatic helium.

1.3.2 The early NAIP mantle

The $^3He/^4He$ values of basalts from the early NAIP are of particular importance and significance because they represent the earliest manifestation of the Iceland plume (e.g. White and McKenzie, 1989; Saunders et al., 1997) and are most likely to sample the high $^3He/^4He$ source. Extremely high $^3He/^4He$ values up to 50 R/R_a (the highest $^3He/^4He$ volcanic rocks yet found on Earth) are widely distributed throughout the early Iceland plume picrites and magnesian basalts from West Greenland and Baffin Island, and were erupted close to the centre of the proposed plume axis (Lawver and Müller, 1994), as shown in Figure 1.18. These values are considerably higher than contemporary OIB (e.g. Hawaii, Iceland, Samoa, Loihi), which tend to converge on $^3He/^4He$ values slightly higher than 30 R/R_a (Kurz, 1982; Kurz and Geist, 1999; Macpherson et al., 2005a; Jackson et al., 2007). High $^3He/^4He$ values have also been reported from locations much farther from the proposed plume axis (Figure 1.18). Two samples from BTIP picrites of the Skye Main Lava Series have $^3He/^4He$ around 21 and 18 R/R_a, and samples from Phase 1 basalts from northeast Greenland and Phase 2 basalts from

east Greenland show $^3He/^4He$ ratios up to 21 R/R_a (Marty et al., 1998) and 18.5 R/R_a (Peate et al., 2003), respectively.

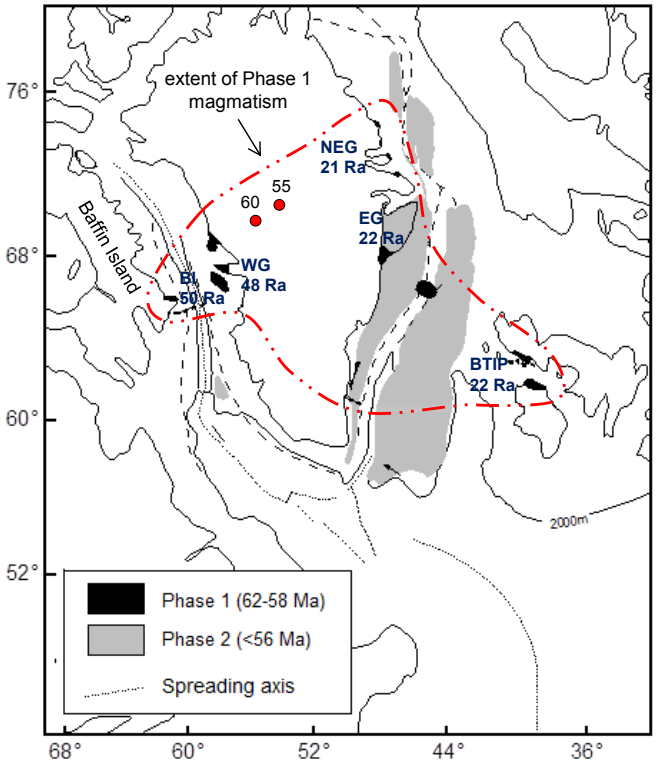

Figure 1.18: Tectonic reconstruction of the NAIP at ~61 Ma showing the distribution of Phase 1 and 2 magmatism and measured $^3He/^4He$ ratios. BI = Baffin Island, WG = West Greenland, NEG = Northeast Greenland, EG = East Greenland, BTIP = British Tertiary Igneous Province. The circles indicate the calculated locations of the centre of the Iceland plume at 55 and 60 Ma, as calculated by Lawver and Müller (1994). Modified from Saunders et al. (1997).

The spatial extent of the high $^3He/^4He$ anomaly of the earliest NAIP basalts is no greater than at the modern plume, as shown in Figure 1.19, however, Phase 1 and 2 magmatism is only present in the North Atlantic in areas where the lithosphere had previously been thinned (Thompson and Gibson, 1991), so it is not possible to know how far it may have extended but not been sampled. What is clear is that the Phase 1 and 2 $^3He/^4He$ anomaly had a far greater amplitude (Figure 1.19) than at present. $^3He/^4He$ values up to 21 R/R_a are present in Skye, 1300 km from the plume axis at 60 Ma. Such high values are only recorded today on Iceland and at a maximum of 200 km from the present-day plume axis. At Baffin Island and West Greenland, $^3He/^4He$ values of up to 50 R/R_a are observed, and are

much higher than the highest $^{3}He/^{4}He$ value found in present-day Iceland. These observations are consistent with the starting plume having a greater contribution from the (likely deep) high $^{3}He/^{4}He$ reservoir.

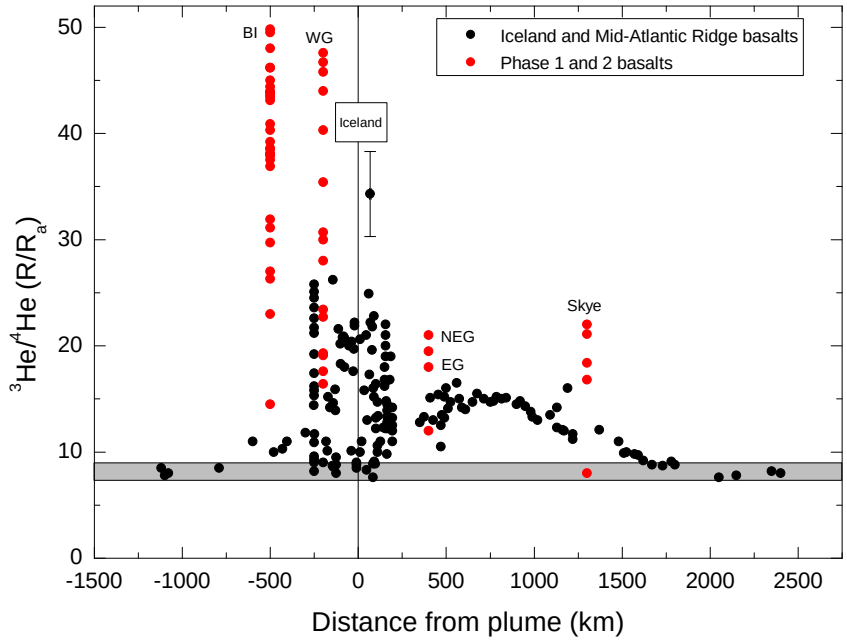

Figure 1.19: A comparison of the modern $^{3}He/^{4}He$ anomaly around Iceland (black circles) as recorded by basalts and geothermal fluids from Iceland, the Reykjanes Ridge and Kolbeinsey Ridge (data from Condomines et al. (1983); Kurz et al. (1985); Hilton et al. (1990); Poreda et al. (1992); Taylor et al. (1997); Hilton et al. (2000); Breddam et al. (2000); Macpherson et al. (2005a); this study) and the $^{3}He/^{4}He$ anomaly recorded by Phase 1 and 2 basalts from the early North Atlantic Igneous Province (data from Marty et al. (1998); Stuart et al. (2000); Peate et al. (2003); Stuart et al. (2003); Starkey et al. (2009)). Values as high as those measured from Skye are today only present on Iceland, demonstrating that the early-NAIP plume $^{3}He/^{4}He$ anomaly was significantly larger than that of the present day. The grey field represents the $^{3}He/^{4}He$ range of N-MORB away from the influence of mantle plumes. BI = Baffin Island, WG = West Greenland, NEG = Northeast Greenland, EG= East Greenland.

In an attempt to identify the high $^{3}He/^{4}He$ reservoir, Stuart et al. (2003) and Ellam and Stuart (2004) measured Nd and Sr radiogenic isotope ratios and trace element concentrations in the Baffin Island, West Greenland and Tertiary Iceland basalts. They found that the majority of samples display coherent linear relationships between $^{3}He/^{4}He$ and $^{87}Sr/^{86}Sr$ and $^{143}Nd/^{144}Nd$. The samples with the

highest $^{3}He/^{4}He$ values were found to have Sr and Nd isotopic ratios that are indistinguishable from the depleted mantle reservoir thought to be the main source of N-MORB (low $^{87}Sr/^{86}Sr$, high $^{143}Nd/^{144}Nd$). Samples with lower $^{3}He/^{4}He$ were found to have a relatively enriched signature (low $^{143}Nd/^{144}Nd$, high $^{87}Sr/^{86}Sr$). This was in agreement with data from Kent et al. (2004), indicating that Baffin Island picrites with the highest $^{143}Nd/^{144}Nd$ have Os and O isotope ratios suggestive of a depleted mantle source. These observations led Ellam and Stuart (2004) to suggest that normal depleted mantle is replenished with primordial helium, thus removing the requirement for a large undegassed primordial reservoir.

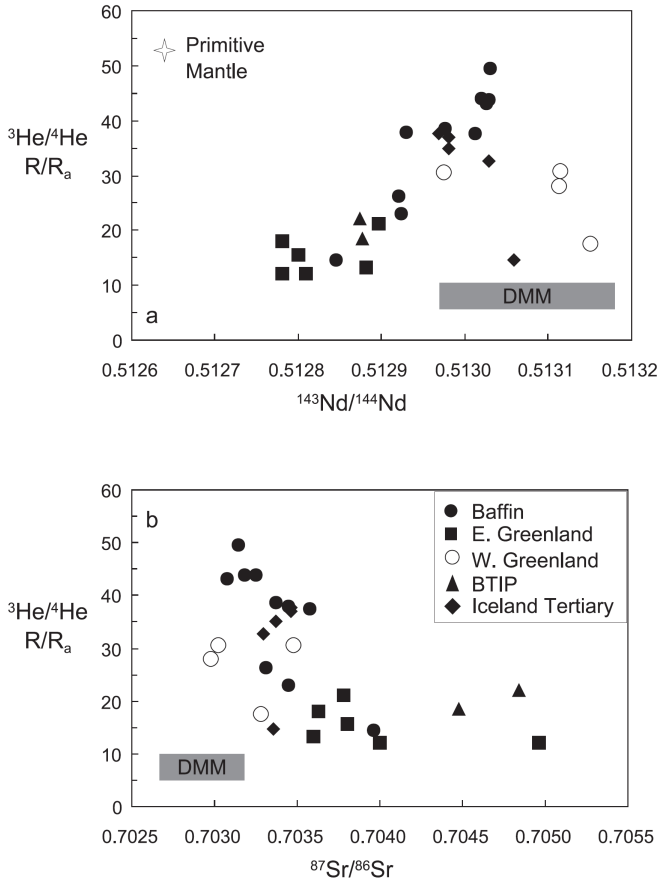

Figure 1.20: The He-Nd (a) and He-Sr (b) isotope trends in NAIP basalts with $^{3}He/^{4}He$ >10 R/R_a. From Ellam and Stuart (2004).

However, Starkey et al. (2009) carried out a more detailed study on Phase 1 picrites from Baffin Island and West Greenland (Figure 1.21), and found that while the association of high $^{3}He/^{4}He$ with Sr and Nd isotopic ratios typical of

depleted mantle is still apparent, several high $^{3}He/^{4}He$ samples have a much more enriched signature (i.e. lower $^{143}Nd/^{144}Nd$ and higher $^{87}Sr/^{86}Sr$) than the ranges previously measured by Stuart et al. (2003) and Ellam and Stuart (2004). This is similar to the observations at the present-day Iceland $^{3}He/^{4}He$ anomaly where the highest $^{3}He/^{4}He$ rocks tend to have a depleted isotopic and trace element signature, although there are a few exceptions where high $^{3}He/^{4}He$ is found in trace element and isotopically enriched rocks (Macpherson et al., 2005a). The linear trend (Figure 1.20) identified by Ellam and Stuart (2004) is therefore no longer applicable. In fact, the compositional range of the high $^{3}He/^{4}He$ picrites is similar to that of the upper mantle sampled by MORB and it seems that the high $^{3}He/^{4}He$ picrites were derived from a mantle source to which high $^{3}He/^{4}He$ material has been added, either by mixing with a high $^{3}He/^{4}He$ source, or alternatively, helium could diffuse in from a discrete, high $^{3}He/^{4}He$ reservoir (Starkey et al., 2009). Any model used to explain $^{3}He/^{4}He$ in mantle plumes must now allow the full range of available upper mantle compositions to attain high $^{3}He/^{4}He$. The fact that $^{3}He/^{4}He$ seems to be decoupled from every other mantle isotopic system both in the early plume head and at the present time seems to suggest that the high $^{3}He/^{4}He$ reservoir is not within the mantle but is diffusing in from elsewhere, for example from the core.

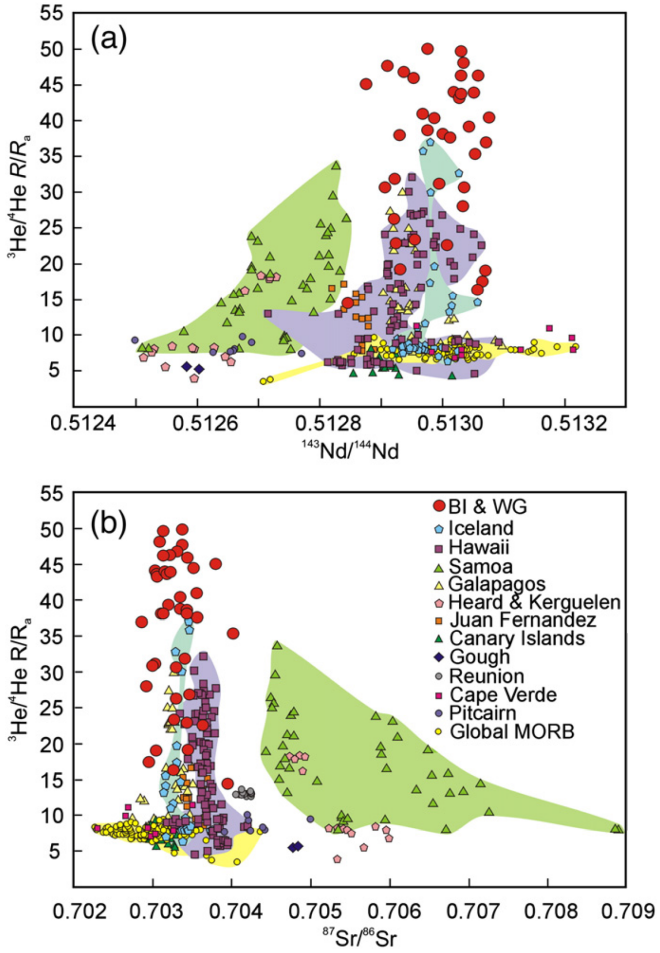

Figure 1.21: $^{3}He/^{4}He$ vs (a) $^{143}Nd/^{144}Nd$ and (b) $^{87}Sr/^{86}Sr$ for global OIB and Baffin Island and West Greenland. $^{143}Nd/^{144}Nd$ and $^{87}Sr/^{86}Sr$ of Baffin Island and West Greenland now span most of the MORB range at both high and low $^{3}He/^{4}He$. From Starkey et al. (2009).

1.3.3 Location of the high $^{3}He/^{4}He$ reservoir

The best way to identify where plumes originate from is to seismically image them to their source. Recent whole-mantle seismic imaging indicates that the Iceland mantle plume extends to the base of the lower mantle (Figure 1.22). This would suggest that the high $^{3}He/^{4}He$ plume source is at least as deep as the base of the mantle, however its true location and relationship with mantle plumes remains enigmatic.

1.4 Chapter outline

A summary of the content of each chapter is as follows: Chapter 2 presents the field geology, petrology, major and trace element data of the primitive, Mg-rich samples, as well as the mineral chemistry results.

Chapter 3 focusses on determining the olivine crystallisation temperature of the samples using three different methods, traditional olivine-melt thermometry, a forward mantle melting model and the newly-developed Al-in-olivine thermometer. For the first time, the three techniques will be compared in detail, and it will be shown that the Al-in-olivine thermometer is a far more robust proxy for mantle temperature. The results show that the maximum temperature anomaly associated with the plume-head phase of volcanic activity was equal on both sides of the NAIP, across an area 2000 km in diameter. In addition, the temperature of the mantle plume is shown to fluctuate on a timescale of 10^7 years, and the data from the Iceland samples indicate that the plume temperature is currently increasing

In Chapter 4, the temperature fluctuation of the plume is placed in a regional context, and it is shown to have had a profound effect on melting dynamics and magmatism in the North Atlantic region. New helium isotope data for the BTIP and zero-age Iceland samples will be then be presented, and alongside existing $^3He/^4He$ data, the relationship between temperature and $^3He/^4He$ within a mantle plume is explored. This has important implications for the inner workings of our planet because $^3He/^4He$ appears to be decoupled from all mantle tracers and the nature of the high $^3He/^4He$ reservoir is still poorly understood. Finally, the results of the study will be placed in a global context, and a model that links the $^3He/^4He$ source, temperature, mantle plumes and mantle dynamics will be presented.

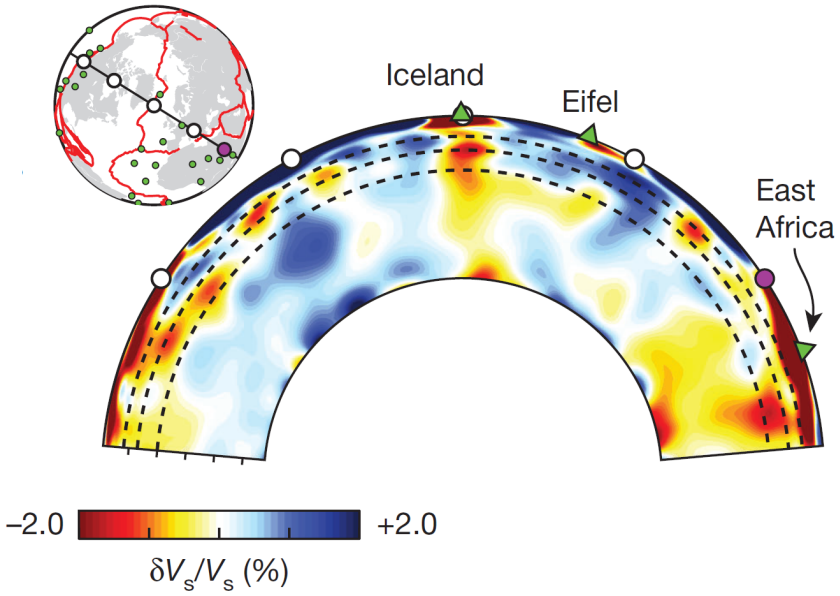

Figure 1.22: Whole-mantle depth cross-section of the mantle beneath Iceland of relative shear velocity variations from the seismic imaging models of French and Romanowicz (2015).

2 Field geology, petrology and geochemistry

2.1 Introduction

This chapter focusses in detail on the field geology, petrology, major and trace element chemistry and mineral chemistry of the new NAIP picrites and primitive basalts used in this study. These are the picritic dykes from Skye, Mull and R10 from Rum and the primitive basalts from the Iceland neovolcanic zones. The Baffin Island, West Greenland and Iceland Tertiary samples and M9 from Mull have been described in previous studies, and so are only briefly mentioned here. This study is primarily concerned with determining the temperature of the NAIP mantle through time, and as such, only the most primitive, Mg-rich samples that are known from each location are considered. Olivine is the first major phase to crystallize in primitive basalts and so is most likely to retain information about the conditions under which the hottest primary melts were formed. Consequently, this study focusses on a suite of olivine-rich basalts containing primitive ($\geq Fo_{85}$) olivines. The petrology, major and trace element chemistry and mineral chemistry will allow the samples to be characterised and will show that they are highly primitive and are therefore suitable for the aims of this study. The whole rock and mineral chemistry data will then be used in Chapter 3 to calculate the olivine crystallisation temperatures recorded by the samples.

2.2 Sampling

The sample suite spans the history of the NAIP and can be divided into three age groups: (i) Phase 1 picrites from the BTIP, Baffin Island and West Greenland;

(ii) picrites from the NW and E of Iceland erupted in the Tertiary that represent some of the oldest rocks on the island; (iii) a suite of picrites and primitive basalts from the neovolcanic zone in Iceland that are effectively zero-age. Three samples are from the RVZ, two from the EVZ and three from the NVZ (Figure 1.14). The Phase 1 picrites are of particular interest because they represent the oldest material erupted from the start-up plume head and therefore will potentially record the highest temperatures. The BTIP sample suite includes the M9 dyke studied by Upton et al. (2002) and contains the most Mg-rich olivines known from the BTIP (up to Fo_{93}). The Baffin Island and West Greenland samples were studied by Starkey (2009) and contain similarly Mg-rich olivines. The Baffin Island and BTIP picrites were separated by a distance of ∼2000 km when they were erupted, and will therefore allow the temperature distribution in the start-up plume head to be investigated. Additionally, the Baffin Island and West Greenland samples record the highest $^3He/^4He$ values yet found on Earth (Starkey et al., 2009), so provide an ideal opportunity to explore the relationship between temperature and $^3He/^4He$. The addition of the Iceland samples will allow the temperature of the plume to be constrained throughout its lifetime. The Iceland suite includes the 13-14 Ma Tertiary picrites studied by Ellam and Stuart (2004) and have the highest magmatic $^3He/^4He$ yet found on the island (up to 37 R/R_a). A new suite of picrites and primitive basalts from the neovolcanic zones of Iceland are also included. The sample names and collection information for each suite are provided in Table 2.1 and their locations are shown in Figure 2.1. A full list of samples and their locations can be found in Appendix C.

Table 2.1: The number of samples from each location used in this study and the sample prefixes used to identify each suite.

Location	Number	Sample prefix	Collected by
Skye	9	S	H. Spice
Rum	2	R, M	H. Spice and Prof. B. Upton (University of Edinburgh)
Mull	3	MU	H. Spice
Baffin Island	7	PAD, DUR, APO	Dr. F. Stuart (SUERC)
West Greenland	5	Numbers	Dr. L. M. Larsen (GEUS, Copenhagen)
Iceland Tertiary	6	ED, KoP, SAU, SD, VEY, VP	Björn Hardarson
Iceland neovolcanic	8	I	Prof. T. Thordarson (University of Iceland)

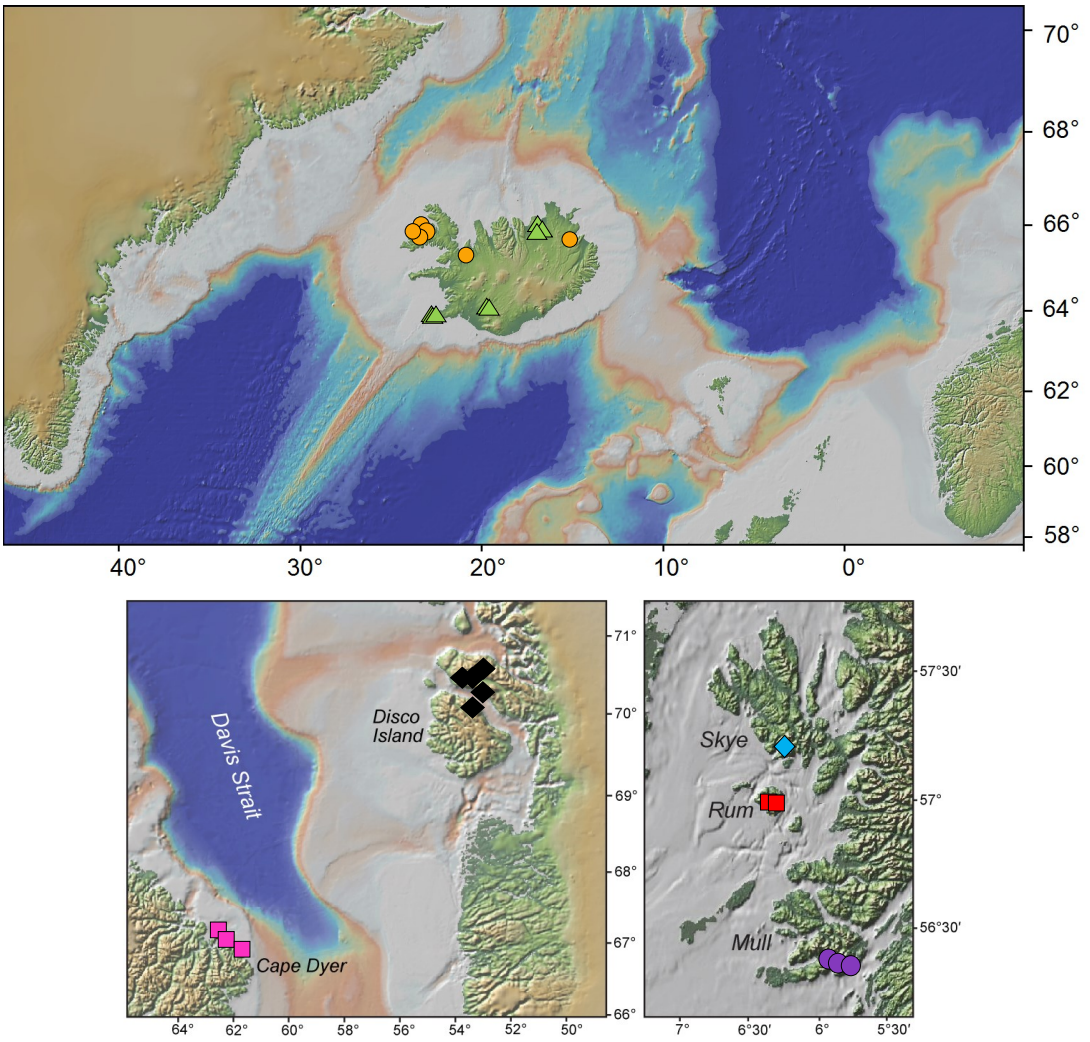

Figure 2.1: The locations of new each sample used in this study.

2.2.1 Sample ages

The Skye picrites intrude the outer gabbros of the Cuillin central complex, which is dated at 58.9 ± 0.1 Ma (Hamilton et al., 1998). The Rum samples intrude the layered rocks of the central complex on Rum, which is dated at 60.5 ± 0.2 Ma (Hamilton et al., 1998). The Mull picrites intrude the Mull plateau lavas and Centre 1 of the central complex, which has been dated at 59.05 ± 0.27 Ma (Chambers and Pringle, 2001). The Baffin Island samples are lava flows from the picritic basal section of the lava pile. Their magnetic polarity implies an age of 62.0-61.7 Ma (Pedersen et al., 2002). The West Greenland samples are lava flows

from the Vaigat Formation, which is dated at 61.7 ± 0.5 Ma (Ganerød et al., 2010). The Iceland Tertiary picrites represent some of the oldest rocks on the island. 5 samples are from the northwest, dated at 14.3-13.1 Ma and one sample is from the east dated at 12 Ma (based on unpublished Ar-Ar data from B. S. Hardarson). The Iceland neovolcanic samples are effectively zero-age.

2.3 Field geology

In this section, the field relations of the BTIP picrites are described. The samples from West Greenland, Baffin Island and Iceland were collected for previous studies by others (Table 2.1) and so are not described here.

2.3.1 Skye

The Skye picrites occur as dykes that intrude the outer gabbros of the Cuillin central complex in Coire Lagan (Figure 1.10), and were first described by Drever and Johnston (1958). They are clearly distinguishable from the grey gabbros due to their brown colouring and striking pitted texture formed from the weathering out of olivine phenocrysts. Both the gabbros and dykes are well exposed at this locality on flat, glaciated slabs, and there is no vegetation cover. The width of the dykes is highly variable, ranging from a few cm to around 60 cm, however the majority of dykes are approximately 30 cm in width. In general, the dykes trend NE-SW to E-W, however they anastomise in a highly irregular fashion across the gabbro surface and commonly have small offshoots. They are often traceable for >100 m before disappearing into a lochan or tapering into small veins. The dykes cut many of the small basaltic sheets and dykes intruding the gabbro body and so are relatively late-stage in the history of the Cuillin complex. The dykes have chilled margins that are a few cm wide, and the number and size of olivine phenocrysts generally increases towards the centre of a dyke. An image of a typical dyke on Skye and its characteristics are shown in Figure 2.2.

Figure 2.2: A typical picritic dyke from Skye, approximately 30 cm in thickness. The dyke traces an irregular pattern and has a small offshoot vein. The pitted texture is due to weathered out olivine phenocrysts. The number and size of olivine phenocrysts clearly increases towards the centre. A pronounced chilled margin a few cm wide is also present and is typical of all the dykes in the suite.

2.3.2 Rum

Sample R10 intrudes the Eastern Layered Intrusion of the Rum Central Complex. As in Skye, the dyke is easily distinguishable from the host gabbros and peridotites due to its brown weathering and pitted texture formed from the weathering out of olivine. The width of the dyke was 30 cm and it trended NE-SW. The dyke has a chilled margin a few cm wide and has olivine phenocrysts up to 1 cm in size.

This study also includes the picritic dyke (M9) first described by (Upton et al., 2002). It intrudes the Western Layered Intrusion of the Rum Central complex and is remarkable in that it contains olivines up to $Fo_{93.3}$, the most Mg-rich known from the BTIP.

2.3.3 Mull

The Mull picrites are a suite of much larger intrusive bodies intruding the Centre 1 Glen More granophyre and the Mull plateau lavas south of Loch Uisg in southern Mull. They are collectively known as the Loch Uisg Picrite Suite (LUPS), and were first described by Westland (2014). The LUPS rocks are very rich in olivine and have well developed layering. All show a distinctive pockmarked weathering, reminiscent of the peridotites of Skye and Rum (Emeleus and Bell, 2005). The best exposed of the three intrusions is the large, irregular, layered Gleann Beag intrusion (GBI). The intrusion is traceable for ∼1.4 km with a variable width from 10 m up to 150 m. The intrusion roughly trends NW-SE which is characteristic of the Mull Dyke Swarm. According to Westland (2014), who mapped the LUPS in detail, no other dykes appear to cut the GBI and there is no evidence of faults disrupting the intrusion (Westland, 2014), suggesting that it was intruded late in the magmatic history of Centre 1. At its far southeastern end, the intrusion appears dyke-like (Figure 2.3a) with near vertical and parallel margins. The margins of the dyke are rarely exposed, but where the contact with the Mull plateau lavas is exposed, a distinct chilled margin of a few cm wide is visible (Figure 2.3c). Layering is present in all three of the Loch Uisg picrites, however it is best exposed in the GBI. The layering occurs on a cm scale and is generally horizontal to sub-horizontal with some cross cutting relationships present (Figure 2.3e). Careful examination of the layers by Westland (2014) found no systematic variations in mineral chemistry, but is instead caused by alternating coarser grained olivine-rich layers with finer grained, slightly less olivine-rich layers (Figure 2.3f).

Figure 2.3: (a) The Gleann Beag intrusion at its southeastern end showing a dyke-like morphology with near vertical and parallel margins. The intrusion is 30 m wide at this point. (b) Looking SE up the GBI from its northwestern end. The yellow dashed lines mark the margins of the intrusion. (c) The contact between the GBI and one of the Mull plateau lava basalts. A chilled margin ∼3 cm wide is clearly visible. (d) Pockmarked weathering reminiscent of peridotite is found in all three of the LUPS intrusions. (e) Layering on a cm scale in the GBI. Cross-cutting relationships are clearly visible. (f) A close-up view of the layering found in the GBI. The layers are made up of coarser, olivine-rich sections (bottom), and finer grained, slightly less olivine-rich sections (top).

2.4 Petrology

The petrography of samples from Skye, Rum, Mull and Iceland are described below. The petrography and geochemistry of the Baffin Island and West Greenland samples was discussed in detail by Starkey (2009), and M9 is discussed in detail by Upton et al. (2002), and so will only be briefly mentioned here when necessary.

2.4.1 Skye

The Skye dykes are highly porphyritic, containing 17-44% by vol. of olivine. A photomicrograph across the margin of a narrow dyke (15 cm wide) is shown in Figure 2.4a. The olivine crystals range up to 1 cm in size and display a variety of morphologies, including strongly euhedral (Figure 2.4b), rounded, irregular or ragged crystal forms and rarely, skeletal forms. Glomerocrysts composed of all sizes of phenocrysts with polygonal grains and 120° grain boundaries are common (Figure 2.4c). Alteration along cracks to serpentine, oxides and iddingsite occurs in all samples, however it is more pronounced in samples that are more altered. Away from the cracks, the olivines are very fresh. Olivine commonly hosts Cr-spinel inclusions, as either clusters or individual grains. Occasionally, strain lamellae can be seen in the larger olivine crystals.

Cr-spinel occurs as a phenocryst and microphenocryst phase up to 1 mm in size (Figure 2.4d). It is often present in clusters and displays typical cubic crystal forms. Melt inclusions are commonly hosted in both the phenocrysts and in the Cr-spinels hosted by olivine. It is likely that Cr-spinel is the first phase to crystallize from a Cr-rich magma and likely provided sites for olivine nucleation (Kerr, 1998).

The groundmass is made up of plagioclase laths sub-ophitically intergrown with augite and rarer small rounded olivines. The plagioclase laths exhibit a variety of textures (Figure 2.4e-g), including variolitic fan-like textures, radiating spherulite textures, and an intergrowth intrafasciculate texture, where gaps in the plagioclase laths are occupied by augite. Away from the dyke margins, the groundmass is coarser, with plagioclase laths reaching up to 1 mm in length. Using petrogra-

phy, the plagioclase laths were found to range in composition from An_{70} to An_{78}. The groundmass commonly contains abundant Fe-Ti oxides, and where altered, calcite and chlorite are common.

2.4.2 Rum

R10 from Rum is highly olivine-rich (48% by vol.) with a very coarse matrix of plagioclase laths (composition An_{67} to An_{71}) subophitically intergrown with interstitial augite (Figure 2.4i). There exists a range of olivine morphologies and the crystals are up to 1 cm in size, similar to those described previously for Skye. The olivines have a brown colouring comparable to that described by Upton et al. (2002) in another picritic dyke from Mull. Upton et al. (2002) considered this to be due to finely exsolved trails of Fe-oxides, likely the result of high temperature oxidation (Haggerty and Baker, 1967). As seen in the Skye picrites, the olivines contain Cr-spinel inclusions which are often rich in melt inclusions.

2.4.3 Mull

The Mull olivine phenocrysts display a range of morphologies similar to those from Skye, except that skeletal olivines are more common. The rocks are very rich in olivine, up to 40% by vol., and are very fresh. The large olivines (Figure 2.4j) are up to 1 cm wide and display either a euhedral habit or a more irregular form. Commonly, olivines are grouped together to form large glomerocrysts. The olivines often enclose Cr-spinels and occasionally exhibit strain lamellae. Zoning is apparent in the large olivines due to different birefringence around the crystal edges.

The matrix consists of coarsely intergrown plagioclase laths (An_{71} to An_{77}) and interstitial augite often showing subophitic, spherulite and intrafasciculate textures. Small rounded olivines and occasional skeletal olivines (Figure 2.4k) are present. The groundmass is coarse, with some plagioclase laths exceeding 1 mm in length.

2.4.4 Iceland neovolcanic zones

The neovolcanic Iceland samples range from almost aphyric (1% olivine phenocrysts), to highly porphyritic, with abundant olivine phenocrysts up to 45% by vol. up to 1 cm wide. In some samples, zoning can be recognised due to the change in birefringence colours at the crystal edges. Olivines exhibit a range of morphologies similar to those found in the Skye rocks. Melt inclusions are often present (Figure 2.4l) in olivine and strain lamellae are occasionally present (Figure 2.4m). Cr-spinel is often hosted in olivine, and occasionally occurs as a phenocryst phase up to 1 mm in size. The groundmass varies from extremely fine grained up to around 300 μm, where the groundmass is composed of plagioclase laths subophitically intergrown with augite, and Fe-Ti oxides and occasionally small rounded olivines.

2.4.5 Iceland Tertiary

Rock or thin section samples were not available for the Iceland Tertiary samples, and so olivine separates were prepared in polished mounts. The olivines chosen for analysis were 1-3 mm wide and occasionally hosted Cr-spinel inclusions.

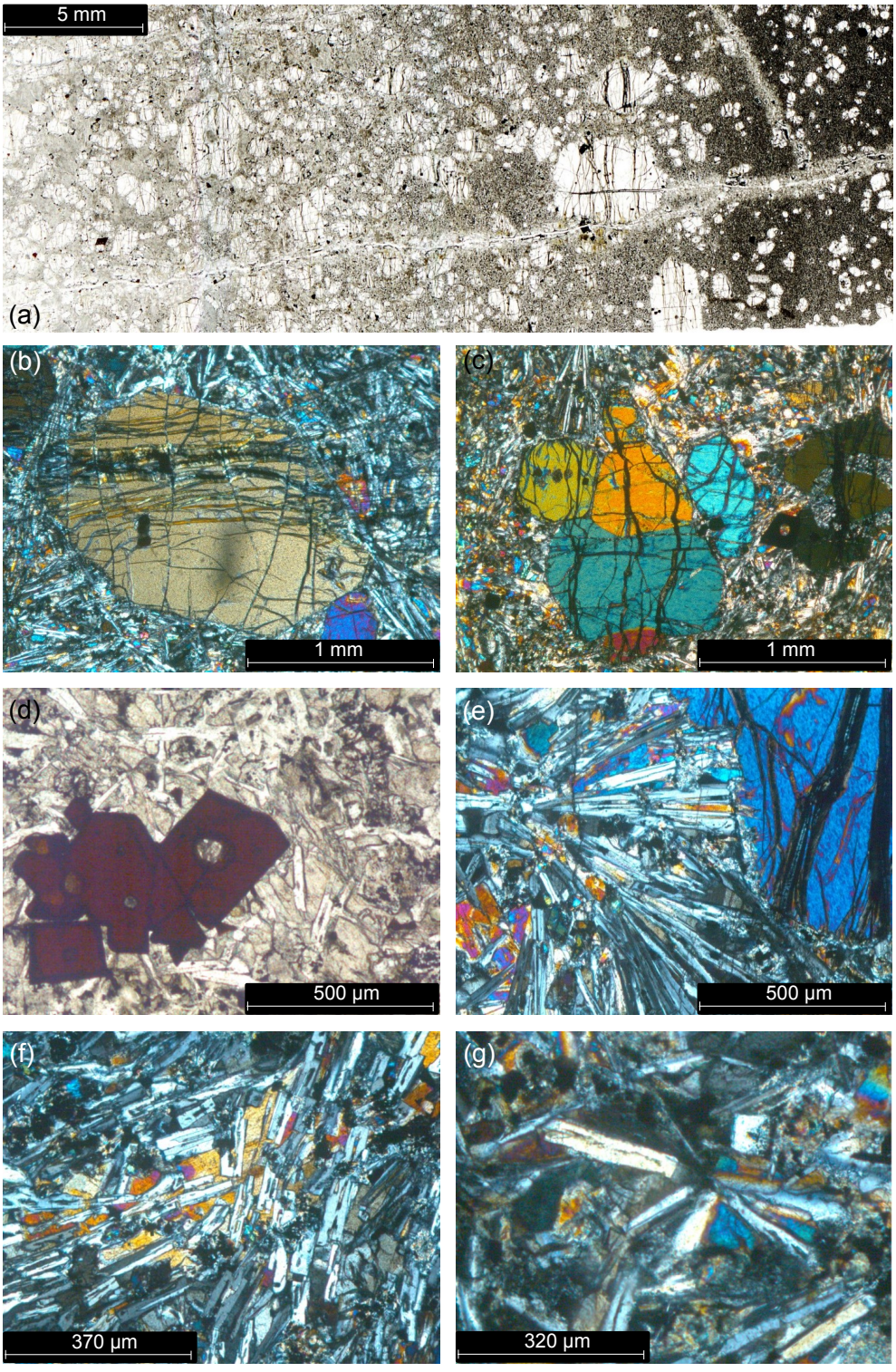

Figure 2.4

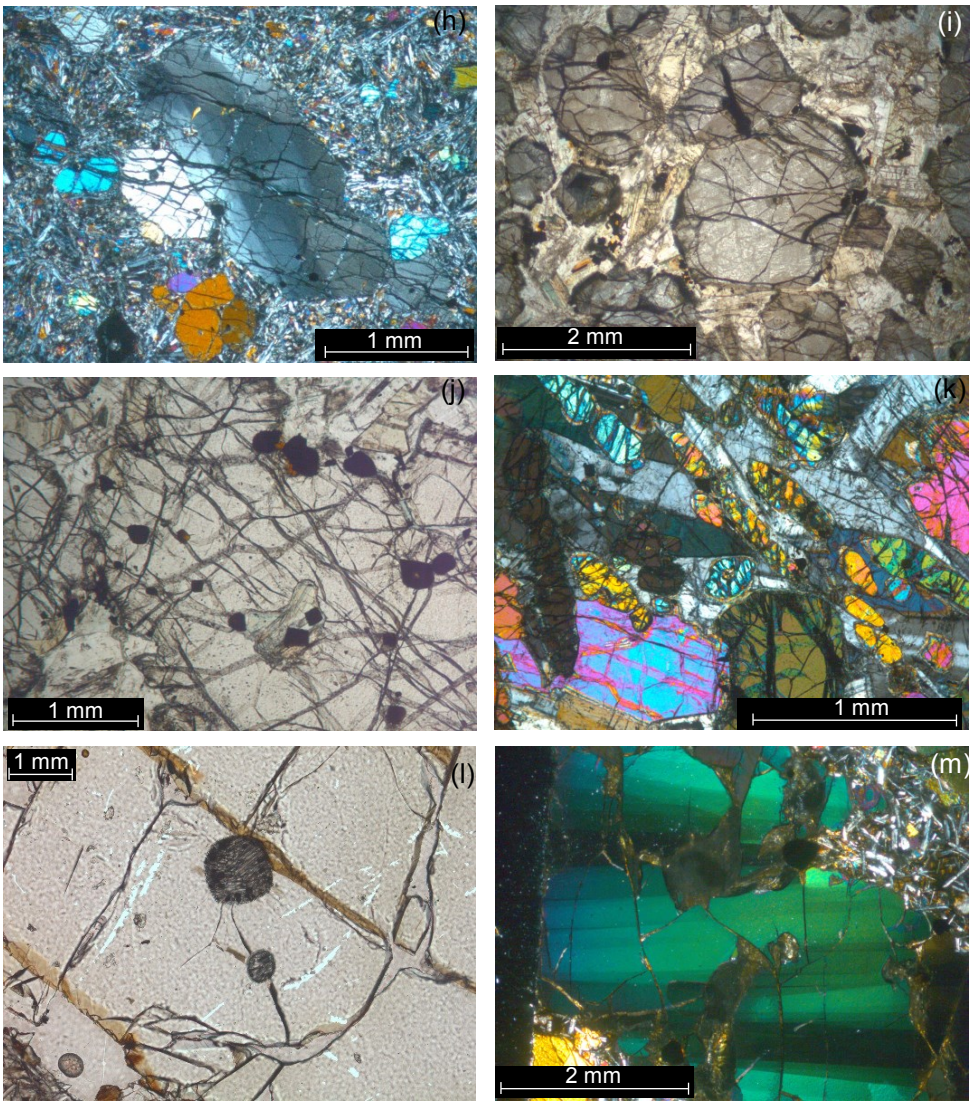

Figure 2.4: (a) Scanned thin section image showing a cross-section of the margin of S5. The fine-grained quenched margin is clearly visible at the right-hand edge. Towards the centre of the dyke the size and number of olivine phenocrysts increases. (b) A euhedral olivine phenocryst from S1 showing alteration along cracks to serpentinite and iddingsite. Away from the cracks the olivine is very fresh. (c) A glomerocryst from S1 composed of several olivine phenocrysts with a 120 ° triple junction at the grain boundaries. (d) A glomerocryst of Cr-spinel phenocrysts rich in melt inclusions from S10. (e) Plagioclase laths forming a diverging fan-like arrangement known as variolitic texture. The plagioclase laths have grown up to the edge of the olivine phenocryst. (f) Plagioclase forming an intergrowth intrafasciculate texture: columnar, hollow plagioclase crystals are filled by pyroxene. (g) An example of spherulite texture: elongate plagioclase crystals radiating from a nucleus. The space between plagioclase is often filled with augite. (h) Strain lamellae visible in an olivine phenocryst from S8. (i) Photomicrograph of R10. It is very olivine-rich and the olivines have a brown colouring thought to be due to a high-T oxidation event. (j) Photomicrograph showing Cr-spinel hosted by a large olivine phenocryst in MU3.1. (k) Photomicrograph showing skeletal and rounded olivines growing in the groundmass of MU1.5. (l) A crystallized melt inclusion in an olivine crystal in I2. (m) Strain lamellae visible in a broken olivine crystal in I5.

2.5 Whole-rock compositions

2.5.1 Major elements

The major-element composition of whole-rock powders was determined by X-ray fluorescence (XRF) spectrometry at the University of Edinburgh (details of analytical methods are presented in Appendix B.1) for the BTIP and neovolcanic Iceland samples. The Iceland Tertiary data are from Hardarson and Fitton (unpublished data). Data were corrected to a total of 100% on a volatile-free basis and all Fe is expressed as FeO. The Skye, Rum and Mull samples had loss on ignition (LOI) values of 1.47-5.86 wt%, however only two samples (S2 and S6) had values above 3 wt%, indicating that most samples have only minor alteration. The Iceland samples have LOI values of <1 wt%, indicating that they are very fresh with almost no alteration.

Based on the classification of Le Bas (2000), all of the Skye, Rum and Mull samples classify as picrites (MgO >12 wt% and <3 wt% total alkalis). Four of the seven neovolcanic Iceland samples classify as picrites, the remaining three are just outside the picrite range, however all have MgO >10 wt% and may still be considered primitive. All of the Tertiary Iceland samples can be classed as picrites.

The total alkali-silica (TAS) diagram is commonly used to classify volcanic rocks. According to this diagram (Figure 2.5), most of the samples from the BTIP plot inside the picrobasalt field, as well as two Iceland samples (I2, I5). The remaining samples are classed as subalkaline basalts.

Full results of bulk-rock major elements are presented in Appendix D.1. The MgO content of the BTIP samples ranges from 22.0-31.94 wt%. As will be discussed in more detail in Section 3.2.2, these high values are due to the accumulation of olivine phenocrysts and do not represent liquid compositions. When plotted against MgO (Figure 2.6), the samples show negative linear trends for SiO_2, Al_2O_3, CaO, Na_2O, K_2O, TiO_2, and P_2O_5. FeO_T and MnO are roughly flat across the MgO range. The sample from Rum (R10) is consistently different in

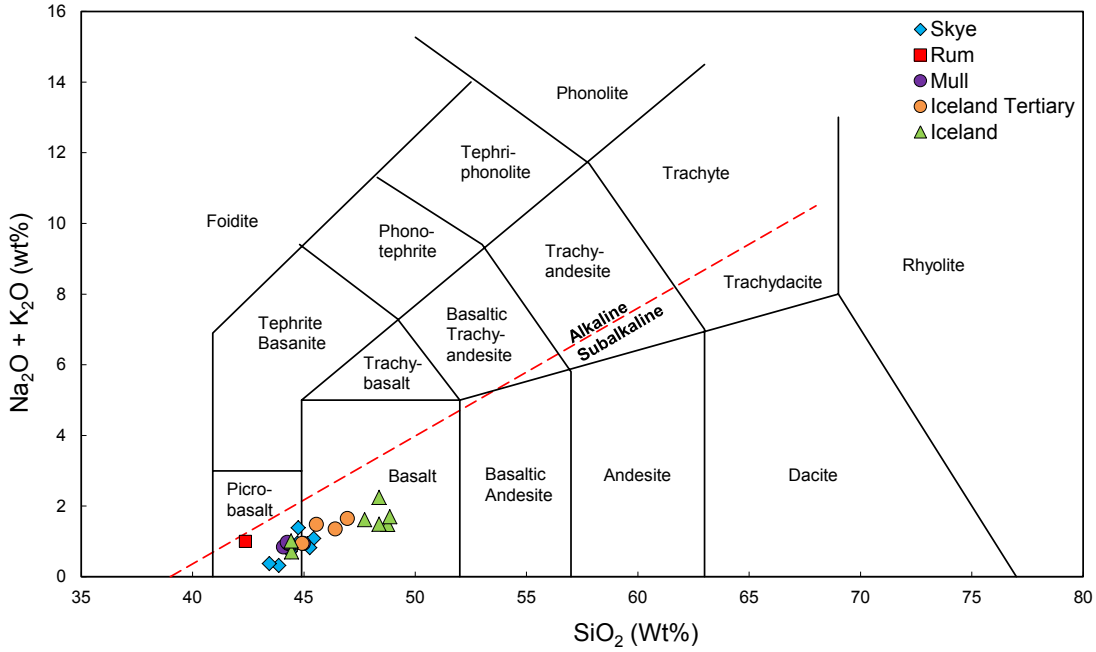

Figure 2.5: TAS diagram for the NAIP volcanic rocks. The field boundaries and alkaline-subalkaline division line are from Le Bas and Streckeisen (1991).

SiO_2, FeO_T, Na_2O, TiO_2 and P_2O_5. R10 has accumulated more olivine than any other sample and the olivines are more evolved than those from Skye and Mull. In addition, the plagioclase crystals from the matrix are more Na-rich than in the rest of the BTIP samples, leading to the systematic offsets observed in Figure 2.6. The data from this study are compared to published data on BTIP volcanics with MgO >10 wt% (Bell and Williamson, 1994; Kent, 1995; Kent and Fitton, 2000; Stuart et al., 2000; Upton et al., 2002; Peate et al., 2012). Most of the published data have lower MgO (<20 wt%) than the samples from this study (with the exception of the M9 dyke from Upton et al. (2002) which contains 34.1 wt% MgO), however, the two data sets generally form a continuous trend, indicating a common liquid line of descent in the magmatic system.

The MgO content of the Iceland neovolcanic samples ranges from 10.3-27.5 wt% and from 13.8-24.7 wt% in the Iceland Tertiary samples. Similar to the BTIP, the Iceland samples also exhibit negative linear trends when SiO_2, Al_2O_3, CaO, Na_2O, K_2O and P_2O_5 are plotted against MgO (Figure 2.6). One sample (I6) from the EVZ plots above or below the general trend of the majority of samples. This sample is enriched in Na_2O, K_2O, TiO_2 and P_2O_5 in particular, and so is

likely to represent a smaller degree (and hence more enriched) melt.

2.5.2 Trace elements

The abundances of Zn, Cu, Ni, Cr, V, Ba, Sc, La, Ce, Nd, U, Th, Pb, Nb, Zr, Sr and Rb were determined on whole-rock powders using XRF spectrometry at the University of Edinburgh. Full results and analytical details are presented in Appendix D.2 and B.1 respectively. The BTIP and Iceland samples follow the same general trends as previously (Figure 2.7) published data. Both the BTIP and Iceland samples show positive correlations between MgO and Ni and Cr (Figure 2.7). Ni and Cr are compatible in the olivine lattice (Kennedy et al., 1993) and so increase with olivine accumulation. In the BTIP, a negative correlation between MgO and Zn, Cu, V, Sc, Zr, Y and Sr is present, while no correlation between MgO and Ba, Nd, Pb Nb or Rb is observed. In Iceland, a negative correlation between MgO and Cu, V, Sc, Nd, Nb, Zr, Y, and Sr exists and there is no correlation between MgO and Zn, Ba, Pb or Rb. Those elements whose concentration decreases with MgO is because they are incompatible in the olivine lattice (Kennedy et al., 1993), and so their concentration is decreased with olivine accumulation. I6 again plots off the general trends. It has notably more Zn, Ba, Nd, Nb, Zr, Y and Rb, all incompatible elements, which supports the idea that this sample came from a more enriched, lower degree melt. The Iceland Tertiary samples generally follow the same trends, however are more enriched in some incompatible elements such as Ba, Nd, Nb, Zr and Sr.

Magmatism during the plume-head stage of activity (Phase 1 and Phase 2) tapped a heterogeneous mantle source, with both depleted N-MORB (negative ΔNb) and enriched Icelandic-type (positive ΔNb) mantle playing a role (Figure 2.8). The plume head is hypothesised to have been zoned as the contribution of enriched mantle decreases away from the centre of the proposed plume axis (Fitton et al., 1997, 1998). Phase 1 NAIP basalts that were erupted from the outer parts of the plume head (e.g. Hatton Bank, BTIP) have mostly N-MORB mantle sources, while basalts erupted closer to the centre of the plume (East Greenland and the Faeroes) have compositions similar to Icelandic basalt. The Baffin Island and West Greenland samples show a bimodal distribution of positive and negative

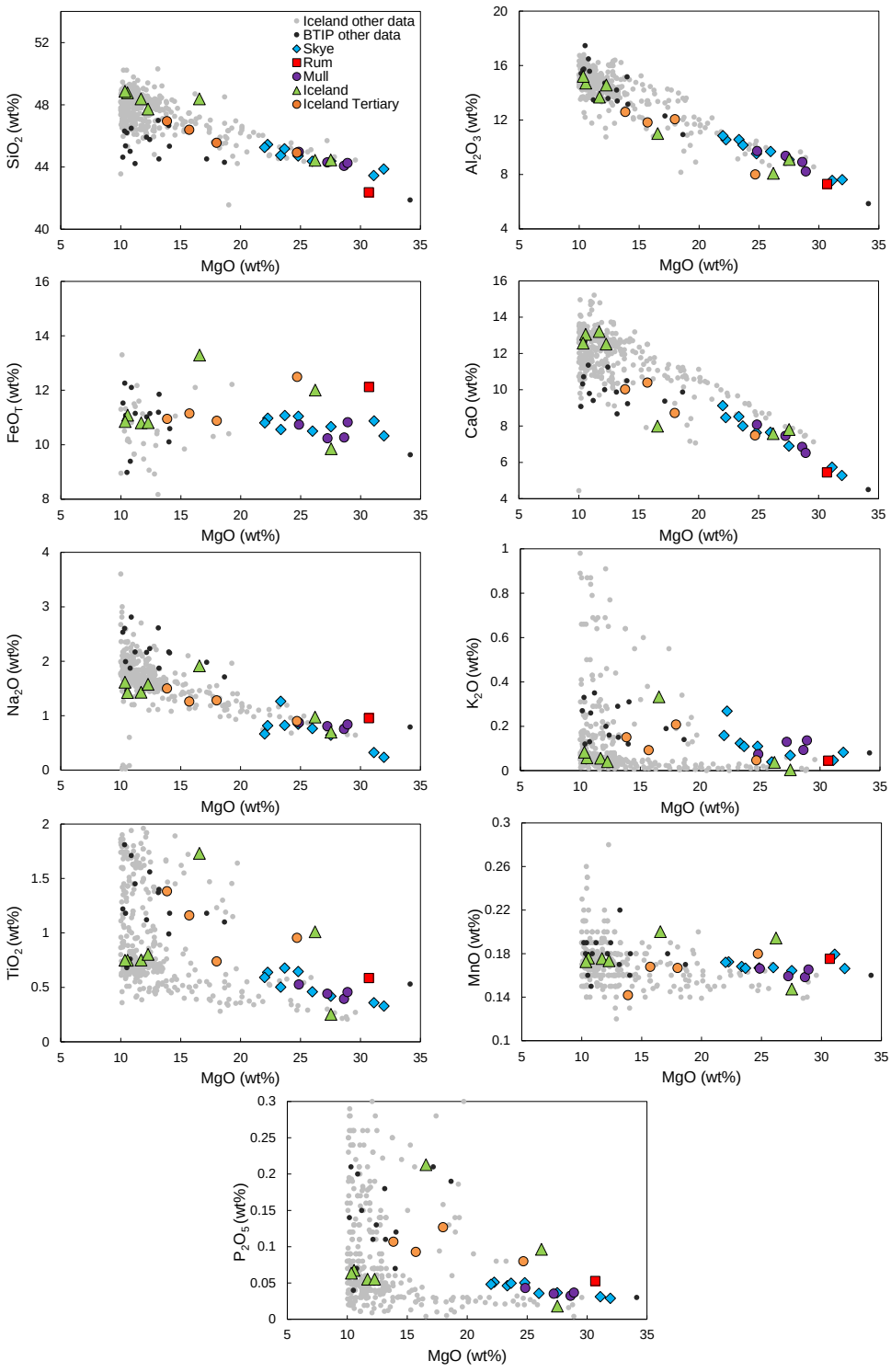

Figure 2.6: Major element vs MgO content in wt% for the BTIP and Iceland samples from this study and other datasets where MgO >10 wt%. Data sources: BTIP from Bell and Williamson (1994); Kent (1995); Kent and Fitton (2000); Stuart et al. (2000); Upton et al. (2002); Peate et al. (2012). Iceland data compiled from the Iceland GEOROC database, www.georoc.mpch-mainz.gwdg.de/georoc).

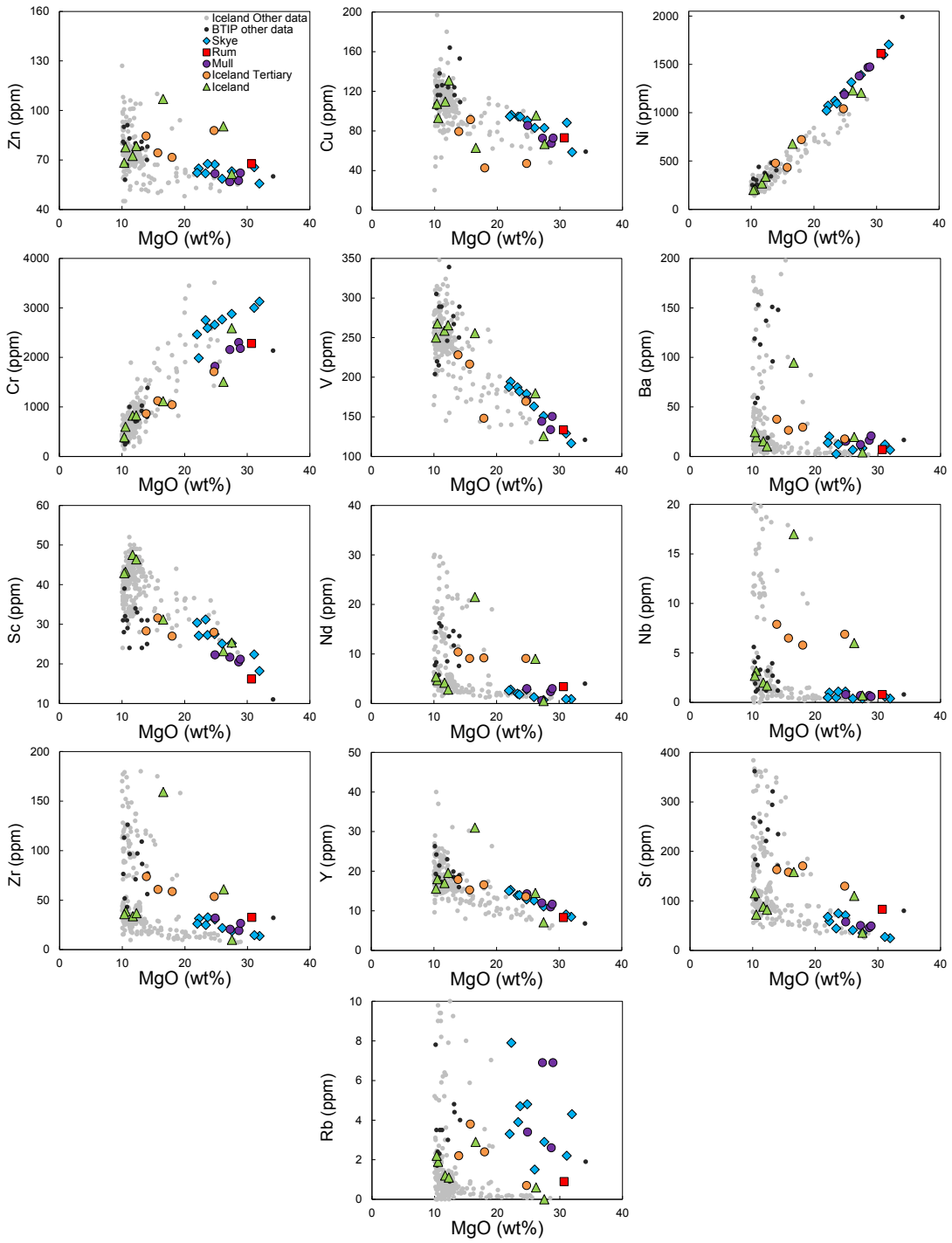

Figure 2.7: Bivarient plots of MgO and selected trace element abundances. Data from previous studies as in Figure 2.6.

ΔNb, indicating that Icelandic-type and N-MORB mantle sources were available close to the plume axis at the onset of magmatism. This is likely to be due to the mixing of plume material with entrained upper mantle during ascent of the plume head (Griffiths and Campbell, 1990; Campbell, 2007).

In the BTIP, although N-MORB is the dominant source mantle type, Icelandic-type mantle source is also tapped (Chambers and Fitton, 2000; Kent and Fitton, 2000). On Mull, ΔNb values fluctuate between positive and negative some 700 m above the base of the lava pile, before returning to a negative ΔNb. Three main magma types have been identified from the BTIP (M1-M3) that appear to be successive (Kent and Fitton, 2000). Basaltic dykes from the BTIP indicate the presence of Icelandic mantle throughout the history of the province. Kent and Fitton (2000) considered the existence of positive ΔNb M1 dykes to result from an initially heterogeneous outer plume head containing blobs of enriched mantle within a dominantly N-MORB source matrix. This heterogeneous margin was then displaced by enriched Icelandic-type material abruptly at 58.66 ± 0.25 Ma (Chambers and Fitton, 2000), to account for the increase in ΔNb sampled by M2 basalts. This 'wave' of enriched material receded at ∼58 Ma, back to a dominantly N-MORB source, but again with heterogeneous blobs, accounting for the presence of positive ΔNb in M3 dykes. The ΔNb anomaly during Phase 1 magmatism in the NAIP was at least twice the size as it is today. Positive ΔNb values are found in the BTIP, erupted around 1500 km from the proposed plume centre at 58 Ma (Lawver and Müller, 1994), whereas the present-day ΔNb anomaly reaches no further than around 700 km (Fitton et al., 1997). This finding is consistent with the idea that Phase 1 and 2 magmatism was the result of a large start-up plume head at least 2000 km in diameter.

When the BTIP samples from this study are plotted on a Nb/Y v Zr/Y diagram (Figure 2.8), two samples each from Skye and Mull exhibit positive ΔNb and the rest have negative ΔNb. This shows that the BTIP picrites sampled a heterogeneous mantle, with both N-MORB and enriched mantle present. All of the Iceland samples from the Tertiary and the neovolcanic zones have positive ΔNb (Figure 2.8), as expected.

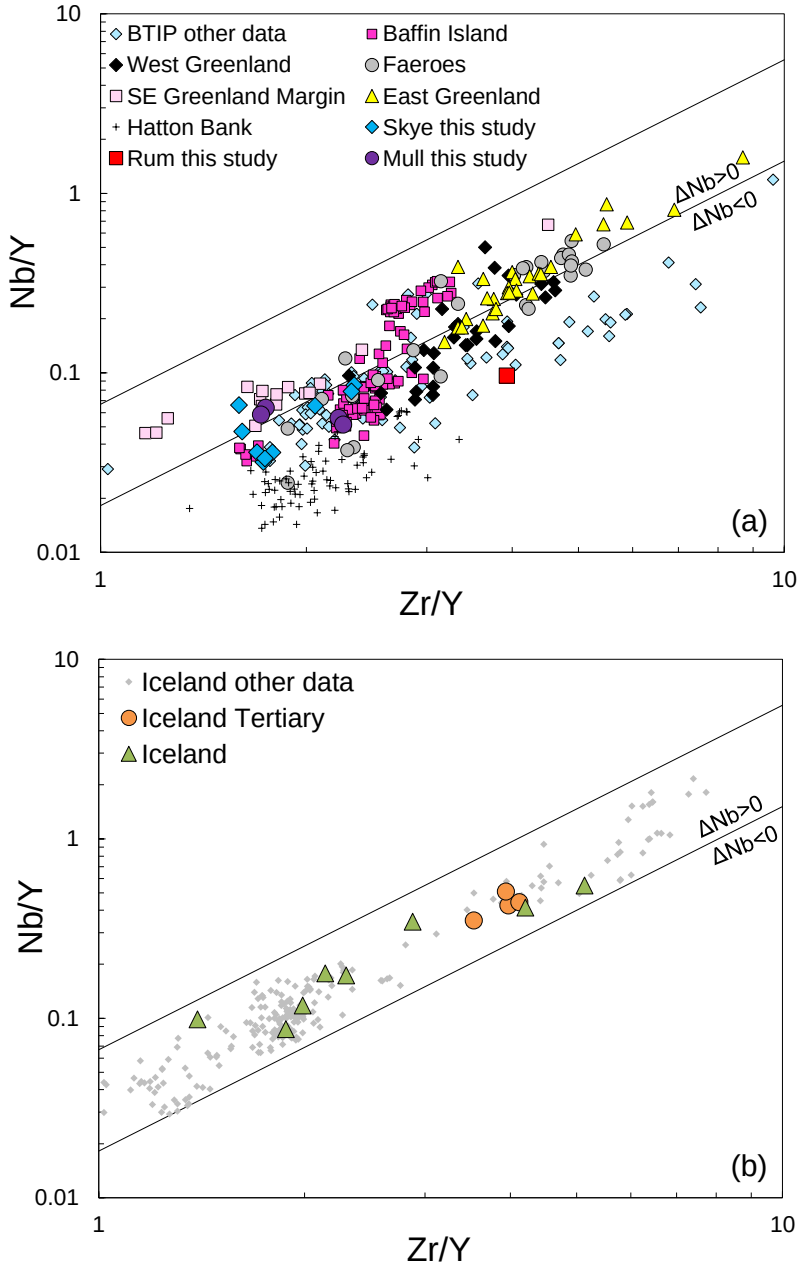

Figure 2.8: (a) Nb/Y and Zr/Y variation of onshore and offshore Phase 1 and 2 basaltic rocks from the NAIP. The parallel lines define the upper and lower bounds of the Iceland array (Fitton et al., 1997). Data sources: Skye, Rum and Mull this study, Baffin Island (Starkey et al., 2009), West Greenland (Holm et al., 1993; Starkey et al., 2009), SE Greenland Margin (Fitton et al., 1998), East Greenland (Upton et al., 1984; Larsen et al., 1989), Faeroes (Gariépy et al., 1983), Hatton Bank (Brodie and Fitton, 1998), BTIP (compiled from the NAIP GEOROC database, www.georoc.mpch-main.gwdg.de/georoc). The data set is filtered to remove crustally contaminated samples with Ba/Zr>2, although none of the samples from this study show any indications of crustal contamination. (b) Nb/Y and Zr/Y variation of Iceland basaltic rocks. Other Iceland data was compiled from the the Iceland GEOROC database, www.georoc.mpch-main.gwdg.de/georoc.

2.6 Mineral chemistry

Olivine phenocryst and Cr-spinel compositions were determined using a Cameca SX100 electron microprobe at the Edinburgh Materials and Micro Analysis Centre, University of Edinburgh (full results can be found in Appendix E and F and analytical details can be found in Appendix B.2).

2.6.1 Skye

Forsterite (Fo) contents (atomic Mg/(Mg+Fe) x 100, also known as Mg number or Mg#) of olivine crystals from Skye (Figure 2.9) indicate that the majority of olivine cores lie in the range Fo_{91-93} (117 out of 133 core analyses). The average composition is $Fo_{91.1}$. There is no correlation between olivine morphology and composition. Out of 13 rim analyses, 6 showed normal zoning with a decrease in Fo content from 0.3-1.6, 4 had negligible change and 3 indicated minor reverse zoning, with an increase in Fo of 0.1-0.25 (Table 2.2). 23 matrix olivines were analysed and these exhibited a systematically lower forsterite content with an average of $Fo_{88.7}$ and ranged from $Fo_{84.8-91.1}$.

If the olivine crystals are subtracted from the bulk-rock composition, matrix compositions ranging from 12.2-16.7 wt% MgO are calculated, with an average of 14.4 wt%. A melt of this composition is calculated to be in equilibrium with an olivine of composition $Fo_{88.6}$ (assuming an olivine-melt Fe-Mg exchange coefficient of 0.32 (Roeder and Emslie, 1970)), very close to the average composition of matrix olivine. The majority of phenocrysts are therefore not in equilibrium with the matrix. These observations suggest that most olivine crystals crystallized from high-MgO melts. Due to their high density, it is likely that the primary liquids remained at depth and that the olivines were picked up by melts with lower MgO. These melts must have ascended very rapidly to the surface (likely in a matter of days) in order for only minor Fe-Mg re-equilibration to occur.

Table 2.2: Olivine compositions of crystals with both core and rim data from Skye

Olivine	Core Mg#	Rim Mg#
S1_2	91.68	91.65
S1_14	91.54	91.16
S3_4	91.50	91.47
S5_7	91.54	91.50
S5_9	91.45	91.61
S5_19	91.53	91.78
S8_1	91.03	90.66
S8_6	90.72	90.89
S9_1	91.65	90.09
S9_4	91.64	91.19
S9_6	91.81	90.94
S9_15	90.91	90.18
S10_3	92.10	92.03

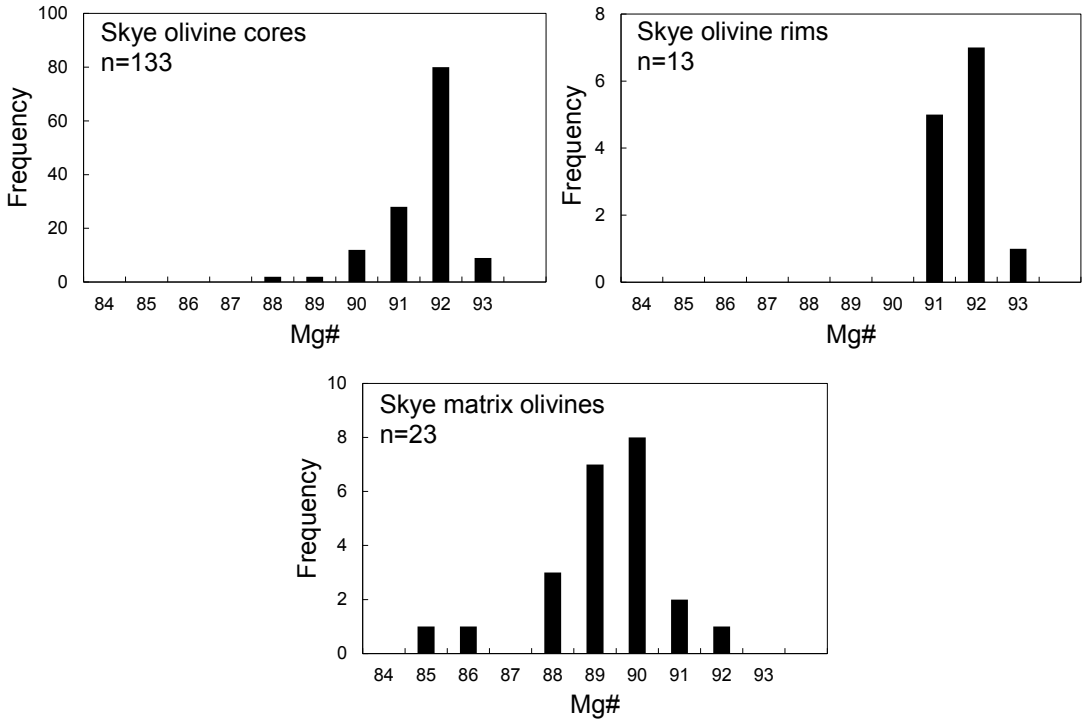

Figure 2.9: Frequency histograms of Skye olivine core, rim and matrix compositions (Mg#).

2.6.2 Mull

Olivines from Mull can be divided into 3 distinct populations (Figure 2.10): a highly magnesian population Fo_{90-93} (average $Fo_{91.7}$) consisting of the large, blocky and smaller euhedral crystal morphologies, a less magnesian population Fo_{83-89} (average $Fo_{86.2}$) made of smaller euhedral crystals, and a population of

elongated crystals in the matrix with composition $Fo_{81.6-84}$. The first two populations are all normally zoned down to $Fo_{82.9-88.5}$ (Table 2.3), and the zoned rim is generally around 200-300 μm thick (Figure 2.10). The composition of the lowest Mg rims and matrix olivine is very similar, suggesting that the rims grew from the same magma that the matrix crystallized from. The emplacement history of the Mull olivines is therefore likely to be very similar to that on Skye, however the presence of much more significant and better developed normal zoning suggests that they either did not ascend as rapidly, or were stored briefly in a shallow magma reservoir before emplacement.

2.6.3 Rum

The olivines from R10 can be divided into 2 distinct populations based on Mg-content (Figure 2.10) and are less Fo-rich than the samples from Skye. The high-Mg population ranged from $Fo_{87.7}$ to $Fo_{89.7}$ (average $Fo_{88.6}$). A less magnesian population with $Fo_{83.8-86.2}$ is present, with an average composition of $Fo_{84.8}$. Both populations exhibit normally zoned rims down to $Fo_{80.1}$ (Table 2.3) with a thickness of up to 200 μm. It is likely the emplacement history of the Rum olivines is very similar to the Mull samples, however the initial primary magma composition would have been less MgO-rich than from Skye or Mull, indicated by the less-forsteritic olivine cores. The olivines from M9 were described in detail by Upton et al. (2002). Two discrete populations are present, a primitive population with compositions ranging up to almost $Fo_{93.0}$, and a less Mg-rich population with compositions ranging from $Fo_{86.2}$ to $Fo_{90.2}$.

The olivines from Skye and Mull are as primitive as the most Mg-rich olivines found in the BTIP. The only other olivines with up to Fo_{93} come from the M9 dyke on Rum (Upton et al., 2002), which will also be included in the temperature calculations in Chapter 3. The samples from Skye and Rum therefore offer an excellent opportunity to try and determine the maximum temperatures that were present during Phase 1 magmatism. The olivines from R10 are not as Mg-rich, and are likely to record lower magmatic temperatures, however they are still primitive enough to record information about the early stages of magmatism, and so are still of interest to this study.

Table 2.3: Olivine compositions of crystals with both core and rim data from Rum and Mull

Olivine	Core Mg#	Rim Mg#
R10_1	87.68	80.14
R10_4	89.65	85.18
R10_6	88.59	84.83
R10_9	83.83	80.46
R10_11	87.90	84.01
R10_13	86.24	80.51
R10_18	84.21	80.56
R10_22	88.81	85.94
MU1.1_1	92.10	88.25
MU1.1_7	92.20	88.53
MU1.1_15	91.84	87.12
MU1.1_19	91.59	85.37
MU1.1_24	92.29	84.01
MU1.1_27	92.06	86.04
MU1.2_1	90.30	84.88
MU1.2_8	91.86	86.96
MU1.2_14	89.81	82.94
MU1.2_17	90.26	86.00
MU1.2_24	85.66	85.68
MU1.2_26	87.13	84.89
MU2.2_3	92.31	82.86
MU2.2_6	90.48	87.40
MU2.2_9	92.05	82.67
MU2.2_11	92.44	85.85
MU2.2_13	86.22	85.42
MU2.2_23	92.26	85.76
MU3.1_1	92.11	86.07
MU3.1_4	90.81	86.11
MU3.1_6	90.86	87.65
MU3.1_8	89.81	83.82

2.6.4 Iceland

The neovolcanic Iceland samples can generally be split into two categories on the basis of olivine composition (Figure 2.11): (i) samples with olivine compositions ranging from $Fo_{89.2-91.3}$ and (ii) samples with olivine compositions ranging from $Fo_{86.1-87.6}$, i.e. a primitive suite and a slightly more evolved suite. In some samples, two olivine populations were present: a more Mg-rich population up to $Fo_{91.3}$ and a less-Mg rich population with core compositions ranging from $Fo_{83.0-87.6}$. A third population was observed in several samples, with core compositions Fo_{81-83}. In two samples (I5 and I9), only one population of olivines (the more Mg-rich population) is present. All samples exhibit normally zoned rims down to Fo_{80} (Table 2.4) and there is substantial compositional overlap between the less Mg-rich olivine cores and the normally zoned rims (Figure 2.11), similar to that observed from Mull and Rum. Compared to Mull and Rum, the normally zoned rims are much thinner, $<$100 μm, and many are only a few 10s of μm wide.

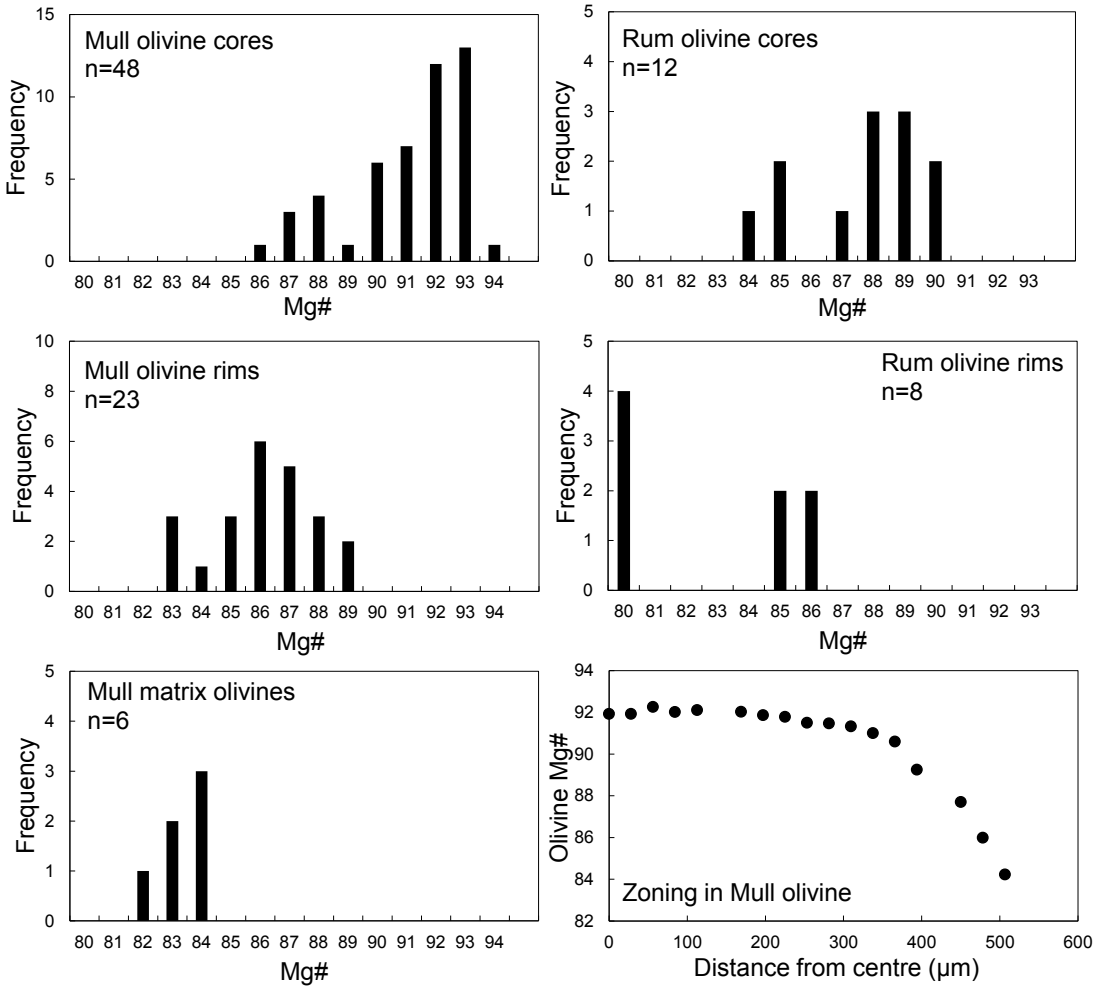

Figure 2.10: Frequency histograms of olivine core and rim compositions (Mg#) from Mull and Rum. Bottom right pane, an example of a zoning profile from an olivine in sample MU3.1. Distance from the centre of the olivine is plotted against olivine Mg#.

Most Iceland Tertiary samples contained only one olivine population (Figure 2.11), ranging from Fo_{83-88}, however two samples (ED and VEY) contained a small number of slightly less Mg-rich olivines down to Fo_{80}, and one sample (VEY), also contained a population of more primitive olivines up to $Fo_{90.7}$. Both normal and reverse zoning is present, however many crystals showed no change in composition between the olivine core and the rim (Table 2.4; Figure 2.11).

Table 2.4: Olivine compositions of crystals with both core and rim data from Iceland

Olivine	Core Mg#	Rim Mg#
ED_8	85.25	85.63
ED_17	85.79	85.90
KoP_10	83.72	86.25
KoP_16	85.88	87.71
SD_1	85.53	85.80
SD_14	85.76	85.94
VEY_1	90.38	90.44
VEY_5	81.56	83.30
VEY_12	90.32	89.88
VP1a_2	87.70	87.98
VP1a_13	86.02	86.22
VP1b_1	85.03	84.20
VP1b_11	87.96	87.50
I2_1	89.67	89.74
I2_6	89.93	81.59
I2_8	89.78	85.76
I2_11	89.81	86.93
I2_18	89.50	89.69
I3_2	85.00	80.27
I3_11	87.62	83.32
I5_2	88.72	85.74
I5_8	89.20	85.77
I5_10	88.46	84.84
I5_13	88.11	87.30
I6_2	89.74	83.41
I6_9	89.97	87.27
I6_15	88.85	86.71
I6_17	87.65	80.97
I7_4	86.12	80.67
I7_7	85.71	80.06
I7_11	85.88	82.02
I7_15	86.09	81.76
I9_3	90.13	87.30
I9_5	89.48	87.73
I9_13	88.75	87.77

2.6.5 Baffin Island and West Greenland

The composition of the Baffin Island and West Greenland olivines is discussed in detail by Starkey (2009), so is only briefly summarised here. Three populations of olivine are present: (i) large, highly magnesian crystals (Fo_{90-93}) with normally zoned rims (Fo_{78-85}), (ii) smaller crystals with normal zoning from Fo_{88} in the core down to Fo_{77-85} at the rim, and (iii) small crystals of Fo_{87-88} with some zoning present down to Fo_{74-84} at the rims. This is very similar to the Mull olivines, and so the crystal growth and evolution history is likely to have been very similar.

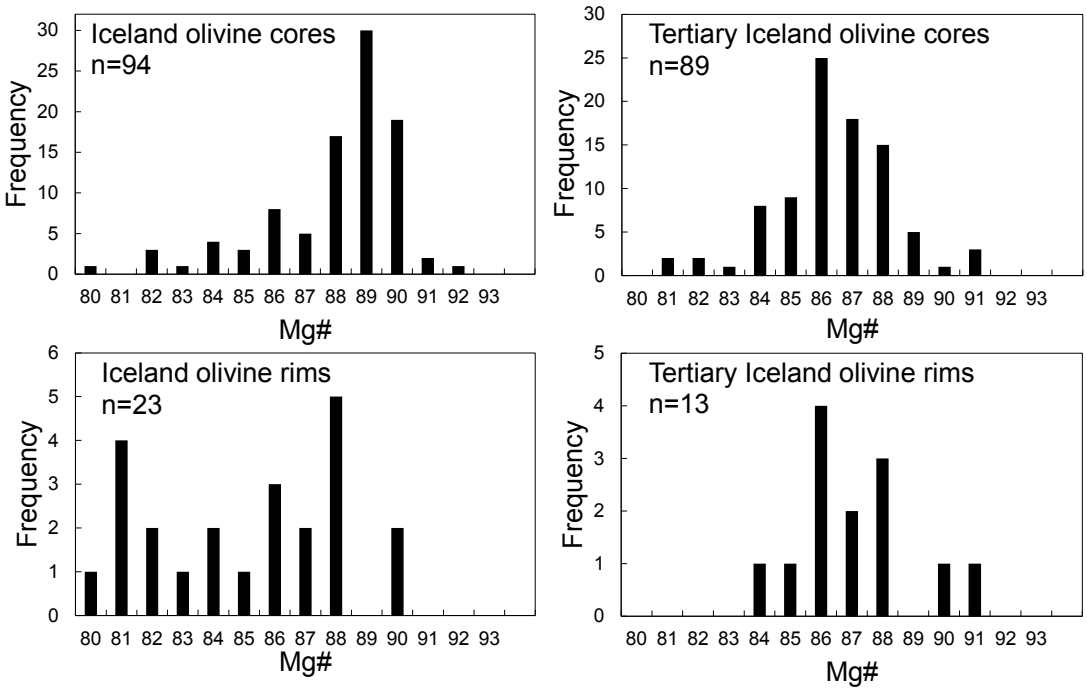

Figure 2.11: Frequency histograms of olivine core and rim compositions (Mg#) from neovolcanic and Tertiary Iceland samples.

2.6.6 The magma system and origin of high-Mg olivines

It has been suggested that highly magnesian crystals (~Fo_{93}) could represent mantle xenocrysts, xenocrysts from dunite cumulates on the magma chamber floor, or phenocrysts that are the product of extreme fractional melts that exited the melting regime (Francis, 1985; Herzberg and O'Hara, 2002; Yaxley et al., 2004). The presence of melt inclusions in all crystal types from each sample location indicates that the crystals were crystallized from melts. The CaO content of individual olivines (Figure 2.12) is much higher than that found in mantle xenocrysts, indicating a magmatic origin. The exception is for R10 from Rum, which contains some olivines with CaO contents that indicate the presence of some mantle xenocrysts. Additionally, oxide variation plots of NiO, Cr_2O_3 and MnO against olivine Mg# (Figure 2.12) show smooth trends, suggesting that within each suite, the olivines crystallized from the same magmatic system.

Kink-banding or strain lamellae, indicated by extinction discontinuities, are present in some high-Mg olivines from Skye, Rum, Mull and Iceland (Figure 2.4). This

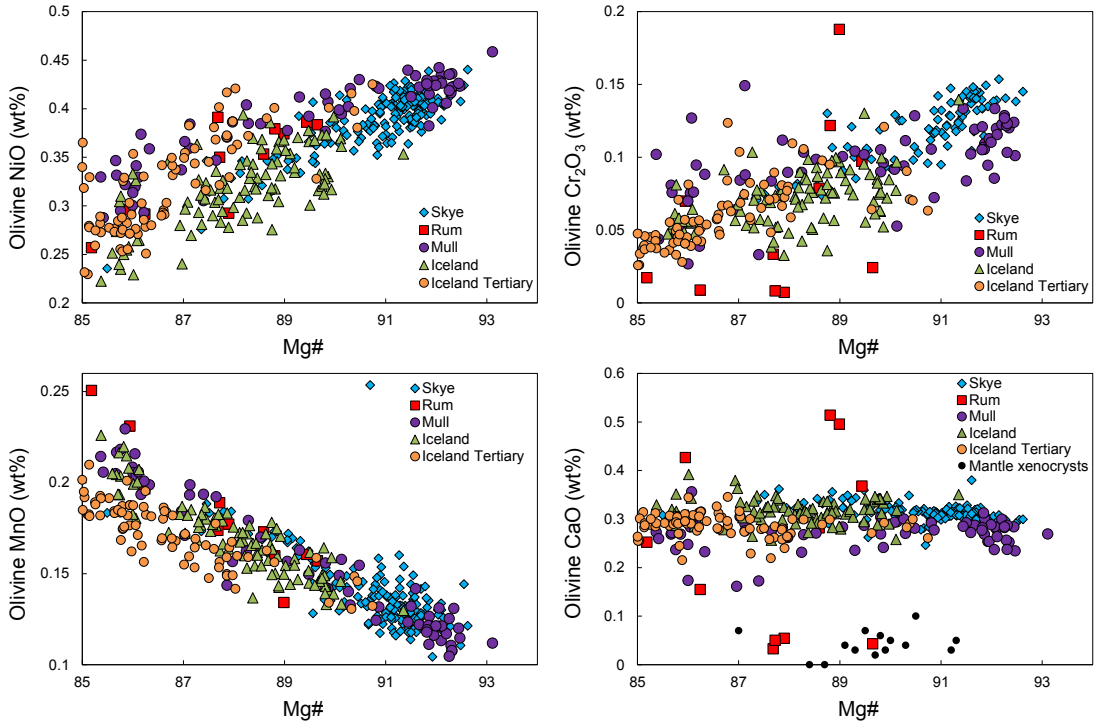

Figure 2.12: Oxide variation diagrams of NiO, Cr_2O_3, MnO and CaO (in wt%) against olivine Mg#. Mantle xenocryst data from Upton et al. (2011).

feature is commonly associated with cumulate deposits (Holness et al., 2007b,c), and has previously been described in Icelandic olivines (Francis, 1985; Helz and Thornber, 1987; Maclennan et al., 2003b; Thompson and Maclennan, 2013) and it is thought that these crystals were derived from cumulate rocks or mush prior to eruption. It is therefore possible that this is the case for the high-Mg olivines from the BTIP and Iceland. The common occurrence of glomerocrysts with 120° grain boundaries further suggests that these crystals may have been derived from cumulates or dense crystal mush. The suggestion by Francis (1985) that the high-Mg crystals may represent early dunite cumulates from the floor of the magma chamber may therefore be valid. Certainly the mineral layering in the Mull intrusive bodies suggests the involvement of a magma chamber in which some kind of cyclical process was occurring. These types of crystal would represent the products of earliest fractional crystallization from the most primitive primary melts in the magmatic system. It has also been suggested that such Mg-rich olivines may be wall-rock xenocrysts or phenocrysts crystallized from advanced fractional melts that exited the melting regime (Herzberg and O'Hara, 2002). Both of these suggestions are a possibility, but are hard to discern petrograph-

ically or chemically. The implications in relation to temperature and primary magma composition calculations of such a scenario is discussed in more detail in Section 3.2.3.

In many magmatic systems, a single pathway of magma evolution cannot account for the varying compositions of crystals in a sample. It has been proposed that many volcanic rocks represent a liquid containing a crystal cargo that is a mix of crystals inherited from prior liquids that existed at different places and times in the magmatic system (Davidson et al., 2007). Such crystals have been termed 'antecrysts' as they are not true phenocrysts or xenocrysts, because they are grown and recycled within the same magmatic system. Many volcanic rocks therefore represent a mixture of liquid, recycled antecrysts and true phenocrysts. In the case of this study, the recycled antecrysts are likely the high-Mg olivines, and the true phenocrysts are crystals with core compositions matching the composition of crystal rims and groundmass olivines. While the minor oxide (NiO, Cr_2O_3, MnO and CaO) trends of olivines in this study show good general trends with forsterite content, there is quite a lot of scatter and variation within an individual sample suite (Figure 2.12). This was noted to be the case in the West Greenland picrites by Larsen and Pedersen (2000), and was interpreted to be the result of crystal mixing from several magma batches and from crystals picked up from conduit sidewalls at depth.

Larsen and Pedersen (2000) envisaged the eruption of the West Greenland picrites to have occurred as crystal-charged magma batches ascending rapidly through steep, dyke-like conduits. High-Mg olivines would have crystallized at depth and less magnesian olivines were crystallized at shallower levels. Pulsating magma ascent would lead to mixing of magma and crystal batches in various stages of fractionation and equilibration. In order to keep the high-Mg olivines in suspension, high magma ascent rates are required. For an olivine with a core composition of $Fo_{92.6}$ with a 400 μm rim down to Fo_{88}, i.e. very similar to some Mull olivines, Larsen and Pedersen (2000) calculate that the rim would form in a period of $\sim$2 months at 1300 ℃. If the crystal formed at 30 km, this represents a magma ascent velocity of 500 m/day or 0.6 cm/s. Similar ascent rates are envisaged for the olivines from Mull and Rum, however the poorly developed zoning in the Skye olivines suggests that they sat around at depth for longer equilibrating with a high-Mg melt and/or their ascent rates were much more rapid. Faster primary

magma ascension rates have been suggested elsewhere, such as up to 10 cm/s at Hawaii (Maaløe, 1973).

2.6.7 Cr-spinel chemistry

Cr-spinel compositions in primitive rocks have been shown to be a complex function of magma composition, source composition, fO_2, crystallization temperature, cooling rate and pressure (Roeder, 1994, and references therein). Fractional crystallization (resulting in decreasing melt Mg# and temperature), leads to a decrease in the Mg# of co-crystallizing spinel and olivine, as shown in Figure 2.13. The range in spinel Mg# at any given olivine composition is due to a range of factors including the relative activities of Cr and Al in spinel, and hence the melt Al_2O_3 content, fO_2, and the cooling rate and post-entrapment re-equilibration (Kamenetsky et al., 2001).

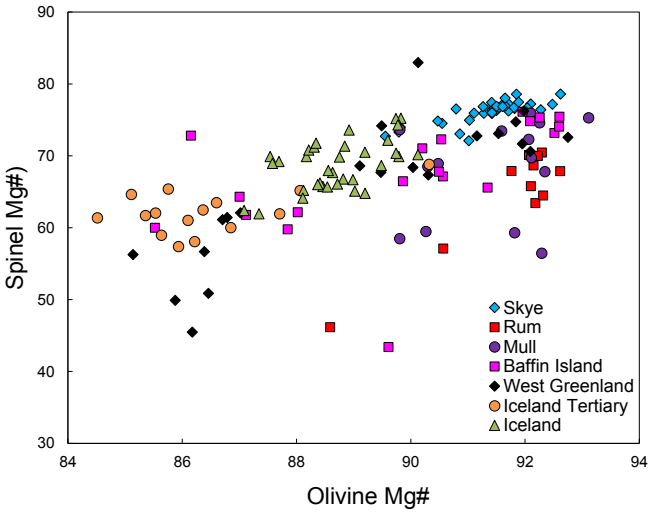

Figure 2.13: Mg# of host olivine and Cr-spinel inclusions.

A positive correlation between Al_2O_3 and TiO_2 contents in coexisting melts and spinels has been demonstrated (Kamenetsky et al., 2001), and it is therefore suggested that an Al_2O_3 vs TiO_2 diagram can be used to discriminate Cr-spinels that crystallized at different tectonic settings, as shown in Figure 2.14. The majority of the samples used in this study plot in the MORB field rather than in

the LIP or ocean island basalt (OIB) field, however it was noted by Kamenetsky et al. (2001) that Cr-spinels from West Greenland picrites plot in a field outside of the main LIP field. The NAIP Cr-spinels have notably much lower TiO_2 and higher Al_2O_3 contents those that plot within the LIP and OIB fields. Since spinel TiO_2 and Al_2O_3 abundance is thought to be primarily controlled by the melt composition, it is likely that these differences are due to variable mantle source compositions and melting conditions (such as pressure, fO_2).

It is also worth noting that the neovolcanic Iceland Cr-spinels have a strong bimodal distribution, forming a high Al_2O_3, low TiO_2, low Cr_2O_3 group and a low Al_2O_3, high TiO_2, high Cr_2O_3 group. This distribution is correlated with geographic location. The high Al_2O_3 group are from samples erupted in the NVZ and RVZ, while the low Al_2O_3 group are from spinels hosted in samples from the EVZ. It is possible that the bimodal distribution reflects the difference in melting conditions experienced at the different volcanic zones. The EVZ is located above the centre of the plume conduit, and hence the highest melt fractions and thickest crust is generated here (e.g. Thordarson, 2007). The RVZ and NVZ samples however, were formed in locations with much lower crustal thicknesses, and hence the melting conditions may have been quite different compared to those at the EVZ.

2.7 Summary

This chapter presents the field geology, petrology, major and trace element data and mineral chemistry data for the new NAIP samples used in this study. These are the Skye, Mull and R10 picritic dykes from the BTIP, and the Iceland neovolcanic samples. The Skye samples and R10 from Rum are small (up to 30 cm wide) dykes that intrude the central complexes. The Mull picrites are larger intrusive bodies that intrude the Mull Central Complex. All of these samples are highly olivine-rich (up to 48% by volume) with Cr-spinel present as inclusions in the olivine and as a phenocryst phase. The neovolcanic Iceland samples range from almost aphyric to highly porphyritic, with up to 45% by volume of olivine crystals. Cr-spinel is again present as inclusions within olivine and as a phenocryst phase. The whole-rock major and trace element data was compared to

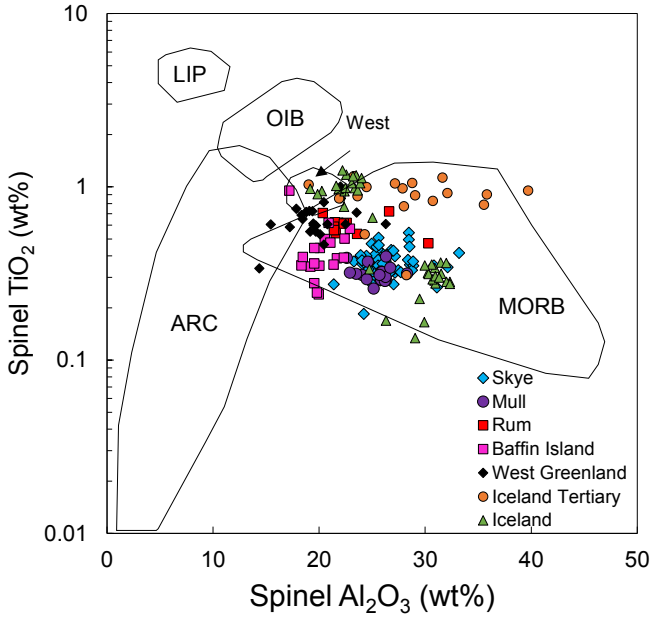

Figure 2.14: Al_2O_3 vs TiO_2 content of Cr-spinel inclusions in primitive olivine (Mg#>85). The fields for MORB, OIB, LIP, West Greenland and island-arc magmas (ARC) are from Kamenetsky et al. (2001).

other available data for each area showing that the samples follow similar trends except that they tend to fall on the high-MgO end of the compositional array. Highly magnesian olivine crystals up to $Fo_{92.6}$ are a common feature of the BTIP picrites and are as Mg-rich as the most primitive olivines found elsewhere in the NAIP (the M9 dyke from Rum and the Baffin Island and West Greenland picrites). The olivines from the Iceland samples are not as primitive as those from the early NAIP. The neovolcanic Iceland samples contain olivines up to $Fo_{91.3}$ and the Iceland tertiary picrites contain olivines up to $Fo_{90.7}$. The highly Mg-rich olivines are shown to have a magmatic origin as their CaO content is much higher than mantle xenocryst olivines. In addition, oxide variation plots of NiO, Cr_2O_3 and MnO against olivine Mg# show smooth trends, indicating that within each suite, the olivines crystallized from the same magmatic system.

3 Thermometry

3.1 Introduction

Olivine is the first major phase to crystallize in primitive melts and equilibrates with magma in the mantle source region (O'Hara, 1968). Consequently, most previous studies that have used a petrologic approach to determining the temperature of the mantle have focused on the temperature at which olivine and melt equilibrate. Traditionally, there have been two main approaches to this. Both use bulk-rock basalt compositions that have only crystallized or accumulated olivine since formation. The first approach, known as olivine-melt thermometry, incrementally adds or subtracts equilibrium olivine to the bulk-rock until a primary liquid composition that would be in equilibrium with the most primitive olivine phenocryst in the sample is calculated. The exchange of Fe and Mg between olivine and melt is temperature dependent, so if the most primitive olivine phenocryst and primary liquid compositions are known, it is possible to estimate the temperature by application of a thermometer (e.g. Roeder and Emslie, 1970; Ford et al., 1983; Beattie, 1993; Putirka, 2005; Putirka et al., 2007). The second approach adds equilibrium olivine to the bulk-rock to produce a range of possible primary magma compositions which are then compared with experimentally determined mantle melt compositions generated from melting of mantle peridotite (e.g. Herzberg and O'Hara, 2002; Green and Falloon, 2005; Herzberg et al., 2007; Herzberg and Asimow, 2008; Herzberg and Gazel, 2009; Herzberg and Asimow, 2015).

Many of these studies suggest a difference in mantle potential temperature between mid-ocean ridge (MOR) and LIP settings of 100-300℃ (Herzberg and O'Hara, 2002; Putirka, 2005; Herzberg et al., 2007; Putirka et al., 2007; Herzberg and Asimow, 2008; Herzberg and Gazel, 2009). Specifically in the NAIP, anomalies of ∼300℃ (Herzberg and Gazel, 2009) and ∼160℃ (Putirka et al., 2007)

are measured from Phase 1 and modern Icelandic basalts, respectively. Unfortunately, both approaches require a number of variably constrained parameters that will be discussed in detail in Section 3.2.3. As a result, there are large uncertainties associated with these types of calculations and contrasting results have been published in the literature. For example, Falloon et al. (2007a,b) calculated that the mantle potential temperature at MORs and Hawaii is the same, whilst others suggest a large temperature anomaly of around 250℃ above that of ambient mantle is present at Hawaii (Putirka et al., 2007; Herzberg and Gazel, 2009).

More recently, it has been noted that elements such as Cr, Al, V, Sc, Ca and Na show large concentration ranges in olivine, and have partition coefficients that are highly temperature sensitive. This will consequently allow for simple geothermometers based on the concentrations of these elements in olivine (De Hoog et al., 2010). A thermometer based on the Al content of olivine was calibrated by Wan et al. (2008), and it is possible to estimate the equilibration temperature of olivine and Cr-spinel to within ±22℃. In addition, empirical tests suggest that this method is free of the uncertainties and problems associated with olivine-melt thermometry, and may therefore be a more reliable method of temperature estimation.

The purpose of this chapter is to use both of the traditional petrologic approaches and Al-in-olivine thermometry to constrain the temperature of the mantle source region of the NAIP samples. The problems associated with the more traditional methods will be investigated, and then the results of all three techniques will be compared in order to identify the best technique. This work is the first study to compare all techniques in detail using the same sample suite.

3.2 Olivine-melt Fe-Mg thermometry

3.2.1 Introduction

Olivine-melt thermometry estimates the temperature at which an olivine was in equilibrium with the melt from which it crystallized. The forsterite-fayalite

phase diagram (Figure 3.1) illustrates the monotonic relationship between the forsterite content of olivine and temperature. Olivines of higher forsterite content equilibrate with liquids with high Mg# at a higher temperature. $Mg\#^{liq} = X^{liq}_{Mg}/(X^{liq}_{Mg}+X^{liq}_{Fe})$, where X^{liq}_{Mg} and X^{liq}_{Fe} are the cation fractions of Mg and Fe in the liquid, with Fe as Fe^{2+}. However in natural systems, Fe and Mg may vary independently, and the monotonic relationship between forsterite content and temperature cannot be applied.

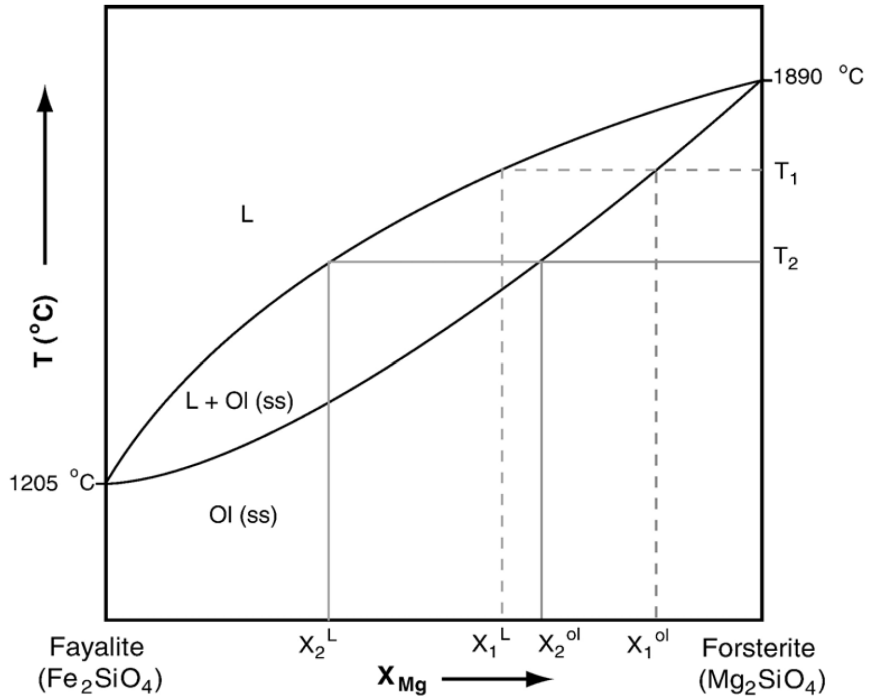

Figure 3.1: The binary phase diagram for forsterite-fayalite. At temperature T_1, a liquid of composition ${X_1}^L$ will equilibrate with an olivine of composition ${X_1}^{ol}$. At a lower temperature, T_2, liquid of composition ${X_2}^L$ will equilibrate with an olivine of composition ${X_2}^{ol}$, which has a lower forsterite content than the olivine equilibrated at T_1. However, in natural systems, Fe and Mg may vary independently, hence the simple monotonic relationship between Fo content and T is not applicable. From Putirka et al. (2007)

Roeder and Emslie thermometer

Roeder and Emslie (1970) were the first to study olivine-melt equilibria, and investigate Fe-Mg partitioning between olivine and liquid. Their landmark study

showed that the equilibrium constant for Fe-Mg partitioning between olivine and liquid, known as the Fe-Mg exchange coefficient, or K_D(Fe-Mg)$^{ol-liq}$ =[X$_{Fe}$/X$_{Mg}$]^{ol}/ [X$_{Fe}$/X$_{Mg}$]^{liq}, in the reaction:

$$MgO^{ol} + FeO^{liq} = MgO^{liq} + FeO^{ol} \tag{3.1}$$

is nearly constant even when temperature and composition are varied. However, later work has shown that K_D(Fe-Mg)$^{ol-liq}$ increases with pressure (Herzberg and O'Hara, 1998), and this has been accounted for in more recent thermometers. Mg# of the liquid therefore still controls the Fo content of an olivine in equilibrium with the liquid, however it is dependent on the value of K_D(Fe-Mg)$^{ol-liq}$, calculated by Roeder and Emslie (1970) to be 0.30 ± 0.03 at atmospheric pressure. While a high Fo olivine can crystallize from a liquid with high Mg#, if the liquid also has low X_{Fe}^{liq}, then X_{Mg}^{liq} must also be low, requiring equilibration at low temperature.

The olivine-saturation surface, experimentally calculated by Roeder and Emslie (1970), shown in Figure 3.2, is a useful means of illustrating this principle. The saturation surface provides a graphical estimation of the Mg and Fe^{2+} contents required of the liquid to crystallize an olivine of a specific forsterite composition at a certain temperature. Lines radiating from the origin are lines of constant olivine composition and are calculated using the olivine forsterite content at a specific K_D(Fe-Mg)$^{ol-liq}$. Crosscutting lines are isotherms and are calculated from the ratio of Mg and Fe between olivine and the liquid, D$_{Mg}^{ol/liq}$ and D$_{Fe}^{ol/liq}$ (Equation 3.2 and 3.3), which are temperature dependent, and the relationship shown in Equation 3.4.

$$D_{Mg}^{ol/liq} = -2.02 + \frac{44905.5}{T} \tag{3.2}$$

$$D_{Fe}^{ol/liq} = -2.66 + \frac{3793.3}{T} \tag{3.3}$$

Olivine stoichiometry requires that $X_{Mg}^{ol} + X_{Fe}^{ol} = 2/3$ and, by definition, D$_{Mg}$= $X_{Mg}^{ol}/X_{Mg}^{liquid}$ and D$_{Fe}$= $X_{Fe}^{ol}/X_{Fe}^{liquid}$. Rearrangement of these expressions gives

X^{ol}_{Mg}=$[X^{liquid}_{Mg}][\mathrm{D}_{Mg}]$ and X^{ol}_{Fe}=$[X^{liquid}_{Fe}][\mathrm{D}_{Fe}]$, which can be substituted into X^{ol}_{Mg} + X^{ol}_{Fe} = 2/3 to yield:

$$\left[X^{liq}_{Mg}\right]\left[D^{ol/liq}_{Mg}\right] + \left[X^{liq}_{Fe}\right]\left[D^{ol/liq}_{Fe}\right] = 0.667 \tag{3.4}$$

The equilibration temperature can be estimated for an olivine of specific composition using the saturation surface if either X^{liq}_{Fe} or X^{liq}_{Mg} is known. The saturation surface illustrates the importance of the independent variation of Fe and Mg of a liquid on temperature. For example, a liquid with X_{Fe}=0.095 and X_{Mg}=0.27 will crystallize an olivine of Fo_{90} at 1600℃, whereas a liquid with X_{Fe}=0.08 will crystallize an olivine of Fo_{90} at a temperature of 1500℃, if the liquid X_{Mg}=0.225. Therefore, it is possible to crystallize a high-Fo olivine across a range of temperatures, dependent on the X^{liq}_{Fe} content of the liquid. While high-Fo olivines are often suggestive of high-T primitive melts, this conclusion cannot be drawn without the application of a thermometer.

Other olivine-melt thermometers

A number of olivine-melt thermometers have since been devised (e.g. Ford et al., 1983; Beattie, 1993; Putirka, 2005; Putirka et al., 2007). By using these thermometers, with knowledge of the olivine and primary magma composition, it is possible to calculate the T at which an olivine equilibrated with the melt. The Beattie (1993) model was considered to be superior by Putirka et al. (2007), however it produces systematic errors at high pressure and temperature, and also overestimates temperature in the presence of water, and so is only useful for anhydrous systems at T <1650℃ (Putirka, 2008). Putirka et al. (2007) presented an updated thermometer to account for $\mathrm{H_2O}$ and $\mathrm{SiO_2}$ content and the pressure sensitivity as noted by Herzberg and O'Hara (1998). The Putirka et al. (2007) thermometer is currently considered the most up-to-date olivine-melt thermometer, and so its application to the NAIP sample suite is explained in detail below.

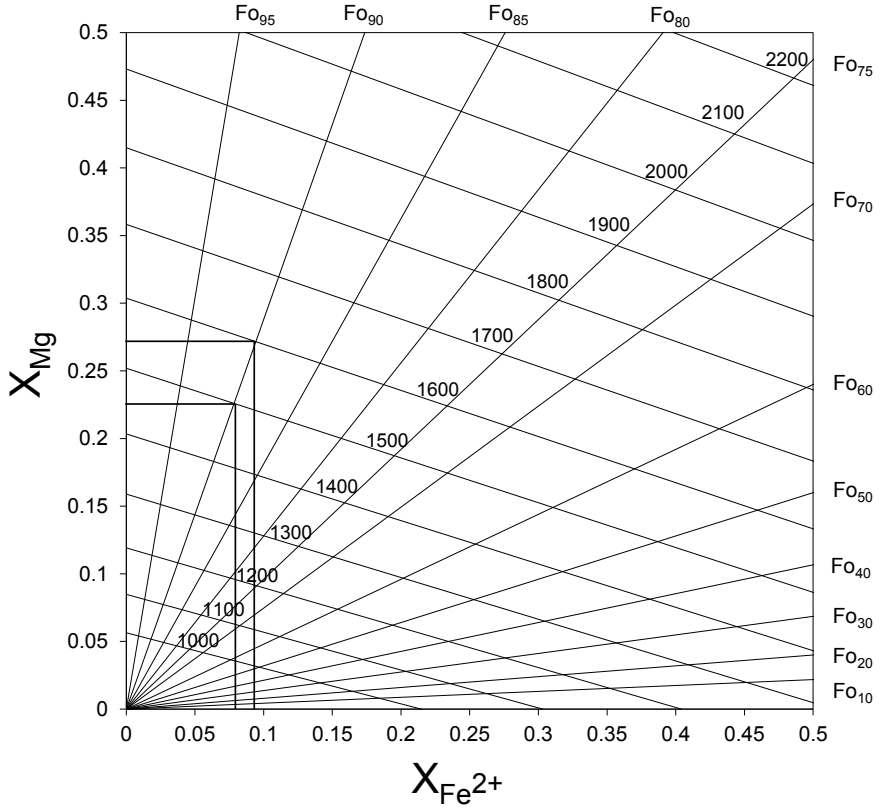

Figure 3.2: The olivine saturation surface calculated by Roeder and Emslie (1970) for a K_D(Fe-Mg)$^{ol-liq}$ value of 0.32 (the average value for the 0.5-2.0 GPa pressure range). Lines radiating from the origin are lines of constant olivine composition while the crosscutting lines are isotherms. The temperature contours (in ℃) are close to horizontal because $D_{Mg}^{ol/liq}$ is much more sensitive to temperature than $D_{Fe}^{ol/liq}$. For a given olivine composition, T can be estimated from the intersection of the respective constant Fo line with a point of fixed X_{Fe}^{liq} and X_{Mg}^{liq}. The black lines represent two liquids with X_{Fe}^{liq}=0.08 and X_{Mg}^{liq}=0.225, and X_{Fe}^{liq}=0.095 and X_{Mg}^{liq}=0.27. Each of these liquids would crystallize a Fo_{90} olivine at 1500℃ and 1600℃, respectively.

3.2.2 Application of olivine-melt thermometry to the NAIP

In order to calculate the olivine-melt equilibrium temperature, the following parameters must be known: the composition of the primary melt, the pressure of olivine-liquid equilibrium, and hence $K_D(\text{Fe-Mg})^{ol-liq}$, the composition of the olivines that equilibrated with the primary melt, and the oxygen fugacity (fO_2). These parameters are discussed in more detail below.

Primary melt composition

The Putirka et al. (2007) thermometer works in much the same way as the Roeder and Emslie (1970) olivine-saturation surface. Primitive MgO liquid contents can be estimated by determining the MgO content of a liquid in equilibrium with the most primitive olivine phenocryst present in the sample. Once the primary magma composition is known, the temperature can be calculated using a saturation surface. As with the Roeder and Emslie (1970) saturation surface, the cation fractions of Fe^{2+} and Mg in the liquid are required. In order to calculate a cation fraction, the content of the other major cation components must be known, and it is therefore necessary to calculate the whole-rock composition of the primary liquid. If the bulk composition of the sample and the composition of the most forsteritic olivine are known, then this can be done by estimating the MgO content of a liquid that must have crystallized that particular olivine, and adding or subtracting equilibrium olivine until this 'target MgO' is achieved.

If the bulk composition of picritic rocks is controlled only by the addition or subtraction of olivine, then they can be plotted along an olivine control line. The olivine control line is constructed using the method of Herzberg et al. (2007). A representative bulk-rock composition for each suite is selected and its equilibrium olivine composition is calculated. Equilibrium olivine is then added or subtracted incrementally to the representative sample to generate the olivine control lines shown in Figure 3.3, allowing the fractional crystallization of olivine to be easily visualised. All of the samples in the present study are picrites, and therefore do lie along olivine control lines.

Commonly in picritic suites, rocks with high MgO do not represent liquids, but are aggregates of primitive olivine phenocrysts and basaltic liquid. This is clearly the case for many of the samples in the present study, with bulk-rock MgO contents ranging up to >30 wt%. Phenocrysts in such rocks are recognised to be early precipitates that are later remobilized, particularly in large-volume eruptions (e.g. Murata and Richter, 1966; Helz and Thornber, 1987; Clague et al., 1991; Baker et al., 1996; Norman and Garcia, 1999). It is therefore unclear where along the olivine control line the MgO content of the primary magma plots. However, because the exchange coefficient of Fe^{2+} between olivine and melt is close to 1, the FeO content of the primitive liquid is nearly constant along the olivine control line, (Figure 3.3) allowing MgO content of the primary magma to be estimated where the most primitive olivine saturation line intersects the olivine control line. If the accumulated olivines are out of equilibrium with the liquids, then this is different from reverse fractional crystallization. However, the differences are small and may be neglected (Herzberg et al., 2007). The choice of the most forsteritic olivine is a key source of uncertainty for the olivine-melt thermometer and its impact will be considered later in more detail.

The NAIP samples are plotted onto olivine control lines in Figure 3.3. This diagram again illustrates the importance of liquid FeO content on olivine melt thermometry, as the MgO content of a primary magma required to equilibrate with an olivine of specific forsterite content increases as the FeO content increases. The Skye, Mull and West Greenland samples all lie along one curve, indicating derivation from primary magmas with similar FeO contents. The Rum samples plot close to the high FeO curve, indicating that their primary magmas had a higher FeO content. The samples from Baffin Island and Iceland do not fall on the same curve, suggesting derivation from primary magmas with variable FeO contents, and therefore either a heterogeneous mantle source (as was suggested by Larsen and Pedersen (2000) for West Greenland picrites using a similar technique) or a difference in pressure of melting. The Iceland samples that plot on the higher curve are from the EVZ (I5 and I6). All other Iceland samples are from the RVZ or the NVZ. The EVZ has the thickest crust in Iceland, so it is possible that the higher FeO contents of I5 and I6 reflect higher melting pressures.

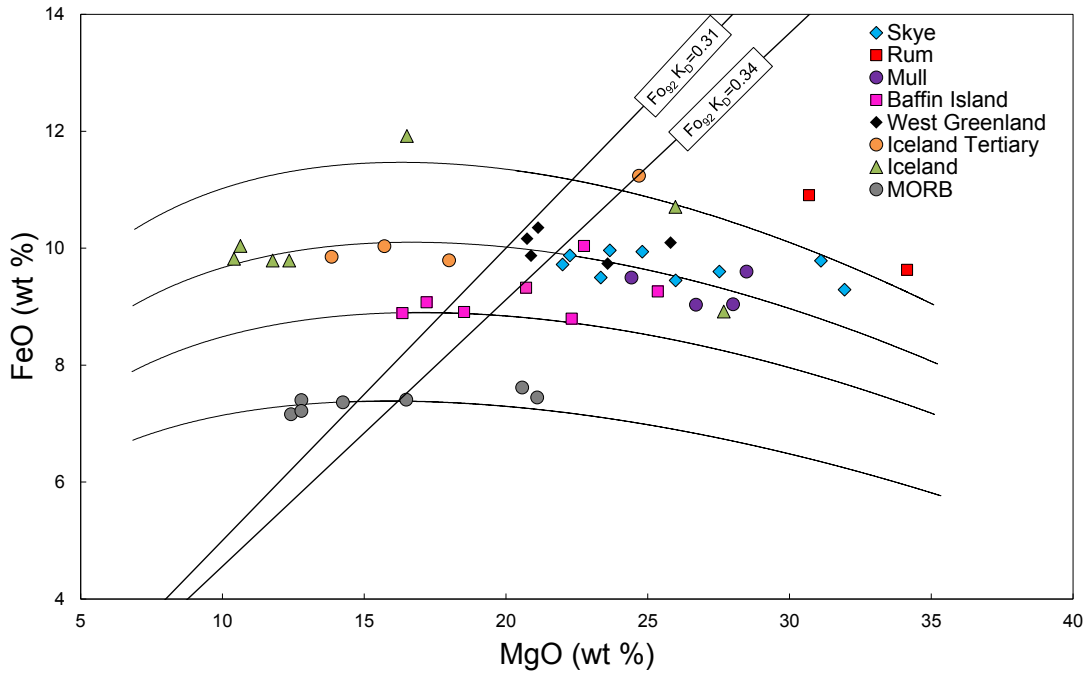

Figure 3.3: Olivine control lines (black curves) with the bulk rock FeO and MgO of each NAIP sample plotted. The upper, second and third curves were generated using samples I5, S9 and PAD6, respectively. In this figure, all samples have an assumed bulk-rock $Fe^{3+}/\sum Fe$=0.1, except for MORB, which has an assumed $Fe^{3+}/\sum Fe$=0.07 (Christie et al., 1986). The MORB rocks are from the Siqueiros transform fault of the East Pacific Rise (Perfit et al., 1996). The MORB olivine control line was generated using sample ALV2384-003 (Perfit et al., 1996). The two straight lines intersecting the olivine control curves represent olivine of composition Fo_{92} at $K_D(\text{Fe-Mg})^{ol-liq}$ of 0.31 and 0.34. The MgO content of the primary magma is calculated from where the line of the most primitive olivine phenocryst in the sample intersects the olivine control line.

Oxidation state

The 'target MgO' of the primary magma for each sample was determined from the intersection of the most primitive olivine composition line with the relevant olivine control curve. This requires knowledge of the FeO and Fe_2O_3 contents of the lava, as only Fe^{2+} can be incorporated into the olivine structure. However, XRF analysis only measures total Fe. It is often assumed that most mantle primary magmas have $Fe^{2+}/\sum Fe$=0.9, based on natural compositions determined analytically by Rhodes and Vollinger (2005). However, evidence suggests that some OIBs might be more oxidised (Herzberg and Asimow, 2008). Larsen and Pedersen (2000) analysed glasses from the West Greenland picrites and found them to be more oxidised, and consequently suggested that a value of $Fe^{3+}/\sum Fe$=0.15 would be more appropriate. The 'target MgO' was therefore determined at $Fe^{3+}/\sum Fe$=0.1 and $Fe^{3+}/\sum Fe$=0.15 in all samples, to account for the possible range in mantle oxidation states. Varying the amount of oxidised iron between 10% and 15% generally resulted in a change of primary magma MgO of ∼1 wt%.

Pressure and K_D(Fe-Mg)$^{ol-liq}$

The value of K_D(Fe-Mg)$^{ol-liq}$ has an important influence in olivine-melt thermometry. While K_D(Fe-Mg)$^{ol-liq}$ is nearly constant across a wide range of temperatures, bulk compositions and fO_2, it is variable with pressure, as demonstrated in Figure 3.4. This variation can be expressed as:

$$K_D(Fe-Mg)^{ol-liq} = 0.29 + 0.002 \cdot \sqrt{P} + 0.04 \cdot tan^{-1}(P) - 0.0005 \cdot P \quad (3.5)$$

where P is the equilibrium pressure in GPa. As will be discussed in Section 3.2.3, the choice of K_D(Fe-Mg)$^{ol-liq}$ is a major source of uncertainty in olivine-melt thermometry techniques, and it is necessary to estimate the pressure of melting and olivine equilibrium for each sample suite. Melting in the BTIP is thought to have initiated at depths well in excess of 100 km (Scarrow and Cox, 1995; Kent and Fitton, 2000; Upton et al., 2002). Similarly, Herzberg and O'Hara (1998)

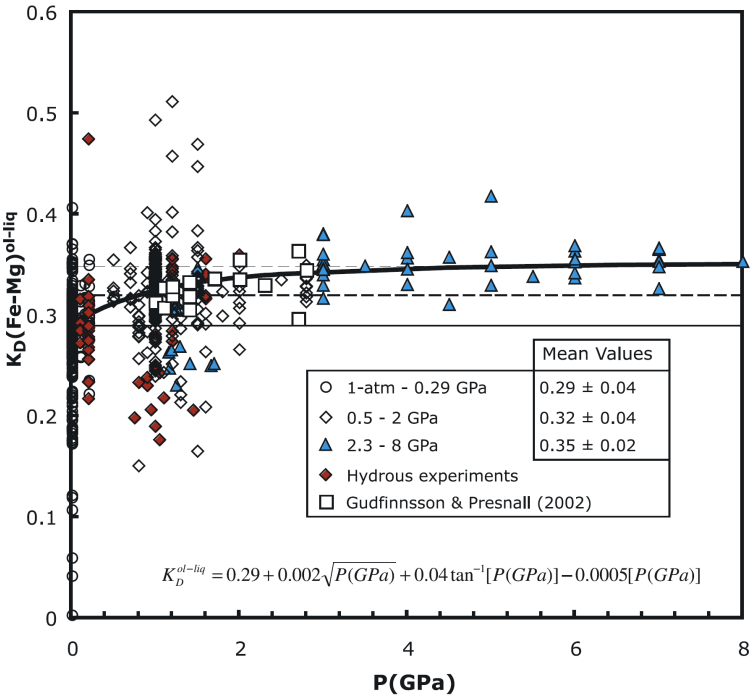

Figure 3.4: K_D(Fe-Mg)$^{ol-liq}$ plotted against pressure. At pressures up to 4 GPa, K_D(Fe-Mg)$^{ol-liq}$ increases significantly with P. From Putirka (2005).

estimated that the average segregation pressures for the West Greenland picrites was ∼38 kbar, with initial melting pressures of ∼45 kbar, and it is thought that the Baffin Island picrites experienced very similar melting conditions (Starkey, 2009). Putirka et al. (2007) assumed olivine equilibration at or near the base of the lithosphere at 3 GPa in Hawaii, and therefore a K_D(Fe-Mg)$^{ol-liq}$ of 0.34. Larsen and Pedersen (2000) argue that the West Greenland primary melts were in equilibrium with the most forsteritic olivines near the base of the lithosphere. If we also assume this occurred for the most primitive olivines in the Baffin Island and BTIP samples, then the same K_D(Fe-Mg)$^{ol-liq}$ as in Hawaii can be applied. A lithosphere of 100 km thickness is thought to have been present in West Greenland (Larsen and Pedersen, 2009), whilst the BTIP lithosphere is estimated to have been around 75 km thick at the onset of magmatism (Kerr, 1994; Kent and Fitton, 2000). Putirka et al. (2007) estimated K_D(Fe-Mg)$^{ol-liq}$=0.33 for Iceland picrites, representing equilibration of olivines at 2.3 GPa, and this value has been applied here.

The value of K_D(Fe-Mg)$^{ol-liq}$ is important in the determination of 'target MgO',

Table 3.1: Maximum forsterite content of olivine and 'target MgO' for each sample used in the olivine-melt thermometry calculation. a and b are 'target MgO' where $Fe^{3+}/\sum Fe$=0.1 and $Fe^{3+}/\sum Fe$=0.15, respectively.

Sample	**Fo$_{max}$**	**'Target MgO' a**	**'Target MgO' b**
S1	91.7	21.0	20.0
S2	92.1	22.2	21.2
S3	91.7	21.0	19.9
S5	92.0	21.8	20.9
S6	91.7	21.1	20.1
S7	91.2	20.1	19.1
S8	91.3	20.4	19.3
S9	92.0	21.8	20.9
S10	92.6	23.3	22.4
R10	89.5	18.9	17.9
M9	92.8	26.4	25.5
MU1.1	92.4	23.1	21.9
MU1.2	90.3	18.2	17.3
MU2.2	92.3	22.8	21.8
MU3.1	92.1	22.0	21.0
PAD4	92.6	21.9	22.0
PAD5	92.2	20.0	19.2
PAD6	92.3	20.4	19.5
DUR6	92.4	20.6	19.7
DUR8	91.1	19.8	18.8
APO4	90.2	15.7	14.9
APO7	92.9	24.5	23.3
138345	92.8	23.6	22.6
340740	92.4	23.0	21.8
354754	92.1	21.6	20.7
362077	92.3	22.3	21.2
400230	92.0	21.7	20.8
ED1	86.3	11.9	11.1
SDA1	85.8	12.9	11.9
VEY1	90.7	18.4	17.6
VP1	88.0	13.9	13.1
I2	90.0	17.8	17.0
I3	87.6	12.9	12.1
I5	89.2	17.4	16.6
I6	90.1	19.0	18.0
I9	90.1	16.8	15.9

and hence the final temperature calculation. Figure 3.3 demonstrates this effect. The two straight lines intersecting the olivine control lines represent olivine of constant composition Fo_{92}, however one has a $K_D(\text{Fe-Mg})^{ol-liq}$=0.31, the other, 0.34. The increase in $K_D(\text{Fe-Mg})^{ol-liq}$ results in a 2 wt% increase in 'target MgO' and will therefore have an important effect on the final temperature calculation. The most primitive olivine composition and 'target MgO' for each sample is presented in Table 3.1.

Once the 'target MgO' content has been determined, equilibrium olivine is added or subtracted incrementally (in steps of 0.1 wt%) to the bulk-rock composition until the 'target MgO' content is achieved. Since olivine is the only major phase

to have fractionated, this provides a means for estimating the content of the other major oxides in the primary melt. This calculated melt composition is taken as the parental melt since it is 'the most primitive magma that can be inferred from direct observation of a rock suite, and the observation that retains the earliest evidence of differentiation is the most magnesian olivine phenocryst composition' (Herzberg et al., 2007).

The average parental melt composition for each suite at the two oxidation states is presented in Tables 3.2 and 3.3. Full results are presented in Appendix G. Under the more oxidising conditions, the BTIP primary magmas range from 17.3-22.4 wt% MgO, except for M9, whose primary magma is estimated to have contained 25.5 wt% MgO. The MgO content of Baffin Island and West Greenland primary magmas is calculated to be 14.9-23.3 wt% MgO, with most samples ranging from 19 to 22 wt% MgO, in excellent agreement with previous estimates. The maximum MgO contents, however, are higher by 1-2 wt% than estimates by Kent (1995) for BTIP lavas, Yaxley et al. (2004) for Baffin Island lavas and Larsen and Pedersen (2000) for West Greenland lavas, as most of these estimates range up to a maximum of 21-22 wt% MgO. Additionally, the estimate for M9 from Rum is extraordinarily high and is unlikely to be correct, as a primary magma with 25 wt% MgO would result in the eruption of komatiitic lava, which is not seen anywhere in the BTIP. Possible explanations for the high primary magma MgO contents will be discussed in Section 3.2.3. For Iceland, the parental liquid MgO content ranges from 12.9-19.0 wt% (neovolcanic) and 11.9-18.4 wt% (Tertiary) in the less oxidised state and 12.1-18.0 wt% (neovolcanic) and 11.1-17.6 wt% (Tertiary) in the more oxidised state, in excellent agreement with the calculations carried out on Icelandic rocks by Putirka et al. (2007).

Table 3.2: Average parental melt composition calculated for each sample suite where $Fe^{3+}/\sum Fe$=0.1.

Suite	wt% olivine added	SiO_2	Al_2O_3	FeO_T	MgO	CaO	Na_2O	K_2O	TiO_2	MnO	Total
Skye	-17.5	45.5	11.3	11.3	21.4	8.8	0.8	0.1	0.6	0.2	100.0
Rum	-41.7	43.4	10.2	13.3	23.0	7.6	1.4	0.1	0.9	0.2	100.0
Mull	-16.9	45.2	11.3	11.1	21.5	8.9	1.0	0.1	0.6	0.2	100.0
Baffin Island	-0.4	46.8	11.0	10.2	20.4	9.4	1.2	0.0	0.8	0.2	100.0
West Greenland	0.7	45.3	10.1	10.9	22.4	8.8	1.2	0.1	0.9	0.2	100.0
Iceland Tertiary	-13.4	47.7	12.8	11.6	14.2	10.6	1.4	0.1	1.2	0.2	100.0
Iceland	-7.2	46.7	12.0	11.7	16.8	10.3	1.3	0.1	0.9	0.2	100.0

Table 3.3: Average parental melt composition calculated for each sample suite where $Fe^{3+}/\sum Fe$=0.15.

Suite	wt% olivine added	SiO_2	Al_2O_3	FeO_T	MgO	CaO	Na_2O	K_2O	TiO_2	MnO	Total
Skye	-20.7	45.7	11.7	11.2	20.4	9.1	0.8	0.1	0.6	0.2	100.0
Rum	-45.0	43.5	10.5	13.6	21.9	7.8	1.4	0.1	0.9	0.2	100.0
Mull	-25.6	45.5	11.7	11.0	20.5	9.3	1.1	0.1	0.6	0.2	100.0
Baffin Island	-3.1	47.1	11.4	10.1	19.6	9.6	1.2	0.0	0.8	0.2	100.0
West Greenland	0.7	45.3	10.1	10.9	22.4	10.0	8.8	1.2	0.1	0.9	100.0
Iceland Tertiary	-15.9	48.3	13.2	11.0	13.4	11.0	1.5	0.1	1.3	0.2	99.9
Iceland	-9.9	46.9	12.4	11.5	15.9	10.6	1.4	0.1	1.0	0.2	100.0

Temperature calculation

Once the parental melt compositions are known, it is possible to plot each sample on the olivine saturation surface. Putirka (2005) recalibrated the olivine saturation surface model to include a correction for compositional variations in the liquid of H_2O, Na_2O+K_2O and SiO_2. Putirka et al. (2007) further refined the thermometer by calibrating a pressure-sensitive model using experimental data. The model encompasses the pressure range 0-15.5 GPa and a temperature range of 965-2080℃, and is valid for water contents ranging from 0-18.6 wt% and is expressed as:

$$lnD_{Mg}^{ol/liq} = -2.158 + 55.09 \cdot \frac{P}{T} - 0.06213 \cdot \left[H_2O^{liq}\right] + \frac{4430}{T} + 0.05115 \cdot \left[Na_2O^{liq} + K_2O^{liq}\right] \tag{3.6}$$

$$lnD_{Fe}^{ol/liq} = -3.3 + 47.57 \cdot \frac{P}{T} - 0.05192 \cdot \left[H_2O^{liq}\right] + \frac{3344}{T} + 0.05595 \cdot \left[Na_2O^{liq} + K_2O^{liq}\right] + 0.01633 \cdot \left[SiO_2^{liq}\right] \tag{3.7}$$

where T is the temperature in ℃ and P is the pressure in GPa. The values for Na_2O^{liq}+K_2O^{liq} and $SiO_2{}^{liq}$ are taken from the calculated parental melt compo-

sitions (wt%). A water content of 0.375 wt% was chosen for Iceland, after Dixon et al. (2002) who characterised the volatile contents of mantle sampled by OIB and MORB. This is higher than the value of 0.05 wt% H_2O in MORB (Dixon et al., 2002), as OIB magmas are recognised to contain more water than MORB magmas. The water content of olivines from West Greenland indicate that the mantle source region had >300 ppm H_2O (Jamtveit et al., 2001), which is significantly higher than the estimated N-MORB mantle source value of 100-200 ppm (Michael, 1988; Bell and Rossman, 1992). Jamtveit et al. (2001) estimated that a mantle source with 400 ppm H_2O would produce melts with 0.2-0.4 wt% H_2O and that the most primitive olivines crystallizing near the base of the lithosphere are likely to have crystallized from melts with the lowest H_2O contents. A water content of 0.375 wt% has therefore been selected for the early NAIP samples, and this is likely to be a maximum estimate.

Each sample was plotted on an olivine saturation surface to determine the temperature of olivine-melt equilibration. These plots are shown in Figures 3.5, 3.6, and 3.7, with results from models run at $Fe^{3+}/\sum Fe$=0.1 and $Fe^{3+}/\sum Fe$=0.15 shown. Straight lines of constant olivine composition are shown on the saturation surface. The isotherms are generated using Equations 3.6 and 3.7. Each sample plots within ± $Fo_{0.5}$ of the maximum forsterite content used to calculate 'target MgO'. This error is well within the approximate model error of ±45°C calculated when the uncertainties from $D_{FMg}^{ol/liq}$ and $D_{Fe}^{ol/liq}$ are propagated through the saturation surface (Putirka, 2005).

A summary of the calculated olivine-melt equilibration temperature for each suite is shown in Table 3.4, and the temperature of each sample compared to MORB is plotted in Figure 3.8. Temperatures range up to 1625°C for the BTIP (excluding the value of 1715°C calculated from M9, which is unreasonably high), 1665°C at Baffin Island and 1635°C at West Greenland. The Putirka et al. (2007) olivine-melt thermometer accounts for differences in H_2O contents between MORB and OIB/LIP, and for variations in major element components (alkalis and SiO_2). Additionally, CO_2 contents as high as 30 wt% in the liquid do not affect $D_{Mg}^{ol/liq}$ or the temperature calculations. The large difference in olivine-melt equilibrium temperature must reflect actual temperature differences between the mantle source region of MORB and the NAIP, and it is not reasonable to argue that volatile content or variations in source composition have influenced the calculations. The

Iceland Tertiary samples record a maximum temperature of 1515℃, and the neovolcanic zone Iceland samples record a maximum of 1550℃, a thermal anomaly of 135 ± 45℃ and 170 ± 45℃, respectively. The results suggest a cooling of the North Atlantic mantle between ∼61 Ma and 13-14 Ma and a slight warming since the eruption of the Iceland Tertiary picrites (13-14 Ma). However these two Iceland temperatures are within the error of the thermometer, so it is not possible to draw this conclusion from the application of olivine-melt Fe-Mg thermometry alone.

The maximum temperature calculated for the neovolcanic zone Iceland samples is in excellent agreement with that of Putirka et al. (2007), who calculated a temperature of 1520℃ using a different suite of rocks. The temperatures calculated for the BTIP are much higher than in a recent study by Hole et al. (2015), which applied the Putirka et al. (2007) method to a suite of dykes from Islay, Jura and Gigha and calculated olivine-melt equilibration temperatures of up to 1400℃. However, the olivines in the present study are far more primitive than those from Islay, Jura and Gigha, which had a maximum Mg# of 89.9, and so it is unsurprising that higher temperatures are calculated here.

There is a large spread in the calculated temperatures within each suite. The Baffin Island and Iceland samples record the largest spread, with a range in temperature of 215℃ and 165℃ (for both the Tertiary and neovolcanic samples), respectively. However, the composition of the most Mg-rich olivine varies between samples, and so a spread in temperature is expected. For example, the most primitive olivine from the Baffin Island sample APO7 had an Mg# of 92.9, whereas the most primitive olivine from APO4 was 90.2. As was discussed in Section 2.6.6 and 3.2.2, it is thought that many primitive volcanic rocks contain a mix of crystals that formed from different melts at different depths and times in the magmatic system. It is likely that the spread in olivine composition both within a sample and between samples from the same suite is a reflection of this. This is in turn reflected in the range in maximum temperatures calculated within a single sample suite.

Table 3.4: Maximum and average temperatures of olivine-melt equilibria for each sample suite using olivine-melt thermometry. ΔT is T_{max} - T_{MORB}, where T_{MORB} = 1380℃ (Putirka et al., 2007). Temperatures are in ℃, and results run at two different oxidation conditions are shown: a, $Fe^{3+}/\sum Fe$=0.1 and b, $Fe^{3+}/\sum Fe$=0.15. The model error is estimated to be ± 45℃.

	a			**b**		
Suite	T_{max}	$T_{average}$	ΔT	T_{max}	$T_{average}$	ΔT
Skye	1625	1591	245	1610	1574	230
Rum	1715	1630	335	1700	1613	320
Mull	1620	1545	240	1605	1574	225
Baffin Island	1665	1569	285	1625	1541	245
West Greenland	1635	1612	255	1610	1595	230
Iceland Tertiary	1515	1414	135	1495	1395	115
Iceland	1550	1471	170	1525	1450	145

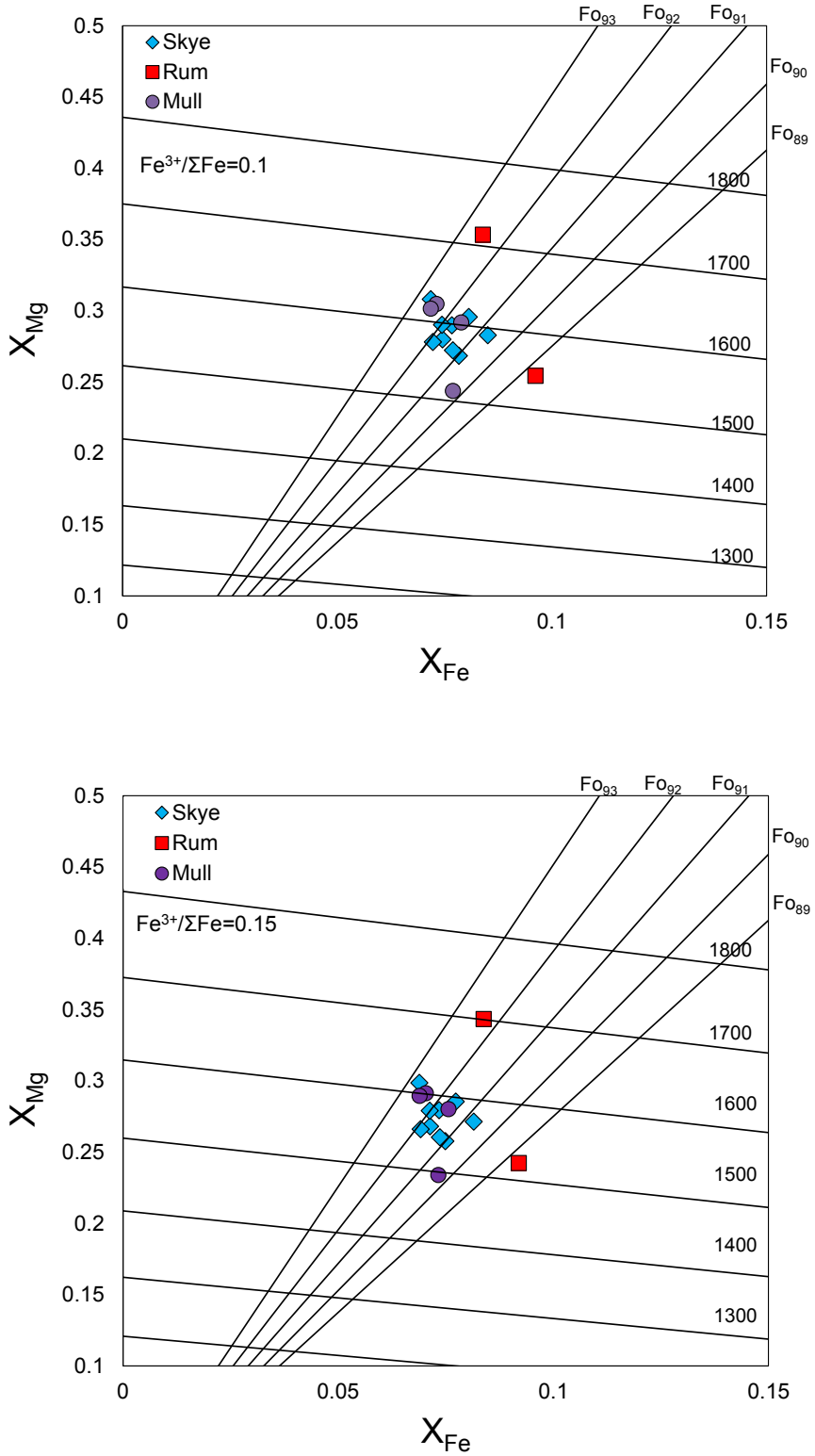

Figure 3.5: Olivine saturation model used to calculate temperatures from the British Tertiary Igneous Province picrites. Results run at two different oxidation conditions are shown. The data are generated from the most primitive olivine present in each sample as in Table 3.1. Isotherms are in ℃.

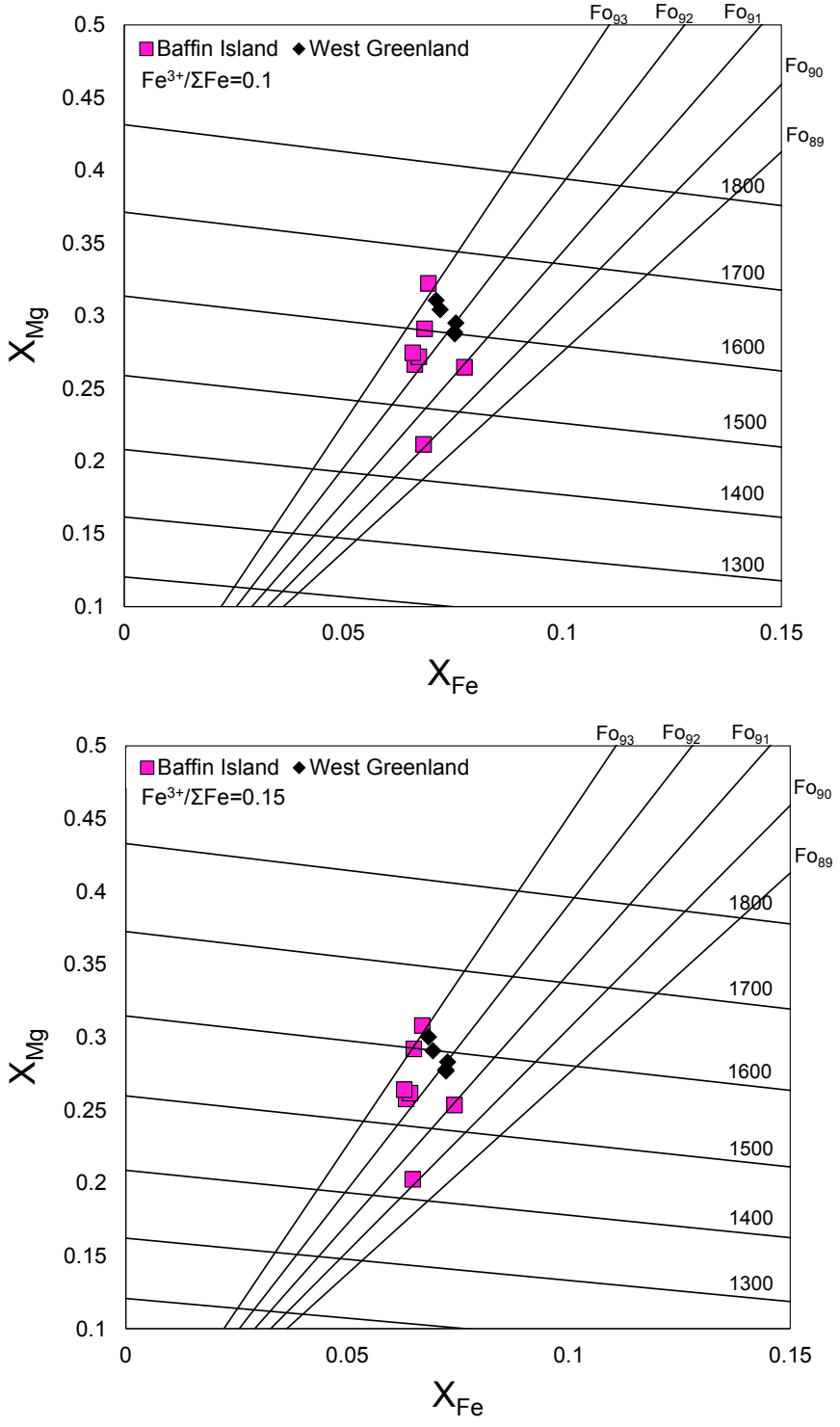

Figure 3.6: Olivine saturation model used to calculate temperatures from Baffin Island and West Greenland picrites. Results run at two different oxidation conditions are shown. The data are generated from the most primitive olivine present in each sample as in Table 3.1. Isotherms are in °C.

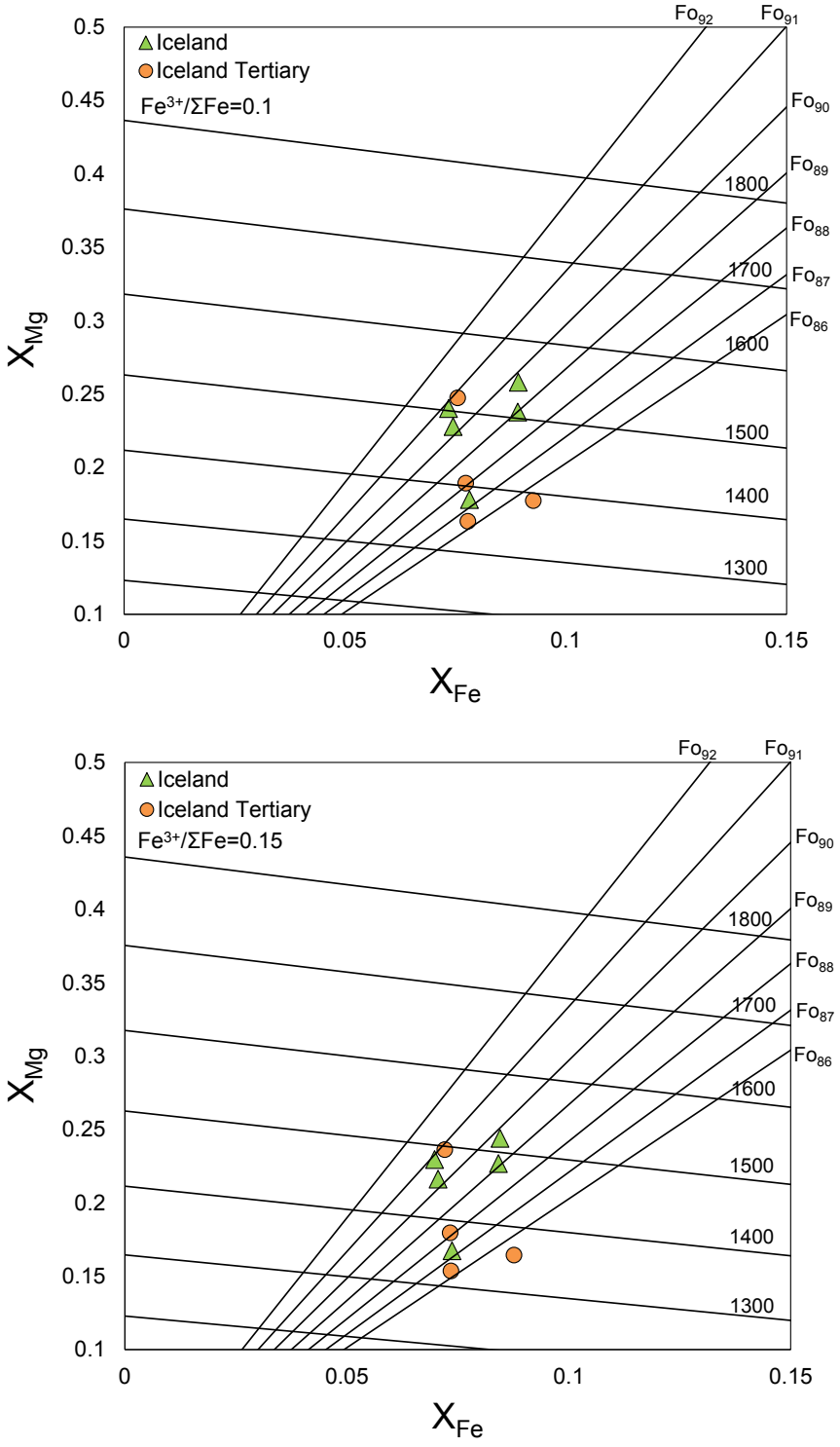

Figure 3.7: Olivine saturation model used to calculate temperatures from the Tertiary and neovolcanic Iceland picrites. Results run at two different oxidation conditions are shown. The data are generated from the most primitive olivine present in each sample as in Table 3.1. Isotherms are in ℃.

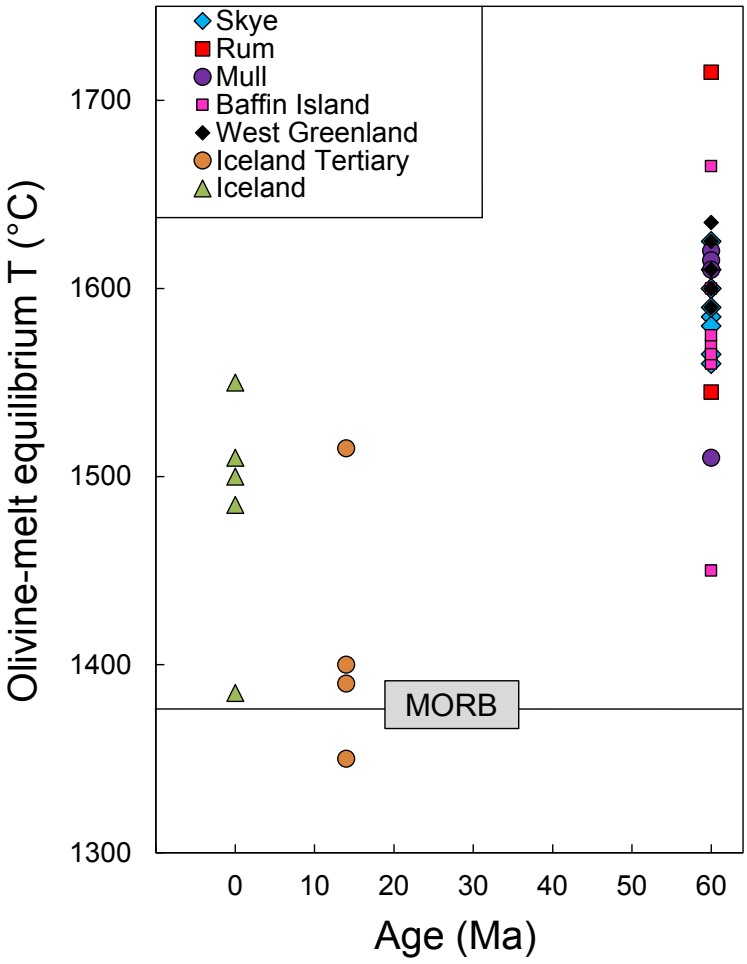

Figure 3.8: Olivine-melt equilibrium temperature in ℃ calculated for the NAIP samples. The results are for calculations carried out where $Fe^{3+}/\sum Fe$=0.1. The olivine-melt equilibrium temperature estimated for MORB by Putirka et al. (2007) is 1380℃.

Crystallization temperatures and comparison to MORB

The temperatures presented here represent the temperature at which olivine equilibrated with its primary melt (T_{OL}). T_{OL} is neither the actual temperature that the mantle began to melt at, nor the mantle potential temperature (mantle Tp), the temperature that the adiabatically convecting asthenosphere would have if it were able to reach the Earth's surface without melting (McKenzie and Bickle, 1988). It has been noted that both T_{OL} and Tp can be used as thermometers of the mantle, and that they are positively correlated (Herzberg, 2011). Olivine forms very early in the crystallization sequence of primitive basalt and it is likely that it appears within a few tens of degrees of the liquidus (Coogan et al., 2014). The most primitive olivine phenocrysts are therefore likely to record a temperature close to that actually experienced in the mantle at the point of melt segregation and may be used as a proxy for mantle temperature.

When comparing temperatures between MOR and LIP/OIB settings, it is most common to use Tp. There are several different ways of calculating Tp (Putirka, 2005; Herzberg et al., 2007; Putirka et al., 2007; Herzberg and Gazel, 2009; Herzberg and Asimow, 2015), and some require assumptions of variables that are hard to constrain, such as the degree of partial melting, the pressure of melt formation and the latent heat of fusion. Unfortunately, using different methods and/or assumptions, it is possible to reach different conclusions about the mantle Tp using similar T_{OL}. At Hawaii for example, Herzberg and O'Hara (2002) calculate a T_{OL} of 1651℃ at 4 GPa and a Tp of 1560℃. On the other hand, Putirka et al. (2007) use the same T_{OL} to calculate a mantle Tp of 1700℃. The discrepancy seems to arise from the pressure at which the degree of melting is applied. Both assumed a partial melt fraction of 14%, however Putirka et al. (2007) applied this at elevated pressure, while Herzberg and O'Hara (2002) applied it at 1 atm, where T_{OL} is estimated to be 1467℃. On this basis, it appears that estimates of mantle Tp can be unreliable, and since there is no robust way of accurately constraining the degree and depth of partial melting, it will not be considered further here.

To calculate the T_{OL} of MORB, data from the Siqueiros Transform fault along the East Pacific Rise is used because it is the only known MOR location where

whole-rock data can be traced to an olivine control line, allowing estimation of mantle temperatures using the olivine-melt technique. The Siqueiros suite yields picrites with up to 21 wt% MgO and a maximum olivine composition of $Fo_{91.5}$. Using these data, a primary melt with 14 wt% MgO is calculated to have equilibrated with $Fo_{91.5}$ at 1380℃ and 0.8 GPa (Putirka et al., 2007). To check that the data presented here are reliable, T_{OL} was calculated for Siqueiros MORB using the same parameters. T_{OL} was calculated to be 1385℃, in excellent agreement with Putirka et al. (2007). With a T_{OL} of 1380℃, Putirka et al. (2007) calculated a mantle Tp of 1441 ± 63℃. However, compared to other studies this value is very high, with other Tp estimates ranging from 1280℃ (McKenzie and Bickle, 1988) to 1350℃ (Herzberg et al., 2007; Herzberg and Gazel, 2009; Herzberg and Asimow, 2015). The T_{OL} temperatures reported here for the NAIP are also substantially higher than previous estimates. Kent and Fitton (2000) and Larsen and Pedersen (2000) both estimate liquidus temperatures of around 1550℃ for the BTIP and West Greenland respectively, while mantle Tp at Iceland is estimated to be in the range of 1400-1450℃ (Herzberg and Gazel, 2009; Herzberg and Asimow, 2015). Possible reasons for this discrepancy will be discussed at length in Section 3.2.3 after the uncertainties and limitations of the olivine-melt thermometry technique have been laid out in detail.

For now, only the difference in T_{OL} between the NAIP samples and MORB is important and the absolute temperature values will be discussed later. From the data presented here, it is clear that there was a widespread thermal anomaly across the NAIP during Phase 1 volcanism. T_{OL} is calculated to be higher than ambient mantle by 245℃ at the BTIP (excluding the temperature calculated from M9), 285℃ at Baffin Island and 255℃ at West Greenland (Table 3.4), indicating that the temperature distribution across the whole NAIP during Phase 1 was uniform, within the error of the thermometer (45℃). The temperature anomaly from West Greenland is in good agreement with that from Herzberg and Gazel (2009), who calculated a thermal anomaly 290℃ above that of ambient mantle using forward models of mantle melting. Herzberg and Gazel (2009) calculated a thermal anomaly of 110℃ at Iceland, which is lower than the value of 170℃ calculated in the present study.

3.2.3 Discussion

Olivine-melt thermometry has a variety of uncertainties associated with assumptions made in the calculations, leading to much debate in the literature about whether olivine-melt thermometry can be used to reliably identify mantle thermal anomalies (e.g. Putirka, 2005; Putirka et al., 2007; Falloon et al., 2007a,b). The main sources of uncertainty and their impact on the conclusions that can be drawn about mantle temperature at OIB/LIP vs MORB source regions are discussed in detail below.

Choice of K_D(Fe-Mg)$^{ol-liq}$

Olivine-melt equilibrium pressure, and hence choice of K_D(Fe-Mg)$^{ol-liq}$, is noted by Falloon et al. (2007a) as being the main cause of disagreements over T_{OL}. To investigate this, T_{OL} was calculated for sample S1 assuming an olivine-melt equilibrium pressure of 1 atmosphere to compare the result to the 3 GPa calculation. A pressure of 1 atmosphere corresponds to a K_D(Fe-Mg)$^{ol-liq}$ of 0.29, and a T_{OL} of 1460℃ is calculated. This is 125℃ lower than T_{OL} at 3 GPa. This result highlights how incorrect assumptions about the pressure of olivine-melt equilibrium can have a dramatic impact on the value of T_{OL}. Although an attempt was made to choose appropriate values for K_D(Fe-Mg)$^{ol-liq}$ in the NAIP T_{OL} calculations, the pressure at which the olivines will have crystallized is poorly constrained, and is therefore a major source of uncertainty in the presented T_{OL} results. However, it is worth noting that when the calculations are carried out using the same K_D(Fe-Mg)$^{ol-liq}$ as at MORB (0.31), a maximum temperature difference of 170℃ is calculated at the BTIP and West Greenland, 190℃ at Baffin Island and 95℃ at Iceland. A large thermal anomaly is therefore still required and differences in temperature are significant such that almost any value of K_D(Fe-Mg)$^{ol-liq}$ can still be used to demonstrate a thermal anomaly in the NAIP.

Oxygen fugacity

Oxygen fugacity is found to have only a minor effect on the calculated temperatures. An increase in $Fe^{3+}/\sum Fe$ from 0.1 to 0.15 resulted in a temperature decrease of around 20-25℃ (maximum 40℃) in each sample. A change in oxygen fugacity of four orders of magnitude from QIF (quartz-iron-fayalite) to Ni-NiO, corresponds to a T_{OL} change of only ∼40℃ (Falloon et al., 2007a). Since most of the upper mantle is thought to fall within ±2 log units of the fayalite-magnetite-quartz (FMQ) buffer, oxygen fugacity is not considered to be a large source of uncertainty here.

Sample choice

The choice of sample selected for study will have an extremely important influence on the conclusions drawn about differences in T_{OL} between MORB and LIP/OIB localities. For example, Green et al. (2001) claim that the mantle temperature beneath Hawaii and MORs is identical, however they include samples from Baffin Island in their MORB data set, making the comparison invalid. Putirka et al. (2007) argue that a temperature anomaly of 268℃ is required at Hawaii, however, Falloon et al. (2007b) advocate that the mantle temperatures beneath Hawaii and MORs are virtually identical at ∼1430℃, using a similar technique to Putirka et al. (2007), but instead applying the Ford et al. (1983) thermometer to the primary melt compositions. Again, the choice of data played an important role in the different conclusions drawn. In a letter to the authors published in the discussion section of Falloon et al. (2007b), Keith D. Putirka and J. Michael Rhodes pointed out that Falloon et al. (2007b) used samples from MORB with the highest FeO contents (and will therefore record the highest T_{OL} for an olivine of a specific composition), but did not use samples with the highest FeO contents from Hawaii. They also noted that Falloon et al. (2007b) overestimated the FeO content of MORB, which would lead to an overestimation in MORB temperature. Both of these inconsistencies may account for the identical T_{OL} calculated for MORB and Hawaiian basalts by Falloon et al. (2007b), and in the light of the many other studies that suggest large differences in mantle temperature between MORB and Hawaii (e.g. Putirka et al., 2007; Herzberg and

Asimow, 2008; Herzberg and Gazel, 2009), it seems unlikely that the conclusions of Falloon et al. (2007b) are correct.

Most primitive olivine composition

The measurement of the olivine crystal with the highest forsterite content is another major source of uncertainty (Herzberg et al., 2007). It is possible that the most forsteritic olivine was not sampled, because it was either left behind at depth, was not present in the thin section used for analysis or was not chosen for analysis. Additionally, Mg and Fe^{2+} diffuse extremely quickly through the olivine lattice (Dohmen and Chakraborty, 2007) and it is possible to rapidly reset the composition of olivine due to evolving melt compositions or mixing with a melt of a different composition. These processes may result in the lowering or raising of apparent olivine-melt equilibrium temperatures if the original olivine composition is completely re-equilibrated.

A very serious problem with olivine-melt thermometry is that highly forsteritic olivines can be crystallized from advanced fractional melt batches and there is no model that takes account of this. For example, ultra-magnesian olivines up to $Fo_{93.3}$ are found in olivine-rich dolerites in the southern Etendeka Province of Namibia (Thompson and Gibson, 2000). Applying olivine-melt thermometry, a primary magma composition of 24 wt% MgO is calculated, implying an extraordinarily high mantle *Tp* of 1680°C (Thompson and Gibson, 2000). However, a more recent study on the melt inclusions in these olivines by Keiding et al. (2011) provides an alternative explanation for their origin. The melt inclusions trapped in the ultra-magnesian olivines were found to contain up to 17.5 wt% MgO at low FeO contents (∼7 wt%), as opposed to the 11 wt% FeO calculated by Thompson and Gibson (2000) for the 24 wt% MgO melts. The crucial point is that both of these melts can crystallize a Fo_{93} olivine because they have the same Mg#. Mantle melts can achieve a high Mg# through advanced fractional melting lowering the FeO content of the melt (Herzberg and O'Hara, 2002; Herzberg et al., 2007; Herzberg, 2011). Small melt droplets formed from partial melting can be efficiently removed by buoyancy-driven draining (Ahern and Turcotte, 1979; McKenzie, 1984). As decompression continues, the residue is continuously melted, and the melt increments can have very low FeO contents with an MgO

that remains unchanged (Herzberg, 2011). Usually it is assumed that these melt droplets will mix to form a primary magma that is the average composition of all the melt increments (Herzberg and Asimow, 2008), a process known as accumulated fractional melting. However, if an advanced fractional melt can remain isolated from the system, it will crystallize olivines with $\sim Fo_{93}$, implying a mantle Tp of 1520℃ when the melt MgO content is 17.5 wt% (Keiding et al., 2011). In this scenario, the Namibia picrites still require a thermal anomaly, but it is much reduced compared to the original estimate of 1680℃ (Thompson and Gibson, 2000).

Olivines with $\geq Fo_{93}$ are also found in the Baffin Island and West Greenland picrites (e.g. Francis, 1985; Larsen and Pedersen, 2000). Herzberg and O'Hara (2002) showed that $>Fo_{93.0}$ olivines would have crystallized from a primary magma with 24-25 wt% MgO, however this composition cannot be produced by equilibrium or fractional partial melting of any peridotite composition. It is therefore highly likely that such olivines from Baffin Island and West Greenland were crystallized from advanced fractional melts that had exited the melting regime, however without direct samples of these fractional melts, the MgO content cannot be constrained. While no olivine of $\geq Fo_{93.0}$ was used in the NAIP olivine-melt thermometry calculations presented here, many had compositions ranging from $Fo_{92.0}$ to $Fo_{92.9}$, and it is very possible that these olivines did not crystallize from true primary magmas. Unfortunately, it is hard to tell where to draw the distinction between a true primary melt and an advanced fractional melt, so if a conclusion is drawn about the mantle temperature of a rock based only on olivine-melt thermometry, the choice of the most forsteritic olivine should be considered a major source of uncertainty in the temperature calculation, and results from samples containing highly forsteritic olivines should be treated with caution.

Clinopyroxene fractionation

Clinopyroxene does not usually begin to fractionate at low pressure until the MgO content of a magma has evolved to 7-10 wt% (Herzberg et al., 2007). However, clinopyroxene can also fractionate in high-MgO liquids in the mantle. It is most likely to occur in the lithosphere during melt transit rather than in the mantle source region (Albarède et al., 1997) and the clinopyroxene will have high CaO

contents (Herzberg and Asimow, 2008). Olivine-melt thermometry requires that a lava sample has only fractionated olivine since melting, and so if clinopyroxene fractionation has played a role, the composition of the primary magma (and hence the final temperature calculation) will be affected. Clinopyroxene fractionation yields magmas that are deficient in CaO but have increased FeO. Modelling by Herzberg et al. (2007) showed that any method that reconstructs primary magma composition by addition/subtraction of olivine to lavas produces primary melts with MgO contents that are too high if the lava has lost clinopyroxene. Herzberg and Asimow (2008) found that clinopyroxene loss can result in the overestimation of the MgO content of the primary magma by up to 4 wt%, which results in temperatures that are up to 100℃ above their actual values. Many Hawaiian primary magmas appear to have been affected by clinopyroxene fractionation (Herzberg and Asimow, 2008), and this could explain why the mantle Tp of 1720℃ calculated by Putirka et al. (2007) is much higher than other estimates: for example, Herzberg and Gazel (2009) calculate Tp at Hawaii to be around 1600℃.

PRIMELT3

It was highlighted in Section 3.2.2 that the absolute T_{OL} values calculated for the NAIP samples in the present study using the Putirka et al. (2007) olivine-melt thermometer are substantially higher than previous estimates. Excluding M9, the maximum T_{OL} calculated here for Phase 1 picrites range from 1620 to 1665℃, around 100℃ higher than previous estimates of 1550℃ (Kent and Fitton, 2000; Larsen and Pedersen, 2000). T_{OL} in present-day Iceland is calculated here to be 1550℃, however other studies calculate the mantle Tp to be 100-150℃ lower than this (Herzberg and Gazel, 2009; Herzberg and Asimow, 2015). To investigate the cause of this discrepancy, the software model PRIMELT3 devised by Herzberg and Asimow (2015) was applied to the NAIP samples. PRIMELT3 is a model used to calculate the primary magma composition, T_{OL} and Tp of primitive basalt. Unlike olivine-melt thermometry, only the bulk-rock composition of the lava must be known, and it does not require knowledge of olivine phenocryst compositions. Instead, it compares modelled primary melt compositions formed by partial melting of fertile mantle peridotite to a suite of primary melt compo-

sitions calculated by incrementally adding or subtracting equilibrium olivine to the sample lava composition and calculates the olivine composition that would have been in equilibrium with the primary melt.

PRIMELT3 also provides several filters for complexities that can lead to overestimations in mantle temperature. These are: (i) a pyroxenite source. Partial melting of a pyroxenite source will generate primary magmas that have low CaO, resulting in calculated primary magmas with MgO contents that are too high by 2-3%; (ii) source volatile content. Melting in the presence of CO_2 can generate low-temperature carbonate-rich melts with very high MgO and FeO contents; (iii) clinopyroxene fractionation. As discussed previously, high pressure clinopyroxene fractionation can result in low CaO, high MgO, FeO primary melts if the clinopyroxene is lost. (iv) advanced fractional melting. Advanced fractional melts that have remained isolated can have high MgO and unusually low FeO contents.

Of the 36 samples used in the olivine-melt thermometry calculations, only 6 were free of all of the complexities that are filtered for in PRIMELT3. These were S1, S3 and S10 from Skye, MU1.1 from Mull and 138345 and 362077 from West Greenland. Most samples were filtered for clinopyroxene fractionation or advanced fractional melting. One sample (R10) was filtered due to a volatile source. All of these processes can result in elevated MgO/FeO, which will result in the crystallization of high Mg# olivines, making the primary magma appear more primitive, and hence have a higher T_{OL} than in reality. Since M9 failed to pass the filters, the extraordinarily high MgO content and calculated T_{OL} of $\sim$26 wt% and 1715°C from the olivine-melt thermometry calculation are highly unlikely to be correct. The number of samples that failed to pass the filters demonstrates the limitations of the olivine-melt thermometry technique and suggests that such processes that modify the MgO and FeO content of primary melts are widespread and commonplace during mantle melting.

The MgO content of the calculated primary magma, T_{OL} and equilibrium olivine for each sample that passed the filters is presented in Table 3.5 below. For comparison, the composition of the most primitive olivine in the sample and the resultant 'target MgO' of the primary magma calculated using olivine-melt thermometry is also provided. PRIMELT3 calculates T_{OL} at 1 atm, however this can be calculated at pressure using the following expression (Herzberg and

Asimow, 2015):

$$T = T_{1atm} + 54P - 2P^2 \tag{3.8}$$

where P is the pressure in GPa. To be consistent, the same pressures from the olivine-melt thermometry calculation were used in the PRIMELT3 calculation and $Fe^{3+}/\sum Fe$ was fixed at 0.1. The presented primary magma compositions were modelled by accumulated fractional melting. The Skye, Mull, and West Greenland primary magma contents were all calculated to have much lower MgO contents than those from olivine-melt thermometry. The maximum MgO content calculated using PRIMELT3 from these samples is 18.9 wt%, compared to 23.8 wt% from olivine-melt thermometry. Subsequently, the composition of olivine calculated to be in equilibrium with the primary melts are also much lower. This indicates that all of these samples contained olivines that were crystallized by advanced fractional melts with lowered FeO, resulting in high Mg#. This scenario is demonstrated in Figure 3.9 for sample S10 from Skye. However, the samples were not filtered out by PRIMELT3, so it is possible that they were better mixed with the accumulated fractional melt than the samples that were filtered. Alternatively, the samples could have experienced augite fractionation to a small enough degree that they were not filtered.

Table 3.5: Comparison of the PRIMELT3 and olivine-melt thermometry results. Olivine Mg# (Fo) in the PRIMELT3 calculation is the olivine composition calculated to be in equilibrium with the primary melt computed by the model. Fo in olivine-melt thermometry is the most primitive olivine composition present in the sample, and was used to calculate the primary magma composition. ΔT = T_{OL} calculated from olivine-melt thermometry - T_{OL} calculated from PRIMELT3. The error in T_{OL} in PRIMELT3 is estimated to be ±46℃ (Herzberg and Asimow, 2015).

	PRIMELT3			**Olivine-melt thermometry**			
	MgO (wt%)	**Fo**	**T(℃)**	**MgO (wt%)**	**Fo**	**T(℃)**	**Δ T(℃)**
S1	18.7	91.7	1563	20.9	91.7	1585	22
S3	17.2	91.2	1540	20.9	91.7	1580	40
S10	18.5	91.8	1554	23.2	92.6	1625	71
MU1.1	18.9	91.8	1566	23.0	92.4	1620	54
138345	18.4	91.7	1557	23.8	92.8	1635	78
362077	18.4	91.3	1560	22.8	92.3	1610	50

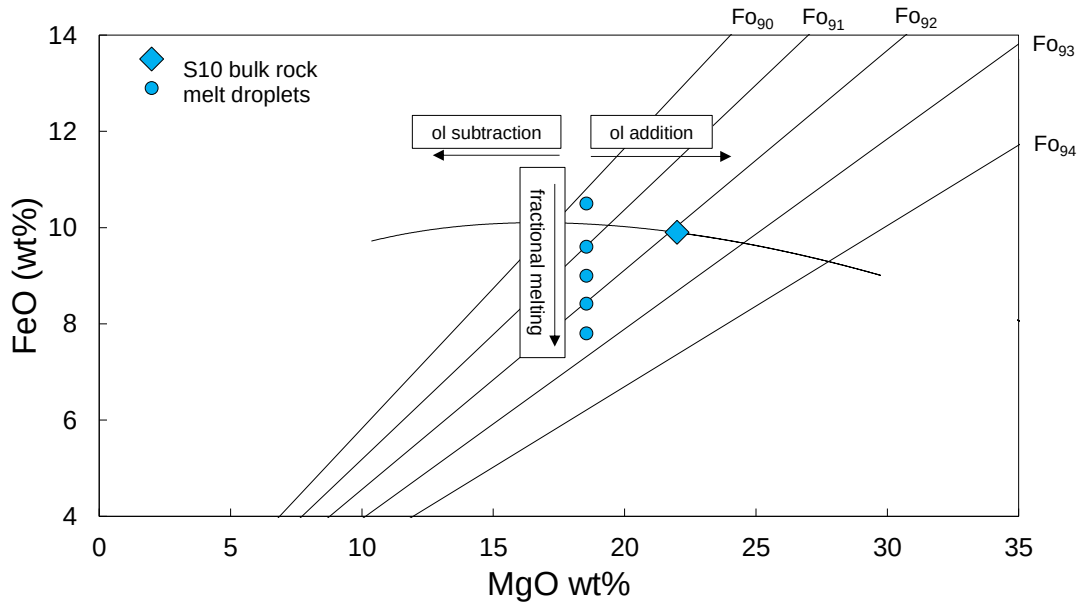

Figure 3.9: Melting model of S10 from Skye showing the effects of fractional melting. The diamond represents the bulk-rock composition of S10, which was used to generate an olivine control line. The small circles represent melt droplets formed during fractional melting. As melting continues, the FeO of the residue decreases at constant MgO. This results in the crystallization of higher Mg# olivine as the process goes on. The range of the melt droplet FeO contents that would be in equilibrium with the range of olivine compositions measured in S10 by EPMA are shown ($Fo_{90.2}$-$Fo_{92.6}$). The most Mg# olivine was likely the last to crystallize from the most Fe-depleted melt droplet. The bulk-rock composition of S10 plots to the right of the mixed primary magma, indicating that it has been affected by addition (accumulation) of olivine.

In all of the Phase 1 samples, T_{OL} calculated by PRIMELT3 is lower than that calculated from olivine-melt thermometry. The maximum decrease is 71℃, 54℃ and 78℃ at Skye, Mull and West Greenland, respectively. The maximum T_{OL} at each location calculated by PRIMELT3 is ∼1560℃, more in line with previous estimates of around 1550℃ (Kent and Fitton, 2000; Larsen and Pedersen, 2000). Using the newly calculated olivine compositions from PRIMELT3, T_{OL} was re-calculated using olivine melt thermometry. The new olivine-melt thermometry T_{OL} is compared to the previous T_{OL} in Table 3.6. Running the calculations with the new olivine compositions resulted in a decrease in T_{OL} of 30-65℃ (except in S1, which remained unchanged as the PRIMELT3 calculated olivine composition was the same as the most primitive olivine measured in the sample). The new maximum T_{OL} in the early NAIP samples from olivine-melt thermometry ranges from 1545 to 1585℃ and, within the error of the thermometer (±45℃), is now comparable with previous estimates and the temperatures calculated from

PRIMELT3.

Table 3.6: T_{OL} calculated using olivine melt thermometry using the most forsteritic olivine present in each sample (Old T_{OL}) compared to T_{OL} calculated using the equilibrium olivine composition calculated by PRIMELT3 (New T_{OL}). All temperatures are in ℃.

Sample	**Old T_{OL}**	**New T_{OL}**	**ΔT**
S1	1585	1585	0
S3	1580	1550	30
S10	1625	1585	40
MU1.1	1620	1585	35
138345	1635	1575	60
362077	1610	1545	65

Perhaps the most useful estimation of the magnitude of the thermal anomaly is to compare T_{OL} calculated by PRIMELT3 for the NAIP samples and Siqueiros MORB at 1 atm, as it allows comparison without the added complication of different crystallization depths. This yields temperature anomalies up to 148℃, 151℃ and 151℃ at Skye, Mull and West Greenland, respectively (with an error of ±46℃). The maximum temperature and magnitude of the thermal anomaly is remarkably uniform across the spatial extent of Phase 1 NAIP volcanism.

As was previously noted, the value of T_{OL} calculated using olivine-melt thermometry for Siqueiros MORB is 1380℃. This is much higher than many estimates of mantle potential temperature, which range from 1280-1350℃ (McKenzie and Bickle, 1988; Herzberg and Gazel, 2009). T_{OL} and Tp calculated by Putirka et al. (2007) for Hawaiian basalts are also extraordinarily high (1620℃ and 1722℃, respectively). Using PRIMELT3, Herzberg and Asimow (2015) calculated a primary melt MgO content of 11.6 wt% and an equilibrium olivine composition of $Fo_{90.4}$ for Siqueiros MORB. As with the NAIP samples, this olivine composition is less Mg-rich than the most primitive olivine present in the sample, which has an Mg# of 91.5. It is likely that the Siqueiros MORB olivines have also been affected by advanced fractional melting, raising the Mg# of the crystallizing olivines. Using the PRIMELT3 olivine composition of $Fo_{90.4}$, T_{OL} calculated using olivine-melt thermometry is 1340℃. This is lower than the previous estimate of 1380℃ by Putirka et al. (2007), and much closer to the PRIMELT3 estimate of T_{OL} at 0.8 GPa of 1313℃. Using data from Putirka et al. (2007), the

samples from Hawaii of Norman and Garcia (1999) were applied to PRIMELT3. Every one of the Hawaii samples were filtered for augite fractionation and this is reflected in the very low CaO contents of the bulk rocks, a characteristic that was also noted by Herzberg and Asimow (2008). It seems clear that for the Hawaii basalts, olivine-melt thermometry is not an appropriate technique to use to measure either T_{OL} or Tp, as high pressure augite fractionation will result in elevated melt MgO/FeO. It is likely that the estimates of temperature at Hawaii by Putirka et al. (2007) are far too high, and it is clear that neither olivine-melt thermometry nor PRIMELT3 are an appropriate technique for measuring temperature here.

3.3 Al-in-olivine thermometry

3.3.1 Introduction

The previous section discussed at length the problems associated with traditional olivine-melt Fe-Mg thermometry such as $K_D(\text{Fe-Mg})^{ol-liq}$ and the choice of the most primitive olivine. In addition, processes that modify the MgO/FeO content of a primary magma seem to be commonplace during mantle melting, and so the PRIMELT3 software developed by Herzberg and Asimow (2015) cannot be applied universally to primitive volcanic rocks, although it does seem to produce more reliable temperature and primary magma compositions than with olivine-melt thermometry. In light of these issues, the purpose of this section is to take a different approach to determining magmatic temperatures using the newly developed Al-in-olivine thermometer. The premise of the technique is described in detail below, and is then applied to the NAIP picrites.

The Al-in-olivine thermometer was first calibrated by Wan et al. (2008) who carried out a series of melting experiments at atmospheric pressure to calibrate the temperature dependence of aluminium partitioning between olivine and spinel between 1250 and 1450°C, under reducing conditions (~1.5 log units below the quartz-magnetite-fayalite redox buffer). The partition coefficient for Al_2O_3 between olivine and spinel is a strong function of both temperature and Cr-content

of the spinel (Wan et al., 2008) and a strong positive correlation between Al_2O_3 content in olivine and temperature is observed. The Al-in-olivine thermometer calculates the temperature of co-saturation of olivine and spinel (T_{Al}), and requires only knowledge of the olivine Al_2O_3 content, and the composition of co-existing Cr-spinel. As in olivine-melt thermometry, this is neither the temperature at which the mantle melted nor Tp, however both phases crystallize early in primitive basalts, likely within a few tens of degrees of the liquidus temperature (Coogan et al., 2014), and so the maximum calculated T_{Al} may be used as a proxy for mantle temperature at the point of melt segregation. The geothermometer calculated by Wan et al. (2008) is expressed as:

$$T_{Al}(℃) = \frac{10000}{0.512 + 0.873 \cdot Cr\# - 0.91 \cdot ln(K_D(Al)^{ol-sp})} - 273 \qquad (3.9)$$

where Cr# = Cr/(Cr + Al) of spinel in atomic proportions and $K_D(\mathrm{Al})^{ol-sp} = {Al_2O_3}^{ol}/{Al_2O_3}^{sp}$. The thermometer is estimated to have an uncertainty of ±22℃ (Wan et al., 2008). The olivines crystallized by Wan et al. (2008) in the melting experiments ranged in composition from Fo_{87} to Fo_{93}, with Al_2O_3 contents varying from 0.045 to 0.15 wt%, very similar to the olivines found in the rocks in the present study, and so the Al-in-olivine thermometer is directly applicable to the NAIP rocks. The Al-in-olivine thermometer has also been applied to peridotites by De Hoog et al. (2010), to calculate the equilibrium temperature of mantle rocks.

The mechanism by which Al substitutes into the olivine lattice was unclear from the Wan et al. (2008) study, and so a set of experiments was devised by Coogan et al. (2014) to investigate the role of SiO_2 activity (αSiO_2) in the incorporation of Al into olivine. The variation in calculated temperature with αSiO_2 was found to be less than ±20℃, similar to the uncertainty in the thermometer, and suggests that αSiO_2 is not important in Al substitution into olivine. On this basis, Coogan et al. (2014) suggested that most Al is incorporated into the olivine structure via the reaction:

$$MgAl_2O_4^{spinel} = (MgAl)AlO_4^{olivine} \qquad (3.10)$$

where Al in olivine is equally split between the M and tetrahedral sites, as this is not dependent on αSiO_2. This finding is consistent with the interpretation of

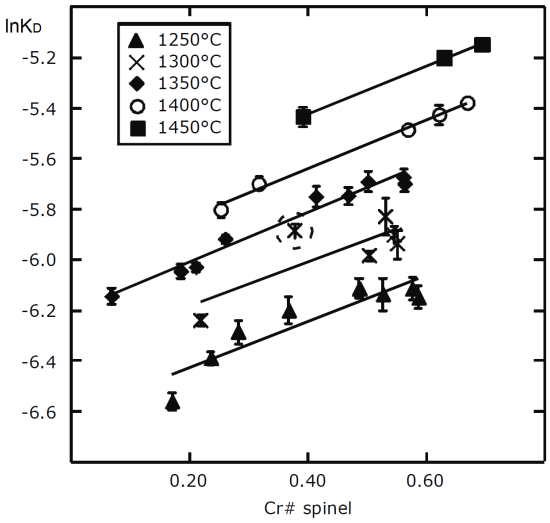

Figure 3.10: The partition coefficient for Al_2O_3 between olivine and Cr-spinel plotted as a function of spinel Cr# for experiments run at 1250 to 1450°C. The partition coefficient increases with increasing temperature at constant spinel Cr#, and with increasing spinel Cr# at fixed temperature. From Wan et al. (2008).

De Hoog et al. (2010), based on mantle olivine compositions.

Coogan et al. (2014) carried out experiments to extend the thermometer to address the role of fO_2, as some primitive basalts contain spinel with greater Fe^{3+} contents than in the calibrations of Wan et al. (2008). However, the effect of fO_2 was found to be insignificant, even when up to 35% of total Fe is present in the melt as Fe^{3+}. By incorporating the experimental data from Coogan et al. (2014), the thermometer can be expanded to include a wider range of αSiO_2, spinel Cr# and spinel Fe^{3+}, and can now be expressed as:

$$T_{Al}(°C) = \frac{10000}{0.575 + 0.884 \cdot Cr\# - 0.897 \cdot ln(K_D(Al)^{ol-sp})} - 273 \qquad (3.11)$$

The updated thermometer was applied by Coogan et al. (2014) to a range of samples from LIPs and Siqueiros MORB including ~60 Ma picrites from Baffin Island and East Greenland. The Baffin Island and East Greenland samples recorded a maximum T_{Al} temperature of 1408°C and 1354°C, respectively. The maximum co-saturation temperature of olivine and Cr-spinel at LIPs and MORs was calculated to be 1486°C and 1270°C, respectively, and the average T_{Al} calculated from MORB is 1193°C. The Al-in-olivine thermometer therefore provides

strong evidence, independent of olivine-melt thermometry, for the involvement of substantial mantle thermal anomalies in LIP volcanism. The T_{Al} for Siqueiros MORB is much lower than the T_{OL} value of 1380℃ calculated using olivine-melt thermometry and is more in line with other estimates. For example, PRIMELT3 calculates a 1 atm T_{OL} of 1271℃ for Siqueiros MORB (Herzberg and Asimow, 2015) and McKenzie and Bickle (1988) calculate a mantle T_P of 1280℃ from the thickness of normal oceanic crust.

A significant problem with olivine-melt thermometry is that $K_D(\text{Fe-Mg})^{ol-liq}$ is very pressure sensitive, and so requires an estimate of the depth at which olivine crystallized. This is a parameter that is often poorly constrained, and as was discussed in Section 3.2.3, can introduce a significant uncertainty into the T_{OL} calculation. Fortunately, empirical evidence suggests that the Al-in-olivine thermometer is insensitive to the range of pressures that melts are likely to experience in the upper mantle. For example, there is no systematic offset in the partitioning of Al between olivine and Cr-spinel in the 1 atmosphere experiments performed by Wan et al. (2008), and a series of melting experiments carried out by Pickering-Witter and Johnston (2000) at 1 GPa. In addition, Wan et al. (2008) applied the thermometer to a series of mantle xenoliths and found no systematic offset in T_{Al} calculated from spinel lherzolites when compared to garnet lherzolites. The apparent lack of pressure dependency is a major advantage of the Al-in-olivine thermometer over olivine-melt thermometry, as it removes uncertainties associated with poorly constrained depths of melting that have plagued the more traditional methods.

3.3.2 Results

Al_2O_3 content of olivine

The aluminium content of olivine and composition of Cr-spinel in the NAIP samples was determined using EPMA (full results can be found in Appendices E and F). The maximum detection limit for Al_2O_3 in olivine was 75 ppm during the first set of analyses on olivines from Skye. During subsequent analyses, the detection limit was lowered to a minimum of 28 ppm by increasing the count

time. The maximum detection limit for each sample suite is as follows: 75 ppm for Skye, 58 ppm for Rum and neovolcanic Iceland, 39 ppm for Iceland Tertiary and Mull and 30 ppm for Baffin Island and West Greenland. The Al_2O_3 detection limits reported here are much lower than in conventional analyses, and as such represent a significant technological advancement. To achieve this, the EPMA analytical conditions were modified to ensure maximum precision of the olivine Al_2O_3 measurement. These conditions are discussed in more detail in Appendix B.2.

The Al_2O_3 content of olivine is plotted against olivine Mg# in Figure 3.11. In general, higher olivine Al contents are associated with more Mg-rich olivines. However, each sample suite forms a parallel horizontal array at different Al_2O_3. Olivines from the early BTIP rocks and Baffin Island and West Greenland are very Mg-rich (commonly $>Fo_{91.5}$) and have high Al contents, often above 0.1 wt%. The typical Tertiary Iceland Al_2O_3 range is 0.03-0.06 wt% at systematically lower olivine Fo than in the early BTIP rocks, with most $<Fo_{88}$. Neovolcanic Iceland olivines generally contain 0.06-0.08 wt% Al_2O_3 with Fo contents intermediate between the Iceland Tertiary and early NAIP arrays.

In individual olivine crystals, the Al-content exhibits a variety of different zoning patterns between the crystal core and rim. Most commonly, the cores of the olivine crystals are nearly homogeneous in Al content (Figure 3.12a, b, c). Occasionally there was a little more scatter in the Al content than would be expected based on the detection limits (Figure 3.12d). This was also found to be the case by Coogan et al. (2014), who attributed the scatter to small-scale oscillatory zoning not resolvable by the analyses. A few olivine crystals had a highly heterogeneous distribution of Al_2O_3 (Figure 3.12e), suggesting disequilibrium, and these were therefore not included in the temperature calculations.

On the rim of the crystal, the Al content may be higher, lower or the same as that of the core. In general, the Mull, Baffin Island and Iceland neovolcanic picrites contain olivines with normally zoned cores with higher Al contents compared to that at the rim (Figure 3.13), as would be expected if the high-Mg olivines came into contact with more evolved and lower temperature melts (either by magma mixing or fractional crystallization), leading to the growth of the less forsteritic rim. However, this is not always the case and there are multiple examples from

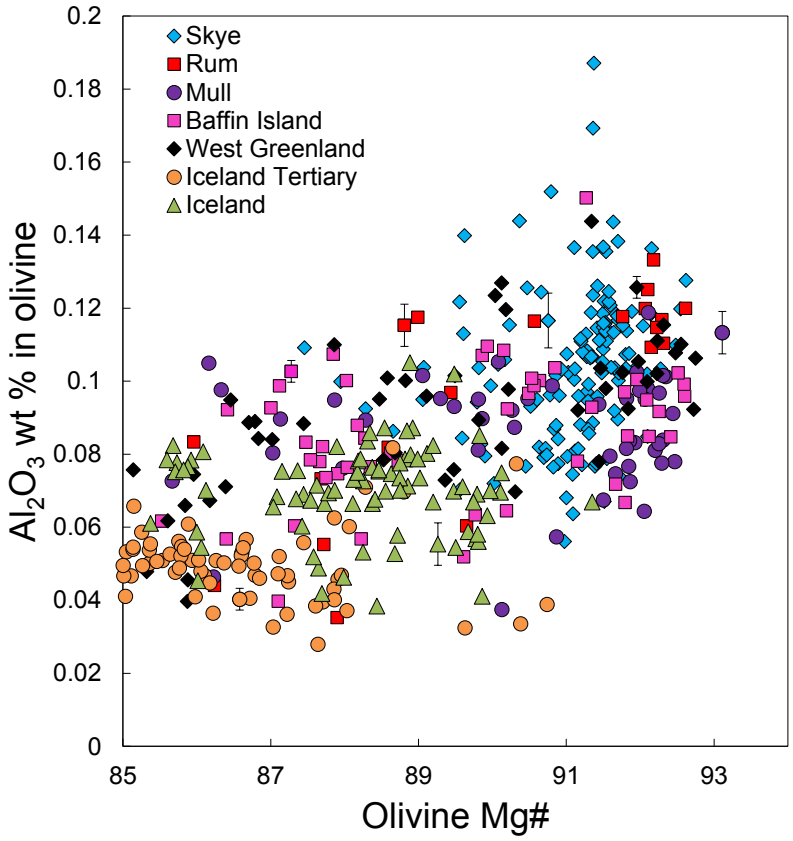

Figure 3.11: Al_2O_3 content vs Mg# of primitive olivines (>Fo_{85}) from the NAIP. Error bars indicate the maximum error in Al_2O_3 content due to the precision of the electron microprobe analyses for representative samples from each suite.

each location where the Al content of the olivine rim is higher, despite exhibiting normal Fe-Mg zoning. In the Skye samples, the general association of more Al-rich cores and less Al-rich rims is not apparent (as might be expected due to their lack of well-developed Fe-Mg zoning) and the Al content tends to be higher on the rim (Figure 3.13). The matrix olivines from Skye however, display systematically lower Al contents, indicating their derivation from lower temperature, more evolved melts. The Al contents of the skeletal matrix olivines from Mull exhibit substantial overlap with the Al-content of the olivine rims, suggesting that the rims grew from the same magma at the same temperature that formed the matrix. The Iceland Tertiary olivines are often associated with very little change in Al content between the crystal core and rim, however small increases and decreases are also observed. This variation in core and rim Al contents is similar to that reported by Coogan et al. (2014). Since the Al content of olivine is dependent both on temperature and the composition of the spinel, changes in the equilibrium Cr-spinel composition due to the evolving magma may result in higher olivine Al_2O_3, even if the temperature has decreased. However, this will not affect the temperature calculation, as both the olivine Al_2O_3 content and Cr-spinel composition are both input parameters in the thermometer.

It is clear that the choice of the analysis point will be very important in the calculation. Since the aim of this study was to determine the maximum temperature recorded by each suite, calculations were based only on the Al content of olivine cores and Cr-spinel inclusions hosted in the respective olivine core. The core will crystallize first and so is most likely to record the maximum magmatic temperature experienced. Since most olivine cores have almost homogeneous Al contents, they are considered to be in equilibrium with their spinel inclusions.

Temperatures

Following Coogan et al. (2014), T_{Al} was calculated using:

$$T(\text{℃}) = \frac{10000}{0.575 + 0.884 \cdot Cr\# - 0.897 \cdot lnK_D} - 273 \tag{3.12}$$

The error in the thermometer is estimated to be ±22℃ (Wan et al., 2008) and includes the error arising from the precision of the olivine Al_2O_3 measurement (30-

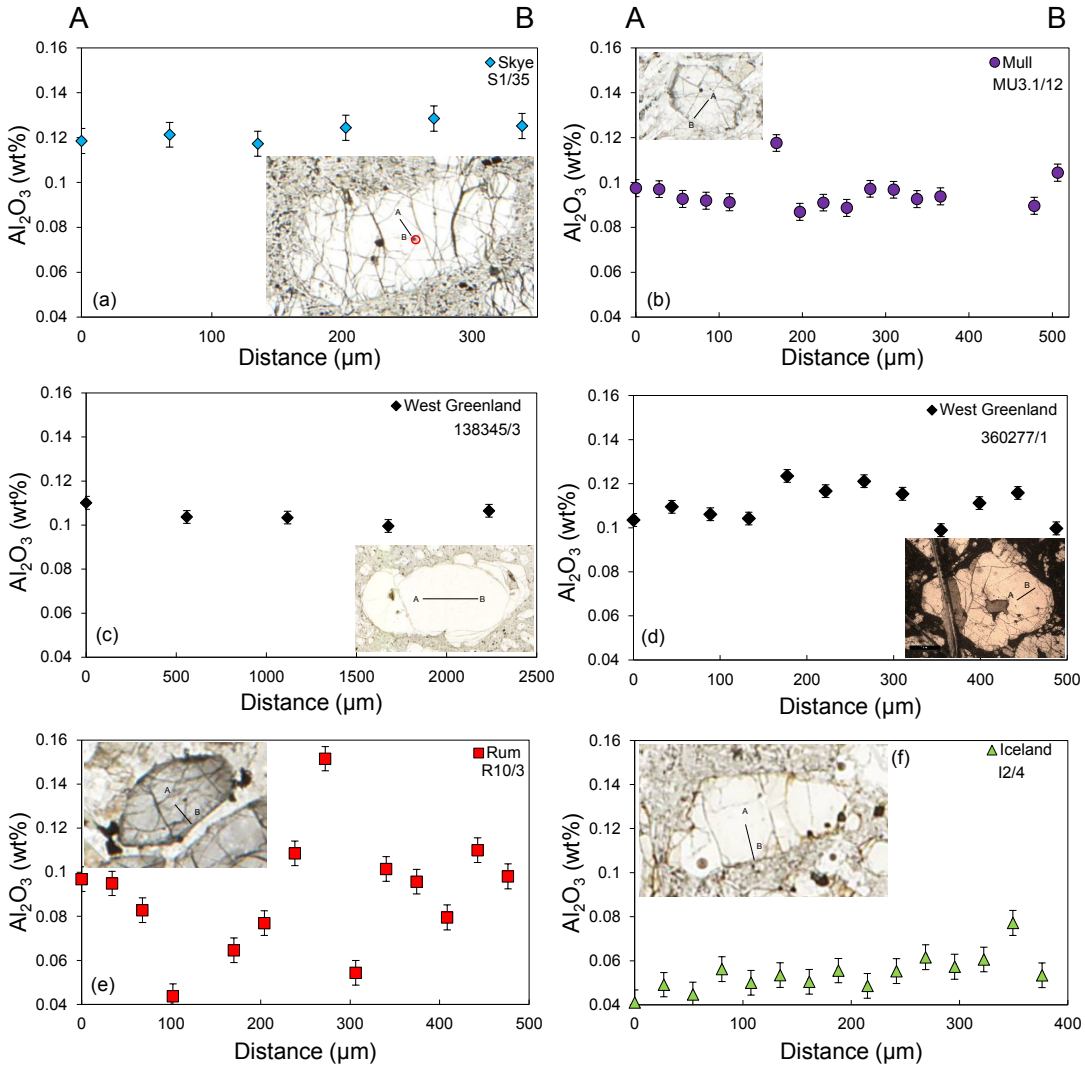

Figure 3.12: Examples of the variation in zoning patterns of Al observed in olivine. Each transect was taken from A to B. (a) A homogenous olivine from Skye. The proximity of the spinel inclusion at B (red circle) has no effect on the Al_2O_3 content of the olivine. (b) A homogeneous olivine from Mull with one point much higher than the rest. It is possible that this point has caught the edge of an inclusion. (c) A homogenous olivine from West Greenland. (d) An olivine from West Greenland with more internal variation in Al_2O_3 content than the previous sample. This is likely to be the result of small-scale oscillatory zoning that is not resolvable within the limits of this study. (e) An olivine from Rum (R10) with a highly heterogeneous Al_2O_3 distribution indicating disequilibrium. (f) An olivine from Iceland that shows a slight increase in Al towards the rim of the crystal, however the last point is lower. Note the much lower Al contents compared to the samples from Skye, Mull and West Greenland.

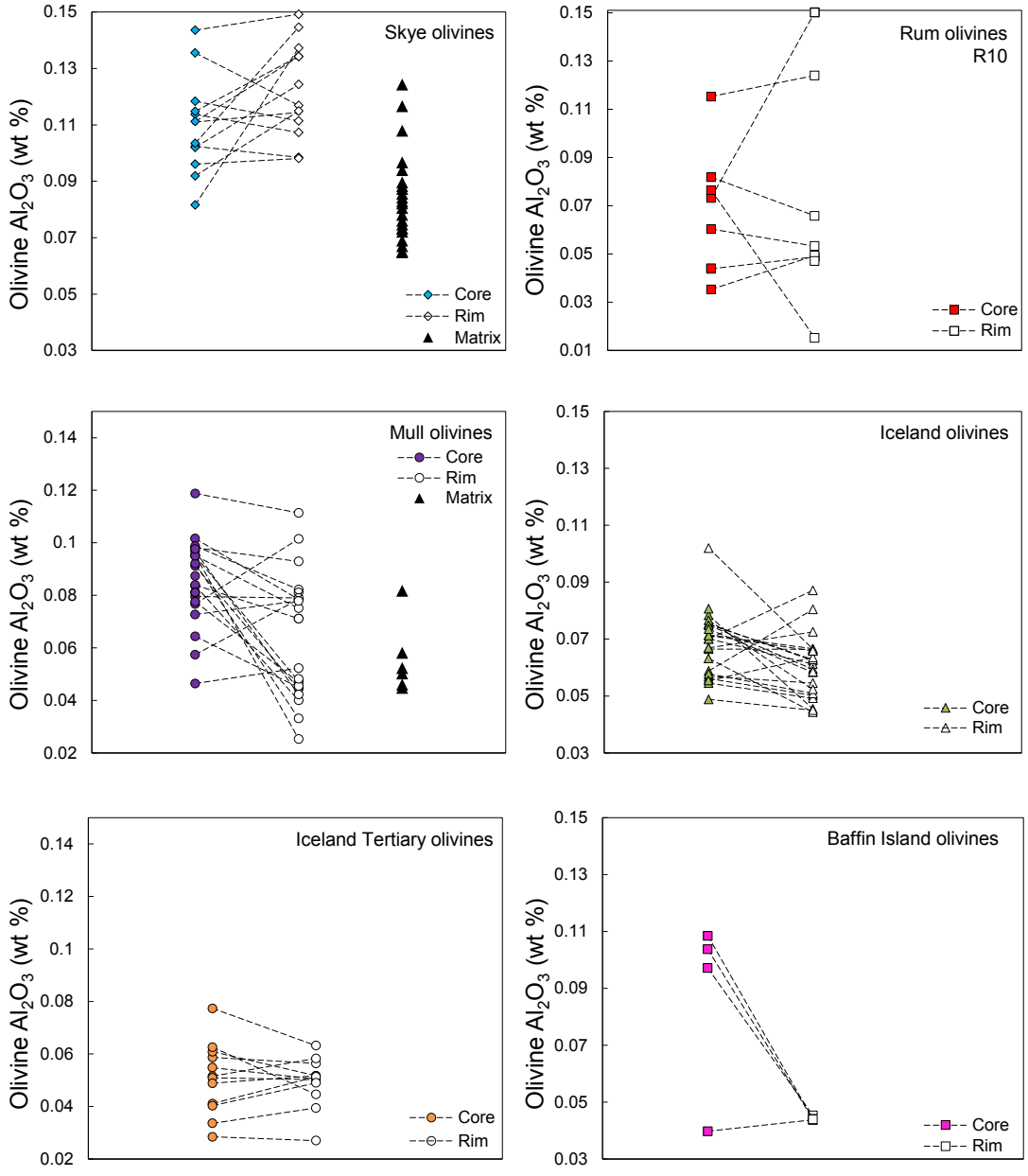

Figure 3.13: Core and rim Al_2O_3 (wt%) contents for olivines from Skye, Rum (R10 only), Mull, Iceland and Baffin Island. Matrix olivine compositions are also plotted for Skye and Mull.

75 ppm). The full results for each olivine-Cr-spinel pair are presented in Appendix H. The maximum, minimum and average T_{Al} for each suite are presented in Table 3.7. The maximum temperatures calculated for Skye, Rum, Baffin Island and West Greenland are 1474℃, 1498℃, 1461℃ and 1484℃ respectively, and are as high (within the error of the thermometer) as the highest temperatures yet measured using this technique (Coogan et al., 2014). As with the results from olivine-melt thermometry, the maximum temperatures recorded by the Phase 1 picrites from across the spatial extent of the NAIP are remarkably uniform. The highest temperature recorded from Mull is 1434℃, slightly lower than that from Skye and Rum. The maximum temperatures from the early NAIP rocks are much higher than those previously reported by Coogan et al. (2014), who calculated temperatures of up to 1408℃ and 1354℃ respectively in 60 Ma Baffin Island and East Greenland rocks. However, the samples used in the present study contain olivines that are more primitive and have higher Al_2O_3 contents than those from Coogan et al. (2014), so it is unsurprising that the maximum recorded temperatures in the present study are higher. Average temperatures at Skye, Baffin Island and West Greenland are all very similar, 1410℃, 1400℃ and 1406℃ respectively. Sample M9 from Rum consistently recorded very high T_{Al}, with none below 1440℃, and so the average T_{Al} for Rum (including the one data point from R10) is 1452℃. A maximum temperature of 1368℃ was measured in the neovolcanic Iceland samples, and a maximum temperature of 1315℃ is calculated from the Iceland Tertiary samples. Average temperatures are 1381℃, 1237℃ and 1315℃ from the Mull, Iceland Tertiary and neovolcanic Iceland samples, respectively.

There is a large range in calculated T_{Al} within a sample suite, and often within a single sample (Table 3.8). The difference in maximum and minimum T_{Al} ranges from 26-194℃. Since Al is far more resistant to re-equilibration in olivine than Fe and Mg (Spandler and O'Neill, 2010), the temperature range within a single sample potentially tracks the rise of the magma through the conduit system, with the 'hottest' olivines being those that crystallized at the deepest levels and the 'coldest' olivines recording crystallization after substantial decompression and possibly storage in a crustal magma chamber. The olivines with the highest temperatures likely crystallized soon after melt segregated from the mantle and will therefore record temperatures close to the actual mantle temperature. It is

thought that mantle melting was initiated at depths of around 100-150 km in the early NAIP, both in the BTIP (Kent and Fitton, 2000) and at West Greenland (Larsen and Pedersen, 2000). Applying a liquid adiabatic gradient of 30 ℃/GPa (McKenzie and Bickle, 1988) would imply a 6 GPa olivine crystallization pressure range in samples where the T_{Al} range is 180℃ or greater, however this is highly unlikely, and so olivines that record temperatures more than 100℃ lower than the maximum T_{Al} probably represent crystals that have cooled and fractionated within crustal magma chambers, which is reflected in their systematically lower Mg#. The maximum range within the Tertiary Iceland samples is much lower (45℃), likely reflecting the lower mantle temperatures and therefore a narrower range in crystallization depths. On the other hand, the range in T_{Al} in the Iceland neovolcanic samples is up to 180℃ within a sample and this is likely to reflect storage, fractionation and cooling within the crust.

Table 3.7: Olivine-spinel equilibrium temperatures (T_{Al}) using the Al-in-olivine thermometer. All temperatures are in ℃. The error on the thermometer is ±22℃ (Wan et al., 2008).

Sample	**Max T_{Al}**	**Min T_{Al}**	**Average T_{Al}**
Skye	1474	1337	1410
Mull	1434	1322	1381
Rum	1498	1350	1452
Baffin Island	1461	1240	1400
West Greenland	1484	1239	1406
Iceland Tertiary	1315	1187	1237
Iceland	1368	1183	1315

Plots of temperature against olivine Al_2O_3, olivine Mg# and $K_D(Al)^{ol-sp}$ are presented in Figure 3.14. The Phase 1 samples record the highest temperatures, the Iceland Tertiary samples record the lowest temperatures, and the Iceland neovolcanic samples are intermediate between the two. There are two temperature trends in the neovolcanic samples (Figure 3.14a), and while both trends cover a similar range in T_{Al} and olivine Al_2O_3 content, the upper trend is defined by higher olivine Al_2O_3 content at fixed T_{Al}. As was noted in Section 2.6.7, the Iceland Cr-spinels exhibit a bimodal distribution related to geographic location. This is reflected in the temperature trends, with the upper trend representing samples erupted in the EVZ and the lower trend representing those erupted in

Table 3.8: Maximum, minimum and range in T_{Al} for each NAIP sample in ℃.

Sample	Max T_{Al}	Min T_{Al}	T_{Al} range
S1	1453	1409	44
S2	1471	1374	97
S3	1470	1370	100
S5	1437	1391	46
S7	1386	1360	26
S8	1431	1337	94
S9	1431	1340	91
S10	1462	1347	115
M9	1498	1440	58
MU1.1	1402	1322	80
MU1.2	1394	1361	33
MU2.2	1417	1376	41
MU3.1	1434	1371	63
PAD4	1421	1390	31
PAD5	1428	1406	22
PAD6	1434	1240	194
APO4	1460	1447	13
APO7	1424	1413	11
DUR6	1425	1307	118
DUR8	1461	1298	163
138345	1484	1437	47
340740	1430	1361	69
354754	1388	1239	149
362077	1486	1398	88
400230	1425	1380	45
ED	1231	1187	44
KoP	1284	1246	38
SAU3199	1236	1218	18
SD	1265	1233	32
VP1a	1236	1201	35
I2	1316	1244	72
I5	1368	1283	85
I9	1368	1183	185

the NVZ and RVZ. As was discussed in Section 2.6.7, the difference in Cr-spinel compositions between the EVZ and the NVZ and RVZ is likely a result of different melting conditions due the thick crust that is present in the EVZ.

In general, higher olivine Mg# correlates with higher temperatures (Figure 3.14b). The early NAIP samples generally have high temperatures and very primitive olivines, while the lower temperature Iceland Tertiary olivines are less Mg-rich. However, several of the relatively evolved olivines from West Greenland and Baffin Island record some of the highest temperatures. The composition of these

olivines matches that of olivine rims from the same rocks (Starkey, 2009), suggesting that Mg and Fe have completely re-equilibrated in some olivines with a more evolved melt. Al, as a trivalent cation, diffuses much more slowly in the olivine lattice (Spandler and O'Neill, 2010) and hence the initial high-T signature is preserved. This result demonstrates one of the advantages of using the Al-in-olivine thermometer over traditional olivine-melt thermometry techniques.

A strong positive correlation exists between $K_D(\mathrm{Al})^{ol-sp}$ and temperature (Figure 3.14c). As expected, the lowest $K_D(\mathrm{Al})^{ol-sp}$ values are calculated for the Iceland Tertiary picrites and the highest are from Phase 1 picrites, with the Iceland neovolcanic samples intermediate between the two. A weaker positive correlation between spinel Cr# and $K_D(\mathrm{Al})^{ol-sp}$ is present (Figure 3.14d) and there is far more scatter present than in Figure 3.14c. This observation suggests that while spinel Cr# does influence the exchange of aluminium into olivine, it is temperature that is the most significant factor. The bimodal distribution of neovolcanic Iceland spinels is also seen in Figure 3.14d, where two distinct populations are present.

Comparison to MORB

Table 3.9: Maximum T_{Al} for each suite. Max ΔT = T_{max} - T_{MORB} where the error is ± 22℃. Average ΔT = average Al-in-olivine T of each suite - T_{MORB}, where T_{MORB} = average olivine-spinel co-precipitation of MORB, calculated as 1193℃ (Coogan et al., 2014).

Sample Suite	**Max T_{Al} ℃**	**Max ΔT_{Al} ℃**	**Average ΔT_{Al} ℃**
Skye	1474	278	217
Mull	1434	241	187
Rum	1498	305	259
Baffin Island	1461	268	207
West Greenland	1486	291	213
Iceland Tertiary	1314	122	44
Iceland zero-age	1368	175	122

In all sample suites, the maximum T_{Al} is higher than any MORB sample measured by Coogan et al. (2014), who recorded a maximum temperature of 1270℃, and an average of 1193℃. The maximum and average temperature differences of

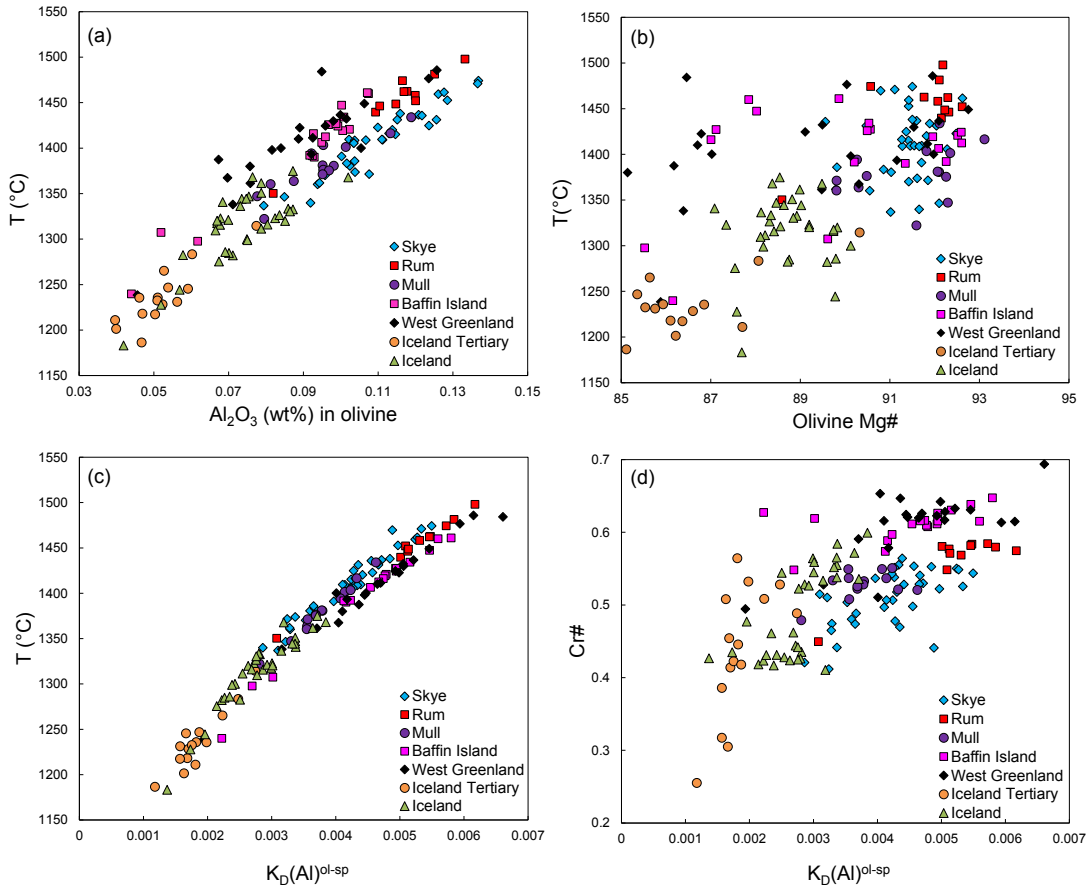

Figure 3.14: T_{Al} (°C) vs (a) olivine Al_2O_3, (b) olivine Mg# and (c) $K_D(\mathrm{Al})^{ol-sp}$. (d) $K_D(\mathrm{Al})^{ol-sp}$ vs Cr# of Cr-spinel.

the NAIP samples calculated using the Al-in-olivine thermometer are compared with MORB and presented in Table 3.9. The difference between maximum T_{Al} and average MORB ranges from 241 to 305 ± 22℃ in the Phase 1 samples, and is 122 ± 22℃ and 175 ± 22℃ in the Iceland Tertiary and neovolcanic zone samples, respectively. The temperature decrease between the Phase 1 picrites and the Iceland Tertiary picrites is similar to that calculated using olivine-melt thermometry and indicates a significant cooling of the mantle plume now underlying Iceland since the flare-up of volcanism at 62-61 Ma. The Al-in-olivine temperatures also suggest a slight warming in the North Atlantic mantle underlying Iceland since 13-14 Ma, similar to the olivine-melt thermometry results. However, the relatively large uncertainty of ±45℃ associated with olivine-melt thermometry means that this conclusion should be treated with caution. Fortunately, the Al-in-olivine thermometer has a much smaller uncertainty, and it is clear that the Iceland picrites indeed record a warming of the mantle since the eruption of the Tertiary picrites. The Al-in-olivine data therefore provide strong evidence for long-term fluctuations in the temperature of the Iceland plume on a timescale of 10^7 years.

If a liquid adiabatic gradient of 30 ℃/GPa (McKenzie and Bickle, 1988) is applied to ΔT_{max}, there is still a 200-250℃ difference in T_{Al} between Phase 1 picrites and MORB, even if it is assumed that olivine-spinel co-precipitation occurred at 3 GPa (a depth of 100 km) in the Phase 1 NAIP picrites and at 0.8 GPa in MORB (at the shallow end of the range of melt pressures at MORs estimated by Kinzler and Grove (1992b)). This conclusion is in good agreement with previous estimates of the excess temperature in plume heads (McKenzie and Bickle, 1988; Campbell, 2007) and indicates that mantle plume heads are associated with thermal anomalies of several hundred degrees across a widespread area at least 2000 km in diameter. Applying the liquid adiabatic gradient to Iceland, if an olivine crystallisation pressure of 2.3 GPa is assumed at Iceland (Putirka et al., 2007), the difference between average MORB and maximum Iceland Tertiary and neovolcanic Iceland temperatures is ∼90℃ and ∼150℃, respectively. The high T_{Al} of the NAIP samples compared to MORB therefore cannot be explained by increased olivine crystallization depths as quite unreasonable differences of several hundred km would be required. Since the Al-in-olivine temperatures are completely independent of those calculated from olivine-melt thermometry and PRIMELT3, the existence of a thermal mantle plume throughout the lifetime of

the NAIP seems irrefutable on the basis of results from this study.

Location of the early plume centre

One of the predictions of the plume model is that the temperature of the plume head will increase towards the centre (Campbell, 2007) due to the greater contribution of hot material from the thermal boundary layer. However, the data here indicate that the thermal anomaly at West Greenland and Baffin Island, which were close to the centre of the proposed plume axis by Lawver and Müller (1994), was as high as that at the BTIP, thought to have been located 1300 km from the axis (Saunders et al., 1997). There are two possible explanations for this. Either hot material is capable of spreading out farther than predicted by the plume model during the initial pulse of magmatism, or the plume axis was located elsewhere. The first option supports modelling by Larsen et al. (1999) who argued that the simultaneous onset of volcanism across the NAIP at 61-62 Ma could be explained by a fast moving plume that spread out horizontally at a rate of 0.5 m/y upon impact with the lithosphere. The second option is in agreement with studies that have suggested that the plume centre was in fact located beneath eastern Greenland (Brooks, 1973; Brooks and Nielsen, 1982; White and McKenzie, 1989), as this marks the centre of NAIP volcanism (Figure 3.15) and the oldest oceanic crust formed just after continental separation is thickest here. If this is the case, the mantle thermal anomaly beneath eastern Greenland was perhaps even greater than the 200-250°C experienced at West Greenland, Baffin Island and the BTIP.

Field observations may provide some insight into which scenario is correct. While the Al-in-olivine data from both sides of the NAIP indicate that the maximum temperature anomaly in the mantle was equal, the volume of picrites in West Greenland and Baffin Island is very much higher than that in the BTIP. Picritic lavas in West Greenland and Baffin Island make up 30-50% of the lava pile (Gill et al., 1992), however in the BTIP, they are restricted to only a few 10s of metres and minor intrusions (Stuart et al., 2000). There are two possible explanations for this. Either high-Mg magmas were simply less abundant in the BTIP, or the most primitive magmas were trapped in the crust. The first option suggests that the West Greenland and Baffin Island source mantle had a higher contribution of

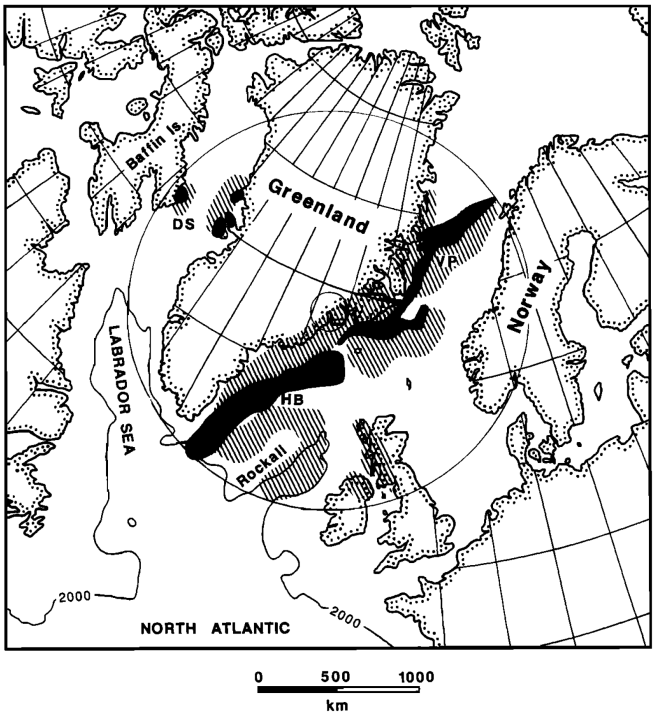

Figure 3.15: Reconstruction of the North Atlantic plate configuration just after the onset of oceanic spreading. Hatching indicates the extent of early Tertiary igneous activity, solid shading indicates the position of extrusive volcanic rocks. The inferred position of the plume axis beneath east Greenland and the extent of the mushroom-shaped plume head of abnormally hot mantle are indicated. From (White and McKenzie, 1989).

high-T material heated by the thermal boundary layer feeding the mantle plume and is consistent with the proposed position of the early plume axis by Lawver and Müller (1994). This would suggest that the initial hot thermal boundary material is capable of spreading out across an area at least 2000 km in diameter, but that its relative contribution will decrease away from the plume axis. However, the latter option is also a possibility as the density of the Hebridean upper crust is sufficient to prevent significant volumes of dense magma reaching the surface (Kent, 1995). Additionally, Brodie and White (1994) indicate the presence of extensive igneous underplating along the northwest European margin during the Early Tertiary, suggesting that a large volume of melt was trapped in the lower crust. While it is likely that density traps similar to that of the Hebrides existed beneath Baffin Island and West Greenland, it is thought that upper crustal extension was greater in these areas during the Late Cretaceous-Early Tertiary, allowing for easier ascension paths for picritic magmas than in the Hebrides (e.g. Keen et al., 1994). From the data presented here, it is not possible to conclusively prove

where plume axis was located at the onset of magmatism between 61 and 62 Ma. However, the key result is that uniform temperatures are found on either side of the province across an area 2000 km in diameter.

3.4 Comparison of thermometry techniques

The data from olivine-melt and Al-in-olivine thermometry and PRIMELT3 all suggest that volcanism in the NAIP is the result of a thermal anomaly in the mantle. However, each technique produces strikingly different results, summarised in Table 3.10. The olivine-melt thermometer consistently gives temperatures 100-200℃ higher than the Al-in-olivine thermometer (Figure 3.16), a discrepancy that was also noted by Coogan et al. (2014). There is a good correlation between olivine-melt thermometry T and Al-in-olivine T, as demonstrated in Figure 3.16, however the olivine-melt thermometry temperatures are systematically higher. There is no correlation between calculated Al-in-olivine temperature and the temperature difference between the two techniques (Figure 3.16) and the temperature offset between the two techniques does not vary systematically with olivine crystallisation temperature.

Table 3.10: Comparison of the maximum temperatures calculated for each suite using olivine-melt thermometry, PRIMELT3 and the Al-in-olivine thermometer. The error for each technique is ±45℃, ±46℃ and ±22℃, respectively. $T_{OL^a} = T_{OL}$ from the original olivine-melt thermometry calculations using the most primitive olivine present in the sample. $T_{OL^b} = T_{OL}$ calculated from olivine-melt thermometry using the olivine composition calculated to be in equilibrium with the primary magma computed by PRIMELT3. n.d. = not determined.

Suite	T_{OL^a}**℃**	$T_{PRIMELT3}$**℃**	T_{OL^b}**℃**	T_{Al}**℃**
Skye	1625	1563	1585	1474
Rum	1715	n.d.	n.d.	1498
Mull	1620	1566	1585	1434
Baffin Island	1665	n.d.	n.d.	1461
West Greenland	1635	1560	1575	1484
Iceland Tertiary	1515	n.d.	n.d.	1315
Iceland	1550	n.d.	n.d.	1368

Section 3.2.3 discussed at length how complexities in the melt system can lead

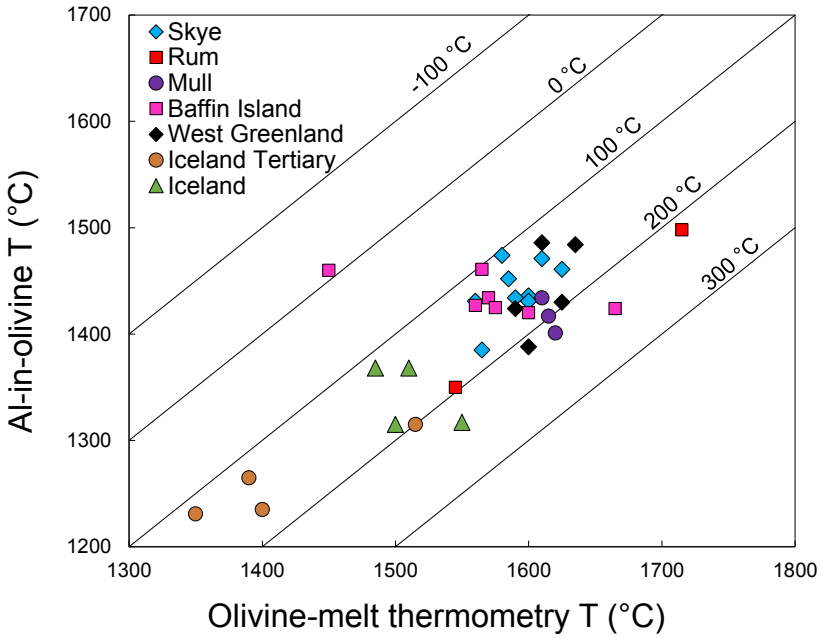

Figure 3.16: Al-in-olivine temperature plotted against olivine-melt thermometry temperature. The diagonal lines represent a fixed temperature difference between olivine-melt thermometry and the Al-in-olivine thermometer.

to overestimation in calculated primary magma MgO, and hence, T_{OL} using olivine-melt thermometry (T_{OL^a} in Table 3.10). The software PRIMELT3 was then applied to the samples to filter for these complexities and the olivine-melt thermometry calculations were performed again (T_{OL^b} in Table 3.10) with the olivine calculated to be in equilibrium with the primary magma from PRIMELT3. However, T_{OL^b} is still substantially higher than T_{Al} by up to 183℃ (Table 3.11). This difference is a cause for concern, as it is highly unlikely that co-saturation of olivine and spinel occurs up to 180℃ lower than the temperature of olivine saturation. This discrepancy was also noted by Coogan et al. (2014) for Siqueiros MORB samples and they suggested that it was the result of mixing of olivines with higher-Mg melts, resulting in re-equilibration of Fe and Mg in olivine, but not Al, evidenced by the presence of reverse zoned olivine crystals. However, it is highly unlikely that this is the case for the NAIP samples as only normally zoned olivine crystals are present.

To investigate the cause of the discrepancy between the techniques, the Putirka et al. (2007) thermometer was applied to the experimental charges of Wan et al. (2008) and Coogan et al. (2014) which were run at known temperatures. The

Table 3.11: Comparison of the maximum temperatures calculated using olivine-melt thermometry and the Al-in-olivine thermometer for each sample that was not filtered by PRIMELT3 for complexities in the melt system. The error for each technique is ±45℃ and ±22℃, respectively. $T_{OL^b} = T_{OL}$ calculated from olivine-melt thermometry using the olivine composition calculated to be in equilibrium with the mixed primary magma computed by PRIMELT3.

Sample	T_{OL^b}℃	T_{Al}℃	T_{OL^b}-T_{Al}℃
S1	1585	1453	132
S3	1550	1470	80
S10	1585	1462	123
MU1.1	1585	1402	183
138345	1575	1484	91
362077	1545	1486	59

results are presented in Figure 3.17. For experiments run at 1250℃ and 1300℃, these temperatures are reproduced by the Putirka et al. (2007) thermometer. However, experiments run between 1350 and 1450℃ plot around 50℃ above the experimental run temperature on the olivine saturation surface (Figure 3.17). This cannot be explained by an incorrect choice of K_D(Fe-Mg)$^{ol-liq}$ because all of the experiments were run at a fixed pressure of 1 atmosphere and K_D(Fe-Mg)$^{ol-liq}$ was therefore known. Neither can it be explained by an incorrect choice of oxidation conditions because varying $Fe^{3+}/\sum Fe$ between 0 and 0.2 did not change the result. It is therefore likely that there is a problem with the calibration of the Putirka et al. (2007) thermometer, which is based on the following equations:

$$lnD_{Mg}^{ol/liq} = -2.158 + 55.09 \cdot \frac{P}{T} - 0.06213 \cdot \left[H_2O^{liq}\right] + \frac{4430}{T} + 0.05115 \cdot \left[Na_2O^{liq} + K_2O^{liq}\right] \tag{3.6}$$

$$lnD_{Fe}^{ol/liq} = -3.3 + 47.57 \cdot \frac{P}{T} - 0.05192 \cdot \left[H_2O^{liq}\right] + \frac{3344}{T} + 0.05595 \cdot \left[Na_2O^{liq} + K_2O^{liq}\right] + 0.01633 \cdot \left[SiO_2^{liq}\right] \tag{3.7}$$

The problem with the Putirka et al. (2007) thermometer cannot, however, explain the temperature discrepancy of up to 183℃ between olivine-melt thermometry and the Al-in-olivine thermometer, although it may contribute. It was shown in Section 3.2.3 that a decrease in olivine-melt equilibrium pressure from 3 GPa

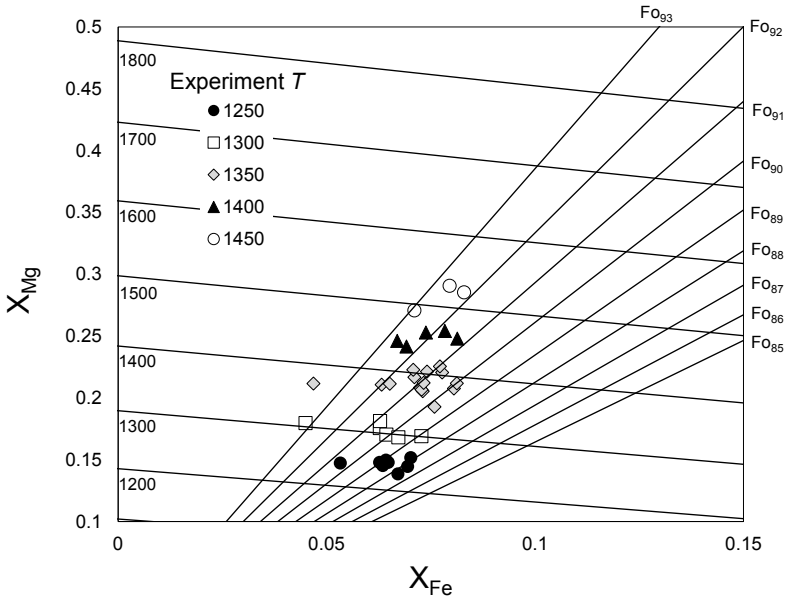

Figure 3.17: Olivine saturation model used to calculate T_{OL} of the experimental run products of Wan et al. (2008) and Coogan et al. (2014) at known temperatures using the Putirka et al. (2007) olivine-melt thermometer. The experiments were run at a pressure of 1 atmosphere, which corresponds to a $K_D(\text{Fe-Mg})^{ol-liq}$ of 0.29. All temperatures are in ℃ and $Fe^{3+}/\sum Fe$=0.1.

to 1 atmosphere can result in a 125℃ decrease in calculated T_{OL}. The discrepancy between T_{OL} and T_{Al} can be reconciled in the BTIP samples in Table 3.11 (within the error of each respective thermometer) if the overestimate in T_{OL} of 50℃ is taken into account, and the olivine-melt equilibrium pressure is decreased by 1-2 GPa. This would suggest equilibration at a depth of 30-60 km, rather than the estimate of 100 km that was used in the original T_{OL} calculations. The discrepancy between T_{OL} and T_{Al} in the West Greenland samples is 59℃ and 91℃. Only a modest decrease in olivine-melt equilibrium pressure of $<$1 GPa is required to reconcile T_{OL} and T_{Al}, suggesting that the West Greenland olivines were equilibrated at greater depths than in the BTIP. This result further highlights the advantage of the Al-in-olivine thermometer over olivine-melt thermometry because it is not pressure dependent.

3.5 Summary

The olivine crystallisation temperatures of the NAIP picrites were calculated using three different approaches. These were the traditional method of olivine-melt thermometry, the mantle melting software PRIMELT3 and the newly developed Al-in-olivine thermometer. It is usual to use mantle T_P when discussing thermal anomalies but unfortunately, converting crystallization temperature to T_P requires assumptions about the depth and degree of melting and latent heat of fusion, which are difficult to constrain accurately. However, T_P and crystallization temperature of the most primitive magmas must be directly correlated and so the maximum olivine crystallization temperatures can be used as a proxy for mantle T_P. All approaches indicate that there has been a thermal anomaly in the North Atlantic mantle since the onset of volcanism at ∼61 Ma. The thermal anomaly was greatest during the plume-head phase of activity when the Phase 1 picrites were erupted, and all three techniques show that the most primitive olivines in each sample suite crystallized at temperatures 250-300℃ above that of ambient mantle. The magnitude of the thermal anomaly on both sides of the NAIP during Phase 1 volcanism was uniform, with the BTIP, Baffin Island and West Greenland samples recording similarly high temperatures, despite being separated by a distance of 2000 km. The Iceland Tertiary picrites record the lowest temperatures, with T_{Al} 122℃ above that of MORBs, indicating a significant cooling of the mantle plume now underlying Iceland since the Phase 1 picrites were erupted. The samples from the neovolcanic zones of Iceland indicate a warming of the plume of around 50℃ since 13-14 Ma. The Al-in-olivine data therefore provide strong evidence for long-term fluctuations in the temperature of the Iceland plume on a timescale of 10^7 years.

Although the three techniques calculate similar temperature differences between the NAIP samples and MORB, the absolute temperatures were strikingly different. Olivine-melt thermometry typically gave T_{OL} that were 100-200℃ higher than T_{Al}. To investigate this discrepancy, the PRIMELT3 mantle melting software of Herzberg and Asimow (2015) was applied to the samples. PRIMELT3 has filters to detect processes that can enhance MgO/FeO of primary magmas, which will lead to an overestimation in T_{OL} calculated using olivine-melt thermometry. Only six of the thirty six NAIP samples survived the filters, indicating that pro-

cesses such as high pressure clinopyroxene fractionation and advanced fractional melting are common during mantle melting. Olivine-melt thermometry is not an appropriate technique for samples that have been affected by these processes as the elevated MgO of the primary magma will appear to enhance the apparent thermal anomaly. Using the olivine composition calculated by PRIMELT3 to be in equilibrium with the primary magmas of the six samples that passed the filters, T_{OL} calculated by olivine-melt thermometry was decreased by up to 65℃, however this new temperature (along with the calculated PRIMELT3 T_{OL}) is still higher than T_{Al} in some samples by up to 183℃. To investigate this, the Putirka et al. (2007) thermometer was applied to the experimental charges of Wan et al. (2008), which were run at a known temperature. It was found that above temperatures of 1350℃, the Putirka et al. (2007) thermometer overestimates T_{OL} by 50℃. The discrepancy in calculated temperature between T_{OL} and T_{Al} can be explained by a combination of the inaccuracy in the Putirka et al. (2007) thermometer calibration, and by lowering the assumed olivine-melt equilibrium pressure by 1-2 GPa.

The results from this chapter clearly demonstrate the limitations of the traditional olivine-melt thermometry technique. Crystallization depths are hard to constrain accurately, introducing a large uncertainty into the calculation. In addition, processes that raise the MgO/FeO of a primary melt appear to be prevalent during mantle melting, which limits the universal application of PRIMELT3 to primitive volcanic rocks and can enhance olivine-melt thermometry temperatures. On this basis, the Al-in-olivine thermometer, which is independent of pressure and is based solely on the temperature-dependent exchange of Al between Cr-spinel and olivine, appears to be a far more robust proxy for mantle temperature and is likely to become the petrographic technique of choice for calculating olivine crystallisation temperature in the future.

4 NAIP melting dynamics and helium isotopes

4.1 Introduction

Since the separation of Greenland from NW Europe at 55 Ma, the North Atlantic ocean floor has provided a continuous, but variable, record of mantle melting. The location of the plume beneath the Mid-Atlantic spreading axis therefore provides a unique insight into the temporal evolution of the mantle plume. The purpose of this chapter is to discuss the temperature of the Iceland mantle plume through time and its influence on magmatism across the NAIP. The first part will link seafloor topography, geophysical constraints and trace element geochemistry with the Al-in-olivine temperature data to show that the long-term (10^7 year) fluctuations in plume temperature indicated by the Al-in-olivine thermometry results have had a hugely significant effect on mantle melting across the region.

The second part of this chapter will focus on helium isotopes and their relationship with mantle plumes. The samples from Baffin Island and West Greenland contain olivines with the highest $^3He/^4He$ values yet found on Earth, and since the magnitude of the thermal anomaly was as high here as it was in the BTIP, a key question concerns whether the BTIP olivines will also contain such high $^3He/^4He$, and whether a link between temperature and $^3He/^4He$ exists. It is clear from previous studies that the high $^3He/^4He$ reservoir on Earth does not have a unique composition for any incompatible trace element or isotope tracer (e.g. Hofmann, 1997; Class and Goldstein, 2005; Starkey et al., 2009), and so investigating its relationship with temperature will allow us to place better constraints on its origin and relationship with mantle plumes. Finally, the results of this study will be placed in a global context and a model that links the $^3He/^4He$ source, temperature, mantle plumes and mantle dynamics will be presented.

4.2 Temperature of the NAIP mantle through time

The results from Al-in-olivine thermometry show that the temperature of the NAIP mantle has changed through time. Phase 1 magmatism is associated with a hot pulse of Mg-rich material due to the arrival of the ancestral Iceland plume at the base of the North Atlantic lithosphere. The Al-in-olivine data indicate that the T_{Al} of early NAIP picrites was 250-300℃ above that of average MORB, and that the temperature distribution across the province at this time was uniform, covering an area 2000 km in diameter, from Baffin Island in the west, to the BTIP in the east. The Al-in-olivine data then indicate that the mantle beneath the North Atlantic region cooled significantly after the initial phases of volcanism, in agreement with the plume model that predicts that plumes become focussed into a narrow mantle upwelling with time (Campbell, 2007). By 13-14 Ma, the maximum difference in T_{Al} between the Tertiary Iceland picrites and average MORB was 122℃. Significantly, the data show that the plume temperature beneath Iceland is currently increasing, with a 50℃ increase in maximum T_{Al} since 13-14 Ma indicated by the picrite and primitive basalt samples from the Icelandic neovolcanic zones. The long-term temperature fluctuations of the plume are highly significant because they have had a profound impact on the melting dynamics and formation of oceanic crust in the region, which are described in detail below.

4.2.1 Bathymetry of the North Atlantic

On a short timescale, the plume has been subject to periodic fluctuations in melt production which has resulted in the formation of V-shaped ridges (VSRs) (Figure 4.1) along the Reykjanes Ridge spreading axis south of Iceland. These are topographic and gravity lineations that converge southwards on the spreading axis and result from variations in thickness of oceanic crust formed as a consequence of melting anomalies that propagate away from Iceland within the asthenosphere. Jones et al. (2014) recently showed that the melting anomalies are caused by fluctuations in mantle temperature and not by changes in mantle lithology (Foulger et al., 2005b) or rift propagation and relocation cycles (Hardarson et al., 1997),

as had been previously suggested. Fluctuations of 25-30℃ in the temperature of the plume over a timescale of 8 million years (Parnell-Turner et al., 2014) are responsible for VSRs that have formed over the past 40-35 Ma. There are indications in the gravity field of similar lineations in the oldest oceanic crust (35-55 Ma), however the thick sediment cover here means that no bathymetric ridges are visible and the magnitude of the gravity signal is greatly attenuated. Nevertheless, it is thought that the weak VSRs in this section of the North Atlantic were formed by small fluctuations in mantle temperature of 5-10℃ over a shorter period of 3 million years (Parnell-Turner et al., 2014).

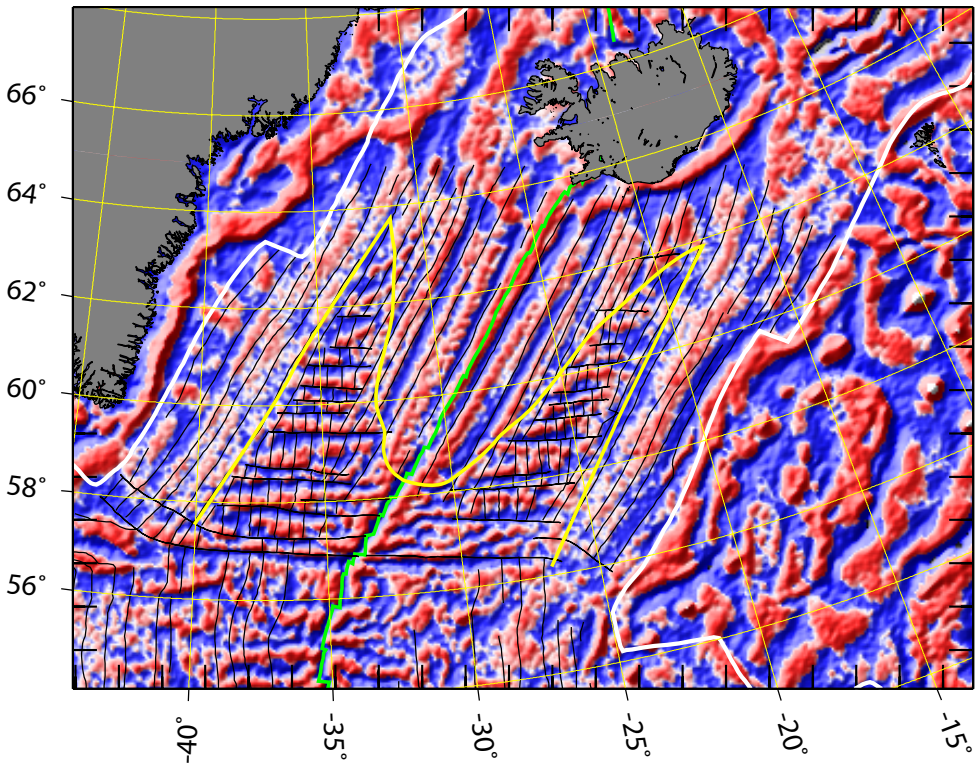

Figure 4.1: Map of short (<250 km)-wavelength free-air gravity anomalies in the North Atlantic (Jones et al., 2002), on which the VSRs extending south of Iceland are prominent. The green line south of Iceland is the Reykjanes Ridge spreading axis. The yellow line represents the boundary between smooth and fractured oceanic crust, the white lines represent the edge of the Greenland and European continental margins. Thin black lines indicate crustal lineations, either as a result of VSRs or oceanic fracture zones.

In the wider North Atlantic Ocean basin, there are three main types of oceanic crust, and the distribution of these are a result of long-term changes in mantle

temperature that are in agreement with the Al-in-olivine data. The arrangement of the three crustal types is shown in Figure 4.2 and are as follows:

(i) Normal oceanic crust with fracture zones: Oceanic ridge segments are separated by fracture zones and is the normal pattern at slow-spreading ridges observed elsewhere in the ocean basins. The crustal thickness here is estimated at 6.3 km (Whitmarsh, 1971), consistent with the idea that it was generated above normal mantle temperatures (e.g. McKenzie and Bickle, 1988).

(ii) Crust unbroken by fracture zones: Oceanic seafloor that is largely unbroken by fracture zone offsets. This type of crust is consistently thicker than normal oceanic crust, on average 10-11 km (White et al., 1992). Increased oceanic crustal thickness is indicative of higher volumes of melt generation and mantle temperatures (White and Lovell, 1997).

(iii) Over-thickened oceanic crust: This is abnormally thick (20-35 km) crust that forms the Greenland-Iceland-Faeroe Ridge and is the result of plume driven mantle upwelling (Maclennan et al., 2001; Shorttle and Maclennan, 2011) and anomalously hot material in the core of the Iceland plume tail (White and Lovell, 1997; Darbyshire et al., 1998).

The strength of the lithosphere is controlled by the temperature of the underlying asthenosphere and determines whether fracture zones are present or not in oceanic crust. The uppermost part of the oceanic crust (about 2 km) is cooled by hydrothermal circulation and is therefore brittle. Below this, the crust remains hot from igneous intrusions and cools mainly by conduction (Henstock et al., 1993), therefore cooling of the mantle, and hence the strength of the lithosphere, is controlled by conductive cooling of the lower crust. At normal slow-spreading centres, intrusion events typically occur on intervals of 10,000-50,000 years, allowing the underlying mantle to cool sufficiently between each event to allow brittle behaviour, resulting in the formation of fracture zones in response to the forces at the spreading centre (White and Lovell, 1997). At spreading axes with higher mantle temperatures, there are three factors that result in ductile behaviour of the lithosphere, producing oceanic crust without fracture zones. Firstly, the increased melt production means that there is an increase in the frequency of in-

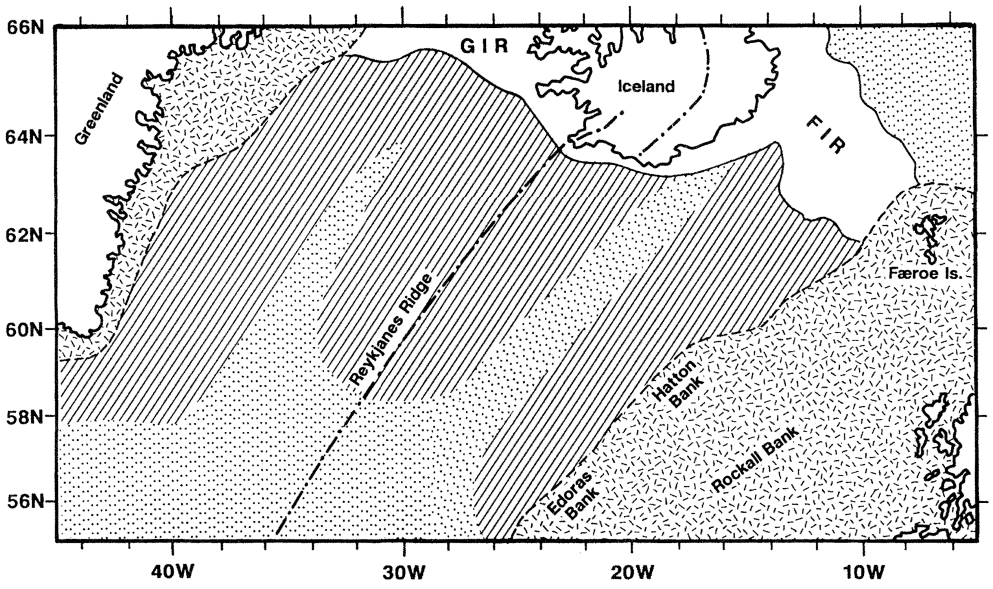

Figure 4.2: Outline of the three main oceanic crustal types found in the North Atlantic. Parallel shading represents oceanic crust formed without fracture zones, dotted shading represents oceanic crust with fracture zones, the blank area represents thick crust generated directly above the mantle plume with the Greenland-Iceland Ridge (GIR) and the Faeroe-Iceland Ridge (FIR) indicated. Together the GIR and FIR form the Greenland-Iceland-Faeroe Ridge (GIFR). Shaded areas in the northwest and southeast corners of the map represent thinned continental crust on the respective Greenland and European continental margins. From White and Lovell (1997).

trusion events, secondly, the mantle temperature itself is hotter so has further to cool before it forms brittle lithosphere, and thirdly (and possibly most importantly) the thicker oceanic crust produced in such regions provides a thicker insulating layer that prevents the underlying mantle from cooling quickly (White and Lovell, 1997).

At the onset of seafloor spreading, the high mantle temperatures associated with the plume-head stage of magmatic activity resulted in the production of oceanic crust 10-11 km thick without fracture zones across the entire ocean basin immediately after continental break-up at 55 Ma (White and Lovell, 1997). As the North Atlantic continued to open, mantle temperatures decreased, resulting in the boundary between smooth and rough oceanic crust migrating rapidly northwards by around 700 km at $\sim$42 Ma (White and Lovell, 1997). The decreased mantle temperatures meant that seafloor spreading became dominated by thinner (6-7 km), fractured oceanic crust. To the south of the GIFR, this phase was relatively short lived, with a reversion to oceanic crust without fracture zones

occurring between 35 and 40 Ma (Figure 4.3), indicating an increase in mantle temperature. The smooth-to-rough transition has continued to extend farther south along the Reykjanes Ridge to the present day (Figure 4.3), and oceanic crust without fracture zones can now be found >1000 km from Iceland (White and Lovell, 1997; Jones et al., 2002), consistent with a continuous expansion of the thermal anomaly due to the increasing temperature in the Iceland plume. Fractured crust near the smooth-to-rough crust boundary is 6.8-7.8 km thick (Navin et al., 1998) whereas unsegmented crust near the boundary is 9.3 ± 0.7 km thick (Bunch and Kennet, 1980). This suggests a critical crustal thickness of 8-9 km is required to produce smooth oceanic crust and implies a critical asthenosphere temperature of 40-50℃ above normal (Brown and White, 1994), assuming melting of uniform dry peridotite.

The segmentation of oceanic crust is thought to be controlled by plate spreading geometry as well as mantle temperature (Vogt and Avery, 1974; White and Lovell, 1997) and it has been proposed that the sudden change to rough oceanic crust at ∼ 42 Ma was a result of a change in spreading obliquity (Jones, 2003). At this time, the spreading obliquity along the Reykjanes Ridge changed from 0° to 30° in response to a reorganisation of seafloor spreading across the North Atlantic region (the onset of spreading along the Kolbeinsey Ridge to the North of Iceland and the cessation of spreading in the Labrador Sea). Oblique spreading requires a component of plate movement parallel to the spreading axis, producing more strain within the lithosphere compared to orthogonal spreading (Jones, 2003). This strain will lead to fracturing of the crust only if it is cool enough to allow brittle deformation. The rapid migration northwards of the smooth-to-rough boundary at 42 Ma may indeed have been triggered by the change in spreading obliquity, however fractured crust requires close to normal mantle temperatures and the fact that it was then formed across a large part of the North Atlantic is in agreement with the Al-in-olivine data that suggests long-term cooling of the mantle after Phase 1 volcanism.

Modelling by Jones (2003) suggests that the southwards migration of the smooth-to-rough boundary could be explained by westwards migration of the Reykjanes Ridge over the Iceland plume, which results in a decrease in the distance between the ridge and the plume stem. While the Al-in-olivine data does not preclude this possibility, it indicates that an increase in mantle temperature of around 50℃ has

also played a role.

The fluctuating temperatures have caused the width of the broad strip of anomalously thick crust forming the GIFR to change through time. The width of the ridge decreases and is at its narrowest at an age of 35 Ma (Figure 4.3), followed by a rapid expansion into the large oceanic plateau now surrounding Iceland. It has been noted that crustal flow plays an important role in shaping the crustal structure of the GIFR (Jones and Maclennan, 2005), however it is the extent and magnitude of the thermal anomaly that determines the areal extent of the over-thickened crust. The narrowing of the ridge at 35 Ma suggests that mantle temperatures were lowest at this time. The expansion of the ridge to form the large basalt plateau around Iceland indicates increased melt production and hence higher temperatures. These observations are in agreement with the location of the smooth-to-rough boundary, which was closest to Iceland between 40 and 35 Ma.

The long-term cooling of the plume following the plume-head phase of activity to around 40-35 Ma is evidenced by crustal thickness profiles in the region. Seismic profiles of the Faroes ridge and the Hatton ridge in the Iceland basin (Figure 4.4) indicate a significant decrease in crustal thickness between 52 and 42 Ma (Parkin and White, 2008). The most rapid decrease occurs during the first 5-6 million years following continental break-up, before decreasing more slowly to 42 Ma. The Faeroes ridge has greater thickness than the Hatton ridge as it is more proximal to the mantle plume axis and exhibits a pulse in thickness similar to that observed in the VSRs south of Iceland. The long-term temperature changes can also be linked to changes in the magmatic flux of the Iceland plume (Mjelde and Faleide, 2009). A rapid decrease in flux from 55 m^3/s post continental break-up to only 4 m^3/s by 40 Ma is observed. Since 23 Ma, the magmatic flux has increased to 7 m^3/s, in agreement with the idea of a gradually warming mantle plume.

The Al-in-olivine data is in agreement with the conclusions of Parnell-Turner et al. (2014), who modelled mantle potential temperatures from the Reykjanes Ridge through time using seismically determined residual depths (deviation from the cooling plate age-depth curve). Their calculations indicate cooling of around 70℃ (which was most rapid following continental break-up) until around 40 Ma,

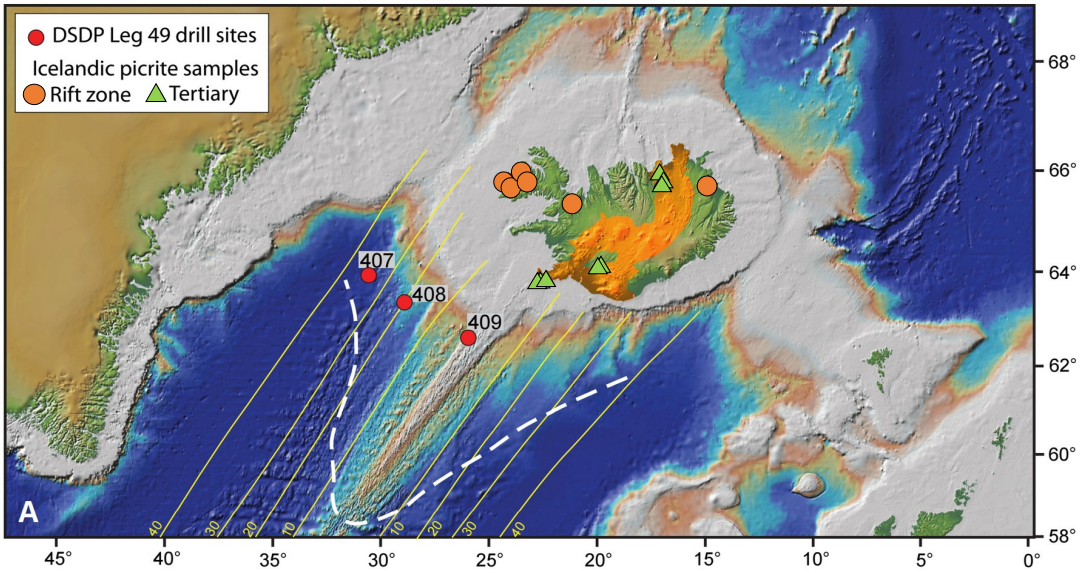

Figure 4.3: Map showing the topography of the seafloor in the North Atlantic region. Iceland sits astride the Mid-Atlantic Ridge and is surrounded by a broad ridge of shallow-ocean extending from Greenland to Faeroe Island, a result of anomalously hot material uplifting the ocean floor. The Greenland-Iceland-Faeroe ridge is at its narrowest at an age of 35 Ma before a rapid expansion to the large oceanic plateau now surrounding Iceland. Yellow lines are the age of the ocean floor (in Ma), the white dashed line is the location of the boundary between smooth and rough oceanic crust (Jones et al., 2002). The rough-to-smooth transition has migrated farther southwards from Iceland through time, and smooth oceanic crust can now be found more than 1000 km from Iceland. The location of Iceland sample sites used in this study are indicated, and red circles show the location of basalts from Deep Sea Drilling Program (DSDP) sites that are presented in Section 4.2.2.

followed by a gradual warming (with fluctuations related to VSRs superimposed) until more recent times (Figure 4.5).

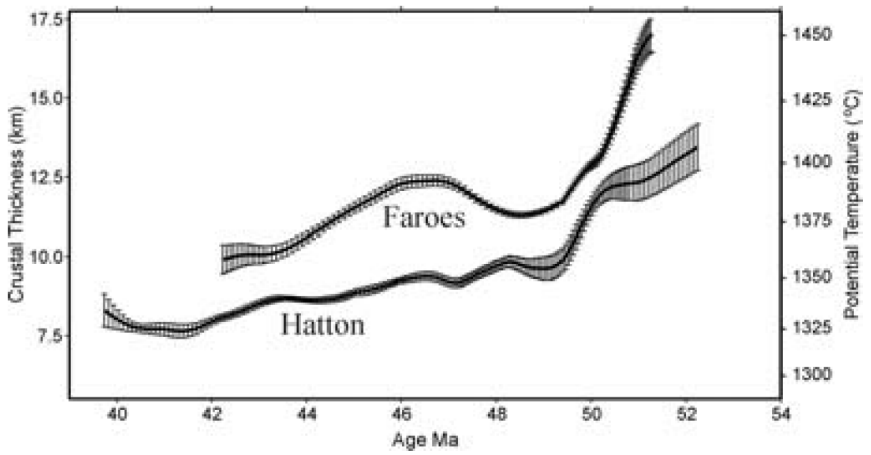

Figure 4.4: Oceanic crustal thickness profiles vs age for the Faeroe and Hatton ridges following continental break-up. Mantle potential temperature is calculated using the method of Brown and White (1994). From Parkin and White (2008).

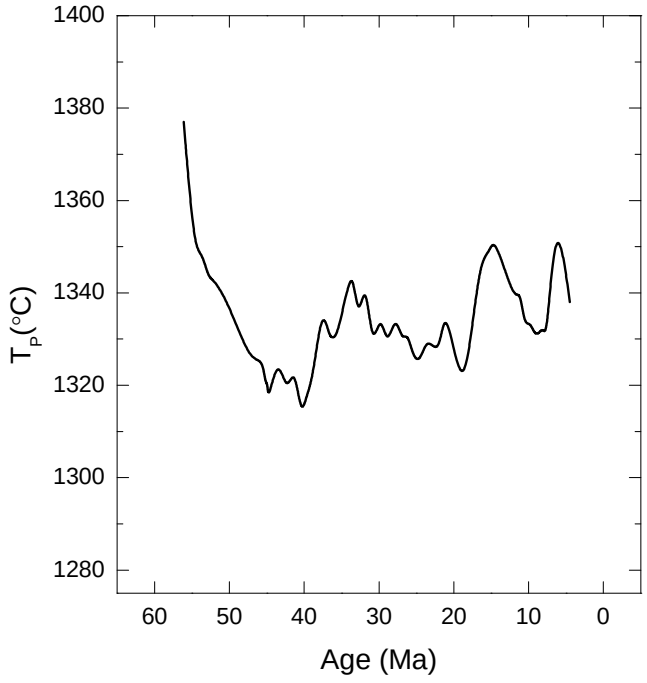

Figure 4.5: Calculated mantle potential temperatures as a function of time at the plume centre based on residual depth calculations. Data from Parnell-Turner et al. (2014).

4.2.2 Geochemistry

The increase in mantle temperature since 35 Ma is reflected in the trace element composition of basalts dredged from the Reykjanes Ridge south of Iceland. Three sites (407, 408, 409 on Figure 4.3) were drilled on the western flank of the Reykjanes Ridge along a mantle flow line away from the ridge crest during DSDP Leg 49 (Kempton et al., 2000). When Zr/Y is plotted against age (Figure 4.6), it is shown to decrease steadily with time. Since Zr is more incompatible in mantle phases than Y, a decrease in Zr/Y indicates increasing melt fraction and is therefore consistent with an increase in mantle temperature over the past 35 Ma.

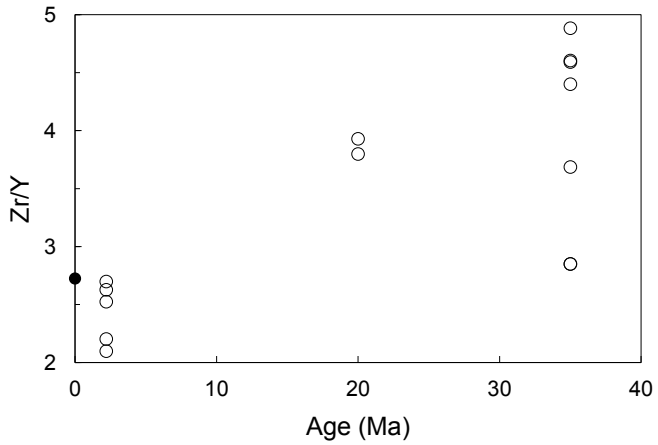

Figure 4.6: Zr/Y vs age for basalt samples collected along a mantle flow line extending west from the Reykjanes Ridge. Data from samples recovered during DSDP Leg 49 (Sites 407, 408 and 409) are shown with open circles (Kempton et al., 2000); the filled circle represents basalt dredged from the ridge axis along the same flow line (Murton et al., 2002). The location of the DSPD sites is shown on Figure 4.3.

4.2.3 Summary

Compiling all of the available data, a temperature vs age diagram for the NAIP is presented in Figure 4.7a. The long-term temperature fluctuations of the plume are highly significant because they have had a profound effect on the melting dynamics and magmatism of the North Atlantic region. Since continental separation at 55 Ma, these changes have been recorded in the bathymetry of the

ocean floor. The arrival of the mantle plume now underlying Iceland was associated with an initial hot pulse of volcanism and the T_{Al} of Phase 1 NAIP picrites is calculated to be 250-300℃ above that of MORB. The Al-in-olivine data suggest that the North Atlantic mantle then cooled considerably. Following the onset of seafloor spreading, this resulted in the rapid migration northwards of the smooth-to-rough oceanic crustal boundary (Figure 4.7b), a decrease in oceanic crustal thickness (Parkin and White, 2008) across the region and a decrease in magmatic flux (Mjelde and Faleide, 2009) of the plume. It is estimated that minimum mantle temperatures were experienced at 40-35 Ma. This conclusion is based on the position of the smooth-to-rough transition boundary closest to Iceland and the narrowing of the GIFR at this time. Following this, the temperature of the plume began to increase again. The T_{Al} of 13-14 Ma Iceland picrites is calculated to be 122℃ higher than that of average MORB. Between 13-14 Ma and the present day, the Al-in-olivine data record a 50℃ increase in the temperature of the mantle plume. The increasing temperatures resulted in the expansion of the oceanic plateau surrounding Iceland at 35 Ma, the gradual migration south of the smooth-to-rough transition boundary (Jones et al., 2002) shown in Figure 4.7b, a change in incompatible element chemistry of Reykjanes Ridge basalts (Kempton et al., 2000) and an increase in magmatic flux of the plume (Mjelde and Faleide, 2009).

4.3 Helium isotopes

High $^3He/^4He$ of primitive basalts is a key characteristic of the Iceland plume. Extremely high values of up to 50 R/R_a (Starkey et al., 2009) are found in the Baffin Island and West Greenland picrites, and picrites from Skye have been found to contain up to 22 R/R_a (Stuart et al., 2000). The Iceland Tertiary picrites have $^3He/^4He$ up to 37 R/R_a (Ellam and Stuart, 2004) and high $^3He/^4He$ basalts are still erupted on Iceland today. Since the olivine crystallisation temperature of the Baffin Island, West Greenland and Skye picrites in this study are the same, a key question concerns whether the $^3He/^4He$ R/R_a is also the same, and whether a relationship between temperature and $^3He/^4He$ exists. In this section, new $^3He/^4He$ measurements from the BTIP and neovolcanic Iceland samples are presented in order to establish the relationship between $^3He/^4He$ and temperature

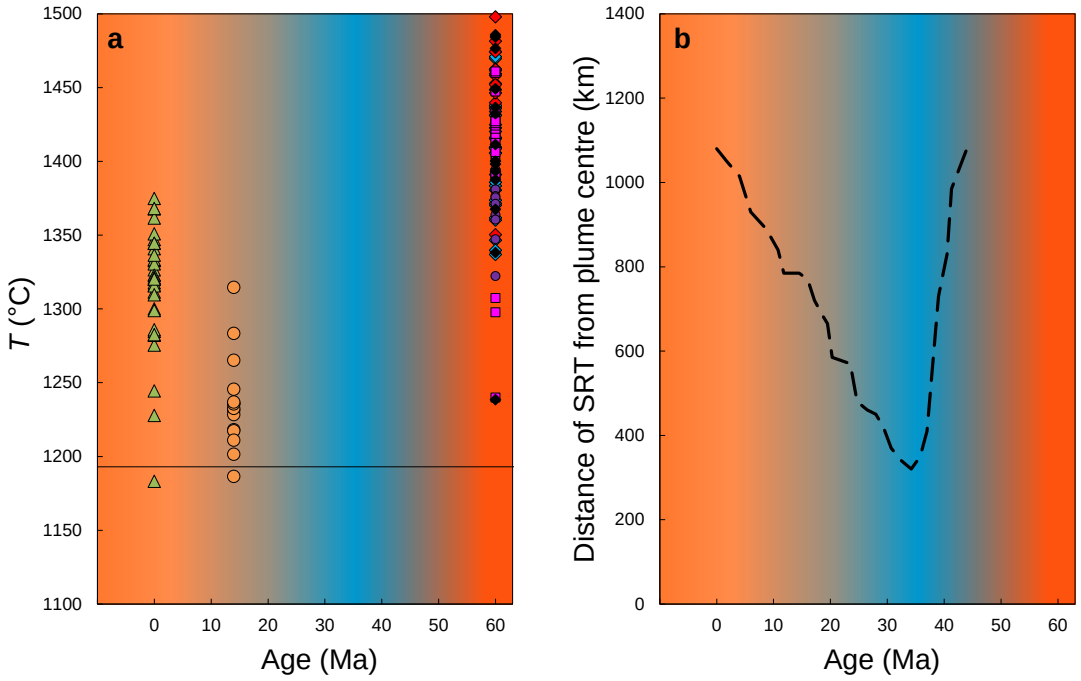

Figure 4.7: (a) Age vs T_{Al} and, (b) age vs distance of the smooth-to-rough oceanic crust boundary from Iceland. The average MORB T_{Al} of 1193°C (Coogan et al., 2014) is indicated by the horizontal line. The dashed curve in (b) is the location of the boundary between fractured and smooth oceanic crust in relation to the plume centre under Iceland (Jones et al., 2002). The boundary is at a minimum distance from Iceland at ∼35 Ma, the best estimate for the age at which the mantle plume was at its coolest. Since 35 Ma, the increasing mantle temperature has resulted in an expansion of the area influenced by the thermal anomaly associated with the plume and the subsequent southwards migration of the boundary, away from Iceland. The background colours provide a schematic indication of North Atlantic mantle temperatures, with orange indicating highest temperatures and blue indicating the lowest temperatures.

now that the T_{Al} of each sample has been determined.

4.3.1 Helium isotope results

Helium isotopes were measured in samples S1, S7, S8, S9, S10, MU1.1, MU1.2, MU2.2, MU3.1, I2, I5, I6, I7 and I8. The analyses were done at the Noble Gas Laboratory at the Scottish Universities Environmental Research Centre (SUERC), East Kilbride by Ana Carracedo Plumed (SUERC, University of Glasgow). Isotope ratios were measured in gases trapped in olivine melt inclusions by *in vacuo* crushing of ∼1 g of olivine crystals. Full analytical details are available in Appendix B.3.

The results are presented below in Table 4.1. Samples with $^3He/^4He$ below 8 R/R_a (the average value of ambient upper mantle) have either been contaminated with radiogenic ^4He or have lost their original $^3He/^4He$ signal. The Skye samples have a $^3He/^4He$ range from 2.9-24.7 R/R_a, slightly extending the highest value previously found in the BTIP of 22.1 R/R_a by Stuart et al. (2000). $^3He/^4He$ ranges from 12.4-15.9 R/R_a in the Mull rocks and these values are similar to the only other published data on $^3He/^4He$ from the BTIP, a 42 Ma dyke from northwestern Ireland, which has $^3He/^4He$ up to 16 R/R_a (Kirstein and Timmerman, 2000). The $^3He/^4He$ anomaly is therefore much more extensive across the BTIP than previous studies indicate. The highest $^3He/^4He$ sample from Skye has a depleted trace element signature ($\Delta Nb < 0$), in agreement with previous studies indicating that the highest $^3He/^4He$ lavas are more likely to derive from a depleted mantle source (Stuart et al., 2003; Ellam and Stuart, 2004; Macpherson et al., 2005a). Two of the Mull samples have an enriched 'Icelandic' mantle trace element signature ($\Delta Nb > 0$), which is in agreement with recent work on the Baffin Island and West Greenland picrites by Starkey et al. (2009) showing that both depleted and enriched samples can carry a high $^3He/^4He$ signature.

The samples from Iceland give $^3He/^4He$ of 12.0 R/R_a from the RVZ, 18.3-18.5 from the EVZ and 5.1-8.7 from the NVZ, and overlap values published in previous studies for each respective volcanic zone of 18-26 R/R_a from the EVZ, 12-16 R/R_a from the RVZ and WVZ and 8-11 R/R_a from the NVZ (Kurz et al., 1985).

A plot of $^3He/^4He$ against ^4He content from olivines across the early NAIP is shown in Figure 4.8. In general, the highest $^3He/^4He$ samples contain the most ^4He, indicating that these samples must have contained relatively large amounts of ^3He. The high $^3He/^4He$ values of Baffin Island and West Greenland picrites across a range of ^4He concentrations indicates that the data reflect magmatic $^3He/^4He$ rather than contamination with ^4He. The fact that the highest Skye $^3He/^4He$ measured in this study (sample S8) contains the same amount of ^4He as the other Skye samples with $^3He/^4He$ much below that of MORB seems to suggest that the low $^3He/^4He$ samples have lost their original magmatic $^3He/^4He$ signature and are not more contaminated than S8.

Table 4.1: Helium contents and isotope ratio results

Sample	^{4}He (10^{-9} ccSTP/g)	Error (10^{-12} ccSTP/g)	^{3}He/^{4}He (R/R_a)	Error R/R_a
S1	2.39	0.95	2.89	0.22
S7	6.62	1.99	4.91	0.20
S8	6.53	1.31	24.71	0.39
S9	9.06	2.72	3.36	0.14
S10	5.45	1.09	2.80	0.14
MU1.1	2.24	0.67	15.49	0.66
MU1.2	2.24	0.67	15.94	0.58
MU2.2	1.31	0.66	14.98	1.10
MU3.1	1.75	0.70	12.40	0.49
I2	0.83	0.67	12.00	0.89
I5	8.52	2.56	18.45	0.31
I6	34.92	6.98	18.26	0.27
I7	0.22	0.44	5.07	1.42
I8	0.66	0.59	8.71	0.93

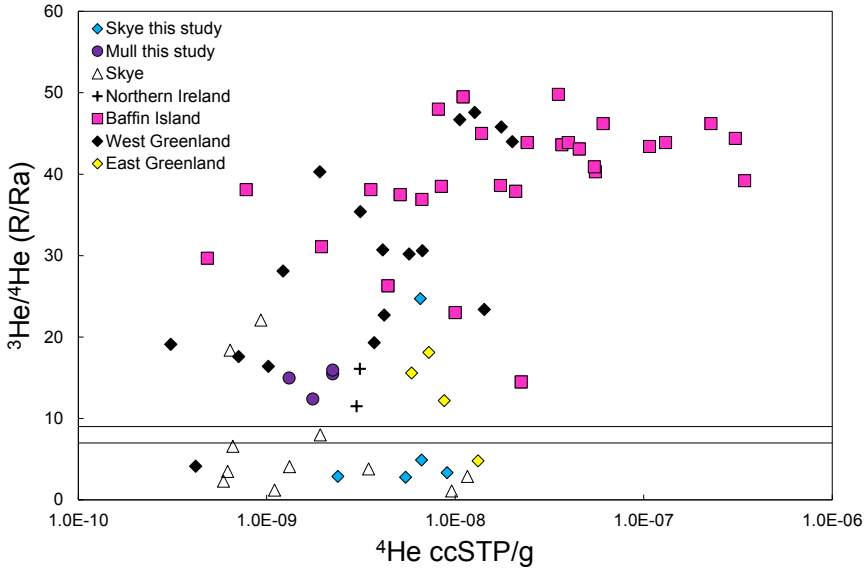

Figure 4.8: ^{3}He/^{4}He vs ^{4}He content for *in vacuo* crushing of olivines from across the early NAIP. Skye from this study and Stuart et al. (2000); Mull from this study; Northern Ireland from Kirstein and Timmerman (2000); Baffin Island from Stuart et al. (2003) and Starkey et al. (2009); West Greenland from Graham et al. (1998) and Starkey et al. (2009); East Greenland from Peate et al. (2003).

4.3.2 Interpretation of helium isotope data

It is well known that *in vacuo* crushing of olivine from young volcanic rocks liberates magmatic He from CO_2 bubbles hosted in melt inclusions, and that radiogenic and cosmogenic He are left behind in the olivine lattice (Kurz, 1986). However, in order to establish that the high $^3He/^4He$ measured in old volcanic rocks is a magmatic signal, it is necessary to rule out the possibility that cosmogenic or nucleogenic ^3He production could have affected the $^3He/^4He$ values.

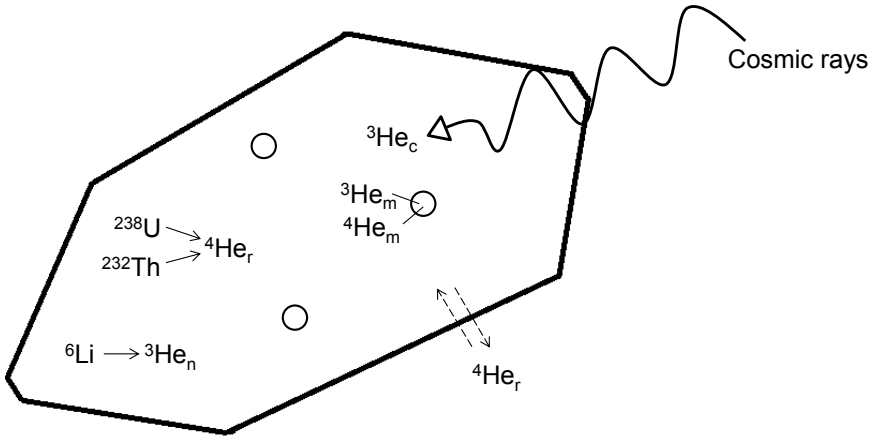

Figure 4.9: Different sources of helium in an olivine phenocryst exposed on the surface of the Earth to cosmic rays. ^3He_m = magmatic ^3He, ^4He_m = magmatic ^4He, ^3He_c = cosmogenic ^3He, ^3He_n = nucleogenic ^3He, ^4He_r = radiogenic ^4He. Modified from Blard and Farley (2008).

Figure 4.9 illustrates the potential sources of He to an olivine phenocryst in a volcanic rock exposed at the Earth's surface. Nucleogenic ^3He can be produced in olivine by thermal neutron capture of ^6Li (Aldrich and Nier, 1948), however, this has been shown not to be an important process in early NAIP basalts (Graham et al., 1998; Marty et al., 1998; Stuart et al., 2000). For example, Stuart et al. (2000) showed that for an olivine from a Skye basalt with a typical Li content of $<$2 ppm, the amount of ^3He produced would be over 20 times less than that released by crush extraction, and so is not considered to contribute to the high $^3He/^4He$ ratios.

Cosmogenic He (ca. 71,500 R/R_a) is produced by spallation reactions where cosmic rays interact with the nuclei of Si, O and Mg in rocks exposed on the

Earth's surface (Kurz, 1986). The BTIP samples from this study are exposed on the surface and therefore have potentially accumulated cosmogenic He. The Skye samples outcrop on a glacially smoothed slab in Coire Lagan. The corrie was occupied by a glacier during the Yonger Dryas glacial event (Sissons, 1977). This event was abruptly terminated at 10.7 kya (Dansgaard et al., 1989). The Mull samples were last covered by ice during the Late Devensian glacial event, the maximum of which occurred around 22 ka (Bowen et al., 1988), although the ice sheets did not retreat until later, e.g. the ice had not retreated from northern Skye until 17.5 kya (Stone et al., 1998).

For basalts from northern Skye, Stuart et al. (2000) estimated that around 7 times the amount of ^{3}He released from crushing of olivines could be produced by exposure to cosmic rays over 17.5 kyr, and could therefore account for high ^{3}He/^{4}He if the cosmogenic helium had diffused into the vapour inclusions. A similar amount of cosmogenic ^{3}He as that in the northern Skye basalts has potentially been produced in the Mull samples, and slightly less for the Skye picrites from this study, since they have been exposed at the surface for less time. However, there is presently no evidence that cosmogenic He is released from old or young minerals unless the mineral is subjected to extreme crushing (Hilton et al., 1993). For example, no measurable cosmogenic ^{3}He was detected after *in vacuo* crushing of olivine phenocrysts with over 180 kyr of exposure to cosmic rays (Harrop, 1996). The crystal lattice is the most likely location for cosmogenic He, and Stuart et al. (2000) measured the ^{3}He/^{4}He of fused olivine powder post crushing (i.e. He stored in the crystal lattice) in their high ^{3}He/^{4}He (18.4 R/R_a) sample that had been exposed for 17.5 ky. A ratio of 0.82 R/R_a was measured, an order of magnitude lower than predicted for cosmic ray exposure for 17.5 kyr. Therefore, cosmogenic helium was not present in significant amounts, and the *in vacuo* crush extraction could not have been compromised by cosmogenic ^{3}He contribution. ^{3}He/^{4}He values presented in this study are therefore not considered to have been contaminated with cosmogenic He.

The low R/R_a of olivine powders from crushing (e.g. Graham et al., 1998; Stuart et al., 2000, 2003) indicates that radiogenic He ingrowth from decay of U and Th dominates the olivine lattice. The highest ^{3}He/^{4}He values presented here should therefore be considered a minimum due to the possibility for diffusion of radiogenic He into melt inclusions. Additionally, preferential diffusional loss of

magmatic ^{3}He and assimilation of melts with radiogenic He-bearing continental crust during their ascent will only serve to lower the ^{3}He/^{4}He of olivines since crystallisation.

4.4 Synthesis

4.4.1 NAIP helium isotopes and temperature

A plot of Al-in-olivine temperature vs ^{3}He/^{4}He for picrites across the NAIP is shown in Figure 4.10. The maximum ^{3}He/^{4}He of the Baffin Island and West Greenland picrites is almost twice that found in the BTIP picrites, however the Al-in-olivine data indicate that the maximum temperature anomaly present across the province was uniform. This suggests that absolute temperature and ^{3}He/^{4}He in start-up plume heads are decoupled. In Iceland, the highest ^{3}He/^{4}He come from Tertiary rocks that record the lowest temperatures measured in this study. Clearly, high ^{3}He/^{4}He is not closely linked to absolute magmatic temperature. However, there is no need for ^{3}He/^{4}He to correlate with temperature other than in very general terms. Helium diffusivity in the mantle is estimated to be in the order of 10^{-10} m^2/s (Hart et al., 2008) whilst thermal diffusivity in the mantle is several orders of magnitude lower, estimated to be $\sim 10^{-6}$ m^2/s in Mg-perovskite (Osako and Ito, 1991) and around 10^{-7} m^2/s in upper mantle rocks (Gibert et al., 2003). Over a timescale of 10 million years, helium is therefore able to diffuse in the order of several 100 m, while heat can diffuse over 10-100s of kilometres. It is therefore possible for temperature and helium to become decoupled very quickly during the lifetime of the plume.

The preserved ^{3}He/^{4}He anomaly is greater at Baffin Island and West Greenland than at the BTIP. In order to determine why this is the case, it is necessary to consider the effects of contamination and degassing of magmatic He. At these locations, lavas were erupted onto Tertiary sediments through Precambrian basement, and so it is possible that they were contaminated with crustal material, however Starkey et al. (2009) ruled this out for the West Greenland and Baffin Island picrites. Ba/Zr of the BTIP picrites is plotted against MgO wt % in

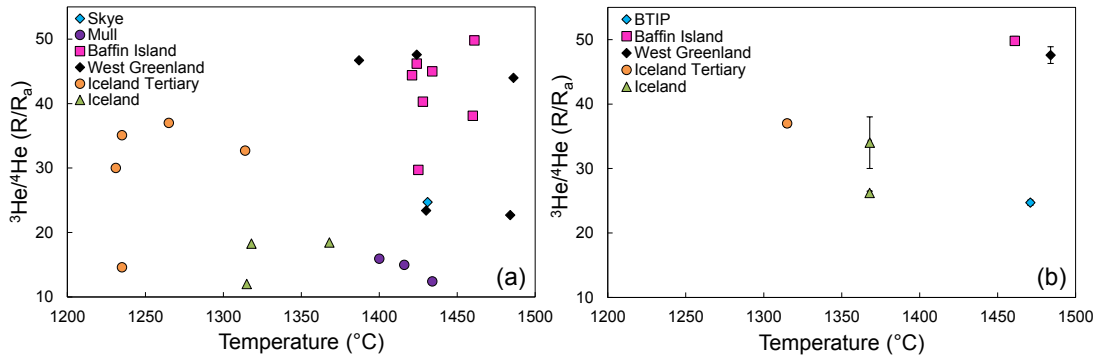

Figure 4.10: (a) Al-in-olivine temperature plotted against ^{3}He/^{4}He for all samples with both helium isotope and Al-in-olivine temperature data. (b) Maximum Al-in-olivine temperature plotted against maximum ^{3}He/^{4}He for the BTIP, Baffin Island, West Greenland, Tertiary Iceland and neovolcanic Iceland. The highest ^{3}He/^{4}He measured from the neovolcanic zones of Iceland is 34.3 R/R_a and has a high error of ± 4 R/R_a, and so the next highest value of 26.2 R/R_a is also shown.

Figure 4.11. The Lewisian crustal rocks forming the basement of NW Scotland are highly enriched in Ba with respect to Zr (Kerr et al., 1995) and so these ratios provide a useful index for crustal contamination. Kent and Fitton (2000) considered primitive BTIP lavas with Ba/Zr >2 to be contaminated. All of the BTIP picrites used in this study have Ba/Zr <2 (Figure 4.11), indicating that they have not been affected by crustal contamination and this therefore cannot explain the lower ^{3}He/^{4}He of BTIP lavas compared to Baffin Island and West Greenland. However, the very low ^{3}He/^{4}He of <8 R/R_a of four of the Skye picrites indicates that they have preferentially lost ^{3}He through degassing, which is in agreement with the observation that they contain the same amount of ^{4}He as the high ^{3}He/^{4}He sample (S8). It is not possible to determine how much ^{3}He S8 (which has an R/R_a of 24.7) has lost (if any), and so it cannot be proved beyond doubt that the BTIP really did have a much lower ^{3}He/^{4}He anomaly than at Baffin Island and West Greenland. On the other hand, it is worth noting that there are a very large number of Baffin Island and West Greenland picrites with ^{3}He/^{4}He above 30 R/R_a, and although this could be due to sampling bias, the lack of any samples from a variety of localities (Northern Ireland, Mull and two locations in Skye) in the BTIP with ^{3}He/^{4}He above 25 R/R_a does seem to suggest that the magnitude of the ^{3}He/^{4}He anomaly was not as great here as it was close to the early plume axis. The Baffin Island samples in particular have a much higher overall helium concentration compared to those of the BTIP (Figure 4.8) which also suggests a higher He contribution from the plume to those

areas close to the plume axis. This pattern in $^{3}He/^{4}He$ values is observed at present day Iceland (Figure 4.12) where the highest $^{3}He/^{4}He$ values are found closest to the current plume centre and in general, gradually decrease farther away (e.g. Kurz et al., 1985; Breddam et al., 2000; Hilton et al., 2000). On the other hand, helium concentrations generally decrease along the Reykjanes Ridge towards Iceland, however this has been attributed to low-pressure, pre-eruptive magmatic degassing due to shallow eruption depths (<1000 m) close to Iceland (Hilton et al., 2000).

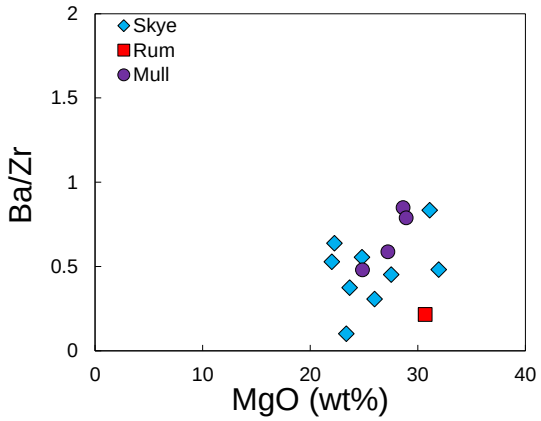

Figure 4.11: Ba/Zr of the BTIP picrites plotted against MgO wt %.

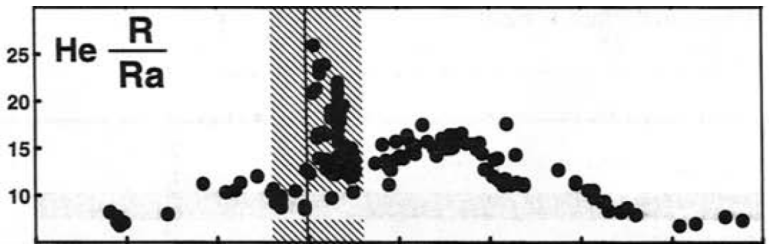

Figure 4.12: Variation in $^{3}He/^{4}He$ along the Mid-Atlantic spreading axis. The hatched shaded area represents the extent of Iceland. The horizontal bar represents the range of values found in N-MORB away from the influence of mantle plumes. From Taylor et al. (1997).

Although a relationship between absolute crystallisation temperature and $^{3}He/^{4}He$ is not apparent, in more general terms, basalts with high $^{3}He/^{4}He$ from the NAIP are more likely to have a depleted isotopic signature (low $^{87}Sr/^{86}Sr$, high $^{143}Nd/^{144}Nd$) (Stuart et al., 2003; Ellam and Stuart, 2004; Macpherson et al.,

2005a; Starkey et al., 2009). This suggests a general relationship between temperature and $^{3}He/^{4}He$. The highest temperature mantle in a mantle plume originates from the plume source (Griffiths and Campbell, 1990; Campbell, 2007), which has high $^{3}He/^{4}He$, and so is most likely to undergo large degrees of partial melting, producing high $^{3}He/^{4}He$ basalts that heavily sample the depleted mantle source. This explains why most of the high $^{3}He/^{4}He$ basalts in the NAIP have depleted geochemical signatures. There are multiple exceptions to this rule however, and $^{3}He/^{4}He$ has not been found to correlate with any mantle isotopic or geochemical tracer. For example, Starkey et al. (2009) found several Baffin Island and West Greenland picrites to have $^{3}He/^{4}He$ of >40 R/R_a, but have enriched isotopic signatures (high $^{87}Sr/^{86}Sr$, low $^{143}Nd/^{144}Nd$). During mantle melting, the enriched basalts represent the highest pressure, lowest degrees of melting. These melts can also carry the high $^{3}He/^{4}He$ signature if their source mantle originates from the plume source, however they are less likely to reach the surface. Therefore, while $^{3}He/^{4}He$ is decoupled from any other mantle isotopic or geochemical tracer, high $^{3}He/^{4}He$ is generally associated with depleted basalts because these are most likely to be formed by large-degree melting at shallow levels of hot material originating from the plume source.

4.4.2 Mantle plumes and origin of the high $^{3}He/^{4}He$ reservoir

The apparent decoupling of $^{3}He/^{4}He$ from any other mantle tracer is consistent with the idea that the high $^{3}He/^{4}He$ reservoir is not within the mantle and is diffused in from a discrete source. The fact that the highest $^{3}He/^{4}He$ on Earth are associated with a major mantle plume suggests that the reservoir is a deep layer beneath the mantle, which is supported by recent whole-mantle seismic imaging that indicates that plumes (including the Iceland plume) extend to the base of the lower mantle (French and Romanowicz, 2015). Consequently, the core-mantle boundary (CMB) (Samuel and Farnetani, 2003) or the core (Porcelli and Halliday, 2001) are the most likely candidates for the location of the high $^{3}He/^{4}He$ reservoir.

A convectively isolated layer, enriched in primordial volatiles with a high time-

integrated ^{3}He(U+Th) at the CMB is a possibility. It has been suggested that primordial volatiles may have come from subducted meteoritic material early in Earth's history (Tolstikhin and Hofmann, 2005), however likely loss of He during subduction poses some problems for this model (Hiyagon, 1994). Alternatively, it has been suggested that cumulates from a crystallizing early magma ocean may sink to produce a volatile-rich reservoir (Labrosse et al., 2007).

It has often been assumed that the partitioning of helium into liquid metal is negligible (e.g. Matsuda et al., 1993), and so the core has often been overlooked as a location for the high ^{3}He/^{4}He reservoir. However, a recent experimental study based on helium partitioning between silicate melts and iron-rich liquids has shown this is not the case, and that significant quantities of He may reside in the core (Bouhifd et al., 2013b). The early core likely formed with a high He/U ratio because U is a highly lithophile element and does not appear to partition into the metal phase (Wheeler et al., 2006; Bouhifd et al., 2013a), hence it is possible that the core has retained a high ^{3}He/^{4}He signature since its formation. Several studies have investigated the core as a potential source of high ^{3}He/^{4}He material. Brandon et al. (1999) argued that Os isotopes from Hawaiian basalts provide evidence of the addition of core material, however this is not supported by W isotope anomalies (Scherstén et al., 2004). Os isotopes in high ^{3}He/^{4}He basalts from Iceland (Brandon et al., 2007) and the near-chondritic Os isotope ratios of the Baffin Island and West Greenland basalts (Dale et al., 2009) do not indicate a contribution of core material. Therefore, if the core is the source of ^{3}He, then He must be diffused across the CMB into the base of the mantle, and be decoupled from any other element transfer.

Overall, it appears that the high ^{3}He/^{4}He signature of the NAIP has decreased through time (Figure 4.13). ^{3}He/^{4}He up to 50 R/R_a is detected in the earliest NAIP lavas (Stuart et al., 2003; Starkey et al., 2009). ^{3}He/^{4}He up to 37 R/R_a is found in 13-14 Ma Iceland picrites (Ellam and Stuart, 2004). The highest ^{3}He/^{4}He detected from the neovolcanic zones of Iceland is 34.3 R/R_a (Macpherson et al., 2005a) however this has a high error (± 4 R/R_a) and is much higher than the next highest values which tend to converge around 26 R/R_a (e.g. Kurz et al., 1985). In order to explain these observations, I suggest a scenario where helium with a high ^{3}He/^{4}He signature is slowly diffused into the lower mantle from the core or the CMB and over millions of years, a high ^{3}He/^{4}He signature is built

up. The helium diffuses into all mantle compositions that are present at the base of the mantle, whether depleted or enriched. A start-up plume rising from the base of the lower mantle samples the heterogeneous mantle with its inherited high ^{3}He/^{4}He signature.

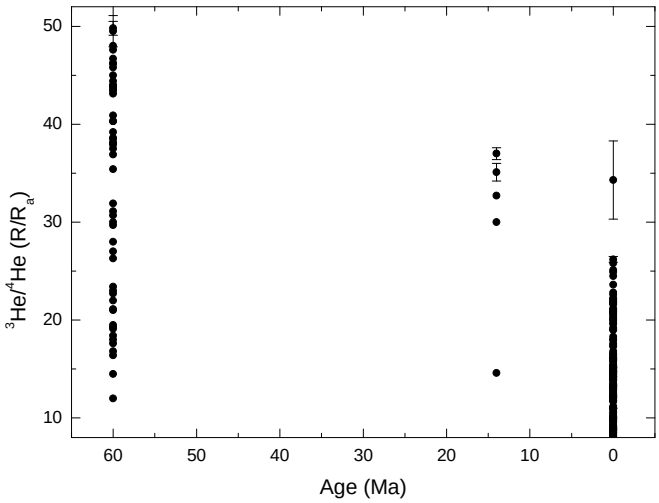

Figure 4.13: ^{3}He/^{4}He through time for the NAIP

Over a timescale of 10 million years, helium can only diffuse by a few 100 m in the mantle. Since the high ^{3}He/^{4}He anomaly associated with the Iceland plume is currently in the order of several 100 km, this suggests that the decreasing ^{3}He/^{4}He signature of the NAIP through time is not due to diffusion of helium with a lower R/R_a from the surrounding ambient mantle. Instead, the low helium diffusion rate means that the helium from the high ^{3}He/^{4}He reservoir cannot diffuse into the lower mantle plume source fast enough to replenish that removed by the plume. Over time, fluctuations in the mantle plume temperature can occur, however the ^{3}He/^{4}He signature of the plume gradually decreases. While high temperature plume-related provinces are generally associated with high ^{3}He/^{4}He, this is because they originate from the same location at the base of the mantle and the relationship need not go further.

On this basis, low ^{3}He/^{4}He plumes may be expected to originate from a shallower level in the mantle, such as the 670 km discontinuity. Recent whole-mantle seismic imaging suggests that many plumes extend to the CMB including those with low ^{3}He/^{4}He signatures (French and Romanowicz, 2015). The plumes that are imaged

to the CMB by French and Romanowicz (2015) and their maximum $^3He/^4He$ values are presented in Table 4.2. All of the plumes can be classed as high $^3He/^4He$ plumes (i.e. they have maximum $^3He/^4He$ values above that of MORB values) with the exception of the Canary, Comores, St Helenna, Tristan and Kerguelen plumes. The maximum $^3He/^4He$ values of basalts from Comores, St Helena, Tristan and Kerguelen are below that of MORB, and so it can be argued that these magmas are degassed and have lost their original magmatic $^3He/^4He$ signature (e.g. Murphy et al., 2005). However, Canary Island lavas have $^3He/^4He$ values that span the MORB range and so may not be degassed. Instead, the low $^3He/^4He$ signature could be due to a lack of high $^3He/^4He$ material at the plume source because helium has not been diffused into the base of the lower mantle at this location. The exact mechanism of helium diffusion at the base of the mantle is unknown, and so it is unclear why this might happen. Alternatively, the whole-mantle seismic imaging models produced by French and Romanowicz (2015) show ponding of low-velocity material beneath the Canary Islands at a depth of 1000 km (Figure 4.14), and so material from the high $^3He/^4He$ plume source may simply not reach the melting zone in the upper mantle because it has been trapped at depth.

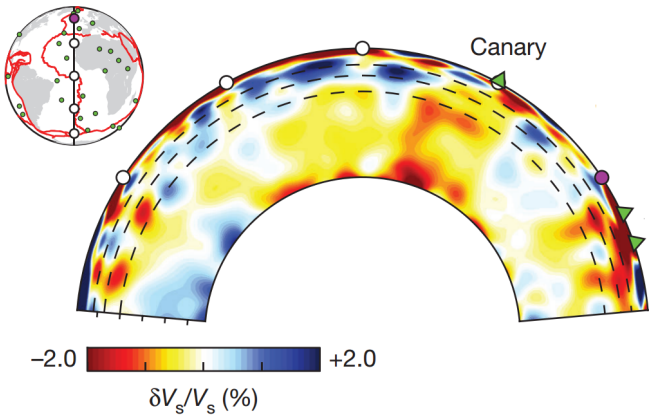

Figure 4.14: Whole-mantle depth cross-section of the mantle beneath the Canary Islands of relative shear velocity variations from the seismic imaging models of French and Romanowicz (2015). The model shows ponding of low-velocity material beneath 1000 km.

Estimates of the temperature of the base of the lower mantle and the top of the inner core suggest that a high heat flow occurs at the CMB arising from a large difference in temperature of 500-1800℃ across a 200 km thermal boundary

Table 4.2: Plumes detected in the lower mantle extending to the CMB by French and Romanowicz (2015) and their maximum $^3He/^4He$ values.

Hotspot name	**Max 3He/4He**	**$^3He/^4He$**	**Data source**
Afar	15.0	High	Hilton et al. (2011)
Canary	9.5	Low	Abedini et al. (2006)
Cape Verde	15.7	High	Abedini et al. (2006)
Comores	7.9	Low	Class et al. (2005)
Hawaii	31.9	High	Abedini et al. (2006)
Iceland	34.3	High	Abedini et al. (2006)
Macdonald	16.0	High	Moreira and Allegre (2004)
Marsqueses	11.8	High	Castillo et al. (2004)
Pitcairn	10.0	High	Abedini et al. (2006)
Samoa	34.0	High	Abedini et al. (2006)
Tahiti/Society	11.3	High	Abedini et al. (2006)
Caroline	no data available	?	
Easter	11.7	High	Poreda et al. (1993)
Galapagos	27.4	High	Abedini et al. (2006)
Louisville	no data available	?	
Reunion	14.3	High	Abedini et al. (2006)
St Helena	7.1	Low	Graham et al. (1992)
Tristan	6.3	Low	Abedini et al. (2006)
Kerguelen	6.2	Low	Abedini et al. (2006)

(Lay et al., 2008). This region is considered to be unstable (Campbell, 2007; Lay et al., 2008) and seismological, geodynamical and mineral physics observations suggest that it is chemically heterogeneous (Lay et al., 2008). Heat conducts non-uniformly across the CMB and is considered to vary both spatially and temporally in response to a variety of mantle processes (Lay et al., 2008; Zhang and Zhong, 2011; Biggin et al., 2012). Subduction is thought to increase CMB heat flow as downgoing slabs displace material ahead of them, resulting in the thinning of the thermal boundary layer (Steinberger and Torsvik, 2012). Accumulation of slabs in the transition zone followed by slab avalanche events (Machetel and Thomassot, 2002) could further enhance variations in CMB heat flow (Olson et al., 2013). It has even been suggested that CMB heat flow changes in response to plate tectonics and supercontinent cycles. On the basis of mantle convection and heat flux models, Zhang and Zhong (2011) argue that the relatively low CMB heat flux following the assembly of Pangea may be due to reduced subduction at this time and that the subsequent increase in heat flux at ∼240 Ma is explicable by enhanced subduction associated with the opening of the Tethys Ocean. Deep mantle plumes can also affect the local CMB heat flow as they remove hot material from the thermal boundary layer (Lay et al., 2008). Large thermochemical piles (piles of hot, dense material at the base of the mantle), possibly enriched in radiogenic material beneath Africa and the Pacific tend to insulate the core (Zhang and Zhong, 2011), and it is thought that the morphology and location of these piles oscillate in response to changes in the convective structure of the surrounding mantle (Yang and Fu, 2014). In addition, true polar wander (rotation of the Earth in respect to its spin axis in response to mantle density anomalies caused by convection) can result in a change of pattern of heat flow across the CMB.

The above processes are all interrelated elements of mantle convection (Tan et al., 2002; Steinberger and Torsvik, 2010, 2012), and given the ever-changing nature of plate tectonics and mantle processes, it is unsurprising that the heat flow at the CMB has been subject to large variations through time. If mantle plumes originate at the CMB as has been advocated here and by others (e.g. French and Romanowicz, 2015), it follows logically that the long-term fluctuations in the temperature of the Iceland plume measured here by Al-in-olivine thermometry reflect the temporal variations of heat flow at the CMB. In this case, the tem-

perature of the Iceland plume would be intricately linked to plate tectonics and mantle convection since these control the heat flux at the CMB. In this study, the difference between the maximum Phase 1 and Iceland Tertiary picrite T_{Al} (these samples represent the hottest and coolest periods respectively in the plume's history as measured by Al-in-olivine thermometry in this study) is ~180°C. Since even small changes in mantle potential temperature can dramatically influence mantle melting (e.g. White and Lovell (1997) argued that an increase of 50°C would result in a 50% increase in the volume of basaltic crust generated at mid-ocean spreading ridges), changes in heat flux at the CMB, and therefore the global processes involved in mantle convection, exert an important control on melting dynamics at plume locations.

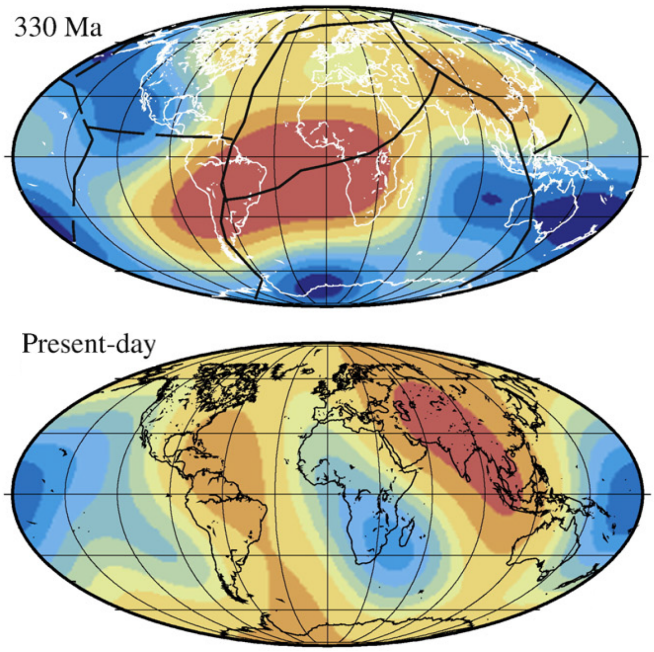

Figure 4.15: Snapshot of the CMB heat flux at 330 Ma and the present day produced by three-dimensional spherical models of mantle convection by Zhang and Zhong (2011). Blue areas represent areas of CMB heat flux whereas red areas represent areas of high heat flux. The locations of high and low CMB heat flux have changed dramatically through time.

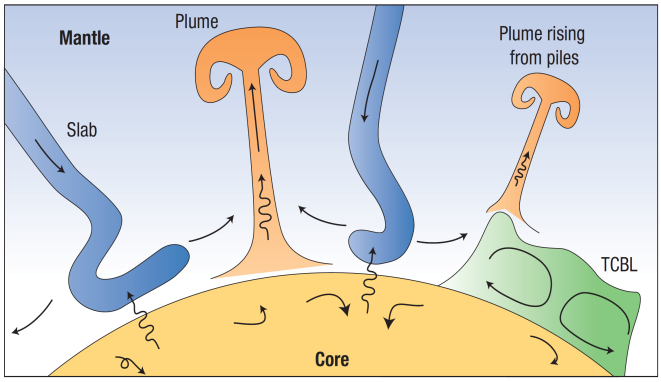

Figure 4.16: Heat flow components in the deep mantle that lead to non-uniform heat flow at the CMB. High heat flux occurs beneath cool, subducted slabs. Heat is lost when a buoyant plume rises through the mantle. A dense thermochemical boundary layer (TCBL) is swept into piles by mantle convection and may concentrate radiogenic heating, resulting in insulation of the core. These piles are thought to change in shape and location through time. From (Lay et al., 2008).

5 Conclusions and future work

5.1 Conclusions

The main purpose of this study was to investigate the relationship between temperature, ^{3}He/^{4}He and mantle melting dynamics within the NAIP, which is unique in the fact that it is the surface expression of a major mantle plume with a complete magmatic history. In order to achieve this, a suite of picrites and primitive basalts spanning the spatial and temporal range of the NAIP were examined. Each suite represents the most primitive, Mg-rich samples that are known from each location and are therefore most likely to be close in composition to primary mantle melts and record the highest temperatures. The suite comprises Phase 1 ($\sim$62-58 Ma) picrites from Skye, Mull, Rum, Baffin Island and West Greenland, which represent the earliest products of NAIP volcanism and the early plume-head stage of volcanic activity. The Baffin Island and West Greenland samples have the highest ^{3}He/^{4}He yet found in volcanic rocks on Earth, up to 50 R/R_a. A suite of picrites with ^{3}He/^{4}He up to 37 R/R_a representing some of the oldest rocks on Iceland (13-14 Ma) and zero-age picrites and primitive basalts from the active neovolcanic zones of Iceland were also included.

The magmatic temperature of the samples was determined using three different methods, the traditional method of olivine-melt thermometry of Putirka et al. (2007), which estimates the temperature at which olivine equilibrated with melt (T_{OL}), PRIMELT3 (Herzberg and Asimow, 2015), which is a forward mantle melting model and also calculates T_{OL}, and the newly developed Al-in-olivine thermometer (Wan et al., 2008; Coogan et al., 2014), which calculates the temperature of Al exchange between equilibrium olivine and Cr-spinel pairs (T_{Al}). This study is the first work to compare all three techniques in detail. PRIMELT3 filters for processes in the melt system that may result in an overestimation of primary melt MgO, and hence, T_{OL}. Only six of the thirty six NAIP sam-

ples were not filtered, suggesting that processes that increase the primary melt MgO such as advanced fractional melting and high-pressure augite fractionation are actually commonplace during mantle melting. PRIMELT3 is therefore not universally applicable to primitive basalts. This also poses a problem for olivine-melt thermometry as it is dependent on an estimate of the MgO content of the primary magma, and hence will lead to an overestimate in T_{OL}. For the six samples that were not filtered by PRIMELT3, there is a large discrepancy between the calculated temperatures using olivine-melt thermometry and the Al-in-olivine thermometer. The olivine-melt thermometry T_{OL} results are up to 183℃ higher than T_{Al}. To address this problem, olivine-melt thermometry was carried out on the melting experiments performed by Wan et al. (2008) as these experiments were done at a known pressure and temperature. It was found that olivine-melt thermometry overestimated the temperature by around 50℃ in experiments run at or above 1350℃, which is likely to be due to an inaccuracy in the calibration of the Putirka et al. (2007) olivine-melt thermometer. Olivine-melt thermometry requires assumptions to be made about the melting conditions, and an estimate of the pressure of olivine-melt equilibrium is particularly important, because it controls the value of $K_D(\text{Fe-Mg})^{ol-liq}$, the olivine-melt Fe-Mg exchange coefficient. In the olivine-melt thermometry calculations, an olivine-melt equilibrium pressure of 3 GPa was assumed on the basis of work from previous studies. However, it was found that T_{OL} becomes comparable with T_{Al} when the 50℃ overestimate of the Putirka et al. (2007) thermometer is combined with a decrease in olivine-melt equilibrium pressure of 1-2 GPa.

On the basis of these results, the Al-in-olivine thermometer appears to be the far more robust technique for calculating crystallisation temperatures and is likely to become the method of choice for petrographic temperature estimation of primitive rocks in the future. It can be applied universally to primitive rocks and is free of many of the problems associated with traditional olivine-melt thermometry as it appears to be unaffected by pressure changes within the upper mantle range and is not dependent on an estimate of the primary magma composition which can be affected by a variety of processes within the melt system.

The results from the Al-in-olivine thermometer calculations indicate that the temperature of the mantle plume now underlying Iceland has fluctuated on a timescale of 10^7 years, which has had profound effects on the melting dynam-

ics and seafloor topography of the region. The early stage of volcanic activity associated with the arrival of the ancestral Iceland plume head resulted in a uniform temperature anomaly across an area 2000 km in diameter, with T_{Al} of early NAIP picrites 250-300℃ above that of average MORB. The temperature of the plume head then began to cool, however it was still high enough for thick oceanic crust without fracture zones to be produced across the entire North Atlantic Ocean basin when sea-floor spreading began between Greenland and NW Europe at 55 Ma. The plume continued to cool until 40-35 Ma, resulting in the rapid northwards migration of the smooth-to-rough oceanic crust boundary, and a large decrease in the volume of magmatic flux produced, which resulted in the narrowing of the Greenland-Iceland-Faeroe Ridge hotspot trail and a dramatic decrease in the thickness of oceanic crust generated across the region. The subsequent increase in temperature since 40-35 Ma has resulted in higher melt production, causing a significant expansion in the size of the Greenland-Iceland-Faeroe Ridge into a large oceanic basalt plateau, the subaerial extent of which, represents Iceland. The Al-in-olivine data indicate that there has been a 50℃ increase in the temperature of the plume since 13-14 Ma. The increasing temperature of the plume has also resulted in the gradual migration southwards of the smooth-to-rough oceanic crust boundary away from Iceland and a change in the incompatible element composition of basalts erupted on the Reykjanes Ridge spreading axis.

An important feature of mantle plumes is their high $^{3}He/^{4}He$ signature. Much work has focussed on identifying the location of the high $^{3}He/^{4}He$ reservoir, however $^{3}He/^{4}He$ is not found to correlate with any mantle isotopic or geochemical tracer and so $^{3}He/^{4}He$ and its relationship with mantle plumes has remained enigmatic. One of the aims of this study was to identify whether a relationship between temperature and $^{3}He/^{4}He$ exists. Using the Al-in-olivine data, no clear relationship between $^{3}He/^{4}He$ and temperature is observable. It is noted, however, that the maximum $^{3}He/^{4}He$ of primitive basalts from the NAIP has decreased through time. On this basis, a model has been put forward where the location of the high $^{3}He/^{4}He$ reservoir is either the CMB or the core itself, which is supported by recent whole-mantle seismic imaging that shows the Iceland mantle plume extending to the base of the mantle (French and Romanowicz, 2015). It is proposed that $^{3}He/^{4}He$ is diffused into the base of the heterogeneous lower mantle

and is decoupled from any other element transfer. $^{3}He/^{4}He$ is incorporated into a plume when heated lower mantle breaks away and rises through the mantle. Over time, the $^{3}He/^{4}He$ source is gradually depleted, and because the diffusion of helium within the mantle is much slower than temperature, they become rapidly decoupled. The temperature of the plume can vary independently in response to changes in heat flow at the CMB, which is in turn related to changes in mantle convection. Global plate tectonics and mantle processes are therefore intricately linked with melting dynamics at hotspot locations and LIPs such as the NAIP.

5.2 Further work

In the NAIP picrites, the Al-in-olivine thermometer often records a substantial range in temperature within a single sample. I have argued that this reflects the decompression path of the melts where 'hotter' olivines represent those that crystallized at higher pressures when compared to the 'cooler' olivines. In theory, this hypothesis could be tested by studying the melt inclusions hosted in the respective olivines. Melting at high pressures will produce smaller degrees of melting compared to melts that are formed after substantial decompression to shallow levels. Therefore, melt inclusions trapped within the 'hot and deep' olivines should have a higher concentration of incompatible elements compared to melt inclusions trapped in 'cold and shallow' olivines that represent larger degree melts. The melt inclusions trapped within the 'hottest' olivines may also be close to the primary magma composition. If this is proven to be the case, crystallization depths could be estimated simply by applying a liquid adiabatic gradient between the hottest and coolest olivine crystals from within one sample/suite. The Al-in-olivine thermometer would then become a very powerful tool for petrologists as it would be possible to estimate both the mantle temperature (to within a few tens of degrees) and the depth of melting/crystallization, the latter of which often represents a large source of uncertainty in mantle melting models.

The Al-in-olivine thermometer has so far been applied only to a small number of samples from LIP settings. A valuable follow-up study would be to apply the Al-in-olivine thermometer to primitive samples associated with mantle plumes that have been studied by olivine-melt thermometry. In particular, it would be worth

using the Al-in-olivine thermometer to calculate the T_{Al} of the Hawaiian picrites used in the Putirka et al. (2007) study. Using olivine-melt thermometry, the Hawaiian picrites were calculated to have a T_{OL} of 1625℃, which corresponds to an extraordinarily high mantle Tp of 1720℃. The Hawaiian picrites were filtered by PRIMELT3 for high-pressure clinopyroxene fractionation, which is likely to have increased the MgO of the primary melt, and hence, enhanced the thermal anomaly calculated by olivine-melt thermometry. Application of Al-in-olivine thermometry could confirm that the T_{OL} at Hawaii calculated by Putirka et al. (2007) are too high. It would also be a worthwhile exercise to calculate the T_{Al} of ultra-magnesian olivines from the Etendeka Province of Namibia. Thompson and Gibson (2000) used olivine melt thermometry to infer a primary magma composition of 24 wt % and a mantle Tp of 1680℃. However, Keiding et al. (2011) noted that the melt inclusions of the ultra-magnesian olivines contained up to 17.5 wt % MgO, suggesting a much lower mantle Tp of 1520℃. In this case, Keiding et al. (2011) argue that the ultra-magnesian olivines were formed by advanced fractional melts. By applying the Al-in-olivine thermometer, it would be possible to determine which scenario is correct.

References

Abedini, A. A., Hurwitz, S., Evans, W. C., 2006. USGS-NoGaDat - a global dataset of noble gas concentrations and their isotopic ratios in volcanic systems. (US Geological Survey Digital Data Series, 202 (http://pubs.usgs.gov/ds/2006/202).

Agee, C. B., 1992. Isothermal compression of molten Fe_2SiO_4. Geophysical Research Letters 19, 1169–1172.

Ahern, J. L., Turcotte, D., 1979. Magma migration beneath an ocean ridge. Earth and Planetary Science Letters 45, 115–122.

Albarède, F., Luais, B., Fitton, J. G., Semet, M., Kaminski, E., Upton, B. G. J., Bachèlery, P., Cheminée, J.-L., 1997. The geochemical regimes of Piton de la Fournaise volcano (Réunion) during the last 530000 years. Journal of Petrology 38, 171–201.

Aldrich, L. T., Nier, A. O., 1948. The occurrence of ^{3}He in natural sources of helium. Physical Review 74, 1590–1594.

Allwardt, J. R., Stebbins, J. F., Terasaki, H., Du, L., Frost, D. J., Withers, A. C., Hirschmann, M. M., Suzuki, A., E., O., 2007. Effect of structural transitions on properties of high-pressure silicate melts: ^{27}Al NMR, glass densities, and melt viscosities. American Mineralogist 92, 1093–1104.

Bailey, E. B., Clough, C. T., Wright, W. B., 1924. Tertiary and Post-Tertiary Geology of Mull, Loch Aline and Oban. In: T. V. V. G. G. G. R. K. Murty. and S. S. Roa (Ed.), Memoir of the Geological Survey of Great Britain. HMSO, London.

Baker, M. B., Alves, S., Stolper, E., 1996. Petrography and petrology of the Hawaii Scientific Drilling Project lavas: Inferences from olivine phenocryst abundances and compositions. Journal of Geophysical Research: Solid Earth 101, 11715–11727.

Baratoux, D., Toplis, M. J., Monnereau, M., Gasnault, O., 2011. Thermal history of Mars inferred from orbital geochemistry of volcanic provinces. Nature 472, 338–342.

Barrat, J., Badro, J., Gillet, P., 1997. A strong to fragile transition in a model of liquid silica. Molecular Simulation 20, 17–25.

Bauccio, M., 1993. ASM Metals Reference Book. ASM International.

Bauchy, M., Guillot, B., Micoulaut, M., Sator, N., 2013. Viscosity and viscosity anomalies of model silicates and magmas: A numerical investigation. Chemical Geology 346, 47–56.

Beattie, P., 1993. Olivine-melt and orthopyroxene-melt equilibria. Contributions to Mineralogy and Petrology 115, 103–111.

Bell, B. R., Williamson, I. T., 1994. Picritic basalts from the Palaeocene lava field of west-central Skye, Scotland; evidence for parental magma compositions. Mineralogical Magazine 58, 347–356.

Bell, D. R., Rossman, G. R., 1992. Water in Earth's mantle: The role of nominally anhydrous minerals. Science 255, 1391–1397.

Biggin, A. J., Steinberger, B., Aubert, J., Suttie, N., Torsvik, T. H., van der Meer, D. G., van Hinsbergen, D. J. J., 2012. Possible links between long-term geomagnetic variations and whole-mantle convection processes. Nature Geoscience 5, 526–533.

Birch, F., 1952. Elasticity and constitution of the Earth's interior. Journal of Geophysical Research 57, 227–286.

Blard, P. H., Farley, K. A., 2008. The influence of radiogenic ^{4}He on cosmogenic ^{3}He determinations in volcanic olivine and pyroxene. Earth and Planetary Science Letters 276, 20–29.

Boehler, R., 1993. Temperatures in the Earth's core from melting-point measurements of iron at high static pressures. Nature 363, 534–536.

Bouhifd, M. A., Andrault, D., Bolfan-Casanova, N., Hammouda, T., Devidal, J. L., 2013a. Metal-silicate partitioning of Pb and U: Effects of metal composition and oxygen fugacity. Geochimica et Cosmochimica Acta 114, 13–28.

Bouhifd, M. A., Jephcoat, A. P., Heber, V. S., Kelley, S. P., 2013b. Helium in the Earth's early core. Nature Geoscience 6, 982–986.

Bowen, D. Q., Sykes, G. A., Turner, C., 1988. Correlation of marine events and glaciations on the northeast Atlantic margin. Philosophical Transactions of the Royal Society of London B 318, 619–635.

Brandon, A. D., Graham, D. W., Waight, T., Gautason, B., 2007. ^{186}Os and ^{187}Os enrichments and high-^{3}He/^{4}He sources in the Earth's mantle: Evidence from Icelandic picrites. Geochimica et Cosmochimica Acta 71, 4570–4591.

Brandon, A. D., Norman, M. D., Walker, R. J., Morgan, J. W., 1999. ^{186}Os-^{187}Os systematics of Hawaiian picrites. Earth and Planetary Science Letters 174, 25–42.

Brearley, M., Dickinson, J. E., Scarfe, C., 1986. Pressure dependence of melt viscosities on the join diopside-albite. Geochimica et Cosmochimica Acta 50, 2563–2570.

Breddam, K., Kurz, M. D., Storey, M., 2000. Mapping out the conduit of the Iceland mantle plume with helium isotopes. Earth and Planetary Science Letters 176, 45–55.

Brodie, J., White, N., 1994. Sedimentary basin inversion caused by igneous underplating: Northwest European continental shelf. Geology 22, 147–150.

Brodie, J. A., Fitton, J. G., 1998. Composition of basaltic lavas from the seaward-dipping reflector sequence recovered during DSDP Leg 81. In: Saunders, A. D., Larsen, H. C., Wise, S., Allen, J. R. (Eds.), Proceedings of the Ocean Drilling Program, Scientific Results. Vol. 152. pp. 431–435.

Brooks, C. K., 1973. Rifting and doming in southern east Greenland. Nature 244, 23–25.

Brooks, C. K., Nielsen, T. F. D., 1982. The E Greenland continental margin: a transition between oceanic and continental magmatism. Journal of the Geological Society 139, 265–275.

Brown, J. W., White, R. S., 1994. Variation with spreading rate of oceanic crustal thickness and geochemistry. Earth and Planetary Science Letters 121, 435–449.

Bunch, A. W. H., Kennet, B. L. N., 1980. The crustal structure of the Reykjanes Ridge at 59°N 30'N. Geophysical Journal International 61, 141–166.

Cahill, J. T. S., Lucey, P. G., Wieczorek, M. A., 2009. Compositional variations of the lunar crust: results from radiative transfer modeling of central peak spectra. Journal of Geophysical Research 114, E09001.

Campbell, I. H., 2007. Testing the plume theory. Chemical Geology 241, 153–176.

Castillo, P. R., Scarsi, P., Craig, H., 2004. He, Sr, Nd, and Pb isotopic constraints on the origin of the Marquesas and other linear volcanic chains. Chemical Geology 240, 205–221.

Chambers, J. E., 2004. Planetary accretion in the inner Solar System. Earth and Planetary Science Letters 223, 241–252.

Chambers, L. M., Fitton, J. G., 2000. Geochemical transitions in the ancestral Iceland plume: evidence from the Isle of Mull Tertiary volcano, Scotland. Journal of the Geological Society 157, 261–263.

Chambers, L. M., Pringle, M. S., 2001. Age and duration of activity at the Isle of Mull Tertiary igneous centre, Scotland, and confirmation of the existence of subchrons during Anomaly 26r. Earth and Planetary Science Letters 193, 333–345.

Christie, D. M., Carmichael, I. S. E., Langmuir, C. H., 1986. Oxidation states of mid-ocean ridge basalt glasses. Earth and Planetary Science Letters 79, 397–411.

Clague, D. A., Weber, W. S., Dixon, J. E., 1991. Picritic glasses from Hawaii. Nature 353, 553–556.

Clarke, D. B., Pedersen, A. K., 1976. Tertiary volcanic province of Baffin Bay. In: Escher, A., Watts, W. S. (Eds.), Geology of Greenland. Geological Survey of Greenland, pp. 365–385.

Class, C., Goldstein, S. L., 2005. Evolution of helium isotopes in the Earth's mantle. Nature 436, 1107–1112.

Class, C., Goldstein, S. L., Stute, M., Kurz, M. D., Schlosser, P., 2005. Grand Comore Island: A well-constrained "low 3He/4H" mantle plume. Earth and Planetary Science Letters 233, 391–409.

Clift, P. D., Turner, J., 1995. Dynamic support by the Iceland Plume and its effect on the subsidence of the northern Atlantic margins. Journal of the Geological Society of London 152, 935–941.

Coffin, M. F., Duncan, R. A., Eldholm, O., Fitton, J. G., Frey, F. A., Larsen, H. C., Mahoney, J. J., Saunders, A. D., Schlich, R., Wallace, P. J., 2001. Large igneous provinces and scientific ocean drilling: Status quo and a look ahead. Oceanography 19, 150–160.

Coffin, M. F., Eldholm, O., 1994. Large igneous provinces: Crustal structure, dimensions, and external consequences. Reviews of Geophysics 32, 1–36.

Condomines, M., Grönvold, K., Hooker, P. J., Muehlenbachs, K., O'Nions, R. K., Óskarsson, N., Oxburgh, E. R., 1983. Helium, oxygen, strontium and neodymium isotopic relationships in Icelandic volcanics. Earth and Planetary Science Letters 66, 125–136.

Coogan, L. A., Saunders, A. D., Wilson, R. N., 2014. Aluminium-in-olivine thermometry of primitive basalts: Evidence of an anomalously hot mantle source for large igneous provinces. Chemical Geology 368, 1–10.

Dale, C. W., Pearson, D. G., Starkey, N. A., Stuart, F. M., Ellam, R. M., Larsen, L. M., Fitton, J. G., Macpherson, C. G., 2009. Osmium isotopes in Baffin Island and West Greenland picrites: Implications for the $^{187}Os/^{188}Os$ composition of the convecting mantle and the nature of high $^{3}He/^{4}He$ mantle. Earth and Planetary Science Letters 278, 267–277.

Dam, G., Larsen, M., Sønderholm, M., 1998. Sedimentary response to mantle plumes: Implications from Paleocene onshore successions, West and East Greenland. Geology 26, 207–210.

Dansgaard, W., White, J. W. C., Johnsen, S. J., 1989. The abrupt termination of the Younger Dryas climate event. Nature 339, 532–534.

Darbyshire, F. A., Bjarnason, I., White, R. S., Flóvenz, Ó, G., 1998. Crustal structure above the iceland mantle plume imaged by the ICEMELT refraction profile. Geophysical Journal International 135, 1131–1149.

Dasgupta, R., Jackson, M., Lee, C. A., 2010. Major element chemistry of ocean island basalts - Conditions of mantle melting and heterogeneity of mantle source. Earth and Planetary Science Letters 289, 377–392.

Davaille, A., Jaupart, C., 1993. Thermal convection in lava lakes. Geophysical Research Letters 20, 1827–1830.

Davidson, J. P., Morgan, D. J., Charlier, B. L. A., Harlou, R., Hora, J. M., 2007. Microsampling and isotopic analysis of igneous rocks: Implications for the study of magmatic systems. Annual Review of Earth and Planetary Sciences 35, 273–311.

Davies, G., 1985. Heat deposition and retention in a solid planet growing by impacts. Icarus 63, 45–68.

De Hoog, J. C. M., Gall, L., Cornell, D. H., 2010. Trace-element geochemistry of mantle olivine and application to mantle petrogenesis and geothermobarometry. Chemical Geology 270, 196–215.

Debaille, V., Trønnes, R. G., Brandon, A. D., Wright, T. E., Graham, D. W., Lee, C. A., 2009. Primitive off-rift basalts from Iceland and Jan Mayen: Os-isotopic evidence for a mantle source containing enriched subcontinental lithosphere. Geochemica et Cosmochimica Acta 73, 3423–3449.

Deer, W. A., Howie, R. A., Zussman, J., 1997. Rock Forming Minerals: Orthosilicates, 2nd Edition. Geological Society of London.

Dickin, A. P., 1981. Isotope geochemistry of Tertiary igneous rocks from the Isle of Skye, N.W. Scotland. Journal of Petrology 22, 155–189.

Dixon, J. E., Leist, L., Langmuir, C., Schilling, J., 2002. Recycled dehydrated lithosphere observed in plume-influenced mid-ocean-ridge basalt. Nature 420, 385–389.

Dohmen, R., Chakraborty, S., 2007. Fe-Mg diffusion in olivine II: point defect chemistry, change of diffusion mechanisms and a model for calculation of diffusion coefficients in natural olivine. Physics of Chemistry and Minerals 34, 409–430.

Dosso, L., Bougault, H., Langmuir, C., Bollinger, C., Bonnier, O., Etoubleau, J., 1999. The age and distribution of mantle heterogeneity along the Mid-Atlantic Ridge ($31 - 41\,^{\circ}$N). Earth and Planetary Science Letters 170, 269–286.

Drever, H., Johnston, R., 1958. The petrology of picritic rocks in minor intrusions - a hebridean group. Transactions of the Royal Society of Edinburgh 63, 459–499.

Drewitt, J. W. E., Jahn, S., Sanloup, C., de Grouchy, C., Garbarino, G., Hennet, L., 2015. Development of chemical and topological structure in aluminosilicate liquids and glasses at high pressure. Journal of Physics: Condensed Matter 27, 105103.

Drewitt, J. W. E., Sanloup, C., Bytchkov, A., Brassamin, S., Hennet, L., 2013. Structure of $(Fe_xCa_{1-x}O)_y(SiO_2)_{1-y}$ liquids and glasses from high-energy x-ray diffraction: Implications for the structure of natural basaltic magmas. Physical Review B 87, 224201.

Elkins-Tanton, L. T., Parmentier, E. M., Hess, P. C., 2003. Magma ocean fractional crystallization and cumulate overturn in terrestrial planets: Implications for Mars. Meteoritics and Planetary Science 38, 1753–1771.

Ellam, R. M., Stuart, F. M., 2004. Coherent He-Nd-Sr isotope trends in high ^{3}He/^{4}He basalts: implications for a common reservoir, mantle heterogeneity and convection. Earth and Planetary Science Letters 228, 511–523.

Emeleus, C. H., 1991. Tertiary igneous activity. In: G. Y. Craig (Ed.), Geology of Scotland. Geological Society, pp. 455–502.

Emeleus, C. H., Bell, B. R., 2005. British Regional Geology: the Palaeogence volcanic districts of Scotland, 4th Edition. British Geological Survey, Nottingham.

Emeleus, C. H., Cheadle, M. J., Hunter, R. H., Upton, B. G. J., Wadsworth, W. J., 1996. The Rum Layered Suite. In: R. G. Cawthorn (Ed.), Layered Intrusions. Elsevier Science, B. V., pp. 403–439.

England, R. W., 1988. The early Tertiary stress regime in NW Britain: evidence from the patterns of volcanic activity. In: Early Tertiary Volcanism and the Opening of the NE Atlantic, Special Publication 39. Geological Society, pp. 381–389.

England, R. W., 1994. The structure of the Skye lava field. Scottish Journal of Geology 30, 33–37.

Ernst, R. E., 2014. Large Igneous Provinces. Cambridge University Press, Cambridge, UK.

Eysteinsson, H., Gunnarsson, K., 1995. Maps of gravity, bathymetry and magnetics for Iceland and surroundings. OS-95055/JHD-07. Orkustofnun, National Energy Authority, Geothermal Division, Reykjavik.

Falloon, T. J., Danyushevsky, L. V., Ariskin, A., Green, D. H., Ford, C. E., 2007a. The application of olivine geothermometry to infer crystallization temperatures of parental liquids: Implications for the temperature of MORB magmas. Chemical Geology 241, 207–233.

Falloon, T. J., Green, D. H., Danyushevsky, L. V., 2007b. Crystallization temperatures of tholeiite parental liquids: Implications for the existence of thermally driven mantle plumes. Geological Society of America Special Papers 430, 235–260.

Faxén, H., 1922. Der widerstand gegen die bewegung einer starren kugel in einer zähen flüssigkeit, die zwischen zwei parallelen ebenen wänden eingeschlossen ist. Annalen der Physik 373, 89–119.

Fiquet, G., Guyot, F., Badro, J., 2008. The Earth's lower mantle and core. Elements 4, 177–182.

Fitton, J. G., 2007. The OIB paradox. Geological Society of America Special Papers 430, 387–412.

Fitton, J. G., Godard, M., 2004. Origin and evolution of magmas on the Ontong Java Plateau. In: Fitton, J. G., Mahoney, J. J., Wallace, P. J., Saunders, A. D. (Eds.), Origin and Evolution of the Ontong Java Plateau, Geological Society Special Publications 229. pp. 151–178.

Fitton, J. G., Saunders, A. D., Kempton, P. D., Hardarson, B. S., 2003. Does depleted mantle form an intrinsic part of the Iceland plume? Geochemistry, Geophysics, Geosystems 4, 1032.

Fitton, J. G., Saunders, A. D., Larsen, H. C., Hardarson, B. S., Norry, M. J., 1998. Volcanic rocks from the southeast Greenland margin at 63 °N: composition, petrogenesis, and mantle sources. In: Saunders, A. D., Larsen, H. C., Wise, S., Allen, J. R. (Eds.), Proceedings of the Ocean Drilling Program, Scientific Results. Vol. 152. pp. 331–350.

Fitton, J. G., Saunders, A. D., Norry, M. J., Hardarson, B. S., Taylor, R. N., 1997. Thermal and chemical structure of the Iceland plume. Earth and Planetary Science Letters 153, 197–208.

Ford, C. E., Russell, D. G., Craven, J. A., Fisk, M. R., 1983. Olivine-liquid equilibria: Temperature, pressure and composition dependence of the crystal/liquid cation partition coefficients for Mg, Fe^{2+}, Ca and Mn. Journal of Petrology 24, 256–266.

Foulger, G. R., Anderson, D. L., 2005a. A cool model for the Iceland hotspot. Journal of Volcanology and Geothermal Research 141, 1–22.

Foulger, G. R., Natland, J. H., Anderson, D. L., 2005b. A source for Icelandic magmas in remelted Iapetus crust. Journal of Volcanology and Geothermal Research 141, 23–44.

Fowler, S. J., Bohrson, W. A., Spera, F. J., 2004. Magmatic evolution of the Skye Igneous Centre, Western Scotland: Modelling of assimilation, recharge and fractional crystallization. Journal of Petrology 45, 2481–2502.

Francis, D., 1985. The Baffin Bay lavas and the value of picrites as analogues of primary magmas. Contributions to Mineralogy and Petrology 89, 144–154.

French, S. W., Romanowicz, B., 2015. Broad plumes rooted at the base of the Earth's mantle beneath major hotspots. Nature 525, 95–99.

Ganerød, M., Smethurst, M. A., Torsvik, T. H., Prestvik, T., S. Rousse, S., McKenna, C., van Hinsbergen, D. J. J., Hendriks, B. W. H., 2010. The North Atlantic Igneous Province reconstructed and its relation to the Plume Generation Zone: the Antrim Lava Group revisited. Geophysical Journal International 182, 183–202.

Gariépy, C., Ludden, J., Brooks, C., 1983. Isotopic and trace element constraints on the genesis of the Faeroe lava pile. Earth and Planetary Science Letters 63, 257–272.

Ghosh, D., Karki, B., 2011. Diffusion and viscosity of Mg_2SiO_4 liquid at high pressure from first-principles simulations. Geochimica et Cosmochimica Acta 75, 4591–4600.

Gibert, B., Seipold, U., Tommasi, A., Mainprice, D., 2003. Thermal diffusivity of upper mantle rocks: Influence of temperature, pressure, and the deformation fabric. Journal of Geophysical Research 108, 2359.

Gill, R. C. O., Pedersen, A. K., Larsen, J. G., 1992. Tertiary picrites from West Greenland: melting at the periphery of a plume? In: B. C. Storey and T. Alabaster and R. J. Pankhurst (Ed.), Magmatism and the Causes of Continental Break-up, Special Publication 68. Geological Society, pp. 335–348.

Giordano, D., Russell, J. K., Dingwell, D. B., 2008. Viscosity of magmatic liquids: A model. Earth and Planetary Science Letters 271, 123–134.

Gonnermann, H. M., Mukhopadhyay, S., 2007. Non-equilibrium degassing and a primordial source for helium in ocean-island volcanism. Nature 449, 1037–1040.

Govindaraju, K., 1994. Compilation of working values and description for 383 geostandards. Geostandards Newsletter 18, 1–158.

Graham, D. W., Humphris, S. E., Jenkins, W. J., Kurz, M. D., 1992. Helium isotope geochemistry of some volcanic rocks from Saint Helena. Earth and Planetary Science Letters 110, 121–131.

Graham, D. W., Larsen, L. M., Hanan, B. B., Storey, M., Pedersen, A. K., Lupton, J. E., 1998. Helium isotope composition of the early Iceland mantle plume inferred from the Tertiary picrites of West Greenland. Earth and Planetary Science Letters 160, 241–255.

Green, D. H., Falloon, T, J., 2005. Primary magmas at mid-ocean ridges, “hotspots", and other intraplate settings: Constraints on mantle potential temperature. Geological Society of America Special Papers 288, 217–247.

Green, D. H., Falloon, T. J., Eggins, S. M., Yaxley, G. M., 2001. Primary magmas and mantle temperatures. European Journal of Mineralogy 13, 437–452.

Griffiths, R. W., Campbell, I. H., 1990. Stirring and structure in mantle starting plumes. Earth and Planetary Science Letters 99, 66–78.

Griffiths, R. W., Campbell, I. H., 1991a. Interaction of mantle plume heads with the Earth's surface and onset of small-scale convection. Journal of Geophysical Research: Solid Earth 96, 18295–18310.

Gubbins, D., Alfè, D., Masters, G., Price, G. D., Gillian, M. J., 2003. Can the Earth's dynamo run on heat alone? Geophysical Journal International 155, 609–622.

Haggerty, S. E., Baker, I., 1967. The alteration of olivine in basaltic and associated lavas. Contributions to Mineralogy and Petrology 16, 233–257.

Hamilton, M. A., Pearson, D. G., Thompson, R. N., Kelley, S. P., Emeleus, C. H., 1998. Rapid eruption of Skye lavas inferred from precise U-Pb and Ar-Ar dating of the Rum and Cuillin plutonic complexes. Nature 394, 260–263.

Hardarson, B. S., Fitton, J. G., Ellam, R. M., Pringle, M. S., 1997. Rift relocation - a geochemical and geochronological investigation of a palaeo-rift in northwest Iceland. Earth and Planetary Science Letters 153, 181–196.

Harrop, P. J., 1996. Dating recent surface processes using cosmic ray generated ^{3}He in rocks. Ph.D thesis, University of Manchester.

Hart, S. R., Hauri, E. H., Oschmann, L. A., Whitehead, J. A., 1992. Mantle plumes and entrainment: Isotopic evidence. Science 256, 517–520.

Hart, S. R., Kurz, M. D., Wang, Z., 2008. Scale length of mantle heterogeneities: Constraints from helium diffusion. Earth and Planetary Science Letters 269, 508–517.

Helz, R. T., Thornber, C. R., 1987. Geothermometry of Kilauea Iki lava lake, Hawaii. Bulletin of Volcanology 49, 651–668.

Hemond, C. Arndt, N. T. L. U., Hofmann, A. W., Oskarsson, N., Steinthorsson, S., 1993. The heterogeneous Iceland plume: Nd-Sr-O isotopes and trace element constraints. Journal of Geophysical Research: Solid Earth 98, 15833–15850.

Henstock, T. J., Woods, A. W., White, R. S., 1993. The accretion of oceanic crust by episodic sill intrusion. Journal of Geophysical Research: Solid Earth 98, 4143–4161.

Herd, C. D. K., Borg, L. E., Jones, J. H., Papike, J. J., 2002. Oxygen fugacity and geochemical variations in the martian basalts: implications for martian basalt petrogenesis and the oxidation state of the upper mantle of Mars. Geochimica et Cosmochimica Acta 66, 2025–2036.

Herzberg, C., 2011. Basalts as temperature probes of Earth's mantle. Geology 39, 1179–1180.

Herzberg, C., Asimow, P. D., 2008. Petrology of some oceanic island basalts: PRIMELT2.XLS software for primary magma calculation. Geochemistry, Geophysics, Geosystems 9, Q09001.

Herzberg, C., Asimow, P. D., 2015. PRIMELT3 MEGA.XLSM software for primary magma calculation: Peridotite primary magma MgO contents from the liquidus to the solidus. Geochemistry, Geophysics, Geosystems 16, 563–578.

Herzberg, C., Asimow, P. D., Arndt, N., Niu, Y., Lesher, C. M., Fitton, J. G., Cheadle, M. J., Saunders, A. D., 2007. Temperatures in ambient mantle and plumes: Constraints from basalts, picrites, and komatiites. Geochemistry, Geophysics, Geosystems 8, Q02006.

Herzberg, C., Gazel, E., 2009. Petrological evidence for secular cooling in mantle plumes. Nature 458, 619–622.

Herzberg, C., O'Hara, M. J., 1998. Phase equilibrium constraints on the origin of basalts, picrites, and komatiites. Earth-Science Reviews 44, 39–79.

Herzberg, C., O'Hara, M. J., 2002. Plume-associated ultramafic magmas of Phanerozoic age. Journal of Petrology 43, 1857–1883.

Hilton, D. R., Grönvold, K., O'Nions, R. K., Oxburgh, E. R., 1990. Regional distribution of ^{3}He anomalies in the Icelandic crust. Chemical Geology 88, 53–67.

Hilton, D. R., Halldorsson, S. A., Barry, P. H., Fischer, T. P., de Moor, J. M., Ramierz, C. J., Mangasini, F., Scarsi, P., 2011. Helium isotopes at Rungwe Volcanic Province, Tanzania, and the origin of East African Plateaux. Geophysical Research Letters 38, L21304.

Hilton, D. R., Hammerschmidt, K., Teufel, S., Friedrichsen, H., 1993. Helium isotope characteristics of Andean geothermal fluids and lavas. Earth and Planetary Science Letters 120, 265–282.

Hilton, D. R., Porcelli, D., 2003. Noble gases as mantle tracers. Treatise on Geochemistry 2, 1–42.

Hilton, D. R., Thirwall, M. F., Taylor, R. N., Murton, B. J., Nicols, A., 2000. Controls on magmatic degassing along the Reykjanes Ridge with implications for the helium paradox. Earth and Planetary Science Letters 183, 43–50.

Hiyagon, H., 1994. Retention of solar helium and neon in IDPs in deep sea sediment. Science 263, 1257–1259.

Ho, C., Taylor, R., 1998. Thermal Expansion of Solids. CINDAS data series on material properties. ASM International.

Hofmann, A. W., 1997. Mantle geochemistry: the message from oceanic volcanism. Nature 385, 219–229.

Hofmann, A. W., 2003. 2.03 - Sampling mantle heterogeneity through oceanic basalts: Isotopes and trace elements. In: Holland., H. D., Turekian, K. K. (Eds.), Treatise on Geochemistry. Pergamon, pp. 1–44.

Hole, M. J., Millet, J. M., Rogers, N. W., Jolley, D. W., 2015. Rifting and mafic magmatism in the Hebridean basins. Journal of the Geological Society 172, 218–236.

Holm, P. M., Gill, R. C. O., Pedersen, A. K., G., L. J., Hald, N., Nielsen, T. F. D., Thirlwall, M. F., 1993. The Tertiary picrites of West Greenland: contributions from 'Icelandic' and other sources. Earth and Planetary Science Letters 115, 227–244.

Holness, M. B., Hallworth, M. A., Woods, A., Sides, R. E., 2007b. Infiltration metasomatism of cumulates by intrusive magma replenishment: the wavy horizon, Isle of Rum, Scotland. Journal of Petrology 48, 563–587.

Holness, M. B., Nielsen, T. F. D., Tegner, C., 2007c. Textural maturity of cumulates: a record of chamber filling, liquidus assemblage, cooling rate and large-scale convection in mafic layered intrusions. Journal of Petrology 48, 141–157.

Ito, G., Mahoney, J. J., 2005a. Flow and melting of a heterogeneous mantle: 1. Method and importance to the geochemistry of ocean island and mid-ocean ridge basalts. Earth and Planetary Science Letters 230, 29–46.

Jackson, M. G., Kurz, M. D., Hart, S. R., Workman, R. K., 2007. New Samoan lavas from Ofu Island reveal a hemispherically heterogeneous high $^{3}He/^{4}He$ mantle. Earth and Planetary Science Letters 264, 260–374.

Jakobsson, S. P., 1972. Chemistry and distribution pattern of recent basaltic rocks in Iceland. Lithos 5, 365–386.

Jamtveit, B., Brooker, R., Brooks, K., Larsen, L. M., Pedersen, T., 2001. The water content of olivines from the North Atlantic Volcanic Province. Earth and Planetary Science Letters 186, 401–415.

Jones, S. M., 2003. Test of a ridge-plume interaction model using oceanic crustal structure around Iceland. Earth and Planetary Science Letters 208, 205–218.

Jones, S. M., Maclennan, J., 2005. Crustal flow beneath Iceland. Journal of Geophysical Research: Solid Earth 110, B09410.

Jones, S. M., Murton, B. J., Fitton, J. G., White, N. J., Maclennan, J., Walters, R. L., 2014. A joint geochemical-geophysical record of time-dependent mantle convection south of Iceland. Earth and Planetary Science Letters 386, 86–97.

Jones, S. M., White, N., Maclennan, J., 2002. V-shaped ridges around Iceland: Implications for spatial and temporal patterns of mantle convection. Geochemistry, Geophysics, Geosystems 3, 1–23.

Kaban, M. K. Flóvenz, O. G., Pálmason, G., 2002. Nature of the crust-mantle transition zone and the thermal state of the upper mantle beneath Iceland from gravity modelling. Geophysical Journal International 149, 281–299.

Kamenetsky, V. S., Crawford, A. J., Meffre, S., 2001. Factors controlling chemistry of magmatic spinel: an empirical study of associated olivine, Cr-spinel and melt inclusions from primitive rocks. Journal of Petrology 42, 655–671.

Karki, B. B., Stixrude, L. P., 2010. Viscosity of $MgSiO_3$ at Earth's mantle conditions: implications for an early magma ocean. Science 328, 740–742.

Keen, C. E., Potter, P., Srivastava, S. P., 1994. Deep seismic reflection data across the conjugate margins of the Labrador Sea. Canadian Journal of Earth Sciences 31, 192–205.

Keiding, J. K., Trumbull, R. B., Veksler, I. V., Jerram, D. A., 2011. On the significance of ultra-magnesian olivines in basaltic rocks. Geology 39, 1095–1098.

Kellogg, L. H., Wasserburg, G. J., 1990. The role of plumes in mantle helium fluxes. Earth and Planetary Science Letters 99, 276–289.

Kempton, P. D., Fitton, J. G., Saunders, A. D., Nowell, G. M., Taylor, R. N., Hardarson, B. S., Pearson, G., 2000. The Iceland plume in space and time: a Sr-Nd-Hf-Pb study of the North Atlantic rifted margin. Earth and Planetary Science Letters 177, 255–271.

Kennedy, A. K., Lofgren, G. E., Wasserburg, G. J., 1993. An experimental study of trace element partitioning between olivine, orthopyroxene and melt in chondrules: equilibrium values and kinetic effects. Earth and Planetary Science Letters 115, 117–195.

Kent, A. J. R., Stolper, E. M., Francis, D., Woodhead, J., Frei, R., Eiler, J., 2004. Mantle heterogeneity during the formation of the North Atlantic Igneous Province: Constraints from trace element and Sr-Nd-Os-O isotope systematics of Baffin Island picrites. Geochemistry, Geophysics, Geosystems 5, Q11004.

Kent, R. W., 1995. Magnesian basalts from the Hebrides, Scotland: chemical composition and relationship to the Iceland plume. Journal of the Geological Society 152, 979–983.

Kent, R. W., Fitton, J. G., 2000. Mantle sources and melting dynamics in the British Palaeogene Igneous Province. Journal of Petrology 41, 1023–1040.

Kerr, A. C., 1994. Lithospheric thinning during the evolution of continental large igneous provinces: A case study from the North Atlantic Tertiary province. Geology 22, 1027–1030.

Kerr, A. C., 1998. Mineral chemistry of the Mull-Morvern Tertiary lava succession, western Scotland. Mineralogical Magazine 62, 295–312.

Kerr, A. C., Kempton, P. D., Thompson, R. N., 1995. Crustal assimilation during turbulent magma ascent (ATA); new isotopic evidence from the Mull Tertiary lava succession, N. W. Scotland. Contributions to Mineralogy and Petrology 119, 142–154.

Kerr, R. C., Lister, J. R., 1991. The effects of shape on crystal settling and on the rheology of magmas . The Journal of Geology 99, 457–467.

King, S. D., Anderson, D. L., 1995. An alternative mechanism of flood basalt formation. Earth and Planetary Science Letters 136, 269–279.

Kinzler, R. J., Grove, T. L., 1992b. Primary magmas of mid-ocean ridge basalts 2. Applications. Journal of Geophysical Research: Solid Earth 34, 6907–6926.

Kirstein, L. A., Timmerman, M. J., 2000. Evidence of the proto-Iceland plume in northwestern Ireland at 42 Ma from helium isotopes. Journal of the Geological Society 157, 923–928.

Klein, E. M., Langmuir, C. H., 1987. Global correlations of ocean ridge basalt chemistry with axial depth and crustal thickness. Journal of Geophysical Research: Solid Earth 92, 8089–8115.

Kohara, S., Suzuya, K., Takeuchi, K., Loong, C. K., Grimsditch, M., Weber, J. K. R., Tangeman, J. A., Key, T. S., 2004. Glass formation at the limit of insufficient network formers. Science 303, 1649–1652.

Kono, Y., Irifune, T., Higo, Y., Inoue, T., Barnhoorn, A., 2010. P-V-T relation of MgO derived by simultaneous elastic wave velocity and in situ X-ray measurements: A new pressure scale for the mantle transition region. Physics of the Earth and Planetary Interiors 183, 196–211.

Kono, Y., Kenney-Benson, C., Park, C., Shen, G., Wang, Y., 2013. Anomaly in the viscosity of liquid KCl at high pressures. Physical Review B 87, 024302.

Kono, Y., Park, C., Kenney-Benson, C., Shen, G., Wang, Y., 2014. Toward comprehensive studies of liquids at high pressures and high temperatures: Combined structure, elastic wave velocity, and viscosity measurements in the Paris-Edinburgh cell. Physics of the Earth and Planetary Interiors 228, 269–280.

Koornneef, J. M., Stracke, A., Bourdon, B., Meier, M. A., Jochum, K. P., Stoll, B., Gronvold, K., 2012. Melting of a two-component source beneath Iceland. Journal of Petrology 53, 127–157.

Kristjansson, L., 1982. Geomagnetic polarity mapping of Icelandic lavas: Comparison with ocean-floor magnetic lineations. Earth Evolution Sciences 2, 126–129.

Kristoffersen, Y., 1978. Sea-floor spreading and the early opening of the North Atlantic. Earth and Planetary Science Letters 38, 273–290.

Kurz, M. D., 1982. Helium isotopic systematics of oceanic islands and mantle heterogeneity. Nature 297, 43–47.

Kurz, M. D., 1986. Cosmogenic helium in a terrestrial igneous rock. Nature 320, 435–439.

Kurz, M. D., Geist, D., 1999. Dynamics of the Galapagos hotspot from helium isotope geochemistry. Geochimica et Cosmochimica Acta 63, 4139–4159.

Kurz, M. D., Meyer, P. S., Sigurdsson, H., 1985. Helium isotopic systematics within the neovolcanic zones of Iceland. Earth and Planetary Science Letters 74, 291–305.

Kushiro, I., 1976. Changes in viscosity and structure of melt of $NaAlSi_2O_6$ composition at high pressures. Journal of Geophysical Research 81, 6347–6350.

Kushiro, I., 1977. Phase transformation in silicate melts under upper mantle conditions. In: M.H. Manghnani and S. Akimoto (Ed.), High-Pressure Research Applications in Geophysics. Academic, pp. 25–37.

Kushiro, I., Yoder, H. S., Mysen, B. O., 1976. Viscosities of basalt and andesite melts at high pressures. Journal of Geophysical Research 81, 6351–6356.

Labrosse, S., Herlund, J. W., Coltice, N., 2007. A crystallizing dense magma ocean at the base of the Earth's mantle. Nature 450, 866–869.

Lacks, D. J., Rear, D. B., Van Orman, J. A., 2007. Molecular dynamics investigation of viscosity, chemical diffusivities and partial molar volumes of liquids along the $MgO-SiO_2$ join as functions of pressure. Geochimica et Cosmochimica Acta 71, 1312–1323.

Larsen, L., Pedersen, A., 2000. Processes in high-Mg, high-T magmas: Evidence from olivine, chromite and glass in Palaeogene picrites from West Greenland. Journal of Petrology 41, 1071–1098.

Larsen, L. M., Pedersen, A. K., 2009. Petrology of the Paleocene picrites and flood basalts on Disko and Nuussuaq, West Greenland. Journal of Petrology 50, 1667–1711.

Larsen, L. M., Watt, W. S., Watt, M., 1989. Geology and petrology of the Lower Tertiary plateau basalts of the Scoresby Sund region, East Greenland. Bulletin of the Geological Survey of Greenland 157, 1–164.

Larsen, T. B., Yuen, D. A., Storey, M., 1999. Ultrafast mantle plumes and implications for flood basalt volcanism in the Northern Atlantic Region. Tectonophysics 311, 31–43.

Lawver, L. A., Müller, R. D., 1994. Iceland hotspot track. Geology 22, 311–314.

Lay, T., Hernlund, J., Buffett, B. A., 2008. Core-mantle boundary heat flow. Nature Geoscience 1, 788–790.

Le Bas, M., 2000. IUGS reclassification of the high-Mg and picritic volcanic rocks. Journal of Petrology 41, 1467–1470.

Le Bas, M. J., Streckeisen, 1991. The IUGS systematics of igneous rocks. Journal of the Geological Society of London 148, 825–833.

le Roux, P., le Roux, A., Schilling, J. G., 2002. MORB melting processes beneath the southern Mid-Atlantic Ridge ($40-55\,^{\circ}$S): a role for mantle plume-derived pyroxenite. Contributions to Mineralogy and Petrology 144, 206–229.

Liebske, C., Schmickler, B., Terasaki, H., Poe, B. T., Suzuki, A., Funakoshi, K., Ando, R., Rubie, D. C., 2005. Viscosity of peridotite liquid up to 13 GPa: Implications for magma ocean viscosities. Earth and Planetary Science Letters 240, 589–604.

Maaløe, S., 1973. Temperature and pressure relations of ascending primary magmas. Journal of Geophysical Research 78, 6877–6886.

Machetel, P., Thomassot, E., 2002. Cretaceous length of day perturbation by mantle avalanche. Earth and Planetary Science Letters 202, 379–386.

Maclennan, J., McKenzie, D., Gronvöld, 2001. Plume-driven upwelling under central Iceland. Earth and Planetary Science Letters 194, 67–82.

Maclennan, J., McKenzie, D., Gronvöld, K., Shimizu, N., Eiler, J. M., Kitchen, N., 2003b. Melt mixing and crystallization under Theistareykir, northeast Iceland. Geochemistry, Geophysics, Geosystems 4, 8624.

Macpherson, C. G., Hilton, D. R., Day, J. M. D., Lowry, D., Grönvold, K., 2005a. High-^{3}He/^{4}He, depleted mantle and low-δ^{18}O, recycled oceanic lithosphere in the source of central iceland magmatism. Earth and Planetary Science Letters 233, 411–427.

Macpherson, C. G., Hilton, D. R., Mertz, D. F., Dunai, T. J., 2005b. Sources, degassing, and contamination of CO_2, H_2O, He, Ne, and Ar in basaltic glasses from Kolbeinsey Ridge, North Atlantic. Geochimica et Cosmochimica Acta 69, 5729–5746.

Marty, B., Upton, B. G. J., Ellam, R. M., 1998. Helium isotopes in early Tertiary basalts, northeast Greenland: Evidence for 58 Ma plume activity in the North Atlantic-Iceland volcanic province. Geology 26, 407–410.

Matsuda, J., Matsumoto, T., Sumino, H., Nagao, K., Yamamoto, Y., Miura, Y., Kaneoka, I., Takahata, N., Sano, Y., 2002. The ^{3}He/^{4}He ratio of the new internal He Standard of Japan (HESJ). Geochemical Journal 36, 191–195.

Matsuda, J., Sudo, M., Ozima, M., Ito, K., Ohtaka, O., Ito, E., 1993. Noble gas partitioning between metal and silicate under high pressures. Science 259, 788–790.

McDonough, W., Sun, S.-s., 1995. The composition of the Earth. Chemical Geology 120, 223–253.

McKenzie, D., 1984. The generation and compaction of partially molten rock. Journal of Petrology 25, 713–765.

McKenzie, D., Bickle, M. J., 1988. The volume and composition of melt generated by extension of the lithosphere. Journal of Petrology 29, 625–679.

McMahon, M. I., 2012. High-pressure crystallography. In: Rissanen, K. (Ed.), Advanced X-Ray Crystallography. Springer Berlin Heidelberg.

McMillan, P. F., Wilding, M. C., 2009. High pressure effects on liquid viscosity and glass transition behaviour, polyamorphic phase transitions and structural properties of glasses and liquids. Journal of Non-Crystalline Solids 355, 722–732.

Michael, P. J., 1988. The concentration, behavior and storage of H_2O in the suboceanic upper mantle: Implications for mantle metasomatism. Geochimica et Cosmochimica Acta 52, 555–566.

Micoulaut, M., Bauchy, M., 2013. Anomalies of the first sharp diffraction peak in network glasses: Evidence for correlations with dynamic and rigidity properties. Physica Status Solidi B 250, 976–982.

Mjelde, R., Faleide, J. I., 2009. Variation of Icelandic and Hawaiian magmatism: evidence for co-pulsation of mantle plumes? Marine Geophysical Research 30, 61–72.

Moreira, M., Allegre, C., 2004. Helium isotopes on the Macdonald seamount (Austral chain): constraints on the origin of the superswell. Comptes Rendus Geoscience 336, 983–990.

Morgan, W. J., 1971. Convection plumes in the lower mantle. Nature 230, 42–43.

Murata, K. J., Richter, D. H., 1966. Chemistry of the lavas of the 1959-1960 eruption of Kilauea volcano, Hawaii. US Geological Survey Professional Paper 537-A, 1–26.

Murphy, D. T., Ballentine, C., Burgess, R., 2005. Defining the Origin and Nature of the Tristan da Cunha Plume Source Using He Isotope and Pb Isotope Modelling, Abstract V13C-0560 presented at 2005 Fall Meeting, AGU, San Francisco, Calif., 5-9 Dec.

Murton, B. J., Taylor, R. N., Thirwall, M. F., 2002. Plume-ridge interaction: a geochemical perspective from the Reykjanes Ridge. Journal of Petrology 43, 1987–2012.

Navin, D. A., Peirce, C., Sinha, M. C., 1998. The RAMESSES experiment-II. Evidence for accumulated melt beneath a slow spreading ridge from wide-angle refraction and multichannel reflection seismic profiles. Geophysical Journal International 135, 746–772.

Norman, M. C., Garcia, M. O., 1999. Primitive magmas and source characteristics of the Hawaiian plume: petrology and geochemistry of shield picrites. Earth and Planetary Science Letters 168, 27–44.

Norrish, K., Hutton, J. T., 1969. An accurate X-ray spectrographic method for the analysis of a wide range of geological samples. Geochimica et Cosmochimica Acta 33, 431–453.

O'Hara, M. J., 1968. Are ocean floor basalts primary magma? Nature 220, 683–686.

Olson, P., Deguen, R., Hinnov, L. A., Zhong, S., 2013. Controls on geomagnetic reversals and core evolution by mantle convection in the Phanerozoic. Physics of the Earth and Planetary Interiors 214, 87–103.

O'Nions, R. K., Tolstikhin, I. N., 1994. Behaviour and residence times of lithophile and rare gas tracers in the upper mantle. Earth and Planetary Science Letters 124, 131–138.

Osako, M., Ito, E., 1991. Thermal diffusivity of $MgSiO_3$ perovskite. Geophysical Research Letters 18, 239–242.

Parkin, C. J., White, R. S., 2008. Influence of the Iceland mantle plume on oceanic crust generation in the North Atlantic. Geophysical Journal International 173, 168–188.

Parnell-Turner, R., White, N., Henstock, T., Murton, B., Maclennan, J., Jones, S. M., 2014. A continuous 55-million-year record of transient mantle plume activity beneath Iceland. Nature Geoscience 7, 914–919.

Peate, D. W., Baker, J. A., Blichert-Toft, J., Hilton, D. R., Storey, M., Kent, A. J. R., Brooks, C. K., Hansen, H., Pedersen, A. K., Duncan, R. A., 2003. The Prinsen of Wales Bjerge Formation lavas, East Greenland: the transition from tholeiitic to alkalic magmatism during Palaeogene continental break-up. Journal of Petrology 44, 279–304.

Peate, D. W., Peate, I. U., Rowe, M. C., Thompson, J. M., Kerr, A. C., 2012. Petrogenesis of high-MgO lavas of the Lower Mull Plateau Group, Scotland: Insights from melt inclusions. Journal of Petrology 53, 1867–1886.

Pedersen, A. K., Larsen, L. M., Dueholm, K. S., 1993. Geological section along the south coast of Nuussuaq, central West Greenland, 1:20 000 Coloured Geological Sheet. Geological Survey of Greenland, Copenhagen.

Pedersen, A. K., Larsen, L. M., Pedersen, G. K., Dueholm, K. S., 1996. Filling and plugging of a marine basin by volcanic rocks: The Tonoqqu Member of the Lower Tertiary Veigat Formation on Nuussuaq, Central West Greenland. Bulletin Grønlands Geologiske Undersøgelse 171, 5–28.

Pedersen, A. K., Larsen, L. M., Riisager, P., Dueholm, K. S., 2002. Rates of volcanic deposition, facies changes and movements in a dynamic basin: the Nuussuaq Basin, West Greenland, around the C27n-C26r transition. In: The North Atlantic Igneous Province: Stratigraphy, Tectonic, Volcanic and Magmatic Processes, Special Publication 68. Geological Society, pp. 157–181.

Pedersen, G. K., Larsen, L. M., Pedersen, A. K., Hjortkjær, B. F., 1998. The syn-volcanic Naajaat lake, Paleocene of West Greenland. Palaeogeography, Palaeoclimatology, Palaeoecology 140, 271–287.

Perfit, M. R., Fornari, D. J., Ridley, W. I., Kirk, P. D., Casey, J., Kastens, K. A., Reynolds, J. R., Edwards, M., Desonie, D., Shuster, R., Paradis, S., 1996. Recent volcanism in the Siqueiros transform fault: picritic basalts and implications for MORB magma genesis. Earth and Planetary Science Letters 141, 91–108.

Pickering-Witter, J., Johnston, A. D., 2000. The effects of variable bulk composition on the melting systematics of fertile peridotitic assemblages. Contributions to Mineralogy and Petrology 140, 190–211.

Poe, B. T., Romano, C., Zotov, N., Cibin, G., Marcelli, A., 2001. Compression mechanisms in aluminosilicate melts: Raman and XANES spectroscopy of glasses quenched from pressures up to 10 GPa. Chemical Geology 174, 21–31.

Porcelli, D., Ballentine, C. J., 2002. Models for distribution of terrestrial noble gases and evolution of the atmosphere. Reviews in Mineralogy and Geochemistry 47, 411–480.

Porcelli, D., Halliday, A. N., 2001. The core as a possible source of mantle helium. Earth and Planetary Science Letters 192, 45–56.

Porcelli, D., Wasserburg, G. J., 1995. Mass transfer of helium, neon, argon, and xenon through a steady-state upper mantle. Geochimica et Cosmochimica Acta 59, 4921–4937.

Poreda, R., Schilling, J.-G., Craig, H., 1986. Helium and hydrogen isotopes in ocean-ridge basalts north and south of Iceland. Earth and Planetary Science Letters 78, 1–17.

Poreda, R. J., Craig, H., Arnórsson, S., Welhan, J. A., 1992. Helium isotopes in Icelandic geothermal systems: I. ^{3}He, gas chemistry, and ^{13}C relations. Geochimica et Cosmochimica Acta 56, 4221–4228.

Poreda, R. J., Schilling, J.-G., Craig, H., 1993. Helium isotope ratios in Easter microplate basalts. Earth and Planetary Science Letters 119, 319–329.

Putirka, K., 2008. Thermometers and barometers for volcanic systems. Reviews in Mineralogy and Geochemistry 69, 61–120.

Putirka, K. D., 2005. Mantle potential temperatures at Hawaii, Iceland, and the mid-ocean ridge system, as inferred from olivine phenocrysts: Evidence for thermally driven mantle plumes. Geochemistry, Geophysics, Geosystems 6, Q05L08.

Putirka, K. D., Perfit, M., Ryerson, F. J., Jackson, M. G., 2007. Ambient and excess mantle temperatures, olivine thermometry, and active vs. passive upwelling. Chemical Geology 241, 177–206.

Reid, J. E., Suzuki, A., Funakoshi, K., Terasaki, H., Poe, B. T., Rubie, D. C., Ohtani, E., 2003. The viscosity of $CaMgSi_2O_6$ liquid at pressures up to 13 GPa. Physics of the Earth and Planetary Interiors 139, 45–54.

Reynolds, R. C. J., 1963. Matrix corrections in trace element analysis by x-ray fluorescence: Estimation of the mass absorption coefficient by Compton scattering. American Mineralogist 48, 1133–1143.

Rhodes, J. M., Vollinger, M. J., 2005. Ferric/ferrous ratios in 1984 Mauna Loa lavas: a contribution to understanding the oxidation state of Hawaiian magmas. Contributions to Mineralogy and Petrology 149, 666–674.

Ringwood, A., 1966. Chemical evolution of the terrestrial planets. Geochimica et Cosmochimica Acta 30, 41–104.

Ringwood, A. E., 1975. Composition and petrology of the Earth's mantle. McGraw-Hill, New York.

Ritchie, J. D., Hitchen, K., 1996. Early Palaeogene offshore igneous activity to the northwest of the UK and its relationship to the North Atlantic Igneous Province. In: R. W. O. Knox and R. M. Corfield and R. E. Dunay (Ed.), Correlation of the Early Paleogene in Northwest Europe, Special Publication 101. Geological Society, pp. 63–78.

Roberts, D. G., Masson, D. G., Miles, P. R., 1981. Age and structure of the southern Rockall Trough: new evidence. Earth and Planetary Science Letters 38, 115–128.

Robinson, M. S., Taylor, G. J., 2001. Ferrous oxide in Mercury's crust and mantle. Meteoritics and Planetary Science 36, 841–847.

Roeder, P. L., 1994. Chromite; from the fiery rain of chondrules to the Kilauea Iki lava lake. Canadian Mineralogist 32, 729–746.

Roeder, P. L., Emslie, R. F., 1970. Olivine-liquid equilibrium. Contributions to Mineralogy and Petrology 29, 275–289.

Rubie, D. C., Melosh, H. J., Reid, J. E., Liebske, C., Righter, K., 2003. Mechanisms of metal-silicate equilibration in the terrestrial magma ocean. Earth and Planetary Science Letters 205, 239–255.

Sæmundsson, K., 1979. Outline of the geology of Iceland. Jökull 29, 7–28.

Sakamaki, T., Wang, Y., Park, C., Yu, T., Shen, G., 2012. Structure of jadeite melt at high pressures up to 4.9 GPa. Journal of Applied Physics 111, 112623.

Salters, V. J. M., Dick, H. J. B., 2002. Mineralogy of the mid-ocean-ridge basalt source from neodymium isotopic composition of abyssal peridotites. Nature 418, 206–229.

Samuel, H., Farnetani, C. G., 2003. Thermochemical convection and helium concentrations in mantle plumes. Earth and Planetary Science Letters 207, 39–56.

Sanloup, C., Drewitt, J. W. E., Crépisson, C., Kono, Y., Park, C., McCammon, C., Hennet, L., Brassamin, S., Bytchkov, A., 2013a. Structure and density of molten fayalite at high pressure. Geochimica et Cosmochimica Acta 118, 118–128.

Sanloup, C., Drewitt, J. W. E., Konôpková, Z., Dalladay-Simpson, P., Morton, D. M., Rai, N., van Westrenen, W., Morgenroth, W., 2013b. Structural change in molten basalt at deep mantle conditions. Nature 503, 104–107.

Sato, M., Hickling, N. L., McLane, J. E., 1973. Oxygen fugacity values of Apollo 12, 14 and 15 lunar samples and reduced state of lunar magmas. Proceedings of the Lunar Science Conference 4, 1061–1079.

Sato, T., Funamori, N., 2010. High-pressure structural transformation of SiO_2 glass up to 100 GPa. Physical Review B 82, 184102.

Saunders, A., Fitton, J., Kerr, A., Norry, M., Kent, R., 1997. The North Atlantic Igneous Province. In: John J. Mahoney and Millard F. Coffin (Ed.), Large Igneous Provinces: Continental, Oceanic, and Planetary Flood Volcanism. American Geophysical Union, Washington DC, pp. 45–93.

Saunders, A. D., Jones, S. M., Morgan, L. A., Pierce, K. L., Widdowson, M., Xu, Y. G., 2007. Regional uplift associated with continental large igneous provinces: The roles of mantle plumes and the lithosphere. Chemical Geology 241, 282–318.

Scarrow, J. H., Cox, K. G., 1995. Basalts generated by decompressive adiabatic melting of a mantle plume: a case study from the Isle of Skye, NW Scotland. Journal of Petrology 36, 3–22.

Scherstén, A., Elliott, T., Hawkesworth, C., Norman, M., 2004. Tungsten isotope evidence that mantle plumes contain no contribution from the Earth's core. Nature 427, 234–237.

Schilling, J, G., 1973. Iceland mantle plume. Nature 246, 141–143.

Schmelzer, J. W. P., Zanotto, E. D., Fokin, V. M., 2005. Pressure dependence of viscosity. The Journal of Chemical Physics 122, 074511.

Shiraishi, Y. K., Ikeda, K., Tamura, A., Saitô, T., 1978. On the viscosity and density of the molten FeO−SiO_2 system. Transactions of the Japan Institute of Metals 19, 264–274.

Shorttle, O., Maclennan, J., 2011. Compositional trends of Icelandic basalts: Implications for short-length scale lithological heterogeneity in mantle plumes. Geochemistry Geophysics Geosystems 12, Q1 1008.

Sigmarsson, O., Steinthórsson, S., 2007. Origin of Icelandic basalts: A review of their petrology and geochemistry. Journal of Geodynamics 43, 87–100.

Sissons, J. B., 1977. The Loch Lomond Readvance in southern Skye and some palaeoclimatic implications. Scottish Journal of Geology 13, 23–36.

Smith, N. J., 1985. Isotope geochemistry of Tertiary igneous rocks from the Isle of Skye, N.W. Scotland. Geological Magazine 122, 439–445.

Solomatov, V., Stevenson, D., 1993. Suspension in convective layers and style of differentiation of a terrestrial magma ocean. Journal of geophysical Research 98, 5375–5390.

Spandler, C., O'Neill, H. S. C., 2010. Diffusion and partition coefficients of minor and trace elements in San Carlos olivine at 1,300 ℃ with some geochemical implications. Contributions to Mineralogy and Petrology 159, 791–818.

Spice, H., Sanloup, C., Cochain, B., de Grouchy, C., Kono, Y., 2015. Viscosity of liquid fayalite up to 9 GPa. Geochimica et Cosmochimica Acta 148, 219–227.

Srivastava, S. P., Tapscott, C. R., 1986. Plate kinematics of the North Atlantic. In: P. R. Vogt and B. E. Tucholke (Ed.), The Western North Atlantic Region. Geological Society of America, pp. 379–404.

Starkey, N., 2009. Evolution of the Earth's mantle-crust-atmosphere system from the trace element and isotope geochemistry of the plume-mantle reservoir. Ph.D thesis, University of Edinburgh.

Starkey, N. A., Stuart, F. M., Ellam, R. M., Fitton, J. G., Basu, S., Larsen, L. M., 2009. Helium isotopes in early iceland plume picrites: Constraints on the composition of high $^3He/^4He$ mantle. Earth and Planetary Science Letters 277, 91–100.

Steinberger, B., Torsvik, T. H., 2010. Toward an explanation for the present and past locations of the poles. Geochemistry, Geophysics, Geosystems 11, Q06W06.

Steinberger, B., Torsvik, T. H., 2012. A geodynamic model of plumes from the margins of Large Low Shear Velocity Provinces. Geochemistry, Geophysics, Geosystems 13, Q01W09.

Stone, J. O., Ballantyne, C. K., Fifield, L. K., 1998. Exposure dating and validation of periglacial weathering limits, northwest Scotland. Geology 26, 587–590.

Storey, M., Duncan, R. A., Tegner, C., 2007. Timing and duration of volcanism in the North Atlantic Igneous Province: Implications for geodynamics and links to the Iceland hotspot. Chemical Geology 241, 264–281.

Stuart, F., Ellam, R., Harrop, P., Fitton, J., Bell, B., 2000. Constraints on mantle plumes from the helium isotopic composition of basalts from the British Tertiary Igneous Province. Earth and Planetary Science Letters 177, 273–285.

Stuart, F. M., Lass-Evans, S., Fitton, J. G., Ellam, R. M., 2003. High $^{3}He/^{4}He$ ratios in picritic basalts from Baffin Island and the role of a mixed reservoir in mantle plumes. Nature 424, 57–59.

Sun, S.-s., McDonough, W. F., 1989. Chemical and isotopic systematics of oceanic basalts: implications for mantle composition and processes. Geological Society, London, Special Publications 42, 313–345.

Suzuki, A., Ohtani, E., Funakoshi, K., Terasaki, H., Kubo, T., 2002. Viscosity of albite melt at high pressure and temperature. Physics of Chemistry and Minerals 29, 159–165.

Suzuki, A., Ohtani, E., Terasaki, H., Funakoshi, K., 2005. Viscosity of silicate melts in $CaMgSi_2O_6$-$NaAlSi_2O_6$ system at high pressure. Physics and Chemisry of Minerals 32, 140–145.

Suzuki, A., Ohtani, E., Terasaki, H., Nishida, K., Hayashi, H., Sakamaki, T., Shibazaki, Y., Kikegawa, T., 2011. Pressure and temperature dependence of the viscosity of a $NaAlSi_2O_6$ melt. Physics and Chemistry of Minerals 38, 59–64.

Tan, E., Gurnis, M., Han, L., 2002. Slabs in the lower mantle and their modulation of plume formation. Geochemistry, Geophysics, Geosystems 3 (11), 1–24.

Taniguchi, H., 1992. Entropy dependence of viscosity and the glass-transition temperature of melts in the system diopside-anorthite. Contributions to Mineralogy and Petrology 109, 295–303.

Taylor, R. N., Thirlwall, M. F., Murton, B. J., Hilton, D. R., Gee, M. A. M., 1997. Isotopic constraints on the influence of the Icelandic plume. Earth and Planetary Science Letters 148, E1–E8.

Thirlwall, M. F., Gee, M. A. M., Taylor, R. N., Murton, B. J., 2004. Mantle components in Iceland and adjacent ridges investigated using double-spike Pb isotope ratios. Geochimica et Cosmochimica Acta 68, 361–386.

Thompson, A., Maclennan, J., 2013. The distribution of olivine compositions in Icelandic basalts and picrites. Journal of Petrology 54, 745–768.

Thompson, R. N., 1982. Geochemistry and magma genesis. In: D. S. Sutherland (Ed.), The Igneous Rocks of the British Isles. John Wiley, pp. 461–477.

Thompson, R. N., Gibson, S. A., 1991. Subcontinental mantle plumes, hotspots and pre-existing thinspots. Journal of the Geological Society of London 148, 973–977.

Thompson, R. N., Gibson, S. A., 2000. Transient high temperatures in mantle plume heads inferred from magnesian olivines in Phanerozoic picrites. Nature 407, 502–506.

Thordarson, T. an Larsen, G., 2007. Volcanism in Iceland in historical time: Volcano types, eruption styles and eruptive history. Journal of Geodynamics 43, 118–152.

Tibaldi, A., Pasquarè, A. F., Rust, D., 2011. New insights into the cone sheet structure of the Cuillin Complex, Isle of Skye, Scotland. Journal of the Geological Society 168, 689–704.

Tolstikhin, I., Hofmann, A. W., 2005. Early crust on top of the Earth's core. Physics of the Earth and Planetary Interiors 148, 109–130.

Tonks, W. B., Melosh, H. J., 1990. The physics of crystal settling and suspension in a turbulent magma ocean. In: N.E. Newsom and J.H. Jones (Ed.), Origin of the Earth. Oxford University Press, New York, pp. 151–174.

Tonks, W. B., Melosh, H. J., 1993. Magma ocean formation due to giant impacts. Journal of geophysical Research 98, 5319–5333.

Tryggvason, K., Husebye, E. S., Stefánsson, R., 1983. Seismic image of the hypothesized Icelandic hot spot. Tectonophysics 100, 97–118.

Ukstins Peate, I., Larsen, M., Lesher, C. E., 2003. The transition from sedimentation to flood volcanism in the Kangerlussuaq Basin, East Greenland: basaltic pyroclastic volcanism during initial Palaeogene continental break-up. Journal of the Geological Society of London 160, 759–772.

Upton, B., 1988. History of Tertiary igneous activity in the N Atlantic borderlands. Geological Society, London, Special Publications 39, 429–453.

Upton, B. G. J., Downes, H., Kirstein, L. A., Bonadiman, C., Hill, P. G., Ntaflos, T., 2011. The lithospheric mantle and lower crust-mantle relationships under Scotland: a xenolithic perspective. Journal of the Geological Society 168, 873–886.

Upton, B. G. J., Emeleus, C. H., Beckinsale, R. D., 1984. Petrology of the northern East Greenland Tertiary flood basalts: Evidence from Hold with Hope and Wollaston Forland. Journal of Petrology 25, 151–184.

Upton, B. G. J., Skovgaard, A. C., McClurg, J., Kirstein, L., Cheadle, M., Emeleus, C. H., Wadsworth, W. J., Fallick, A. E., 2002. Picritic magmas and the rum ultramafic complex, scotland. Geological Magazine 139, 437–452.

van der Hilst, R. D., Widiyantoro, S., Engdahl, E. R., 1997. Evidence for deep mantle circulation from global tomography. Nature 386, 578–584.

Vink, G. E., 1984. A hotspot model for iceland and the Vøring plateau. Journal of Geophysical Research: Solid Earth 89, 9949–9959.

Vogt, P. R., Avery, O. E., 1974. Detailed magnetic surveys in the Northeast Atlantic and Labrador Sea. Journal of Geophysical Research 79, 363–389.

Vohra, Y. K., Duclos, S. J., Ruoff, A. L., 1987. High-pressure x-ray diffraction studies on rhenium up to 216 GPa (2.16 Mbar). Physical Review B 36, 9790–9792.

Waagstein, R., 1988. Structure, composition and age of the Faeroe basalt plateau. In: A. C. Morton and L. M. Larsen (Ed.), Early Tertiary Volcanism and the Opening of the NE Atlantic. Geological Society Special Publication 39, pp. 225–238.

Waff, H. S., 1975. Pressure-induced coordination changes in magmatic liquids. Geophysical Research Letters 2, 193–196.

Walker, G. P. L., 1971. The distribution of amygdale minerals in Mull and Morvern (Western Scotland). In: T. V. V. G. G. G. R. K. Murty. and S. S. Roa (Ed.), Studies in Earth Sciences, W. D. West commemorative volume. pp. 181–194.

Wan, Z., Coogan, L. A., Canil, D., 2008. Experimental calibration of aluminium partitioning between olivine and spinel as a geothermometer. American Mineralogist 93, 1142–1147.

Watkins, N. D., Walker, G. P. L., 1977. Magnetostratigraphy of eastern Iceland. American Journal of Science 277, 513–584.

Westland, J., 2014. Chapter 3: The Loch Uisg Picrite Suite (LUPS). In: Unpublished Master's Thesis. University of Glasgow, UK.

Wheeler, K. T., Walker, D., Fei, Y., Minarik, W. G., McDonough, W. F., 2006. Experimental partitioning of uranium between liquid iron sulfide and liquid silicate: Implications for radioactivity in the Earth's core. Geochimica et Cosmochimica Acta 70, 1537–1547.

White, N., Lovell, B., 1997. Measuring the pulse of a plume with the sedimentary record. Nature 387, 888–891.

White, R., McKenzie, D., 1989. Magmatism at rift zones: The generation of volcanic continental margins and flood basalts. Journal of Geophysical Research 94, 7685–7729.

White, R. S., McKenzie, D., O'Nions, R. K., 1992. Oceanic crustal thickness from seismic measurements and rare earth element inversions. Journal of Geophysical Research: Solid Earth 97, 19683–19715.

Whitmarsh, R. B., 1971. Seismic anisotropy of the uppermost mantle absent beneath the east flank of the Reykjanes Ridge. Bulletin of the Seismological Society of America 61, 1351–1368.

Wilding, M., Guthrie, M., Kohara, S., Bull, C. L., Akola, J., Tucker, M. G., 2012. Corrigendum: The structure of mgo-SiO_2 glasses at elevated pressure. Journal of Physics: Condensed Matter 24, 339501.

Williams, Q., Jeanloz, R., 1988. Spectroscopic evidence for pressure-induced coordination changes in silicate glasses and melts. Science 239, 902–905.

Williamson, I. T., Bell, B. R., 1994. The Palaeocene lava field of west-central Skye, Scotland: Stratigraphy, palaeogeography and structure. Transactions of the Royal Society of Edinburgh: Earth Sciences 85, 39–75.

Wilson, J. T., 1963. A possible origin of the Hawaiian Islands. Canadian Journal of Physics 41, 863–870.

Wolfe, C. J., Bjarnason, I. T., VanDecar, J. C., Solomon, S., 1997. Seismic structure of the Iceland mantle plume. Nature 385, 245–247.

Yamada, A., Wang, Y., Inoue, T., Yang, W., Park, C., Yu, T., Shen, G., 2011. High-pressure x-ray diffraction studies on the structure of liquid silicate using a Paris-Edinburgh type large volume press. Review of Scientific Instruments 82, 015103.

Yang, T., Fu, R., 2014. Thermochemical piles in the lowermost mantle and their evolution. Physics of the Earth and Planetary Interiors 236, 109–116.

Yaxley, G. M., Kamenetsky, V. S., Kamenetsky, M., Norman, M. D., Francis, D., 2004. Origins of compositional heterogeneity in olivine-hosted melt inclusions from the Baffin Island picrites. Contributions to Mineralogy and Petrology 148, 426–442.

Zhang, N., Zhong, S., 2011. Heat fluxes at the Earth's surface and core-mantle boundary since Pangea formation and their implications for the geomagnetic superchrons. Earth and Planetary Science Letters 306, 205–216.

Zindler, A. Hart, S. R., Frey, F. A., 1979. Nd and Sr isotope ratios and rare earth element abundances in Reykjanes Peninsula basalts evidence for mantle heterogeneity beneath Iceland. Earth and Planetary Science Letters 45, 249–262.

Appendix A. Viscosity results

Table A.1: Experimental conditions, parameters and results from the fayalite melt viscosity measurements

Run	P GPa	T °C	d_s μm	W	E	v	ρ_s mm·s^{-1}	ρ_l mm·s^{-1}	η mPa·s	η error %
A5	2.0 ± 0.5	1350 ± 70	174 ± 2	0.675 ± 0.003	1.065 ± 0.011	3.7 ± 0.1	22.54 ± 0.15	3.94 ± 0.05	52.1 ± 2.8	8.8
A8	9.2 ± 0.6	1850 ± 95	185 ± 2	0.656 ± 0.008	1.069 ± 0.013	7.2 ± 0.1	24.28 ± 0.08	4.64 ± 0.05	31.3 ± 2.7	5.4
A10	3.6 ± 0.5	1550 ± 80	171 ± 2	0.680 ± 0.006	1.064 ± 0.012	5.1 ± 0.2	23.07 ± 0.11	4.09 ± 0.05	38.3 ± 3.7	8.6
A12	6.3 ± 0.5	1600 ± 80	185 ± 2	0.657 ± 0.006	1.069 ± 0.012	6.4 ± 0.2	23.80 ± 0.06	4.39 ± 0.05	34.7 ± 2.7	9.5
B7	4.3 ± 0.5	1640 ± 80	108 ± 2	0.794 ± 0.004	1.040 ± 0.011	2.3 ± 0.1	23.30 ± 0.08	4.16 ± 0.05	41.0 ± 3.6	7.6
B11	3.8 ± 0.5	1600 ± 80	133 ± 2	0.748 ± 0.003	1.049 ± 0.011	3.2 ± 0.1	23.16 ± 0.10	4.11 ± 0.05	41.0 ± 2.8	8.8
B13	5.1 ± 0.5	1650 ± 85	173 ± 2	0.676 ± 0.003	1.065 ± 0.011	5.3 ± 0.2	23.50 ± 0.08	4.25 ± 0.05	37.6 ± 2.3	6.7
B14	2.8 ± 0.5	1570 ± 80	155 ± 2	0.708 ± 0.003	1.058 ± 0.011	4.0 ± 0.2	22.86 ± 0.12	3.99 ± 0.05	42.0 ± 3.7	8.9
B17	1.3 ± 0.5	1580 ± 80	183 ± 2	0.659 ± 0.003	1.069 ± 0.011	4.0 ± 0.2	22.24 ± 0.22	3.80 ± 0.05	51.9 ± 4.0	7.6

Appendix B. Analytical set-ups

B.1 Whole-rock major and trace element analysis: (XRF) spectrometry

Whole-rock major and trace element analyses were determined using X-ray fluorescence (XRF) spectrometry at the University of Edinburgh. The techniques used are similar to those described by Fitton et al. (1998), with modifications noted by Fitton and Godard (2004).

The rock samples from Skye, Mull, Rum and Iceland were prepared into powder at the university of Edinburgh. Weathered surfaces, veins and altered areas were removed using a diamond-bladed mechanical rock saw. Samples were then crushed to a coarse grit (<2 mm) in a jaw crusher with tungsten carbide plates. Portions of the crushed rock were separated and powdered in tungsten carbide barrels.

Major-element concentrations were determined after fusion with a lithium borate flux containing La_2O_3 as a heavy absorber, by a method similar to that developed by Norrish and Hutton (1969). Rock powder was dried at 110 ℃ for at least 1 hour, and a nominal but precisely-weighed 1-g aliquot ignited at 1100 ℃ to determine loss on ignition (LOI). The residue was then mixed with Johnson Matthey Spectroflux^{TM} 105 in a sample:flux ratio of 1:5, based on the unignited sample mass, and fused in a muffle furnace in a Pt5% Au crucible. After the initial fusion, the crucible was reweighed and any flux weight loss was made up with extra flux. After a second fusion over a Meker burner, the molten mixture was swirled several times to ensure homogeneity, cast onto a graphite mold, and flattened with an aluminium plunger into a thin disk. The mold and plunger were maintained at a temperature of 220℃ on a hotplate.

Trace-element concentrations were determined on pressed-powder samples. Eight grams of rock powder were mixed thoroughly with eight drops of a 2% aqueous solution of polyvinyl alcohol. The mixture was loaded into a 40-mm diameter aluminium cup in a stainless steel die and compressed against a polished tungsten carbide disc in a hydraulic press at 0.6 tons/cm^2.

The fused and pressed samples were analyzed using a Philips PW 2404 automatic X-ray fluorescence spectrometer with a Rh-anode X-ray tube. Trace-element background positions were placed as close as possible to peaks, and long count times were used at both peak and background positions. Where background count rates were measured on either side of the peak, as in most trace-element determinations, the count time was divided between the two positions. Analytical conditions are given in Fitton et al. (1998) and Fitton and Godard (2004).

Corrections for matrix effects on the intensities of major-element lines were made using theoretical alpha coefficients calculated on-line using the Philips software. The coefficients were calculated to allow for the amount of extra flux replacing volatile components in the sample so that analytical totals should be 100% less the measured LOI. Intensities of the longer wavelength trace-element lines (La, Ce, Nd, Cu, Ni, Co, Cr, V, Ba, and Sc) were corrected for matrix effects using alpha coefficients based on major-element concentrations measured at the same time on the powder samples. Matrix corrections were applied to the intensities of the other trace-element lines by using the count rate from the RhK_a Compton scatter line as an internal standard (Reynolds, 1963). Line-overlap corrections were applied using synthetic standards.

The spectrometer was calibrated against USGS and CRPG geochemical reference standards using the values given by Govindaraju (1994). Excellent calibration lines were obtained using these standards. Analytical precision and accuracy are comparable to the values reported by Fitton et al. (1998) and Fitton and Godard (2004). Four USGS geostandards were analysed along with the Skye, Mull, Rum and Iceland samples (Table B.1). The acquired values display excellent correlation with certified values of Govindaraju (1994).

Table B.1: Trace element concentrations in international standards measured at the University of Edinburg by XRF compared with recommended values. R = recommended values from Govindaraju (1994). E = Mean and standard deviation of six measurements determined at the University of Edinburgh in this study.

	BCR			BEN			BHVO-1			BIR		
	R	**E**	**1σ**	**R**	**E**	**1σ**	**R**	**E**	**1σ**	**R**	**E**	**1σ**
Zn	129.5	125.1	0.28	120.0	131.8	1.21	105.0	103.7	0.26	71.0	66.7	0.43
Cu	19.0	19.9	0.25	72.0	77.0	0.56	136.0	134.3	0.26	126.0	126.8	0.09
Ni	13.0	16.0	0.29	267.0	276.7	2.26	121.0	118.4	0.65	166.0	156.0	0.53
Cr	16.0	6.0	0.54	360.0	378.0	1.15	289.0	286.7	0.92	382.0	372.4	0.53
V	407.0	395.8	2.30	235.0	251.6	2.08	317.0	312.8	2.34	313.0	309.7	1.25
Ba	681.0	679.4	3.61	1025.0	1037.5	5.95	139.0	124.7	1.55	7.0	5.6	0.26
Sc	32.6	30.8	0.25	22.0	25.1	0.81	31.8	33.1	0.48	44.0	41.0	0.24
La	24.9	23.5	0.22	82.0	83.2	0.51	15.8	12.1	0.09	0.6	-	-
Ce	53.7	53.3	0.69	152.0	156.3	1.00	39.0	37.5	1.27	2.0	-	-
Nd	28.8	28.8	0.17	67.0	66.3	0.05	25.2	24.8	0.49	2.5	4.4	0.50
U	1.8	2.5	0.12	2.4	2.9	0.21	0.4	0.8	0.33	0.0	0.4	0.33
Th	6.0	5.9	0.43	10.4	11.8	0.41	1.1	0.8	0.14	0.0	-	-
Pb	13.6	14.0	0.45	4.0	4.3	0.19	2.6	2.5	0.25	3.0	3.6	0.29
Nb	14.0	12.9	0.05	105.0	117.8	0.17	19.0	19.3	0.05	0.6	0.7	0.08
Zr	190.0	191.1	0.31	260.0	270.4	0.98	179.0	172.9	0.45	15.5	16.5	0.17
Y	38.0	37.8	0.17	30.0	29.9	0.05	27.6	27.1	0.00	16.0	16.2	0.08
Sr	330.0	331.2	0.22	1370.0	1387.8	1.79	403.0	389.3	0.45	108.0	107.2	0.25
Rb	47.2	47.9	0.21	47.0	48.1	0.26	11.0	9.8	0.42	0.3	0.7	0.12

B.2 Mineral compositions: EPMA

Samples were prepared as carbon-coated polished thin sections for major element analysis of olivine and Cr-spinel compositions using electron microprobe analysis (EPMA). The analyses were performed on a Cameca SX100 electron microprobe at the Edinburgh Materials and Micro-Analysis Centre (EMMAC), University of Edinburgh with the assistance of Dr. Chris Hayward. Analyses were carried out in wavelength-dispersive (WDS) mode with an accelerating voltage of 15 keV on five spectrometers: PET, LLIF, LPET, TAP, LTAP. Primary standards for the EPMA calibration of major elements in both phases were as follows: Mg-Kα and Si-Kα on forsterite, Fe-Kα on fayalite, Na-Kα on jadeite-BL7, Al-Kα on spinel-BL8, P-Kα on P K4, Ca-Kα on wollastonite-BL8, Ti-Kα on rutile-BL8, Mn-Kα, Ni-Kα and Cr-Kα on pure metals. The composition of each standard is presented in Table B.2. Two column conditions were used, condition 1: 15 keV 4 nA, condition 2: 15 keV 100 nA. Condition 1 was used to analyse Na, Mg, Fe and Si. Condition 2 was used to analyse P, Ca, Ti, Mn, Ni and Al. A beam size of 1 μm was used in all analyses.

Table B.2: Compositions of the primary standards used in the EPMA analyses expressed as atomic wt%.

Forsterite	O : 45.5%, Mg : 34.5%, Si : 20.%
Fayalite	Fe : 54.81%, Si : 13.78%, O : 31.41%
Jadeite-BL7	Na : 11.34%, Al : 13.23%, Si : 27.78%, Fe : 0.17%, O : 47.65%
Spinel-BL8	Mg : 17.08%, Al : 37.93%, O : 44.99%
P K4	O : 38.77%, F : 3.53%, Na : 0.17%, Si : 0.16%, P : 17.8%, Cl : 0.41%, Ca : 38.61%, Sr : 0.06%, Ce : 0.85%
Wollastonite-BL8	Mg : 0.17%, Al : 0.03%, Si : 24.%, Ca : 34.32%, Mn : 0.05%, Fe : 0.28%, O : 41.37%
Rutile-BL8	Ti : 59.34%, O : 39.89%, Mg : 0.01%, Fe : 0.59%, Nb : 0.17%

Detection limits were calculated from count rates by the Cameca EPMA software. In order to carry out Al-in-olivine thermometry, a high precision measurement of the olivine Al-content is required. Al was measured with a TAP crystal. The analyses were carried out over several sessions. The first set were carried out on the Skye samples with a maximum detection limit of 75 ppm Al_2O_3 in olivine. During subsequent analyses, the detection limit was lowered to a minimum of 28 ppm by increasing the count time. The maximum detection limit for each sample suite is as follows: 75 ppm for Skye, 58 ppm for Rum and neovolcanic Iceland, 39 ppm for Iceland Tertiary and Mull and 30 ppm for Baffin Island and West Greenland. Average detection limits for all oxides and count times for olivine and Cr-spinel are presented in Tables B.3 and B.4, respectively. The average detection limit for two samples is given, S1, which was analysed in the first session, and 354754, which was analysed in the last session once the Al_2O_3 detection limit had been reduced to 28-30 ppm. In both cases, the uncertainty in the Al_2O_3 measurement is within those reported by Wan et al. (2008), and therefore the error in the Al-in-olivine thermometer temperature calculation includes the uncertainty arising from the precision of the olivine Al_2O_3 measurement. One analysis of each olivine and Cr-spinel pair was taken. The olivine spot was taken at least 100 μm from the Cr-spinel grain.

Table B.3: Average detection limits in wt% for olivine analyses in samples S1 and 354754. Average count times are also shown. n.d. = not determined.

Sample	NaO	MgO	FeO	SiO_2	P_2O_5	CaO	TiO_2	MnO	NiO	Al_2O_3	Cr_2O_3	Count time (s)
S1	0.035	0.038	0.157	0.089	0.007	0.007	0.008	0.032	0.029	0.007	n.d.	344
354754	0.004	0.038	0.180	0.087	0.007	0.005	0.005	0.018	0.020	0.003	0.008	514

Table B.4: Average detection limits in wt% for Cr-spinel analyses in samples S1 and 354754. Average count times are also shown.

Sample	MgO	FeO	SiO_2	CaO	TiO_2	MnO	NiO	Al_2O_3	Cr_2O_3	ZnO	Count time (s)
S1	0.005	0.187	0.006	0.004	0.044	0.033	0.026	0.051	0.284	0.043	432
354754	0.004	0.233	0.005	0.004	0.048	0.024	0.022	0.053	0.266	0.038	465

B.3 Helium isotopes

Helium isotope analyses were carried out at the Noble Gas Laboratory at the Scottish Universities Environmental Research Centre (SUERC), East Kilbride. Olivine phenocrysts were separated from coarsely crushed rock by picking under binocular microscope. Care was taken to select fresh phenocrysts unaffected by alteration without any adhering basalt matrix. Approximately 1 g of olivine phenocrysts from each sample were picked. The samples were cleaned ultrasonically in acetone for 15 minutes and then rinsed in de-ionised water.

The olivine phenocrysts were crushed *in vacuo* in order to be analysed. Approximately 1 g of olivine was loaded into 25 mm diameter stainless steel pots with two layers of crystals separated by 2 mm thick stainless steel plates. The pots were loaded into the multi-sample hydraulic crusher and the samples were crushed between 500 and 2000 psi. Crushing was ceased before the crystals were reduced to powder in order to prevent the release of lattice-stored He. Before releasing the crush gas into the mass spectrometer, the gas was cleaned for 15 minutes by two SAES GP50 getters at 250℃ to remove the active gases and then by one activated charcoal cold finger cooled to 77 K by liquid nitrogen to remove the heavy gases. Another SAES GP50 getter at room temperature and a second cold finger were used to minimise the partial pressure of the residual gases during analysis.

Helium isotope ratios were determined in a Helix SFT mass spectrometer at SUERC. ^{3}He was measured by a secondary electron multiplier. ^{4}He was measured on a Faraday cup. Procedural blanks were measured prior to the first crush analysis of each batch and strategically between samples in order to assess the potential for increased blank-level due to insufficient pump time between analyses or the potential for 'memory-effect' in the mass spectrometer itself. Helium

isotope abundances were calculated by peak height comparison to pipettes of 2.9 x 10^{12} atoms of helium from an artificial standard (He Standard of Japan) with ^{3}He/^{4}He of 20.63 $\pm$ 0.10 relative to the air value (R/R_a) of 1.4 x 10^{-6} (Matsuda et al., 2002).

Appendix C. Sample list and locations

Table C.1: Sample list and locations of BTIP samples.

Sample	Location	Grid Reference
S1	Skye	NG 4428 2081
S2	Skye	NG 4433 2082
S3	Skye	NG 4438 2083
S5	Skye	NG 4434 2077
S6	Skye	NG 4429 2079
S7	Skye	NG 4426 2089
S8	Skye	NG 4429 2090
S9	Skye	NG 4437 2084
S10	Skye	NG 4432 2072
R10	Rum	NM 3762 9784
M9	Rum	NM 351 983
MU1.1	Mull	NM 6669 2401
MU1.2	Mull	NM 6636 2421
MU2.2	Mull	NM 6453 2502
MU3.1	Mull	NM 5861 2720

Table C.2: Sample list and locations of Baffin Island, West Greenland and Iceland samples.

Sample	Location	Latitude	Longitude
PAD4	Baffin Island	67.17	-62.44
PAD5	Baffin Island	67.17	-62.44
PAD6	Baffin Island	67.17	-62.45
DUR6	Baffin Island	67.08	-62.22
DUR8	Baffin Island	67.07	-62.19
APO4	Baffin Island	66.93	-61.74
APO7	Baffin Island	66.93	-61.74
138345	West Greenland	70.13	-53.27
340740	West Greenland	70.33	52.98
354754	West Greenland	70.49	53.29
362077	West Greenland	70.49	53.57
400230	West Greenland	70.59	53.11
I1	Iceland (RVZ)	63.82	-22.71
I2	Iceland (RVZ)	63.82	-22.64
I3	Iceland (RVZ)	63.86	-22.35
I5	Iceland (EVZ)	64.14	-19.80
I6	Iceland (EVZ)	64.12	-19.94
I7	Iceland (NVZ)	65.74	-16.96
I8	Iceland (NVZ)	65.82	-16.92
I9	Iceland (NVZ)	65.96	-17.08
VEY	Iceland (NW)	65.84	-23.25
SD	Iceland (NW)	65.79	-24.00
ED	Iceland (NW)	65.96	-23.32
VP1	Iceland (E)	65.75	-14.83
KoP	Iceland (NW)	65.80	-24.09
SAU3199	Iceland (NW)	65.39	-21.19

Appendix D. Whole-rock compositions

D.1 Major elements

Table D.1: Major element abundances (wt%) for BTIP and Iceland samples determined by XRF. The Iceland Tertiary data are from Hardarson and Fitton (unpublished data). Major elements are recalculated to 100% on a volatile free basis.

Sample	SiO_2	Al_2O_3	FeO	MgO	CaO	Na_2O	K_2O	TiO_2	MnO	P_2O_5	Total	LOI
S1	44.37	9.69	10.50	25.98	7.65	0.76	0.04	0.46	0.16	0.04	99.66	1.88
S2	43.87	7.63	10.32	31.94	5.28	0.24	0.08	0.33	0.16	0.03	99.88	5.86
S3	44.75	10.57	10.56	23.34	8.52	1.26	0.12	0.50	0.16	0.05	99.84	2.22
S5	44.38	9.10	10.67	27.52	6.90	0.64	0.07	0.42	0.16	0.04	99.89	3.03
S6	43.45	7.56	10.87	31.11	5.73	0.32	0.05	0.36	0.17	0.03	99.65	5.69
S7	44.71	9.53	11.04	24.80	7.63	0.84	0.11	0.65	0.16	0.05	99.54	2.17
S8	45.16	10.16	11.07	23.66	8.01	0.82	0.11	0.68	0.16	0.05	99.88	1.94
S9	45.45	10.56	10.97	22.25	8.46	0.82	0.27	0.64	0.17	0.05	99.64	2.43
S10	45.26	10.85	10.80	22.00	9.12	0.67	0.16	0.59	0.17	0.05	99.67	2.34
R10	42.38	7.31	12.12	30.69	5.44	0.95	0.05	0.59	0.17	0.05	99.75	2.04
MU1.1	44.97	9.73	10.74	24.85	8.08	0.87	0.08	0.53	0.16	0.04	100.06	1.72
MU1.2	44.08	8.93	10.27	28.62	6.85	0.75	0.09	0.39	0.16	0.03	100.17	2.16
MU2.2	44.30	9.38	10.24	27.22	7.46	0.81	0.13	0.44	0.16	0.04	100.18	1.94
MU3.1	44.25	8.23	10.82	28.91	6.52	0.84	0.14	0.46	0.16	0.04	100.37	1.47
I1	48.73	14.42	13.51	7.14	11.68	1.97	0.16	1.55	0.21	0.15	99.52	-0.67
I2	44.45	9.10	9.85	27.52	7.81	0.70	0.00	0.25	0.15	0.02	99.86	-0.56
I3	48.77	14.72	11.09	10.56	13.05	1.42	0.06	0.75	0.18	0.07	100.66	-0.62
I5	44.43	8.09	12.01	26.20	7.58	0.97	0.04	1.01	0.19	0.10	100.62	0.88
I6	48.38	11.02	13.29	16.56	7.99	1.91	0.33	1.73	0.20	0.21	101.63	0.36
I7	48.86	15.21	10.85	10.34	12.57	1.61	0.08	0.75	0.17	0.06	100.52	-0.58
I8	48.38	13.70	10.81	11.69	13.21	1.43	0.06	0.75	0.18	0.06	100.25	-0.65
I9	47.73	14.58	10.81	12.27	12.51	1.58	0.04	0.80	0.17	0.06	100.56	-0.64
ED	46.40	11.83	11.15	15.71	10.40	1.26	0.09	1.16	0.17	0.09	98.27	
SD	44.92	8.01	12.49	24.69	7.49	0.90	0.05	0.96	0.18	0.08	99.76	
VEY	45.56	12.07	10.88	17.99	8.72	1.28	0.21	0.74	0.17	0.13	97.74	
VP1	46.95	12.60	10.95	13.85	10.03	1.50	0.15	1.38	0.14	0.11	97.66	

D.2 Trace elements

Table D.2: Trace element abundances (ppm) for BTIP and neovolcanic Iceland samples determined by XRF.

Sample	Zn	Cu	Ni	Cr	V	Ba	Sc	La	Ce	Nd	U	Th	Pb	Nb	Zr	Y	Sr	Rb
S1	58.6	83.0	1316	2768	163	6.7	25.1	0.3	n.d.	1.3	0.0	0.8	0.7	0.4	21.8	12.6	41.1	1.5
S2	55.7	58.5	1705	3128	117	6.6	18.2	1.0	n.d.	0.9	n.d.	0.0	0.6	0.4	13.7	8.5	24.9	4.3
S3	61.9	94.5	1124	2753	187	2.5	31.2	n.d.	n.d.	2.0	n.d.	0.8	1.1	0.5	24.8	13.9	44.4	3.9
S5	63.1	82.9	1390	2879	151	8.5	25.2	0.4	n.d.	0.7	n.d.	1.5	0.8	0.4	18.8	11.1	35.3	2.9
S6	65.6	88.3	1599	3001	129	12.1	22.4	0.3	n.d.	0.9	n.d.	1.2	1.1	0.6	14.5	9.1	27.4	2.2
S7	67.3	90.4	1204	2662	179	16.8	27.5	0.0	n.d.	2.8	0.1	0.5	0.8	1.1	30.3	12.9	71.0	4.8
S8	67.6	94.4	1094	2594	182	12.2	27.3	n.d.	n.d.	1.8	0.2	n.d.	1.1	1.1	32.6	14.0	74.9	4.7
S9	64.8	96.2	1072	1988	194	20.1	27.1	0.9	n.d.	2.8	n.d.	0.2	0.9	1.0	31.5	15.3	58.9	7.9
S10	62.2	94.5	1020	2465	188	13.8	30.4	1.7	n.d.	2.6	0.3	n.d.	1.1	0.5	26.1	15.0	67.8	3.3
R10	67.7	73.1	1614	2282	134	7.0	16.2	0.4	n.d.	3.4	n.d.	0.2	1.4	0.8	32.6	8.3	83.0	0.9
MU1.1	61.7	85.4	1187	1820	171	15.3	22.3	1.3	2.2	3.0	0.0	0.8	0.6	0.8	31.9	14.3	57.8	3.4
MU1.2	57.5	67.4	1468	2303	134	16.3	20.5	n.d.	1.0	2.4	0.0	0.7	0.0	0.7	19.2	11.0	46.1	2.6
MU2.2	56.8	72.7	1380	2160	144	12.1	21.7	0.2	0.1	0.6	0.1	1.5	0.4	0.7	20.6	12.0	50.4	6.9
MU3.1	62.1	72.8	1474	2182	151	20.9	21.2	0.2	0.4	3.0	0.0	1.6	0.6	0.6	26.5	11.7	49.5	6.9
I1	111.0	148.1	93	197	375	43.1	48.1	5.7	21.1	12.3	n.d.	0.5	1.1	9.4	78.6	27.3	142.6	3.0
I2	61.5	66.7	1205	2590	126	4.2	25.4	0.1	-2.0	0.5	n.d.	2.0	0.8	0.7	9.9	7.1	35.8	0.0
I3	77.7	93.0	208	600	268	19.5	43.2	0.7	8.7	4.7	0.6	n.d.	0.6	3.2	38.6	18.0	72.3	1.9
I5	90.4	95.6	1230	1507	180	19.7	23.2	3.6	11.2	9.0	0.4	n.d.	0.8	6.0	61.0	14.5	110.2	0.6
I6	106.9	62.9	678	1116	256	94.7	31.2	13.7	37.0	21.5	0.5	n.d.	1.6	17.0	159.2	31.0	158.5	2.9
I7	68.3	107.3	200	389	250	24.7	42.9	1.7	6.4	5.4	0.4	n.d.	0.7	2.7	35.9	15.6	115.4	2.2
I8	72.4	109.5	269	826	259	15.4	47.5	n.d.	3.3	4.2	0.8	n.d.	1.0	2.0	33.8	17.0	88.6	1.2
I9	78.4	131.0	337	828	266	10.3	46.4	n.d.	5.9	2.8	0.7	n.d.	0.8	1.7	36.8	19.6	82.2	1.1
ED	74.3	91.4	434	1124	217	26.5	31.6	4.6	17.0	9.1	n.d.	n.d.	n.d.	6.5	60.8	15.3	158.1	3.8
SD	87.8	47.1	1041	1715	170	17.7	28.0	5.4	13.7	9.1	n.d.	n.d.	n.d.	6.9	53.6	13.6	129.9	0.7
VEY	71.6	42.6	721	1046	148	29.6	27.0	4.6	12.9	9.2	n.d.	n.d.	n.d.	5.8	58.7	16.6	170.8	2.4
VP1	84.5	79.4	477	864	228	37.6	28.3	4.6	17.8	10.4	n.d.	n.d.	n.d.	7.9	73.8	17.9	163.3	2.2

Appendix E. Olivine compositions

E.1 Olivine core compositions

Table E.1: Major element abundances (wt%) in olivine cores determined by EPMA. n.d. = not determined.

Data point	SiO_2	Al_2O_3	MgO	FeO	CaO	TiO_2	MnO	NiO	Cr_2O_3	Total	Mg#
S1_2	39.87	0.1184	50.95	8.24	0.32	0.01	0.13	0.41	n.d.	100.0	91.7
S1_4	40.70	0.0809	50.38	8.75	0.31	0.00	0.12	0.41	n.d.	100.7	91.1
S1_5	40.29	0.1167	51.07	8.24	0.31	0.00	0.14	0.40	n.d.	100.6	91.7
S1_6	40.65	0.0767	50.56	8.49	0.31	0.00	0.13	0.43	n.d.	100.6	91.4
S1_7	40.90	0.1244	49.87	9.15	0.32	0.01	0.12	0.38	n.d.	100.9	90.7
S1_8	40.62	0.1693	50.59	8.52	0.31	0.01	0.13	0.41	n.d.	100.8	91.4
S1_9	41.52	0.1083	50.24	8.55	0.31	0.00	0.13	0.40	n.d.	101.3	91.3
S1_10	40.99	0.0775	50.45	8.45	0.31	0.01	0.13	0.42	n.d.	100.8	91.4
S1_11	41.40	0.1088	50.31	8.33	0.30	0.01	0.13	0.41	n.d.	101.0	91.5
S1_12	41.12	0.1145	50.56	8.32	0.31	0.01	0.14	0.40	n.d.	101.0	91.5
S1_13	39.44	0.1092	48.04	12.27	0.28	0.00	0.19	0.35	n.d.	100.7	87.5
S1_14	40.37	0.1355	50.77	8.36	0.30	0.01	0.12	0.41	n.d.	100.5	91.5
S1_16	41.32	0.0886	50.75	8.55	0.32	0.00	0.15	0.40	n.d.	101.6	91.4
S1_17	40.78	0.0881	50.63	8.71	0.31	0.00	0.13	0.40	n.d.	101.1	91.2
S1_18	40.58	0.1129	50.80	8.66	0.31	0.01	0.16	0.38	n.d.	101.0	91.3
S1_19	40.96	0.0971	50.67	8.62	0.32	0.01	0.15	0.42	n.d.	101.3	91.3
S1_30	40.74	0.1067	50.85	8.66	0.31	0.01	0.14	0.40	0.12	101.2	91.3
S1_33	41.16	0.1236	50.14	8.44	0.32	0.01	0.13	0.40	0.14	100.7	91.4
S1_35	40.53	0.1285	50.48	8.44	0.31	0.01	0.13	0.39	0.15	100.4	91.4
S1_38	40.72	0.1146	50.49	8.45	0.31	0.01	0.12	0.42	0.12	100.6	91.4
S2_1	41.04	0.1383	49.99	8.06	0.30	0.00	0.13	0.39	0.14	100.1	91.7
S2_2	40.52	0.0863	48.07	10.96	0.33	0.01	0.16	0.35	0.07	100.5	88.7
S2_3	41.25	0.1871	50.35	8.47	0.32	0.00	0.13	0.41	0.13	101.1	91.4
S2_4	40.99	0.1366	50.07	8.70	0.32	0.00	0.13	0.40	0.12	100.7	91.1
S2_6	41.01	0.1038	50.19	8.19	0.31	0.00	0.13	0.39	0.10	100.3	91.6
S2_8	40.73	0.1355	50.37	8.49	0.31	0.01	0.13	0.39	0.14	100.6	91.4
S2_9	40.83	0.1399	49.09	10.13	0.31	0.00	0.16	0.36	0.10	101.0	89.6
S2_10	41.01	0.1116	50.15	8.63	0.31	0.00	0.14	0.42	0.13	100.8	91.2
S3_1	41.55	0.1005	50.12	8.71	0.31	0.00	0.13	0.40	n.d.	101.3	91.1
S3_2	41.17	0.1023	50.33	8.35	0.31	0.01	0.13	0.38	n.d.	100.8	91.5
S3_3	41.24	0.1064	50.27	8.51	0.31	0.01	0.13	0.40	n.d.	101.0	91.3
S3_4	41.38	0.1148	50.26	8.32	0.32	0.01	0.13	0.42	n.d.	101.0	91.5
S3_7	40.52	0.0925	47.94	11.33	0.33	0.01	0.17	0.31	n.d.	100.7	88.3
S3_8	41.70	0.0771	49.98	8.58	0.31	0.00	0.14	0.39	n.d.	101.2	91.2
S3_9	41.33	0.1161	50.54	8.33	0.32	0.00	0.14	0.41	n.d.	101.2	91.5
S3_15	41.35	0.0774	50.18	8.96	0.32	0.01	0.15	0.40	n.d.	101.4	90.9
S3_25	40.41	0.1519	49.61	8.96	0.30	0.00	0.14	0.38	0.11	100.0	90.8
S3_27	40.29	0.1138	50.61	8.03	0.31	0.01	0.13	0.41	0.13	99.9	91.8
S3_29	40.62	0.1368	49.72	8.23	0.31	0.01	0.12	0.41	0.19	99.6	91.5
S3_31	40.86	0.1112	50.17	8.35	0.31	0.01	0.12	0.42	0.13	100.3	91.5
S3_33	40.13	0.0958	50.48	8.44	0.31	0.01	0.13	0.41	0.13	100.0	91.4
S5_2	40.96	0.0992	50.68	8.60	0.32	0.00	0.13	0.41	n.d.	101.2	91.3
S5_3	41.28	0.1157	50.13	8.27	0.31	0.00	0.12	0.38	n.d.	100.6	91.5
S5_5	41.32	0.0869	50.27	8.54	0.33	0.01	0.13	0.40	n.d.	101.1	91.3
S5_6	39.83	0.0788	51.04	8.39	0.31	0.01	0.12	0.39	n.d.	100.2	91.5
S5_7	40.97	0.1110	50.95	8.39	0.31	0.00	0.15	0.41	n.d.	101.3	91.5
S5_9	40.94	0.1112	50.75	8.46	0.30	0.01	0.12	0.36	n.d.	101.0	91.4
S5_11	40.62	0.0844	48.75	10.09	0.33	0.01	0.16	0.35	n.d.	100.4	89.6
S5_13	40.97	0.1179	50.80	8.20	0.31	0.01	0.13	0.41	n.d.	100.9	91.7
S5_14	40.88	0.0671	50.64	8.37	0.33	0.01	0.13	0.39	n.d.	100.8	91.5

Table E.1: Major element abundances (wt%) in olivine cores determined by EPMA. n.d. = not determined.

Data point	SiO_2	Al_2O_3	MgO	FeO	CaO	TiO_2	MnO	NiO	Cr_2O_3	Total	Mg#
S5_15	40.60	0.1188	50.22	8.49	0.32	0.01	0.12	0.40	n.d.	100.3	91.3
S5_16	41.01	0.1059	49.37	9.59	0.33	0.01	0.13	0.38	n.d.	100.9	90.2
S5_18	41.16	0.1219	50.84	8.40	0.31	0.00	0.13	0.42	n.d.	101.4	91.5
S5_19	40.64	0.1137	50.68	8.35	0.32	0.01	0.10	0.39	n.d.	100.6	91.5
S5_21	40.94	0.1130	48.86	10.09	0.32	0.01	0.15	0.34	n.d.	100.8	89.6
S5_30	40.21	0.1439	50.08	9.51	0.35	0.00	0.15	0.36	n.d.	100.8	90.4
S5_31	41.00	0.0820	49.81	9.17	0.32	0.01	0.13	0.38	n.d.	100.9	90.6
S5_32	41.60	0.0740	50.60	8.14	0.32	0.00	0.13	0.40	n.d.	101.3	91.7
S5_33	40.80	0.1208	50.29	8.22	0.31	0.01	0.13	0.39	0.14	100.3	91.6
S5_35	40.23	0.1153	50.31	8.04	0.30	0.01	0.13	0.40	0.14	99.5	91.8
S5_39	40.78	0.1067	50.10	8.45	0.31	0.00	0.13	0.41	0.12	100.3	91.4
S5_40	39.99	0.1073	50.22	7.99	0.30	0.00	0.12	0.41	0.14	99.1	91.8
S5_44	40.00	0.1002	49.87	8.04	0.30	0.01	0.12	0.38	0.15	98.8	91.7
S5_46	40.44	0.1217	48.38	10.05	0.32	0.01	0.14	0.35	0.10	99.8	89.6
S6_2	41.15	0.1067	50.50	8.53	0.31	0.01	0.14	0.40	0.12	101.2	91.3
S6_3	40.78	0.0946	50.25	8.54	0.31	0.01	0.12	0.40	0.12	100.5	91.3
S6_5	41.06	0.1075	49.93	8.79	0.31	0.00	0.13	0.37	0.13	100.7	91.0
S6_6	41.05	0.1191	50.43	7.93	0.31	0.01	0.12	0.39	0.15	100.4	91.9
S6_8	41.14	0.1246	50.28	8.24	0.31	0.01	0.14	0.39	0.14	100.6	91.6
S6_9	40.34	0.0720	49.40	9.76	0.32	0.01	0.14	0.38	0.09	100.4	90.0
S6_10	40.04	0.0795	49.85	9.98	0.32	0.00	0.15	0.39	0.09	100.8	89.9
S6_11	41.21	0.1034	50.13	8.71	0.32	0.00	0.12	0.37	0.12	101.0	91.1
S6_12	40.85	0.1154	49.62	9.57	0.31	0.01	0.14	0.37	0.13	101.0	90.2
S6_13	40.78	0.1134	50.64	8.23	0.31	0.00	0.13	0.40	0.14	100.6	91.6
S6_14	40.32	0.0879	50.08	8.97	0.31	0.01	0.14	0.36	0.13	100.3	90.9
S6_17	40.95	0.1032	50.19	8.91	0.30	0.00	0.14	0.37	0.13	101.0	90.9
S6_18	41.08	0.1184	50.71	7.70	0.31	0.00	0.13	0.40	0.15	100.5	92.1
S7_1	40.98	0.1109	50.25	8.64	0.31	0.00	0.12	0.41	0.14	100.8	91.2
S7_3	40.06	0.0681	50.05	8.82	0.30	0.01	0.13	0.38	0.09	99.8	91.0
S7_4	40.66	0.0950	48.25	10.56	0.32	0.01	0.17	0.35	0.09	100.4	89.1
S7_5	40.36	0.1037	49.36	9.97	0.31	0.01	0.15	0.37	0.10	100.6	89.8
S7_8	40.93	0.0842	50.12	8.95	0.31	0.00	0.14	0.40	0.12	100.9	90.9
S7_9	40.43	0.1166	48.39	8.78	0.28	0.02	0.14	0.38	0.12	98.5	90.8
S7_10	40.00	0.0767	49.70	9.35	0.31	0.01	0.14	0.38	0.10	100.0	90.5
S7_11	39.46	0.1046	49.63	9.74	0.32	0.01	0.13	0.36	0.10	99.8	90.1
S7_13	40.02	0.0943	49.42	10.01	0.32	0.00	0.14	0.36	0.12	100.4	89.8
S7_15	40.15	0.0745	50.42	8.79	0.30	0.00	0.13	0.42	0.11	100.3	91.1
S8_1	40.60	0.1024	49.84	8.75	0.31	0.01	0.14	0.36	n.d.	100.1	91.0
S8_3	40.97	0.0999	47.69	11.64	0.32	0.01	0.18	0.33	n.d.	101.3	87.9
S8_4	40.05	0.1038	48.87	10.68	0.32	0.00	0.17	0.35	n.d.	100.6	89.1
S8_6	39.97	0.0816	50.52	9.21	0.31	0.01	0.14	0.39	n.d.	100.6	90.7
S8_8	41.35	0.0561	49.93	8.82	0.31	0.01	0.15	0.39	n.d.	101.0	91.0
S8_9	40.62	0.0765	50.43	9.07	0.31	0.00	0.15	0.36	n.d.	101.0	90.8
S8_11	40.53	0.0703	49.33	10.24	0.26	0.01	0.13	0.41	n.d.	101.0	89.6
S8_12	39.86	0.0815	50.45	8.72	0.31	0.01	0.12	0.43	n.d.	100.0	91.2
S8_13	41.39	0.2205	49.88	8.88	0.31	0.01	0.15	0.40	n.d.	101.2	90.9
S8_14	41.10	0.0869	50.01	8.99	0.31	0.00	0.13	0.35	n.d.	101.0	90.8
S8_16	40.21	0.0828	49.74	10.02	0.32	0.01	0.15	0.37	n.d.	100.9	89.8
S8_17	40.13	0.0637	50.08	8.73	0.30	0.01	0.14	0.40	n.d.	99.9	91.1
S8_18	40.81	0.0988	49.53	9.83	0.32	0.00	0.14	0.39	n.d.	101.1	90.0
S8_19	40.94	0.0857	50.53	8.57	0.31	0.00	0.12	0.40	n.d.	101.0	91.3
S8_26	40.73	0.0938	50.11	9.32	0.32	0.01	0.15	0.38	0.10	101.1	90.5
S8_28	40.42	0.0931	50.03	9.34	0.32	0.01	0.13	0.37	0.54	100.7	90.5
S8_29	40.62	0.1016	50.23	9.00	0.32	0.00	0.16	0.40	0.12	100.8	90.9
S8_31	41.21	0.0794	50.55	8.89	0.31	0.00	0.14	0.41	0.12	101.6	91.0
S8_38	40.46	0.1256	50.08	9.40	0.32	0.01	0.14	0.37	0.11	100.9	90.5
S9_1	40.71	0.0919	50.01	8.12	0.30	0.01	0.12	0.40	0.12	99.8	91.7
S9_4	40.44	0.1436	50.04	8.14	0.30	0.00	0.13	0.41	0.15	99.6	91.6
S9_6	40.74	0.1035	50.29	8.00	0.30	0.01	0.14	0.39	0.13	100.0	91.8
S9_9	40.89	0.1217	50.22	8.23	0.30	0.01	0.13	0.41	0.14	100.3	91.6
S9_10	40.59	0.1054	50.27	8.33	0.31	0.01	0.13	0.39	0.13	100.1	91.5
S9_12	40.85	0.0798	49.76	9.05	0.31	0.00	0.14	0.40	0.10	100.6	90.7
S9_13	40.32	0.0962	49.36	8.93	0.32	0.01	0.14	0.38	0.12	99.6	90.8
S9_15	40.20	0.0961	49.50	8.82	0.31	0.01	0.13	0.40	0.12	99.5	90.9
S9_17	40.88	0.0959	49.66	8.57	0.31	0.00	0.13	0.39	0.13	100.0	91.2
S9_19	40.39	0.1151	50.21	7.74	0.31	0.02	0.13	0.41	0.14	99.3	92.0
S10_1	41.18	0.1363	50.51	7.66	0.30	0.00	0.12	0.40	n.d.	100.3	92.2
S10_2	41.30	0.1198	50.77	7.28	0.30	0.01	0.14	0.42	n.d.	100.4	92.5
S10_3	40.46	0.1020	51.09	7.81	0.30	0.01	0.13	0.41	n.d.	100.3	92.1

Table E.1: Major element abundances (wt%) in olivine cores determined by EPMA. n.d. = not determined.

Data point	SiO_2	Al_2O_3	MgO	FeO	CaO	TiO_2	MnO	NiO	Cr_2O_3	Total	Mg#
S10_5	40.52	0.0791	49.69	9.08	0.25	0.00	0.25	0.38	n.d.	100.3	90.7
S10_6	40.77	0.1080	50.52	8.66	0.31	0.01	0.13	0.38	n.d.	100.9	91.2
S10_7	40.37	0.0896	50.48	8.14	0.31	0.01	0.13	0.38	n.d.	99.9	91.7
S10_12	40.15	0.0950	50.27	9.29	0.28	0.00	0.13	0.40	n.d.	100.6	90.6
S10_20	40.75	0.1022	50.71	8.17	0.30	0.01	0.13	0.41	0.13	100.6	91.7
S10_22	40.39	0.1159	49.98	8.27	0.30	0.00	0.12	0.41	0.15	99.6	91.5
S10_25	40.69	0.1261	49.90	8.34	0.29	0.01	0.13	0.40	0.14	99.9	91.4
S10_28	40.83	0.0849	50.26	7.68	0.30	0.01	0.13	0.39	0.14	99.7	92.1
S10_30	40.07	0.1033	50.78	7.95	0.29	0.00	0.10	0.41	0.13	99.7	91.9
S10_31	40.60	0.1276	50.74	7.20	0.30	0.01	0.12	0.44	0.15	99.5	92.6
S10_33	40.27	0.1037	50.10	8.13	0.31	0.01	0.12	0.40	0.15	99.4	91.7
S10_35	40.87	0.1034	50.65	7.55	0.30	0.01	0.12	0.41	0.14	100.0	92.3
S10_37	40.74	0.1099	50.75	7.35	0.29	0.00	0.11	0.41	0.14	99.8	92.5
S10_39	40.68	0.1076	50.24	7.94	0.29	0.01	0.14	0.44	0.11	99.8	91.8
R10_1	40.00	0.0733	47.81	11.97	0.03	0.00	0.17	0.39	0.03	100.4	87.7
R10_3	40.45	0.1175	47.99	10.58	0.50	0.00	0.13	0.37	0.19	100.1	89.0
R10_4	40.46	0.0604	49.18	10.12	0.04	0.01	0.16	0.38	0.02	100.4	89.7
R10_6	40.55	0.0819	48.03	11.02	0.28	0.02	0.17	0.35	0.08	100.5	88.6
R10_7	40.09	0.0658	45.61	14.53	0.03	0.01	0.29	0.33	0.01	101.0	84.8
R10_9	39.09	0.0439	44.88	15.42	0.30	0.01	0.24	0.17	0.04	100.2	83.8
R10_11	39.83	0.0353	47.95	11.76	0.05	0.00	0.18	0.29	0.01	100.1	87.9
R10_13	40.06	0.0441	46.52	13.23	0.15	0.01	0.20	0.29	0.01	100.5	86.2
R10_18	39.34	0.0765	45.04	15.04	0.02	0.01	0.27	0.35	0.02	100.1	84.2
R10_19	40.65	0.0969	49.24	10.36	0.37	0.02	0.16	0.39	0.10	101.3	89.4
R10_22	40.36	0.1153	48.65	10.92	0.51	0.01	0.16	0.38	0.12	101.1	88.8
R10_26	40.16	0.0553	48.23	12.03	0.05	0.01	0.19	0.35	0.01	101.1	87.7
M9_1	41.49	0.1093	50.85	7.72	0.29	n.d	0.11	0.45	0.15	101.2	92.1
M9_3	41.67	0.1199	50.49	7.75	0.26	n.d	0.12	0.48	0.13	101.0	92.1
M9_5	41.39	0.1200	50.90	7.23	0.28	n.d	0.10	0.47	0.13	100.6	92.6
M9_9	40.82	0.1165	49.47	9.18	0.29	n.d	0.12	0.36	0.14	100.5	90.6
M9_13	41.37	0.1332	50.91	7.69	0.32	n.d	0.11	0.46	0.14	101.1	92.2
M9_15	41.28	0.1104	51.02	7.57	0.28	n.d	0.10	0.46	0.14	101.0	92.3
M9_17	40.13	0.1177	49.55	7.93	0.24	n.d	0.11	0.48	0.13	98.7	91.8
M9_21	40.59	0.1169	50.54	7.52	0.28	n.d	0.12	0.48	0.15	99.8	92.3
M9_23	40.62	0.1147	50.93	7.65	0.29	n.d	0.11	0.45	0.15	100.3	92.2
M9_25	39.56	0.1251	50.74	7.75	0.28	n.d	0.11	0.47	0.15	99.2	92.1
MU1.1_1	40.76	0.0981	51.14	7.82	0.28	0.01	0.11	0.43	0.12	100.6	92.1
MU1.1_5	41.08	0.0747	50.55	8.19	0.29	0.00	0.12	0.42	0.12	100.7	91.7
MU1.1_6	41.07	0.0675	50.51	8.36	0.29	0.01	0.13	0.41	0.08	100.8	91.5
MU1.1_7	40.92	0.0811	51.30	7.73	0.30	0.01	0.12	0.41	0.12	100.9	92.2
MU1.1_9	40.89	0.1013	51.19	7.56	0.25	0.01	0.13	0.42	0.12	100.6	92.3
MU1.1_11	40.30	0.0375	49.61	9.68	0.29	0.00	0.16	0.39	0.05	100.5	90.1
MU1.1_12	41.24	0.0725	50.51	7.97	0.30	0.01	0.13	0.42	0.11	100.6	91.9
MU1.1_13	40.24	0.1054	48.69	9.55	0.29	0.01	0.15	0.40	0.09	99.4	90.1
MU1.1_14	41.00	0.0780	50.76	7.37	0.23	0.00	0.11	0.42	0.10	100.0	92.5
MU1.1_15	40.72	0.0767	50.61	8.01	0.31	0.01	0.12	0.42	0.11	100.3	91.8
MU1.1_17	40.17	0.0894	48.07	11.36	0.27	0.01	0.18	0.38	0.10	100.5	88.3
MU1.1_19	40.62	0.0795	50.64	8.28	0.27	0.01	0.14	0.43	0.10	100.5	91.6
MU1.1_22	40.81	0.0937	50.33	8.40	0.29	0.01	0.12	0.44	0.13	100.5	91.4
MU1.1_24	41.07	0.0776	50.57	7.52	0.26	0.01	0.11	0.42	0.12	100.0	92.3
MU1.1_27	40.45	0.0951	50.55	7.76	0.28	0.01	0.12	0.43	0.13	99.7	92.1
MU1.1_31	41.01	0.0832	50.98	7.98	0.25	0.00	0.12	0.40	0.09	100.8	91.9
MU1.2_1	40.39	0.0874	49.03	9.39	0.27	0.01	0.13	0.42	0.11	99.7	90.3
MU1.2_4	40.16	0.1016	48.23	10.56	0.28	0.01	0.16	0.38	0.10	99.9	89.1
MU1.2_6	40.50	0.0898	49.10	9.87	0.24	0.00	0.14	0.41	0.10	100.4	89.9
MU1.2_7	40.16	0.0804	47.39	12.59	0.30	0.01	0.17	0.37	0.08	101.1	87.0
MU1.2_8	40.93	0.0837	50.74	8.02	0.27	0.00	0.11	0.38	0.11	100.5	91.9
MU1.2_12	39.27	0.1050	46.46	13.30	0.29	0.01	0.19	0.37	0.09	100.0	86.2
MU1.2_14	40.27	0.0812	48.71	9.85	0.27	0.02	0.14	0.38	0.09	99.7	89.8
MU1.2_17	40.35	0.0921	49.24	9.46	0.30	0.01	0.14	0.40	0.09	100.0	90.3
MU1.2_24	39.52	0.0727	45.93	13.69	0.27	0.01	0.21	0.35	0.08	100.0	85.7
MU1.2_26	39.97	0.0897	46.95	12.35	0.28	0.00	0.20	0.38	0.09	100.2	87.1
MU1.2_27	39.78	0.0977	46.33	13.07	0.23	0.01	0.20	0.36	0.09	100.1	86.3
MU2.2_1	40.13	0.1025	50.45	7.87	0.25	0.01	0.12	0.43	0.11	99.4	92.0
MU2.2_3	41.30	0.0839	51.15	7.59	0.24	0.01	0.11	0.42	0.10	100.9	92.3
MU2.2_6	41.01	0.0953	49.50	9.28	0.28	0.01	0.15	0.43	0.13	100.8	90.5
MU2.2_9	41.55	0.0644	50.74	7.80	0.24	0.01	0.13	0.44	0.09	101.0	92.1
MU2.2_11	41.04	0.0912	50.57	7.37	0.28	0.01	0.12	0.43	0.12	99.9	92.4
MU2.2_13	39.97	0.0464	46.43	13.22	0.31	0.01	0.20	0.29	0.04	100.5	86.2

Table E.1: Major element abundances (wt%) in olivine cores determined by EPMA. n.d. = not determined.

Data point	SiO_2	Al_2O_3	MgO	FeO	CaO	TiO_2	MnO	NiO	Cr_2O_3	Total	Mg#
MU2.2_15	41.02	0.1016	50.43	7.49	0.29	0.01	0.11	0.44	0.12	99.9	92.3
MU2.2_18	40.83	0.0829	50.53	7.56	0.28	0.00	0.10	0.44	0.13	99.8	92.3
MU2.2_19	40.57	0.1133	51.03	6.73	0.27	0.01	0.11	0.46	0.32	99.3	93.1
MU2.2_21	40.52	0.0762	48.44	11.80	0.26	0.00	0.16	0.39	0.09	101.6	88.0
MU2.2_22	40.12	0.0949	47.46	11.68	0.28	0.01	0.14	0.37	0.11	100.2	87.9
MU2.2_23	40.53	0.0968	50.81	7.60	0.28	0.01	0.13	0.42	0.13	99.9	92.3
MU3.1_1	40.98	0.1188	50.32	7.68	0.26	0.01	0.12	0.43	0.12	99.9	92.1
MU3.1_4	40.64	0.0988	49.94	9.01	0.29	0.01	0.12	0.42	0.11	100.5	90.8
MU3.1_6	40.63	0.0574	49.96	8.95	0.28	0.00	0.13	0.42	0.07	100.4	90.9
MU3.1_8	40.55	0.0951	49.02	9.91	0.30	0.01	0.16	0.42	0.11	100.5	89.8
MU3.1_12	40.77	0.0975	51.04	7.92	0.29	0.01	0.12	0.42	0.11	100.7	92.0
MU3.1_13	40.37	0.0953	48.61	10.38	0.24	0.01	0.16	0.41	0.10	100.3	89.3
MU3.1_14	40.87	0.0953	50.65	8.04	0.28	0.00	0.12	0.43	0.12	100.5	91.8
MU3.1_15	40.81	0.0816	50.43	8.01	0.28	0.00	0.12	0.43	0.11	100.2	91.8
MU3.1_17	41.10	0.0931	49.02	10.27	0.29	0.01	0.15	0.39	0.10	101.3	89.5
APO4_1	40.44	0.0821	48.07	12.01	0.32	0.01	0.16	0.36	0.10	101.5	87.7
APO4_2	40.82	0.0645	49.44	9.58	0.25	0.01	0.13	0.38	0.11	100.7	90.2
APO4_3	39.88	0.0879	48.06	11.48	0.31	0.01	0.17	0.37	0.09	100.4	88.2
APO4_4	39.94	0.0844	48.43	11.46	0.30	0.01	0.16	0.39	0.09	100.8	88.3
APO4_5	39.58	0.1074	47.83	11.79	0.28	0.00	0.17	0.39	0.11	100.2	87.8
APO4_6	39.66	0.1002	48.11	11.66	0.27	0.01	0.16	0.39	0.12	100.4	88.0
APO4_7	40.26	0.0747	47.76	11.71	0.30	0.00	0.17	0.37	0.08	100.6	87.9
APO7_1	40.95	0.0959	51.20	7.29	0.28	0.01	0.11	0.44	0.18	100.4	92.6
APO7_2	41.29	0.0668	50.92	8.11	0.28	0.00	0.13	0.46	0.14	101.3	91.8
APO7_3	41.04	0.0849	51.03	7.78	0.29	0.01	0.11	0.46	0.14	100.8	92.1
APO7_4	40.62	0.0992	51.31	7.31	0.28	0.01	0.10	0.46	0.16	100.2	92.6
APO7_5	40.00	0.0833	47.74	12.17	0.29	0.01	0.17	0.36	0.10	100.8	87.5
APO7_6	40.24	0.0568	46.49	13.04	0.34	0.01	0.20	0.35	0.06	100.7	86.4
DUR6_1	40.75	0.0848	51.00	7.46	0.28	0.00	0.10	0.45	0.14	100.1	92.4
DUR6_2	39.65	0.0917	51.19	7.66	0.29	0.01	0.11	0.44	0.17	99.4	92.3
DUR6_4	41.12	0.0781	49.97	8.64	0.29	0.00	0.13	0.46	0.13	100.7	91.2
DUR6_5	39.37	0.0519	48.77	10.07	0.33	0.00	0.15	0.39	0.08	99.1	89.6
DUR6_7	40.59	0.0967	49.62	9.29	0.28	0.01	0.14	0.42	0.11	100.4	90.5
DUR6_9	39.67	0.0766	47.89	11.25	0.30	0.00	0.16	0.37	0.08	99.7	88.3
DUR8_1	38.90	0.0468	45.35	15.03	0.34	0.01	0.21	0.24	0.06	100.1	84.3
DUR8_2	38.94	0.0987	47.31	12.46	0.31	0.00	0.18	0.33	0.11	99.6	87.1
DUR8_4	40.14	0.1027	47.07	12.23	0.32	0.01	0.17	0.32	0.09	100.4	87.3
DUR8_5	39.71	0.0617	46.08	13.90	0.32	0.01	0.20	0.32	0.06	100.6	85.5
DUR8_7	40.17	0.1071	49.25	9.90	0.29	0.01	0.14	0.44	0.15	100.3	89.9
PAD4_1	40.25	0.0568	48.08	11.43	0.33	0.01	0.15	0.35	0.06	100.7	88.2
PAD4_2	40.76	0.0718	50.39	8.16	0.28	0.00	0.12	0.46	0.13	100.2	91.7
PAD4_3	40.56	0.1023	50.58	7.29	0.28	0.00	0.11	0.46	0.16	99.4	92.5
PAD4_4	39.84	0.0604	47.15	12.19	0.34	0.00	0.19	0.34	0.07	100.1	87.3
PAD4_5	40.67	0.0929	50.14	8.46	0.28	0.01	0.11	0.46	0.13	100.2	91.3
PAD4_6	39.72	0.0736	47.33	11.78	0.30	0.01	0.17	0.36	0.08	99.7	87.7
PAD4_9	40.23	0.0634	49.06	9.96	0.28	0.01	0.14	0.43	0.10	100.2	89.8
PAD4_10	40.44	0.1002	49.95	9.19	0.27	0.01	0.15	0.46	0.16	100.6	90.6
PAD4_11	39.97	0.0780	47.73	11.96	0.31	0.01	0.17	0.36	0.10	100.6	87.7
PAD5_1	40.30	0.0803	48.37	11.06	0.34	0.01	0.14	0.38	0.08	100.7	88.6
PAD5_2	40.50	0.0850	50.76	8.05	0.30	0.01	0.11	0.45	0.11	100.3	91.8
PAD5_3	40.60	0.0949	50.79	7.77	0.29	0.01	0.11	0.45	0.14	100.1	92.1
PAD5_4	40.79	0.1005	50.97	7.94	0.29	0.01	0.10	0.46	0.14	100.7	92.0
PAD5_5	40.37	0.1502	49.86	8.50	0.28	0.01	0.14	0.43	0.15	99.7	91.3
PAD5_6	39.96	0.0764	47.93	11.61	0.34	0.01	0.17	0.36	0.09	100.4	88.0
PAD5_7	39.61	0.0785	46.98	11.92	0.30	0.01	0.18	0.36	0.08	99.4	87.5
PAD5_5_2	40.78	0.0988	50.37	9.35	0.28	0.01	0.14	0.43	0.14	101.5	90.6
PAD6_1	40.18	0.0924	49.14	9.51	0.29	0.01	0.15	0.42	0.10	99.8	90.2
PAD6_3	39.64	0.0398	47.32	12.48	0.32	0.00	0.18	0.33	0.06	100.3	87.1
PAD6_5	39.43	0.0922	46.74	13.09	0.32	0.01	0.20	0.34	0.08	100.2	86.4
PAD6_6	40.73	0.0971	50.62	8.07	0.29	0.01	0.13	0.45	0.15	100.4	91.8
PAD6_8	40.05	0.1008	50.43	9.40	0.28	0.01	0.12	0.44	0.15	100.8	90.5
PAD6_10	39.94	0.1085	49.80	9.69	0.28	0.00	0.14	0.40	0.15	100.4	90.2
PAD6_12	40.02	0.1037	49.73	8.93	0.29	0.01	0.14	0.45	0.15	99.7	90.8
PAD6_15	39.70	0.0927	47.31	12.59	0.31	0.00	0.18	0.35	0.09	100.5	87.0
PAD6_17	40.01	0.0782	48.59	11.00	0.29	0.01	0.16	0.38	0.11	100.5	88.7
PAD6_18	40.37	0.1096	49.52	9.88	0.30	0.02	0.14	0.43	0.09	100.8	89.9
138345_1	40.55	0.0999	50.68	7.75	0.27	0.01	0.11	0.43	0.15	99.9	92.1
138345_3	40.07	0.1101	50.97	7.31	0.26	0.01	0.12	0.47	0.15	99.3	92.6
138345_4	40.52	0.1269	49.50	9.66	0.25	0.01	0.14	0.40	0.13	100.6	90.1

Table E.1: Major element abundances (wt%) in olivine cores determined by EPMA. n.d. = not determined.

Data point	SiO_2	Al_2O_3	MgO	FeO	CaO	TiO_2	MnO	NiO	Cr_2O_3	Total	Mg#
138345_5	40.25	0.1078	51.00	7.39	0.27	0.01	0.11	0.47	0.15	99.6	92.5
138345_6	40.46	0.1063	51.15	7.12	0.27	0.01	0.09	0.45	0.16	99.7	92.8
138345_8	40.91	0.1021	50.88	7.64	0.27	0.01	0.12	0.46	0.16	100.4	92.2
138345_9	39.08	0.0843	45.35	15.05	0.27	0.01	0.21	0.33	0.08	100.4	84.3
138345_10	38.85	0.0949	46.45	12.96	0.26	0.01	0.19	0.40	0.11	99.2	86.5
138345_14	41.03	0.0923	51.13	7.15	0.27	0.01	0.10	0.47	0.16	100.2	92.7
138345_15	39.22	0.1100	47.82	11.77	0.25	0.01	0.15	0.38	0.11	99.7	87.9
138345_16	39.06	0.0372	44.62	16.14	0.32	0.01	0.21	0.29	0.03	100.7	83.1
138345_18	39.13	0.0702	44.59	14.86	0.32	0.02	0.21	0.32	0.07	99.5	84.2
340740_1	39.65	0.0758	48.97	10.26	0.28	0.02	0.14	0.45	0.10	99.8	89.5
340740_3	40.33	0.0921	50.32	8.70	0.28	0.01	0.13	0.47	0.14	100.3	91.2
340740_5	40.46	0.0978	49.46	9.56	0.27	0.01	0.12	0.44	0.12	100.4	90.2
340740_6	39.36	0.0804	48.40	11.00	0.27	0.01	0.15	0.44	0.09	99.7	88.7
340740_7	40.43	0.0894	48.77	9.85	0.27	0.01	0.13	0.45	0.12	100.0	89.8
340740_8	40.21	0.0697	49.79	9.52	0.28	0.01	0.14	0.48	0.11	100.5	90.3
340740_10	40.66	0.0729	48.41	10.27	0.28	0.01	0.15	0.44	0.09	100.3	89.4
340740_11	40.17	0.0925	50.92	8.06	0.28	0.01	0.13	0.49	0.12	100.1	91.8
340740_13	40.50	0.0980	50.56	8.33	0.28	0.01	0.12	0.47	0.14	100.4	91.5
340740_15	39.33	0.0951	48.16	11.18	0.27	0.01	0.16	0.42	0.11	99.6	88.5
354754_1	35.67	0.0711	45.72	12.84	0.30	0.01	0.16	0.37	0.08	95.1	86.4
354754_3	35.77	0.0479	45.15	13.84	0.30	0.00	0.19	0.33	0.06	95.6	85.3
354754_4	39.61	0.0673	46.18	13.20	0.17	0.02	0.18	0.41	0.06	99.8	86.2
354754_6	39.14	0.0397	45.86	13.44	0.34	0.00	0.20	0.35	0.05	99.4	85.9
354754_7	39.34	0.0660	46.11	13.55	0.33	0.01	0.19	0.35	0.06	99.9	85.8
354754_8	39.46	0.0745	46.46	13.52	0.32	0.01	0.18	0.35	0.07	100.4	86.0
354754_9	39.31	0.0456	46.49	13.62	0.34	0.01	0.18	0.34	0.06	100.3	85.9
354754_11	38.12	0.0486	44.81	14.99	0.34	0.01	0.21	0.31	0.06	98.8	84.2
354754_13	38.46	0.0618	45.79	13.72	0.32	0.01	0.18	0.35	0.06	98.9	85.6
360277_1	40.35	0.1235	49.08	9.67	0.27	0.01	0.14	0.43	0.15	100.1	90.0
360277_3	39.87	0.1015	48.96	10.24	0.28	0.01	0.14	0.42	0.13	100.0	89.5
360277_5	40.42	0.1196	49.29	9.56	0.27	0.01	0.13	0.44	0.14	100.2	90.2
360277_6	41.01	0.1257	50.94	7.94	0.28	0.01	0.12	0.47	0.16	100.9	92.0
360277_8	39.84	0.1438	50.47	8.52	0.27	0.01	0.11	0.45	0.17	99.8	91.3
360277_9	40.83	0.1036	50.70	8.43	0.29	0.01	0.11	0.44	0.13	100.9	91.5
360277_10	40.39	0.0816	49.62	9.68	0.29	0.01	0.13	0.42	0.12	100.6	90.1
360277_12	40.46	0.0780	50.65	8.44	0.28	0.01	0.13	0.43	0.12	100.5	91.4
360277_13	40.82	0.0785	48.39	11.17	0.28	0.01	0.15	0.39	0.09	101.3	88.5
360277_14	40.51	0.1111	50.47	7.57	0.27	0.01	0.11	0.46	0.17	99.5	92.2
360277_15	40.78	0.1154	50.84	7.54	0.28	0.01	0.11	0.47	0.14	100.1	92.3
400230_1	39.10	0.0840	46.88	12.46	0.26	0.01	0.17	0.41	0.10	99.4	87.0
400230_3	39.58	0.0959	48.96	10.66	0.28	0.01	0.14	0.43	0.12	100.1	89.1
400230_5	39.34	0.0884	47.60	12.18	0.28	0.01	0.16	0.41	0.10	100.1	87.4
400230_6	39.02	0.0843	46.92	12.68	0.28	0.01	0.17	0.43	0.12	99.6	86.8
400230_7	39.38	0.0887	47.07	12.86	0.29	0.01	0.18	0.41	0.10	100.3	86.7
400230_9	39.89	0.1009	48.23	11.08	0.27	0.01	0.15	0.42	0.12	100.1	88.6
400230_10	39.43	0.0757	45.50	14.15	0.30	0.01	0.19	0.34	0.07	100.0	85.1
400230_12	40.27	0.1024	50.72	8.11	0.28	0.01	0.11	0.48	0.11	100.1	91.8
400230_13	40.16	0.1054	50.64	7.87	0.26	0.01	0.12	0.49	0.13	99.7	92.0
400230_15	39.88	0.1002	48.09	10.78	0.27	0.01	0.15	0.39	0.10	99.7	88.8
400230_16	38.66	0.0890	46.71	12.67	0.27	0.01	0.17	0.40	0.10	99.0	86.8
400230_18	39.04	0.0676	45.49	14.98	0.34	0.02	0.21	0.33	0.06	100.5	84.4
ED_1	39.52	0.0524	45.36	15.16	0.27	0.01	0.20	0.22	0.04	100.8	84.2
ED_2	40.12	0.0455	45.21	15.20	0.30	0.00	0.21	0.23	0.03	101.3	84.1
ED_3	40.37	0.0497	44.78	14.79	0.30	0.01	0.20	0.23	0.02	100.7	84.4
ED_4	39.47	0.0316	43.16	18.05	0.28	0.02	0.25	0.18	0.01	101.5	81.0
ED_6	40.03	0.0467	45.26	14.11	0.31	0.01	0.18	0.23	0.04	100.2	85.1
ED_7	40.33	0.0509	46.31	13.14	0.32	0.01	0.18	0.25	0.04	100.6	86.3
ED_8	39.54	0.0587	46.10	14.21	0.29	0.01	0.19	0.26	0.05	100.6	85.3
ED_10	39.39	0.0391	43.51	17.43	0.30	0.02	0.22	0.19	0.02	101.1	81.6
ED_11	39.64	0.0533	45.43	14.23	0.30	0.00	0.19	0.23	0.03	100.1	85.0
ED_13	40.35	0.0562	45.89	13.58	0.31	0.02	0.18	0.26	0.05	100.6	85.8
ED_14	39.70	0.0456	44.80	15.37	0.31	0.01	0.21	0.23	0.02	100.7	83.9
ED_15	40.27	0.0546	45.14	14.48	0.31	0.01	0.19	0.23	0.03	100.7	84.7
ED_16	39.75	0.0329	43.85	16.61	0.30	0.02	0.22	0.17	0.02	101.0	82.5
ED_17	40.15	0.0548	45.71	13.49	0.31	0.01	0.19	0.25	0.05	100.2	85.8
KoP_1	40.47	0.0530	46.88	12.91	0.28	0.00	0.19	0.30	0.05	101.1	86.6
KoP_2	40.67	0.0558	47.59	12.17	0.28	0.01	0.17	0.32	0.07	101.3	87.4
KoP_4	40.02	0.0602	47.81	11.55	0.30	0.00	0.16	0.36	0.11	100.3	88.1
KoP_5	40.61	0.0567	46.59	12.77	0.30	0.01	0.18	0.30	0.07	100.8	86.7

Table E.1: Major element abundances (wt%) in olivine cores determined by EPMA. n.d. = not determined.

Data point	SiO_2	Al_2O_3	MgO	FeO	CaO	TiO_2	MnO	NiO	Cr_2O_3	Total	Mg#
KoP_6	41.09	0.0451	47.29	12.32	0.23	0.01	0.17	0.32	0.06	101.5	87.2
KoP_7	40.11	0.0710	47.69	11.28	0.30	0.00	0.16	0.37	0.11	100.0	88.3
KoP_8	40.27	0.0818	48.61	11.09	0.29	0.01	0.16	0.39	0.10	100.9	88.6
KoP_9	40.47	0.0697	48.29	10.85	0.30	0.01	0.16	0.40	0.10	100.5	88.8
KoP_10	39.99	0.0516	45.24	15.68	0.29	0.01	0.21	0.25	0.03	101.7	83.7
KoP_12	39.98	0.0478	44.52	15.97	0.26	0.01	0.23	0.25	0.03	101.3	83.2
KoP_13	40.13	0.0591	45.22	14.76	0.27	0.00	0.21	0.25	0.04	100.9	84.5
KoP_15	40.87	0.0458	47.84	11.72	0.24	0.02	0.16	0.33	0.07	101.2	87.9
KoP_16	40.08	0.0609	45.86	13.43	0.22	0.01	0.20	0.28	0.03	100.1	85.9
SAU3199_1	39.96	0.0469	46.31	13.32	0.31	0.01	0.17	0.27	0.06	100.4	86.1
SAU3199_2	40.34	0.0510	46.85	13.66	0.31	0.02	0.18	0.30	0.06	101.7	85.9
SAU3199_5	39.80	0.0349	44.83	15.28	0.29	0.01	0.20	0.21	0.03	100.7	83.9
SAU3199_7	39.97	0.0503	46.26	13.01	0.30	0.01	0.18	0.28	0.05	100.1	86.4
SAU3199_8	40.10	0.0540	46.22	14.38	0.28	0.01	0.18	0.28	0.04	101.5	85.1
SAU3199_9	40.36	0.0448	46.49	13.29	0.28	0.01	0.17	0.30	0.04	100.9	86.2
SAU3199_10	40.63	0.0365	46.27	13.18	0.31	0.01	0.16	0.29	0.06	100.9	86.2
SAU3199_12	39.85	0.0523	46.46	12.81	0.31	0.00	0.18	0.29	0.06	100.0	86.6
SAU3199_13	39.90	0.0410	46.20	13.43	0.29	0.01	0.16	0.29	0.05	100.3	86.0
SAU3199_14	40.24	0.0544	46.55	12.80	0.30	0.01	0.18	0.29	0.05	100.4	86.6
SAU3199_15	40.15	0.0480	46.30	13.37	0.29	0.02	0.18	0.28	0.04	100.6	86.1
SAU3199_16	40.56	0.0494	46.56	12.87	0.33	0.00	0.17	0.29	0.06	100.8	86.6
SAU3199_17	40.32	0.0469	46.67	12.66	0.29	0.01	0.18	0.33	0.07	100.5	86.8
SD_1	40.12	0.0509	46.20	13.92	0.29	0.01	0.19	0.28	0.03	101.1	85.5
SD_4	40.07	0.0501	45.65	13.95	0.31	0.01	0.19	0.28	0.05	100.5	85.4
SD_6	39.96	0.0527	46.09	13.77	0.31	0.01	0.18	0.27	0.06	100.7	85.6
SD_7	40.07	0.0477	45.98	13.66	0.29	0.01	0.19	0.28	0.04	100.5	85.7
SD_8	39.82	0.0546	45.72	14.22	0.29	0.01	0.21	0.28	0.04	100.6	85.1
SD_9	40.01	0.0522	46.31	13.67	0.30	0.01	0.18	0.29	0.05	100.8	85.8
SD_10	40.07	0.0538	46.30	14.15	0.28	0.01	0.18	0.29	0.04	101.3	85.4
SD_12	39.73	0.0487	45.21	14.69	0.29	0.01	0.20	0.27	0.03	100.4	84.6
SD_13	40.09	0.0555	45.42	13.87	0.29	0.02	0.19	0.27	0.04	100.2	85.4
SD_14	39.93	0.0489	46.14	13.65	0.29	0.01	0.17	0.27	0.03	100.5	85.8
SD_16	39.78	0.0495	45.92	14.14	0.30	0.01	0.19	0.27	0.04	100.7	85.3
VEY_1	40.11	0.0336	49.57	9.40	0.29	0.01	0.15	0.40	0.07	100.0	90.4
VEY_3	39.85	0.2036	44.35	15.25	0.31	0.02	0.22	0.29	0.07	100.5	83.8
VEY_4	39.24	0.0265	44.39	15.46	0.20	0.01	0.21	0.29	0.02	99.8	83.6
VEY_5	39.67	0.0285	43.63	17.57	0.19	0.02	0.23	0.26	0.02	101.6	81.6
VEY_7	38.60	0.0302	43.01	17.98	0.20	0.01	0.25	0.23	0.03	100.3	81.0
VEY_8	40.59	0.0325	48.53	10.00	0.27	0.01	0.16	0.33	0.06	99.9	89.6
VEY_9	39.68	0.0287	44.39	15.65	0.20	0.02	0.22	0.25	0.03	100.4	83.5
VEY_10	39.67	0.0315	44.53	15.49	0.20	0.01	0.23	0.27	0.03	100.4	83.7
VEY_11	41.00	0.0389	49.61	9.02	0.26	0.00	0.13	0.43	0.06	100.5	90.7
VEY_12	40.93	0.0774	49.69	9.49	0.28	0.01	0.13	0.42	0.09	101.0	90.3
VEY_15	41.13	0.0280	47.12	11.84	0.22	0.00	0.18	0.37	0.05	100.9	87.6
VEY_16	39.22	0.0354	44.73	14.95	0.22	0.01	0.22	0.27	0.04	99.7	84.2
VP1a_2	40.69	0.0396	47.78	11.93	0.26	0.01	0.15	0.40	0.09	101.3	87.7
VP1a_3	40.62	0.0626	47.74	11.75	0.28	0.02	0.15	0.42		101.0	87.9
VP1a_5	39.62	0.0372	47.34	11.47	0.27	0.01	0.14	0.42	0.06	99.3	88.0
VP1a_6	40.17	0.0385	47.50	11.97	0.26	0.01	0.16	0.38	0.07	100.5	87.6
VP1a_7	40.04	0.0520	47.35	12.48	0.27	0.01	0.16	0.38	0.07	100.7	87.1
VP1a_8	39.58	0.0468	47.08	12.29	0.30	0.01	0.16	0.34	0.08	99.8	87.2
VP1a_10	40.04	0.0461	46.68	12.59	0.27	0.01	0.17	0.34	0.06	100.1	86.8
VP1a_11	40.99	0.0327	47.14	12.51	0.31	0.01	0.17	0.35	0.07	101.5	87.0
VP1a_13	40.23	0.0511	46.02	13.32	0.29	0.00	0.18	0.34	0.06	100.4	86.0
VP1a_15	40.30	0.0431	47.60	11.72	0.28	0.01	0.16	0.37	0.08	100.5	87.9
VP1a_16	40.26	0.0362	47.25	12.33	0.28	0.01	0.15	0.36	0.06	100.7	87.2
VP1a_17	40.09	0.0402	47.55	11.71	0.26	0.01	0.15	0.37	0.07	100.2	87.9
VP1b_1	40.09	0.0411	45.64	14.31	0.26	0.02	0.20	0.32	0.03	100.9	85.0
VP1b_3	40.05	0.0658	45.82	14.24	0.29	0.01	0.18	0.33	0.05	101.0	85.1
VP1b_4	39.51	0.1945	45.10	14.81	0.25	0.02	0.19	0.35	0.05	100.4	84.4
VP1b_7	40.00	0.0507	46.11	13.98	0.25	0.00	0.18	0.33	0.04	100.9	85.5
VP1b_8	39.77	0.0467	45.41	14.27	0.25	0.02	0.19	0.37	0.03	100.3	85.0
VP1b_10	39.95	0.0473	47.17	12.45	0.30	0.00	0.15	0.34	0.08	100.4	87.1
VP1b_11	40.73	0.0469	47.51	11.59	0.26	0.01	0.17	0.36	0.08	100.7	88.0
VP1b_13	40.30	0.0403	46.68	12.89	0.28	0.01	0.17	0.34	0.06	100.7	86.6
VP1b_14	40.17	0.0496	45.98	14.45	0.26	0.01	0.20	0.34	0.05	101.5	85.0
VP1b_16	39.59	0.0577	45.11	15.10	0.24	0.01	0.18	0.33	0.04	100.6	84.2
VP1b_17	40.25	0.0406	46.54	12.70	0.29	0.00	0.16	0.35	0.06	100.3	86.7
VP1b_18	39.60	0.0540	46.16	13.58	0.24	0.01	0.18	0.33	0.05	100.1	85.8

Table E.1: Major element abundances (wt%) in olivine cores determined by EPMA. n.d. = not determined.

Data point	SiO_2	Al_2O_3	MgO	FeO	CaO	TiO_2	MnO	NiO	Cr_2O_3	Total	Mg#
VP1b_19	39.71	0.0502	46.92	12.74	0.30	0.01	0.17	0.35	0.08	100.2	86.8
I1_1	38.67	0.0400	40.70	20.41	0.29	0.01	0.30	0.15	0.02	100.6	78.0
I1_3	38.31	0.0454	40.58	19.83	0.29	0.01	0.29	0.17	0.02	99.5	78.5
I1_8	38.19	0.0322	37.27	24.71	0.31	0.02	0.37	0.14	0.02	101.0	72.9
I1_12	38.01	0.0357	40.80	20.34	0.29	0.01	0.29	0.15	0.02	99.9	78.1
I1_13	38.85	0.0309	40.50	21.08	0.29	0.01	0.29	0.15	0.01	101.2	77.4
I1_16	37.26	0.0307	36.09	26.19	0.31	0.02	0.38	0.12	0.02	100.4	71.1
I1_20	39.00	0.0446	42.17	18.37	0.29	0.01	0.27	0.20	0.03	100.3	80.4
I1_21	38.62	0.0276	41.00	20.83	0.31	0.01	0.30	0.14	0.01	101.2	77.8
I1_22	38.05	0.0401	40.34	20.54	0.30	0.01	0.30	0.14	0.02	99.7	77.8
I2_1	40.61	0.0588	49.33	10.12	0.34	0.00	0.15	0.32	0.07	100.9	89.7
I2_4	40.66	0.0411	49.38	9.93	0.33	0.01	0.14	0.33	0.05	100.8	89.9
I2_6	40.60	0.0632	49.31	9.84	0.35	0.00	0.16	0.32	0.07	100.6	89.9
I2_8	40.28	0.0569	49.12	9.96	0.34	0.00	0.16	0.31	0.07	100.2	89.8
I2_11	40.75	0.0561	49.27	9.96	0.34	0.00	0.14	0.33	0.08	100.9	89.8
I2_13	40.02	0.0454	46.33	13.42	0.39	0.01	0.20	0.23	0.06	100.6	86.0
I2_14	40.80	0.0581	49.04	9.92	0.34	0.00	0.14	0.33	0.06	100.6	89.8
I2_16	39.53	0.0393	45.13	15.19	0.40	0.00	0.22	0.20	0.05	100.7	84.1
I2_17	40.79	0.0528	48.17	10.96	0.34	0.00	0.16	0.31	0.06	100.8	88.7
I2_18	40.96	0.0545	49.14	10.27	0.34	0.01	0.16	0.30	0.06	101.2	89.5
I2_20	41.14	0.0691	49.26	9.98	0.34	0.00	0.15	0.32	0.06	101.3	89.8
I3_1	39.03	0.0739	43.01	17.65	0.31	0.00	0.25	0.23	0.05	100.6	81.3
I3_2	39.97	0.0784	45.36	14.26	0.34	0.00	0.20	0.23	0.05	100.4	85.0
I3_6	39.85	0.0824	46.12	13.73	0.32	0.01	0.20	0.27	0.05	100.6	85.7
I3_7	39.50	0.0570	43.21	17.56	0.32	0.00	0.25	0.21	0.04	101.1	81.4
I3_8	40.12	0.0784	46.45	13.56	0.31	0.00	0.21	0.26	0.05	101.0	85.9
I3_10	39.94	0.0668	44.00	15.93	0.31	0.01	0.24	0.22	0.04	100.7	83.1
I3_11	40.41	0.0715	47.27	11.90	0.31	0.01	0.18	0.30	0.07	100.5	87.6
I3_14	40.18	0.0753	46.89	12.31	0.33	0.00	0.19	0.27	0.05	100.2	87.2
I5_1	40.68	0.0802	48.52	10.56	0.31	0.02	0.14	0.35	0.08	100.7	89.1
I5_2	40.73	0.0578	48.00	10.88	0.30	0.01	0.17	0.39	0.07	100.5	88.7
I5_4	39.95	0.0690	47.15	12.06	0.30	0.01	0.18	0.32	0.08	100.0	87.4
I5_6	40.34	0.0678	47.28	12.21	0.30	0.01	0.18	0.31	0.07	100.7	87.3
I5_7	40.47	0.0782	47.95	11.45	0.31	0.01	0.17	0.39	0.08	100.8	88.2
I5_8	40.76	0.0669	48.67	10.50	0.32	0.02	0.16	0.33	0.08	100.8	89.2
I5_10	40.75	0.0754	48.40	11.25	0.30	0.01	0.16	0.33	0.08	101.3	88.5
I5_13	40.83	0.0665	47.66	11.46	0.31	0.01	0.17	0.31	0.07	100.8	88.1
I5_15	40.44	0.0727	48.02	11.38	0.30	0.02	0.15	0.35	0.07	100.7	88.3
I5_16	40.47	0.0665	48.04	11.26	0.31	0.01	0.17	0.34	0.07	100.7	88.4
I5_20	40.68	0.0731	47.59	11.43	0.29	0.01	0.17	0.34	0.07	100.6	88.1
I5_21	39.91	0.0665	47.73	11.90	0.33	0.02	0.16	0.32	0.07	100.4	87.7
I5_23	40.77	0.0787	48.47	10.87	0.31	n.d.	0.15	0.32	0.08	101.0	88.8
I5_25	39.96	0.0677	48.29	11.28	0.32	n.d.	0.15	0.32	0.08	100.4	88.4
I5_27	40.34	0.0684	47.28	12.49	0.30	n.d.	0.18	0.30	0.07	101.0	87.1
I5_30	39.35	0.0735	48.03	10.55	0.28	n.d.	0.15	0.36	0.09	98.8	89.0
I5_32	40.25	0.0872	47.88	11.04	0.30	n.d.	0.15	0.36	0.09	100.1	88.5
I5_34	40.04	0.0747	47.79	10.92	0.30	n.d.	0.17	0.33	0.08	99.6	88.6
I5_37	40.86	0.0799	48.29	10.75	0.31	n.d.	0.14	0.37	0.08	100.8	88.9
I5_39	39.88	0.0787	48.21	10.63	0.28	n.d.	0.15	0.37	0.10	99.6	89.0
I5_42	39.65	0.0699	48.57	11.18	0.29	n.d.	0.16	0.37	0.09	100.3	88.6
I5_45	39.68	0.0764	48.22	11.30	0.27	n.d.	0.14	0.37	0.10	100.1	88.4
I6_1	41.47	0.0699	48.78	10.22	0.29	0.01	0.15	0.38	0.10	101.4	89.5
I6_2	40.98	0.0669	49.22	10.02	0.29	0.01	0.15	0.37	0.08	101.1	89.7
I6_5	40.76	0.0696	49.18	9.62	0.26	0.01	0.15	0.37	0.08	100.4	90.1
I6_6	40.69	0.0656	47.26	12.54	0.33	0.01	0.17	0.30	0.06	101.4	87.0
I6_7	40.59	0.0694	47.54	11.79	0.34	0.01	0.17	0.33	0.07	100.8	87.8
I6_8	40.09	0.0545	46.29	13.36	0.34	0.01	0.18	0.33	0.06	100.7	86.1
I6_9	41.31	0.0700	49.26	9.78	0.29	0.01	0.14	0.39	0.08	101.2	90.0
I6_11	40.59	0.0603	47.09	12.07	0.31	0.00	0.19	0.31	0.06	100.6	87.4
I6_12	37.20	0.0280	33.37	29.27	0.24	0.02	0.39	0.15	0.02	100.7	67.0
I6_13	40.70	0.0701	47.90	11.79	0.30	0.02	0.18	0.32	0.08	101.3	87.9
I6_14	40.46	0.0755	46.87	12.08	0.35	0.01	0.18	0.28	0.08	100.3	87.4
I6_15	40.43	0.0713	48.23	10.78	0.28	0.01	0.16	0.35	0.08	100.3	88.9
I6_17	40.09	0.0488	47.68	11.97	0.26	0.01	0.18	0.34	0.04	100.6	87.6
I6_20	39.99	0.0587	46.19	13.40	0.31	0.00	0.18	0.33	0.06	100.5	86.0
I6_22	41.33	0.0554	48.55	10.40	0.30	0.01	0.15	0.37	0.07	101.2	89.3
I7_1	39.43	0.0636	45.21	15.26	0.30	0.00	0.23	0.22	0.05	100.7	84.1
I7_2	39.82	0.0611	45.99	14.04	0.33	0.01	0.23	0.22	0.05	100.7	85.4
I7_3	40.04	0.0777	46.39	13.76	0.31	0.01	0.22	0.24	0.04	101.0	85.7

Table E.1: Major element abundances (wt%) in olivine cores determined by EPMA. n.d. = not determined.

Data point	SiO_2	Al_2O_3	MgO	FeO	CaO	TiO_2	MnO	NiO	Cr_2O_3	Total	Mg#
I7_4	39.80	0.0701	46.44	13.33	0.29	0.01	0.21	0.26	0.05	100.4	86.1
I7_6	40.27	0.0785	46.39	13.91	0.30	0.01	0.21	0.25	0.05	101.4	85.6
I7_7	40.34	0.0752	46.68	13.87	0.29	0.01	0.19	0.27	0.05	101.7	85.7
I7_9	39.36	0.0684	44.88	15.65	0.32	0.00	0.23	0.20	0.05	100.7	83.6
I7_11	39.57	0.0766	45.95	13.46	0.30	0.00	0.21	0.25	0.06	99.8	85.9
I7_13	39.54	0.0783	43.78	16.05	0.34	0.01	0.26	0.17	0.05	100.2	82.9
I7_15	40.66	0.0807	46.47	13.38	0.30	0.00	0.20	0.26	0.06	101.4	86.1
I7_17	39.32	0.0589	44.09	15.61	0.33	0.00	0.22	0.18	0.04	99.8	83.4
I7_18	40.01	0.1051	44.75	15.53	0.33	0.01	0.22	0.18	0.05	101.1	83.7
I7_19	40.21	0.0757	45.85	13.50	0.31	0.01	0.22	0.25	0.06	100.4	85.8
I8_5	40.41	0.1051	48.82	10.88	0.33	0.00	0.14	0.30	0.06	101.0	88.9
I8_6	41.07	0.0757	48.50	11.27	0.32	0.01	0.16	0.29	0.05	101.7	88.5
I8_9	40.84	0.0776	48.75	11.01	0.34	0.00	0.16	0.28	0.04	101.4	88.8
I8_12	39.90	0.0878	43.21	17.81	0.32	0.01	0.25	0.21	0.05	101.8	81.2
I8_13	41.67	0.0669	50.18	8.47	0.35	0.00	0.13	0.35	0.14	101.2	91.3
I8_17	40.57	0.0821	48.23	11.83	0.32	0.01	0.16	0.28	0.03	101.5	87.9
I8_19	40.73	0.0532	48.04	11.40	0.32	0.01	0.17	0.29	0.04	101.0	88.3
I9_1	39.99	0.0674	47.76	12.11	0.32	0.01	0.17	0.32	0.07	100.8	87.5
I9_2	40.90	0.0750	47.68	11.39	0.33	0.01	0.17	0.29	0.07	100.8	88.2
I9_3	40.54	0.0749	49.51	9.66	0.32	0.00	0.13	0.36	0.10	100.6	90.1
I9_5	41.33	0.1020	48.93	10.24	0.32	0.00	0.14	0.37	0.13	101.4	89.5
I9_9	40.45	0.0463	47.74	11.61	0.32	0.00	0.18	0.30	0.05	100.6	88.0
I9_10	40.68	0.0824	48.71	10.51	0.32	0.00	0.15	0.34	0.09	100.8	89.2
I9_13	40.41	0.0735	48.03	10.85	0.31	0.01	0.18	0.32	0.08	100.2	88.7
I9_16	39.60	0.0711	48.43	10.02	0.32	0.01	0.14	0.37	0.09	99.0	89.6
I9_24	39.99	0.0787	47.56	11.32	0.31	n.d.	0.16	0.32	0.09	99.7	88.2
I9_26	40.22	0.0851	48.54	9.80	0.31	n.d.	0.13	0.37	0.10	99.5	89.8
I9_28	40.60	0.0872	48.43	10.75	0.32	n.d.	0.17	0.33	0.10	100.7	88.9
I9_30	40.08	0.0836	48.10	11.34	0.32	n.d.	0.18	0.33	0.09	100.4	88.3
I9_32	39.55	0.0419	47.62	11.91	0.33	n.d.	0.18	0.31	0.04	99.9	87.7
I9_34	40.13	0.0519	47.70	12.05	0.33	n.d.	0.18	0.29	0.06	100.7	87.6
I9_36	40.12	0.0859	48.17	11.32	0.31	n.d.	0.17	0.33	0.08	100.5	88.3
I9_38	40.36	0.0701	48.42	10.93	0.31	n.d.	0.15	0.34	0.09	100.6	88.8
I9_40	39.82	0.0864	48.61	10.87	0.31	n.d.	0.17	0.36	0.10	100.2	88.8
I9_42	40.24	0.0384	48.18	11.22	0.29	n.d.	0.17	0.32	0.05	100.5	88.4

E.2 Olivine rim compositions

Table E.2: Major element abundances (wt%) in olivine rims determined by EPMA. n.d. = not determined.

Data point	SiO_2	Al_2O_3	MgO	FeO	CaO	TiO_2	MnO	NiO	Cr_2O_3	Total	Mg#
S1_3	40.21	0.1114	51.01	8.28	0.31	0.01	0.13	0.42	n.d.	100.5	91.7
S1_15	40.85	0.1169	50.23	8.68	0.33	0.01	0.13	0.42	n.d.	100.8	91.2
S3_5	41.49	0.1343	50.00	8.31	0.31	0.01	0.12	0.39	n.d.	100.8	91.5
S5_8	41.17	0.1144	50.29	8.33	0.32	0.02	0.14	0.42	n.d.	100.8	91.5
S5_10	40.90	0.1342	50.06	8.17	0.38	0.01	0.12	0.39	n.d.	100.2	91.6
S5_20	40.01	0.1073	51.21	8.17	0.32	0.01	0.14	0.42	n.d.	100.4	91.8
S8_2	40.07	0.0985	50.36	9.24	0.28	0.01	0.12	0.39	n.d.	100.6	90.7
S8_7	41.04	0.1373	49.83	8.90	0.30	0.01	0.12	0.39	n.d.	100.7	90.9
S9_2	40.22	0.1149	49.35	9.67	0.31	0.01	0.14	0.41	0.13	100.4	90.1
S9_5	40.91	0.1492	49.87	8.58	0.31	0.01	0.13	0.39	0.15	100.5	91.2
S9_7	40.66	0.1446	49.58	8.80	0.31	0.00	0.12	0.41	0.14	100.2	90.9
S9_16	40.19	0.0981	49.42	9.59	0.32	0.01	0.13	0.39	0.13	100.3	90.2
S10_4	40.93	0.1243	50.96	7.86	0.30	0.01	0.13	0.41	n.d.	100.7	92.0
R10_2	39.46	0.1502	41.56	18.35	0.86	0.01	0.30	0.27	0.14	101.1	80.1
R10_5	39.94	0.0533	45.95	14.24	0.25	0.04	0.25	0.26	0.02	101.0	85.2
R10_7	40.09	0.0658	45.61	14.53	0.03	0.01	0.29	0.33	0.01	101.0	84.8
R10_10	38.90	0.0488	42.30	18.30	0.24	0.02	0.32	0.19	0.03	100.4	80.5
R10_13	39.42	0.0493	44.86	15.22	0.04	0.01	0.26	0.25	0.01	100.1	84.0
R10_15	38.86	0.0471	42.42	18.30	0.11	0.03	0.30	0.26	0.02	100.3	80.5

Table E.2: Major element abundances (wt%) in olivine rims determined by EPMA. n.d. = not determined.

Data point	SiO_2	Al_2O_3	MgO	FeO	CaO	TiO_2	MnO	NiO	Cr_2O_3	Total	Mg#
R10_17	38.85	0.0152	42.76	18.38	0.05	0.04	0.33	0.26	0.02	100.7	80.6
R10_23	39.67	0.124	46.47	13.54	0.43	0.01	0.23	0.30	0.07	100.8	85.9
MU1.1_2	40.27	0.0929	48.02	11.39	0.23	0.00	0.16	0.40	0.09	100.7	88.2
MU1.1_8	40.70	0.0811	48.25	11.14	0.27	0.01	0.17	0.38	0.10	101.1	88.5
MU1.1_16	39.74	0.1015	47.22	12.44	0.29	0.01	0.19	0.36	0.15	100.5	87.1
MU1.1_20	39.70	0.079	46.24	14.12	0.27	0.01	0.21	0.33	0.10	101.1	85.4
MU1.1_25	39.39	0.0469	44.81	15.19	0.25	0.01	0.25	0.29	0.04	100.3	84.0
MU1.1_28	39.43	0.0751	46.29	13.38	0.28	0.01	0.22	0.32	0.08	100.1	86.0
MU1.2_2	39.58	0.0454	45.73	14.51	0.18	0.02	0.24	0.30	0.05	100.7	84.9
MU1.2_9	40.35	0.04	47.03	12.56	0.16	0.03	0.18	0.34	0.06	100.8	87.0
MU1.2_15	38.59	0.0711	43.91	16.09	0.24	0.01	0.28	0.29	0.07	99.6	82.9
MU1.2_18	39.72	0.0331	46.15	13.38	0.17	0.02	0.21	0.31	0.03	100.0	86.0
MU1.2_25	39.57	0.0779	45.95	13.68	0.27	0.00	0.22	0.33	0.08	100.2	85.7
MU1.2_28	39.81	0.0482	45.14	14.31	0.24	0.01	0.24	0.30	0.04	100.2	84.9
MU2.2_4	39.69	0.0711	44.18	16.28	0.23	0.01	0.27	0.27	0.06	101.1	82.9
MU2.2_7	40.04	0.0253	46.92	12.05	0.17	0.03	0.19	0.31	0.03	99.8	87.4
MU2.2_10	39.12	0.0449	43.77	16.35	0.24	0.01	0.27	0.26	0.04	100.1	82.7
MU2.2_12	39.98	0.0444	46.07	13.53	0.27	0.01	0.23	0.32	0.05	100.5	85.8
MU2.2_14	39.82	0.0523	45.69	13.90	0.26	0.01	0.21	0.29	0.04	100.3	85.4
MU2.2_24	39.66	0.0422	45.96	13.60	0.24	0.00	0.22	0.30	0.05	100.1	85.8
MU3.1_2	40.20	0.1114	46.31	13.35	0.36	0.01	0.20	0.34	0.13	101.0	86.1
MU3.1_5	39.75	0.0822	46.47	13.36	0.29	0.01	0.21	0.33	0.08	100.6	86.1
MU3.1_7	39.86	0.0785	47.47	11.92	0.28	0.00	0.19	0.35	0.08	100.2	87.6
MU3.1_9	39.60	0.0472	45.00	15.48	0.18	0.02	0.24	0.31	0.05	100.9	83.8
PAD6_4	39.36	0.0438	45.97	13.78	0.36	0.01	0.20	0.29	0.05	100.0	85.6
PAD6_7	39.25	0.0454	46.53	13.38	0.34	0.01	0.20	0.35	0.05	100.2	86.1
PAD6_11	39.50	0.0441	46.33	13.35	0.35	0.01	0.20	0.29	0.06	100.1	86.1
PAD6_13	39.11	0.044	46.62	13.35	0.36	0.01	0.19	0.32	0.05	100.1	86.2
ED_9	40.36	0.0564	46.02	13.76	0.29	0.01	0.18	0.28	0.04	101.0	85.6
ED_18	40.29	0.0505	45.94	13.44	0.30	0.01	0.18	0.26	0.04	100.5	85.9
KoP_11	39.88	0.0583	46.27	13.14	0.32	0.01	0.20	0.28	0.05	100.2	86.3
KoP_17	40.32	0.0517	47.51	11.86	0.29	0.01	0.16	0.32	0.07	100.6	87.7
SD_3	39.99	0.0502	45.81	13.51	0.29	0.02	0.17	0.28	0.04	100.2	85.8
SD_15	40.00	0.0517	45.84	13.36	0.30	0.01	0.19	0.27	0.04	100.1	85.9
VEY_2	41.14	0.0395	49.73	9.36	0.30	0.01	0.15	0.38	0.07	101.2	90.4
VEY_6	39.26	0.027	44.16	15.78	0.20	0.01	0.23	0.29	0.03	100.0	83.3
VEY_13	39.94	0.0632	49.07	9.85	0.29	0.00	0.13	0.40	0.12	99.9	89.9
VP1a_4	40.68	0.0446	47.67	11.61	0.26	0.02	0.15	0.39	0.08	100.9	88.0
VP1a_14	39.98	0.0399	46.03	13.11	0.28	0.01	0.19	0.33	0.05	100.0	86.2
VP1b_2	39.12	0.0513	45.10	15.08	0.25	0.01	0.19	0.34	0.01	100.2	84.2
VP1b_12	39.73	0.049	47.53	12.09	0.28	0.01	0.15	0.35	0.08	100.3	87.5
I2_2	41.41	0.0804	48.87	9.95	0.34	0.00	0.15	0.32	0.09	101.2	89.7
I2_7	39.49	0.0443	43.49	17.48	0.38	0.01	0.22	0.23	0.05	101.4	81.6
I2_9	39.36	0.0545	46.05	13.62	0.35	0.01	0.20	0.23	0.05	99.9	85.8
I2_12	40.57	0.0502	47.01	12.59	0.38	0.01	0.18	0.28	0.06	101.1	86.9
I2_19	40.90	0.0492	48.88	10.01	0.35	0.00	0.15	0.33	0.06	100.7	89.7
I3_3	39.11	0.0455	42.32	18.54	0.35	0.01	0.28	0.18	0.04	100.9	80.3
I3_12	39.30	0.0666	44.29	15.80	0.34	0.01	0.23	0.22	0.05	100.3	83.3
I5_3	40.30	0.0509	45.37	13.45	0.31	0.02	0.19	0.30	0.06	100.1	85.7
I5_9	39.50	0.0725	45.96	13.59	0.32	0.02	0.18	0.31	0.08	100.0	85.8
I5_12	39.89	0.0624	45.69	14.55	0.31	0.03	0.22	0.29	0.07	101.1	84.8
I5_14	40.39	0.0664	47.43	12.29	0.32	0.02	0.18	0.33	0.07	101.1	87.3
I6_3	40.09	0.0659	44.14	15.65	0.28	0.01	0.19	0.35	0.10	100.9	83.4
I6_10	40.58	0.0871	47.02	12.22	0.26	0.01	0.17	0.36	0.10	100.8	87.3
I6_16	40.15	0.0658	46.94	12.82	0.28	0.01	0.17	0.35	0.09	100.9	86.7
I6_18	39.64	0.045	43.09	18.04	0.26	0.01	0.21	0.32	0.04	101.7	81.0
I7_5	38.94	0.0612	42.61	18.19	0.34	0.01	0.25	0.16	0.03	100.6	80.7
I7_8	39.34	0.0628	42.52	18.87	0.33	0.00	0.26	0.16	0.03	101.6	80.1
I7_12	39.10	0.0523	43.71	17.08	0.35	0.01	0.26	0.15	0.04	100.8	82.0
I7_16	39.08	0.0585	43.26	17.20	0.33	0.01	0.26	0.17	0.04	100.4	81.8
I9_4	40.22	0.0594	47.70	12.36	0.34	0.01	0.18	0.29	0.05	101.2	87.3
I9_6	40.17	0.0665	47.46	11.82	0.35	0.01	0.18	0.28	0.05	100.4	87.7
I9_14	40.09	0.0583	47.47	11.78	0.34	0.01	0.18	0.29	0.05	100.3	87.8

E.3 Olivine matrix compositions

Table E.3: Major element abundances (wt%) in matrix olivine determined by EPMA. n.d. = not determined.

Data point	SiO_2	Al_2O_3	MgO	FeO	CaO	TiO_2	MnO	NiO	Cr_2O_3	Total	Mg#
S1_26	40.16	0.0652	45.88	14.67	0.36	0.01	0.19	0.28	n.d.	101.6	84.8
S1_27	40.72	0.0805	48.62	10.64	0.34	0.01	0.17	0.34	n.d.	100.9	89.1
S1_37	40.05	0.0856	48.52	10.85	0.36	0.01	0.17	0.35	0.11	100.5	88.9
S1_41	39.23	0.076	47.95	11.87	0.36	0.01	0.18	0.31	0.08	100.1	87.8
S3_11	40.10	0.0873	48.25	10.85	0.34	0.00	0.17	0.32	n.d.	100.1	88.8
S3_12	40.52	0.0967	48.99	10.26	0.36	0.01	0.16	0.37	n.d.	100.8	89.5
S3_39	39.69	0.0747	48.46	10.33	0.34	0.01	0.17	0.33	0.09	99.5	89.3
S3_40	39.23	0.0821	47.67	12.12	0.35	0.01	0.18	0.31	0.07	100.0	87.5
S3_41	39.15	0.1079	48.56	10.52	0.35	0.01	0.17	0.35	0.11	99.3	89.2
S5_12	41.09	0.1166	49.84	9.96	0.34	0.01	0.14	0.36	n.d.	101.9	89.9
S7_2	40.17	0.0781	48.79	10.99	0.29	0.02	0.16	0.35	0.09	100.9	88.8
S7_16	40.08	0.0732	48.98	10.47	0.31	0.01	0.16	0.39	0.10	100.6	89.3
S8_20	38.64	0.1243	46.15	13.95	0.31	0.01	0.18	0.24	n.d.	99.6	85.5
S8_33	40.19	0.0732	48.33	11.56	0.31	0.01	0.17	0.35	0.08	101.1	88.2
S8_34	40.31	0.0896	48.59	10.97	0.30	0.01	0.17	0.32	0.13	100.9	88.8
S8_35	39.97	0.069	48.42	11.63	0.32	0.01	0.17	0.33	0.08	101.0	88.1
S8_36	40.09	0.0648	47.47	12.24	0.33	0.01	0.17	0.28	0.07	100.7	87.4
S8_37	39.75	0.0829	49.32	10.28	0.30	0.01	0.16	0.38	0.11	100.4	89.5
S9_14	41.07	0.0721	49.32	8.55	0.31	0.00	0.13	0.37	0.11	99.9	91.1
S10_13	40.41	0.094	49.92	9.63	0.32	0.01	0.15	0.41	n.d.	100.9	90.2
S10_19	39.79	0.0842	48.89	9.56	0.32	0.01	0.15	0.37	0.09	99.3	90.1
S10_27	40.48	0.067	48.40	11.14	0.34	0.01	0.17	0.32	0.08	101.0	88.6
S10_43	39.99	0.0883	48.72	10.47	0.34	0.01	0.16	0.35	0.12	100.3	89.2
MU1.2_11	39.18	0.0523	44.27	16.83	0.20	0.01	0.28	0.28	0.05	101.1	82.4
MU1.2_13	39.57	0.0503	44.47	15.19	0.29	0.01	0.24	0.31	0.05	100.2	83.9
MU1.2_20	39.51	0.0817	44.60	15.61	0.25	0.01	0.25	0.30	0.06	100.7	83.6
MU1.2_21	39.04	0.0581	44.65	16.17	0.18	0.02	0.27	0.29	0.04	100.7	83.1
MU1.2_22	38.99	0.046	44.02	16.29	0.21	0.01	0.26	0.28	0.02	100.1	82.8
MU1.2_23	38.65	0.0448	43.27	17.33	0.25	0.03	0.29	0.28	0.02	100.2	81.6
I2_13	40.02	0.0454	46.33	13.42	0.39	0.01	0.20	0.23	0.06	100.7	86.0
I2_16	39.53	0.0393	45.13	15.19	0.40	0.00	0.22	0.20	0.05	100.8	84.1
I3_5	39.64	0.0801	42.62	17.95	0.36	0.01	0.27	0.17	0.04	101.1	80.9
I3_9'	39.25	0.0565	42.52	18.20	0.36	0.01	0.27	0.18	0.03	100.9	80.6
I5_17	39.63	0.048	43.43	16.94	0.33	0.02	0.24	0.21	0.05	100.9	82.0
I5_22	39.53	0.0422	42.73	17.99	0.38	0.02	0.26	0.18	0.04	101.2	80.9
I7_10	39.29	0.048	40.93	19.78	0.39	0.01	0.29	0.13	0.02	100.9	78.7
I8_18	40.30	0.057	47.32	12.63	0.36	0.00	0.19	0.24	0.07	101.2	87.0
I9_12	16.85	0.1943	0.01	43.77	0.02	0.45	0.02	0.26	0.04	61.6	0.0

Appendix F. Spinel compositions

Table F.1: Major element abundances (wt%) of Cr-spinel determined by EPMA.

Data point	Cr_2O_3	SiO_2	MgO	FeO	Al_2O_3	CaO	TiO_2	MnO	NiO	ZnO	Total
S1_22	41.81	0.13	15.44	16.80	25.13	0.01	0.39	0.18	0.23	0.03	100.1
S1_23	41.79	0.15	17.31	13.60	25.96	0.01	0.35	0.17	0.26	0.04	99.6
S1_24	39.07	0.17	17.49	14.10	28.57	0.02	0.36	0.12	0.29	0.05	100.2
S1_25	43.19	0.15	16.91	13.50	24.52	0.00	0.37	0.16	0.25	0.03	99.1
S1_31	43.40	0.14	16.50	13.99	25.01	0.01	0.30	0.19	0.27	0.02	99.8
S1_32	43.49	0.15	16.55	13.92	25.08	0.01	0.32	0.17	0.25	0.04	100.0
S1_34	39.40	0.14	17.18	14.12	28.89	0.02	0.35	0.14	0.29	0.04	100.6
S1_36	42.12	0.17	16.83	13.91	25.86	0.00	0.41	0.16	0.25	0.03	99.7
S1_39	41.37	0.17	17.16	13.37	27.03	0.01	0.27	0.17	0.26	0.05	99.9
S1_40	41.98	0.17	16.75	13.48	26.23	0.01	0.36	0.16	0.24	0.06	99.4
S2_5	42.26	0.18	16.74	14.18	25.61	0.01	0.51	0.16	0.26	0.04	99.9
S2_7	36.32	0.31	17.65	14.22	30.83	0.01	0.35	0.14	0.28	0.04	100.1
S3_6	42.36	0.15	16.61	14.93	25.99	0.01	0.41	0.18	0.23	0.05	100.9
S3_10	43.23	0.16	16.36	14.42	25.05	0.01	0.27	0.17	0.21	0.00	99.9
S3_26	36.57	0.19	17.01	13.95	31.11	0.00	0.26	0.15	0.30	0.05	99.6
S3_28	43.01	0.14	16.63	13.59	25.77	0.01	0.29	0.15	0.26	0.02	99.9
S3_30	34.93	1.16	15.49	19.42	21.39	0.00	0.27	0.29	0.26	0.05	93.3
S3_32	41.13	0.17	16.74	13.70	26.85	0.01	0.33	0.18	0.29	0.04	99.4
S3_34	40.76	0.18	16.79	13.81	26.79	0.00	0.43	0.18	0.26	0.03	99.2
S3_35	40.78	0.17	16.83	13.46	26.98	0.01	0.33	0.15	0.27	0.03	99.0
S3_36	40.90	0.18	16.68	13.38	27.16	0.01	0.40	0.17	0.27	0.03	99.2
S3_37	41.06	0.18	16.65	14.14	27.16	0.00	0.32	0.16	0.26	0.02	100.0
S5_4	43.08	0.17	17.48	13.32	26.31	0.01	0.32	0.17	0.26	0.05	101.2
S5_17	42.56	0.17	17.50	13.37	26.40	0.02	0.40	0.15	0.26	0.03	100.9
S5_22	43.03	0.16	17.27	13.23	26.10	0.01	0.34	0.13	0.27	0.06	100.6
S5_26	37.07	0.16	16.59	16.16	28.47	0.01	0.54	0.17	0.27	0.05	99.5
S5_27	42.49	0.19	17.37	13.29	25.79	0.07	0.34	0.18	0.27	0.03	100.0
S5_34	43.05	0.18	16.93	13.48	25.62	0.00	0.40	0.14	0.26	0.03	100.1
S5_36	43.35	0.16	17.06	13.39	25.52	0.00	0.44	0.17	0.25	0.05	100.4
S5_37	42.56	0.17	17.02	12.93	25.30	0.01	0.40	0.17	0.26	0.03	98.8
S5_38	39.78	0.18	16.94	13.73	27.03	0.00	0.33	0.14	0.27	0.04	98.5
S5_41	42.46	0.18	16.99	13.08	26.41	0.00	0.40	0.15	0.27	0.02	100.0
S5_45	43.60	0.17	16.85	13.25	25.26	0.01	0.41	0.15	0.25	0.03	100.0
S5_47	39.53	0.15	15.97	16.01	26.73	0.01	0.32	0.18	0.24	0.01	99.2
S5_48	39.46	0.16	16.02	15.95	26.28	0.01	0.30	0.17	0.23	0.03	98.6
S5_49	39.33	0.16	16.23	15.75	27.48	0.01	0.33	0.18	0.24	0.04	99.8
S5_50	43.24	0.16	16.81	13.91	25.41	0.01	0.45	0.16	0.24	0.02	100.4
S6_4	42.12	0.17	16.86	13.48	25.88	0.01	0.32	0.15	0.24	0.03	99.3
S6_7	42.76	0.18	17.12	13.30	25.58	0.04	0.38	0.17	0.25	0.03	99.8
S7_6	38.11	0.14	16.49	15.49	28.39	0.02	0.38	0.18	0.27	0.03	99.5
S7_14	37.24	0.15	16.42	15.98	28.76	0.00	0.33	0.16	0.25	0.05	99.3
S8_5	38.55	0.13	15.89	17.82	27.02	0.00	0.43	0.17	0.22	0.06	100.3
S8_15	40.24	0.14	16.66	16.17	26.29	0.01	0.37	0.16	0.25	0.03	100.3
S8_25	39.23	0.16	16.95	15.14	28.47	0.01	0.50	0.17	0.27	0.02	100.9
S8_27	38.37	0.14	16.75	15.31	28.53	0.01	0.45	0.19	0.26	0.04	100.0
S8_30	39.41	0.14	16.20	15.98	27.70	0.00	0.32	0.18	0.25	0.06	100.3
S8_32	40.52	0.16	15.68	16.22	25.63	0.03	0.46	0.19	0.29	0.02	99.2
S8_39	38.10	0.15	16.94	15.21	28.87	0.01	0.37	0.15	0.26	0.03	100.1
S9_3	34.77	0.22	17.92	13.48	32.12	0.00	0.34	0.13	0.31	0.04	99.4
S9_8	43.29	0.21	16.73	13.57	24.48	0.02	0.40	0.16	0.25	0.03	99.1
S9_20	43.28	0.24	16.74	13.62	24.67	0.01	0.33	0.15	0.26	0.02	99.3
S10_21	44.92	0.19	16.40	13.67	23.29	0.01	0.37	0.18	0.26	0.03	99.3
S10_23	44.04	0.18	16.60	13.33	23.92	0.00	0.39	0.16	0.25	0.03	98.9
S10_26	43.90	0.19	16.44	13.88	24.08	0.01	0.36	0.17	0.23	0.05	99.3
S10_29	41.00	0.23	17.05	13.44	26.40	0.00	0.35	0.15	0.26	0.02	98.9
S10_32	43.86	0.19	17.16	12.49	24.21	0.00	0.18	0.16	0.26	0.03	98.6
S10_34	44.52	0.19	16.66	13.35	23.93	0.03	0.40	0.16	0.27	0.02	99.5

Table F.1: Major element abundances (wt%) of Cr-spinel determined by EPMA.

Data point	Cr_2O_3	SiO_2	MgO	FeO	Al_2O_3	CaO	TiO_2	MnO	NiO	ZnO	Total
S10_36	44.37	0.16	16.59	13.69	24.22	0.01	0.37	0.17	0.25	0.04	99.9
S10_38	44.39	0.17	16.67	13.19	24.04	0.01	0.38	0.16	0.27	0.01	99.3
S10_40	34.64	0.20	17.85	13.01	33.20	0.00	0.42	0.14	0.32	0.04	99.8
R10_8	32.39	0.12	9.66	30.12	26.61	0.02	0.72	0.31	0.20	0.21	100.4
R10_20	29.41	0.21	10.67	27.16	30.30	0.01	0.47	0.30	0.17	0.15	98.9
M9_2	44.98	0.11	14.79	18.05	21.81	0.01	0.62	0.22	0.23	0.04	100.9
M9_4	44.35	0.14	15.09	17.20	22.59	0.01	0.62	0.21	0.24	0.08	100.5
M9_6	42.70	0.16	14.33	18.14	23.59	0.02	0.54	0.23	0.21	0.04	99.9
M9_10	42.67	0.11	11.87	23.84	20.36	0.01	0.71	0.38	0.18	0.15	100.3
M9_14	43.46	0.11	13.13	20.24	21.59	0.03	0.54	0.26	0.18	0.04	99.6
M9_16	43.82	0.20	13.52	19.92	21.56	0.02	0.56	0.23	0.21	0.04	100.1
M9_18	44.90	0.10	14.56	18.40	21.49	0.01	0.63	0.22	0.22	0.03	100.6
M9_22	44.40	0.15	15.33	17.18	21.41	0.01	0.59	0.22	0.24	0.04	99.6
M9_24	44.31	0.18	15.17	17.39	22.34	0.01	0.61	0.20	0.23	0.03	100.5
M9_26	43.98	0.27	13.84	19.25	21.40	0.02	0.56	0.31	0.21	0.08	99.9
MU1.1_3	43.99	0.22	16.25	13.76	25.88	0.00	0.32	0.17	0.24	0.02	100.8
MU1.1_4	40.54	0.20	11.30	22.84	24.04	0.02	0.31	0.32	0.19	0.07	99.8
MU1.1_10	42.30	0.21	14.45	18.35	24.49	0.01	0.29	0.23	0.21	0.06	100.6
MU1.1_21	38.80	0.24	16.03	15.48	28.31	0.01	0.32	0.17	0.26	0.06	99.7
MU1.1_26	40.15	0.22	11.15	23.00	23.51	0.02	0.31	0.29	0.12	0.11	98.9
MU1.1_29	41.98	0.25	15.21	15.58	25.16	0.01	0.26	0.19	0.23	0.05	98.9
MU1.2_3	42.54	0.60	14.21	17.46	24.61	0.03	0.37	0.24	0.21	0.07	100.3
MU1.2_16	41.61	0.18	12.00	22.77	22.91	0.02	0.32	0.28	0.18	0.11	100.4
MU1.2_19	41.12	0.15	12.49	22.74	22.62	0.01	0.39	0.25	0.18	0.11	100.1
MU2.2_2	41.64	0.34	14.97	15.70	25.93	0.02	0.32	0.22	0.23	0.03	99.4
MU2.2_8	42.14	0.19	14.31	17.24	25.85	0.00	0.29	0.22	0.21	0.06	100.5
MU2.2_16	41.94	0.22	15.21	15.90	26.33	0.01	0.29	0.20	0.19	0.03	100.3
MU2.2_17	42.46	0.20	15.04	15.58	26.32	0.01	0.40	0.22	0.17	0.04	100.4
MU2.2_20	42.56	0.52	15.76	13.81	26.20	0.01	0.29	0.20	0.20	0.06	99.6
MU2.2_25	43.38	0.22	15.89	14.46	26.27	0.01	0.30	0.16	0.22	0.05	101.0
MU3.1_3	41.61	0.23	14.72	17.07	25.69	0.00	0.31	0.21	0.23	0.08	100.2
MU3.1_10	41.12	0.23	15.97	15.25	26.72	0.01	0.34	0.20	0.24	0.05	100.1
MU3.1_11	31.97	0.18	6.17	46.61	8.20	0.00	3.88	0.44	0.19	0.15	97.8
MU3.1_16	41.19	0.21	12.45	22.85	22.54	0.04	0.28	0.27	0.15	0.09	100.1
APO4_8	45.71	0.08	12.10	21.76	19.19	0.07	0.35	0.23	0.17	0.08	99.7
APO4_9	48.29	0.09	12.47	20.30	18.35	0.03	0.35	0.23	0.17	0.06	100.3
APO7_7	49.02	0.19	15.61	13.58	20.53	0.02	0.50	0.20	0.24	0.04	99.9
APO7_8	50.14	0.19	15.29	14.32	20.07	0.01	0.44	0.21	0.21	0.00	100.9
DUR6_3	47.87	0.14	15.68	13.73	21.68	0.02	0.39	0.19	0.22	0.07	100.0
DUR6_6	41.64	0.09	8.93	31.12	17.20	0.01	0.95	0.29	0.15	0.11	100.5
DUR6_8	47.73	0.09	13.96	17.73	19.56	0.00	0.44	0.22	0.21	0.08	100.0
DUR8_3	47.65	0.09	11.95	19.76	19.97	0.01	0.24	0.24	0.16	0.06	100.1
DUR8_6	41.40	0.08	12.41	22.12	22.90	0.01	0.57	0.25	0.18	0.07	100.0
DUR8_8	50.56	0.09	13.09	17.65	18.47	0.00	0.39	0.22	0.19	0.08	100.7
PAD4_7	49.32	0.12	14.73	14.44	21.37	0.03	0.36	0.21	0.21	0.09	100.9
PAD4_8	47.61	0.10	11.34	15.91	22.34	0.01	0.39	0.19	0.20	0.09	98.2
PAD5_8	47.01	0.13	13.56	17.75	20.03	0.02	0.35	0.22	0.18	0.07	99.3
PAD5_9	49.02	0.15	15.48	13.92	20.90	0.02	0.62	0.19	0.24	0.05	100.6
PAD5_10	49.06	0.14	15.68	13.14	21.08	0.00	0.48	0.18	0.23	0.05	100.0
PAD6_2	44.93	0.10	14.95	16.29	22.40	0.01	0.50	0.19	0.25	0.05	99.7
PAD6_9	49.75	0.17	14.74	15.10	19.55	0.01	0.28	0.20	0.20	0.07	100.1
PAD6_14	49.66	0.15	14.80	14.77	19.81	0.01	0.24	0.19	0.21	0.07	99.9
PAD6_16	46.84	0.10	13.09	19.43	19.56	0.01	0.36	0.23	0.18	0.06	99.9
138345_2	49.22	0.16	14.36	15.98	19.16	0.01	0.55	0.19	0.19	0.10	99.9
138345_7	49.62	0.13	15.00	15.15	19.48	0.00	0.60	0.19	0.21	0.07	100.5
138345_11	48.50	0.07	9.93	25.64	14.36	0.02	0.34	0.27	0.17	0.11	99.4
138345_13	33.16	0.07	10.17	31.03	23.44	0.01	0.71	0.27	0.20	0.12	99.2
138345_17	31.46	0.07	10.34	31.03	23.92	0.02	0.97	0.27	0.22	0.12	98.4
138345_19	31.15	0.06	8.64	38.86	16.25	0.05	2.89	0.29	0.20	0.12	98.5
340740_2	44.01	0.12	14.62	18.65	20.46	0.02	0.81	0.21	0.26	0.09	99.2
340740_4	45.14	0.17	15.72	15.72	22.06	0.01	0.86	0.18	0.28	0.07	100.2
340740_9	48.39	0.13	14.09	18.27	17.25	0.03	0.58	0.21	0.24	0.08	99.3
340740_12	49.11	0.15	15.58	14.08	19.69	0.01	0.60	0.19	0.26	0.07	99.7
340740_14	48.80	0.16	15.41	15.16	19.38	0.00	0.72	0.20	0.25	0.05	100.1
354754_2	37.53	0.05	11.95	24.43	22.52	0.01	0.61	0.24	0.21	0.07	97.6
354754_5	42.11	0.08	9.74	31.23	15.44	0.01	0.61	0.28	0.21	0.10	99.8
354754_10	34.34	0.09	10.68	28.65	23.55	0.02	0.71	0.27	0.22	0.12	98.6
354754_12	35.55	0.07	10.71	31.19	19.69	0.01	0.55	0.27	0.21	0.08	98.3
362077_2	49.22	0.15	16.12	13.04	20.80	0.00	0.61	0.18	0.23	0.04	100.4
362077_4	48.23	0.13	14.82	15.93	20.10	0.01	0.53	0.21	0.22	0.07	100.2

Table F.1: Major element abundances (wt%) of Cr-spinel determined by EPMA.

Data point	Cr_2O_3	SiO_2	MgO	FeO	Al_2O_3	CaO	TiO_2	MnO	NiO	ZnO	Total
362077_7	48.64	0.19	15.47	14.65	20.45	0.00	0.46	0.19	0.25	0.04	100.4
362077_11	45.42	0.13	12.37	22.56	18.34	0.08	0.69	0.24	0.16	0.06	100.1
400230_2	45.85	0.09	12.76	20.85	18.79	0.01	0.72	0.24	0.21	0.08	99.6
400230_4	47.86	0.13	14.30	17.49	19.46	0.00	0.61	0.22	0.24	0.08	100.4
400230_8	46.38	0.07	12.42	21.13	19.09	0.01	0.72	0.23	0.23	0.09	100.4
400230_11	44.05	0.08	11.70	24.33	18.46	0.01	0.65	0.23	0.19	0.08	99.8
400230_14	40.85	0.11	16.46	13.72	26.29	0.01	0.61	0.16	0.31	0.05	98.6
400230_17	47.75	0.12	12.50	21.00	17.85	0.01	0.75	0.23	0.20	0.10	100.5
400230_19	39.58	0.09	12.39	24.27	22.02	0.01	1.00	0.23	0.21	0.08	99.9
ED_5	20.27	0.18	15.13	22.13	39.71	0.01	0.95	0.16	0.22	0.10	98.9
ED_12	24.82	0.17	14.96	21.18	35.83	0.01	0.90	0.17	0.23	0.10	98.4
KoP_3	40.55	0.19	13.76	19.66	24.31	0.02	0.53	0.20	0.23	0.09	99.5
KoP_14	23.27	0.17	14.24	23.96	35.56	0.00	0.79	0.17	0.23	0.08	98.5
SAU3199_3	33.55	0.14	11.86	23.55	28.00	0.01	0.77	0.23	0.19	0.07	98.4
SAU3199_4	34.59	0.14	12.95	22.11	27.88	0.00	0.98	0.22	0.20	0.09	99.2
SAU3199_6	30.06	0.15	13.36	21.46	32.10	0.00	0.92	0.20	0.23	0.08	98.6
SAU3199_11	32.36	0.15	13.80	21.21	30.74	0.00	0.83	0.20	0.22	0.10	99.6
SD_2	31.68	0.14	13.76	22.50	29.05	0.02	0.89	0.21	0.22	0.09	98.6
SD_5	36.42	0.15	12.74	23.69	23.62	0.01	0.88	0.22	0.18	0.06	98.0
SD_11	30.81	0.16	13.85	22.99	28.78	0.01	1.05	0.19	0.23	0.08	98.1
VEY_14	40.21	0.16	13.13	15.89	28.24	0.02	0.31	0.19	0.21	0.12	98.5
VP1a_1	42.25	0.15	12.84	21.09	21.89	0.02	0.86	0.22	0.23	0.10	99.6
VP1a_9	39.45	0.16	12.09	21.52	23.27	0.01	1.15	0.23	0.19	0.10	98.2
VP1a_12	37.68	0.14	12.03	23.21	24.48	0.01	1.00	0.22	0.22	0.10	99.1
VP1b_6	30.38	0.15	13.08	21.80	31.65	0.01	1.13	0.18	0.25	0.15	98.8
VP1b_9	43.47	0.14	11.74	23.24	19.03	0.01	1.03	0.25	0.20	0.11	99.2
VP1b_15	33.69	0.14	12.33	23.58	27.17	0.01	1.05	0.22	0.24	0.12	98.5
I2_3	38.33	0.11	16.17	14.27	29.94	0.00	0.17	0.17	0.21	0.06	99.4
I2_10	39.51	0.13	15.84	14.64	29.06	0.01	0.13	0.17	0.20	0.04	99.7
I2_21	37.59	0.12	14.46	16.64	29.49	0.02	0.23	0.20	0.19	0.05	99.0
I2_22	43.33	0.12	15.52	14.76	26.31	0.00	0.17	0.19	0.17	0.03	100.6
I3_4	36.12	0.90	11.59	25.02	25.05	0.07	0.66	0.25	0.12	0.08	99.8
I3_9	36.42	0.17	11.76	26.47	24.76	0.02	0.33	0.25	0.16	0.10	100.4
I5_5	40.28	0.11	13.63	22.39	22.57	0.01	1.18	0.23	0.22	0.07	100.7
I5_11	41.61	0.10	14.52	20.23	22.40	0.00	0.94	0.20	0.20	0.05	100.3
I5_18	46.67	0.10	14.54	18.24	19.16	0.00	0.97	0.21	0.20	0.06	100.2
I5_24	40.58	0.18	14.85	19.76	23.38	0.00	0.98	0.20	0.21	0.08	100.2
I5_26	39.46	0.15	14.77	20.15	23.64	0.01	0.95	0.20	0.22	0.06	99.6
I5_28	42.43	0.11	13.69	22.05	20.27	0.00	0.95	0.22	0.20	0.07	100.0
I5_29	41.96	0.11	14.23	20.67	22.21	0.04	1.24	0.20	0.20	0.07	101.0
I5_31	42.37	0.08	14.30	20.50	21.85	0.01	0.97	0.21	0.23	0.06	100.6
I5_33	40.40	0.10	14.13	19.75	23.50	0.55	1.16	0.22	0.19	0.07	100.1
I5_35	41.28	0.10	15.14	19.32	22.49	0.01	0.99	0.21	0.20	0.05	99.8
I5_36	41.06	0.08	14.76	20.25	23.08	0.01	1.05	0.20	0.27	0.07	100.8
I5_40	43.03	0.14	14.66	19.57	21.62	0.01	1.01	0.19	0.23	0.05	100.5
I5_41	39.52	0.15	14.72	21.00	23.20	0.01	1.15	0.21	0.23	0.03	100.2
I5_43	39.57	0.09	15.42	19.43	23.88	0.00	1.05	0.17	0.26	0.05	99.9
I5_44	39.13	0.14	14.28	21.37	24.00	0.01	1.12	0.23	0.22	0.07	100.6
I5_46	44.32	0.14	14.29	19.67	19.88	0.01	0.91	0.22	0.23	0.05	99.7
I6_4	43.13	0.13	15.29	17.22	22.35	0.00	0.77	0.19	0.24	0.05	99.4
I9_11	36.04	0.15	15.30	17.12	30.27	0.01	0.32	0.18	0.20	0.06	99.7
I9_17	34.87	0.19	15.87	18.05	30.87	0.03	0.29	0.18	0.22	0.08	100.6
I9_18	33.56	0.14	15.90	18.30	31.51	0.04	0.31	0.19	0.22	0.03	100.2
I9_19	33.73	0.13	15.77	18.15	31.48	0.01	0.37	0.18	0.21	0.06	100.1
I9_20	33.21	0.16	15.50	18.91	32.00	0.04	0.36	0.19	0.22	0.04	100.6
I9_21	33.83	0.18	16.12	17.55	32.34	0.01	0.28	0.18	0.22	0.07	100.8
I9_23	35.04	0.14	16.34	16.84	32.03	0.00	0.28	0.19	0.23	0.06	101.2
I9_24	34.48	0.13	15.82	17.43	30.91	0.01	0.34	0.20	0.21	0.05	99.6
I9_27	35.43	0.16	17.09	15.04	32.33	0.01	0.28	0.18	0.25	0.07	100.8
I9_29	35.58	0.19	16.41	15.75	30.98	0.00	0.28	0.19	0.22	0.06	99.7
I9_31	35.78	0.19	15.87	17.15	30.32	0.02	0.31	0.19	0.24	0.06	100.1
I9_33	33.97	0.17	15.57	18.52	30.62	0.05	0.36	0.19	0.21	0.07	99.7
I9_35	34.38	0.14	15.58	18.76	29.98	0.04	0.35	0.18	0.21	0.05	99.7
I9_37	34.00	1.04	15.90	16.73	30.70	0.03	0.29	0.16	0.22	0.05	99.1
I9_39	34.98	0.16	15.75	18.19	30.97	0.03	0.30	0.20	0.20	0.05	100.8
I9_41	34.46	0.25	16.00	17.17	31.31	0.01	0.30	0.18	0.23	0.07	100.0

Appendix G. Olivine-melt thermometery primary melt compositions

Table G.1: The primary melt composition for each sample calculated for olivine-melt thermometry where $Fe^{3+}/\sum Fe$=0.1. All oxides and olivine added are in wt %.

Sample	Olivine added	SiO_2	Al_2O_3	FeO_T	MgO	CaO	Na_2O	K_2O	TiO_2	MnO	Total
S1	-18.4	45.3	11.7	11.0	21.0	9.2	0.9	0.05	0.56	0.18	100.0
S2	-40.6	45.5	11.5	11.9	22.2	7.8	0.4	0.12	0.49	0.19	100.0
S3	-8.5	45.3	11.5	10.7	21.0	9.3	1.4	0.13	0.55	0.17	100.0
S5	-21.9	45.4	11.4	11.3	21.8	8.6	0.8	0.09	0.52	0.17	100.0
S6	-40.9	45.1	11.5	12.5	21.1	8.6	0.5	0.07	0.54	0.20	100.0
S7	-17.4	45.8	11.4	11.5	20.1	9.1	1.0	0.13	0.77	0.17	100.0
S8	-11.8	45.9	11.5	11.3	20.4	9.0	0.9	0.12	0.77	0.17	100.0
S9	-1.9	45.8	10.8	11.0	21.8	8.7	0.8	0.27	0.65	0.17	100.0
S10	4.2	45.3	10.5	10.6	23.3	8.8	0.6	0.15	0.57	0.17	100.0
M9	-35.9	43.1	8.5	12.6	27.0	6.5	1.2	0.12	0.77	0.20	99.9
R10	-47.4	43.7	11.8	14.0	18.9	8.7	1.6	0.07	0.95	0.20	100.0
MU1.1	-6.7	45.3	10.4	10.8	23.1	8.6	0.9	0.08	0.56	0.17	100.0
MU1.2	-38.3	45.6	13.1	11.2	18.2	9.9	1.1	0.14	0.58	0.19	100.0
MU2.2	-16.6	44.9	11.1	10.7	22.8	8.8	1.0	0.15	0.52	0.17	100.0
MU3.1	-26.8	45.2	10.7	11.7	22.0	8.4	1.1	0.18	0.60	0.18	100.0
PAD4	4.4	46.5	10.6	10.1	21.9	8.8	1.0	0.03	0.75	0.18	100.0
PAD5	4.7	47.0	11.3	9.8	20.0	9.8	1.2	0.03	0.77	0.18	100.0
PAD6	10.2	47.1	11.1	9.9	20.4	9.4	1.2	0.03	0.78	0.17	100.0
DUR6	13.4	47.2	11.0	9.7	20.6	9.3	1.2	0.04	0.68	0.17	100.0
DUR8	-10.8	46.1	11.1	11.4	19.8	9.2	1.3	0.05	0.82	0.20	100.0
APO4	-21.4	48.0	13.0	9.9	15.7	11.0	1.4	0.04	0.79	0.18	100.0
APO7	-3.6	45.9	9.2	10.3	24.5	8.1	1.0	0.03	0.75	0.17	100.0
138345	0.8	45.3	10.1	10.6	23.6	8.2	1.0	0.23	0.87	0.17	100.0
340740	7.4	44.9	9.6	10.7	23.0	9.3	1.2	0.06	1.13	0.18	100.0
354754	3.0	45.6	10.4	11.1	21.6	8.7	1.2	0.17	0.91	0.18	100.0
362077	-11.2	44.9	10.1	11.2	22.3	9.1	1.3	0.04	0.85	0.19	99.9
400230	3.3	45.6	10.4	11.1	21.7	8.7	1.2	0.16	0.91	0.18	100.0
I2	-34.5	46.1	12.9	10.7	17.8	11.0	1.0	0.01	0.36	0.17	100.0
I3	7.1	47.9	13.6	11.2	12.9	12.1	1.3	0.05	0.69	0.18	100.0
I5	-31.3	45.6	11.0	12.8	17.4	10.2	1.3	0.05	1.38	0.21	100.0
I6	8.7	47.1	10.0	12.9	19.0	7.3	1.7	0.30	1.57	0.19	100.0
I9	13.8	46.6	12.7	10.8	16.8	10.9	1.4	0.03	0.70	0.17	100.0
ED	-12.1	48.3	13.7	11.1	11.9	12.0	1.5	0.11	1.34	0.17	99.9
SD	-40.3	47.6	12.1	13.2	12.9	11.2	1.4	0.07	1.44	0.19	100.0
VEY	0.0	46.6	12.4	11.1	18.4	8.9	1.3	0.21	0.76	0.17	99.9
VP1	-1.0	48.2	13.0	11.2	13.9	10.4	1.6	0.16	1.43	0.15	99.9

Table G.2: The primary melt composition for each sample calculated for olivine-melt thermometry where $Fe^{3+}/\sum Fe$=0.15. All oxides and olivine added are in wt %.

Sample	Olivine added	SiO_2	Al_2O_3	FeO_T	MgO	CaO	Na_2O	K_2O	TiO_2	MnO	Total
S1	-21.8	45.6	12.2	10.9	20.0	9.5	1.0	0.05	0.58	0.18	100.0
S2	-43.6	45.8	11.9	11.8	21.2	8.1	0.4	0.13	0.51	0.19	100.0
S3	-12.0	45.5	12.0	10.6	19.9	9.6	1.4	0.14	0.57	0.17	100.0
S5	-25.0	45.6	11.8	11.3	20.9	8.8	0.8	0.09	0.54	0.18	100.0
S6	-44.1	45.4	11.9	12.4	20.1	8.9	0.5	0.07	0.56	0.21	100.0
S7	-20.4	46.1	11.8	11.4	19.1	9.4	1.0	0.14	0.80	0.18	100.0
S8	-15.2	46.2	11.9	11.2	19.3	9.3	1.0	0.13	0.79	0.17	100.0
S9	-5.3	46.0	11.2	10.9	20.9	9.0	0.9	0.28	0.68	0.17	100.0
S10	1.0	45.5	10.8	10.6	22.4	9.1	0.7	0.16	0.59	0.17	100.0
M9	-50.5	44.0	12.3	13.9	17.9	9.0	1.6	0.08	0.98	0.21	100.0
R10	-39.4	42.9	8.8	13.3	26.0	6.7	1.2	0.12	0.80	0.20	100.0
MU1.1	-10.9	45.6	10.9	10.8	21.9	9.0	1.0	0.08	0.59	0.17	100.0
MU1.2	-40.7	45.8	13.5	11.1	17.3	10.2	1.1	0.14	0.59	0.19	100.0
MU2.2	-20.3	45.1	11.5	10.6	21.8	9.1	1.0	0.16	0.54	0.17	100.0
MU3.1	-30.3	45.4	11.1	11.6	21.0	8.7	1.1	0.19	0.62	0.19	100.0
PAD4	4.3	46.6	10.6	10.0	22.0	8.8	1.0	0.03	0.75	0.18	100.0
PAD5	2.1	47.2	11.6	9.7	19.2	10.0	1.2	0.03	0.79	0.18	100.0
PAD6	7.2	47.3	11.4	9.8	19.5	9.6	1.2	0.03	0.80	0.17	100.0
DUR6	10.3	47.5	11.4	9.6	19.7	9.6	1.2	0.04	0.71	0.17	100.0
DUR8	-13.9	46.4	11.5	11.3	18.8	9.6	1.3	0.05	0.85	0.20	100.0
APO4	-23.5	48.3	13.3	9.8	14.9	11.3	1.4	0.04	0.81	0.18	100.0
APO7	-8.2	46.2	9.7	10.4	23.3	8.5	1.1	0.03	0.79	0.18	100.0
138345	-2.7	45.5	10.4	10.6	22.6	8.5	1.1	0.24	0.91	0.18	100.0
340740	3.1	45.1	10.0	10.7	21.8	9.7	1.2	0.06	1.18	0.18	100.0
354754	-0.4	45.9	10.8	11.1	20.7	9.0	1.2	0.17	0.94	0.18	100.0
362077	-15.0	45.1	10.5	11.2	21.2	9.5	1.3	0.04	0.89	0.19	100.0
400230	-0.1	45.9	10.8	11.1	20.8	9.0	1.2	0.17	0.94	0.18	100.0
I2	-36.9	46.3	13.3	10.6	17.0	11.3	1.0	0.01	0.37	0.17	100.0
I3	4.7	48.2	14.0	11.0	12.1	12.4	1.4	0.06	0.71	0.18	100.0
I5	-33.5	45.9	11.3	12.7	16.6	10.5	1.4	0.05	1.41	0.22	100.0
I6	5.3	47.4	10.3	12.8	18.0	7.5	1.8	0.31	1.62	0.20	100.0
I9	10.9	46.8	13.0	10.7	15.9	11.2	1.4	0.04	0.72	0.17	100.0
ED	-14.2	48.8	14.0	10.5	11.1	12.3	1.5	0.11	1.38	0.17	99.9
SD	-43.0	48.3	12.5	12.4	11.9	11.6	1.4	0.07	1.50	0.20	99.9
VEY	-3.0	47.2	12.8	10.5	17.6	9.3	1.4	0.22	0.79	0.17	99.9
VP1	-3.3	48.7	13.4	10.5	13.1	10.7	1.6	0.16	1.48	0.15	99.9

Appendix H. Al-in-olivine thermometery results

Table H.1: Al-in-olivine thermometry results

Olivine				**Spinel**					**T (°C)**
Data point	**Al_2O_3 (wt%)**	**± (ppm)**	**Mg#**	**Data point**	**Al_2O_3 (wt%)**	**Cr_2O_3 (wt%)**	**Cr#**	**K_D**	
S1_30	0.1067	37	91.3	**S1_31**	25.01	43.40	0.5379	0.00427	1408.9
S1_33	0.1236	37	91.4	**S1_34**	28.89	39.40	0.4777	0.00428	1424.8
S1_35	0.1285	37	91.4	**S1_36**	25.86	42.12	0.5222	0.00497	1452.7
S1_38	0.1146	38	91.4	**S1_39**	27.03	41.37	0.5066	0.00424	1415.3
S1_18	0.1129	73	91.3	**S1_40**	26.23	41.98	0.5177	0.00430	1416.3
S2_4	0.1366	38	91.1	**S2_5**	25.61	42.26	0.5254	0.00533	1471.0
S2_6	0.1038	38	91.6	**S2_7**	30.83	36.32	0.4414	0.00337	1373.8
S3_25	0.1519	38	90.8	**S3_26**	31.11	36.57	0.4409	0.00488	1469.6
S3_27	0.1138	38	91.8	**S3_28**	25.77	43.01	0.5282	0.00442	1420.2
S3_29	0.1368	36	91.5	**S3_35**	24.89	44.20	0.5437	0.00550	1474.2
S3_31	0.1112	38	91.5	**S3_32**	26.85	41.13	0.5068	0.00414	1409.2
S3_33	0.0958	36	91.4	**S3_37**	27.16	41.06	0.5036	0.00353	1370.2
S5_33	0.1208	37	91.6	**S5_34**	25.62	43.05	0.5298	0.00471	1436.8
S5_7	0.111	37	91.5	**S5_38**	27.03	39.78	0.4968	0.00411	1409.6
S5_44	0.1002	38	91.7	**S5_45**	25.26	43.60	0.5366	0.00397	1391.0
S5_46	0.1217	37	89.6	**S5_47**	26.73	39.53	0.4980	0.00455	1435.9
S6_6	0.1191	56	91.9	**S6_7**	25.58	42.76	0.5286	0.00466	1433.8
S7_5	0.1037	57	89.8	**S7_6**	28.39	38.11	0.4738	0.00365	1385.9
S7_13	0.0943	56	89.8	**S7_14**	28.76	37.24	0.4649	0.00328	1361.8
S8_1	0.1024	71	91.0	**S8_25**	28.47	39.23	0.4804	0.00360	1380.5
S8_26	0.0938	37	90.5	**S8_27**	28.53	38.37	0.4743	0.00329	1360.2
S8_29	0.1016	37	90.9	**S8_30**	27.70	39.41	0.4883	0.00367	1383.4

Table H.1: Al-in-olivine thermometry results

Olivine				**Spinel**					**T (°C)**
Data point	**Al_2O_3 (wt%)**	**± (ppm)**	**Mg#**	**Data point**	**Al_2O_3 (wt%)**	**Cr_2O_3 (wt%)**	**Cr#**	**K_D**	
S8_31	0.0794	37	91.0	**S8_32**	25.63	40.52	0.5147	0.00310	1336.8
S8_38	0.1256	38	90.5	**S8_39**	28.87	38.10	0.4695	0.00435	1431.3
S9_1	0.0919	38	91.7	**S9_3**	32.12	34.77	0.4207	0.00286	1339.8
S9_6	0.1035	38	91.8	**S9_8**	24.48	43.29	0.5426	0.00423	1405.5
S9_19	0.1151	38	92.0	**S9_20**	24.67	43.28	0.5406	0.00466	1431.2
S10_20	0.1022	38	91.7	**S10_21**	23.29	44.92	0.5640	0.00439	1409.6
S10_22	0.1159	38	91.5	**S10_23**	23.92	44.04	0.5525	0.00484	1438.1
S10_25	0.1261	37	91.4	**S10_26**	24.08	43.90	0.5502	0.00524	1459.4
S10_28	0.0849	38	92.1	**S10_29**	26.40	41.00	0.5102	0.00322	1346.5
S10_31	0.1276	38	92.6	**S10_32**	24.21	43.86	0.5486	0.00527	1461.5
S10_33	0.1037	38	91.7	**S10_34**	23.93	44.52	0.5552	0.00433	1408.6
S10_35	0.1034	38	92.3	**S10_36**	24.22	44.37	0.5513	0.00427	1405.7
S10_37	0.1099	37	92.5	**S10_38**	24.04	44.39	0.5533	0.00457	1422.7
S10_39	0.1076	38	91.8	**S10_40**	33.20	34.64	0.4117	0.00324	1371.6
R10_6	0.0819	56	88.6	**R10_8**	26.61	32.39	0.4495	0.00308	1350.3
M9_1	0.1093	37	92.1	**M9_2**	21.81	44.98	0.5804	0.00501	1439.7
M9_3	0.1199	37	92.1	**M9_4**	22.59	44.35	0.5684	0.00531	1458.2
M9_5	0.12	37	92.6	**M9_6**	23.59	42.70	0.5484	0.00509	1452.1
M9_9	0.1165	37	90.6	**M9_10**	20.36	42.67	0.5844	0.00572	1474.3
M9_13	0.1332	36	92.2	**M9_14**	21.59	43.46	0.5746	0.00617	1497.9
M9_15	0.1104	37	92.3	**M9_16**	21.56	43.82	0.5769	0.00512	1446.3
M9_17	0.1177	36	91.8	**M9_18**	21.49	44.90	0.5836	0.00548	1462.6
M9_21	0.1169	36	92.3	**M9_22**	21.41	44.40	0.5818	0.00546	1462.2
M9_23	0.1147	37	92.2	**M9_24**	22.34	44.31	0.5709	0.00513	1448.6
MU1.1_1	0.0981	37	92.1	**MU1.1_3**	25.88	43.99	0.5328	0.00379	1380.7
MU1.1_9	0.1013	38	92.3	**MU1.1_10**	24.49	42.30	0.5368	0.00414	1401.5
MU1.1_19	0.0795	38	91.6	**MU1.1_21**	28.31	38.80	0.4790	0.00281	1322.3
MU1.1_24	0.0776	38	92.3	**MU1.1_26**	23.51	40.15	0.5340	0.00330	1347.2
MU1.1_27	0.0951	37	92.1	**MU1.1_29**	25.16	41.98	0.5282	0.00378	1381.2
MU1.2_1	0.0874	38	90.3	**MU1.2_3**	24.61	42.54	0.5369	0.00355	1363.9
MU1.2_14	0.0812	37	89.8	**MU1.2_16**	22.91	41.61	0.5492	0.00354	1360.5

Table H.1: Al-in-olivine thermometry results

Olivine				**Spinel**					**T (°C)**
Data point	**Al_2O_3 (wt%)**	**± (ppm)**	**Mg#**	**Data point**	**Al_2O_3 (wt%)**	**Cr_2O_3 (wt%)**	**Cr#**	**K_D**	
MU1.2_17	0.0921	38	90.3	**MU1.2_19**	22.62	41.12	0.5494	0.00407	1394.3
MU2.2_6	0.0953	37	90.5	**MU2.2_8**	25.85	42.14	0.5224	0.00369	1376.4
MU2.2_19	0.1133	36	93.1	**MU2.2_20**	26.20	42.56	0.5214	0.00432	1416.5
MU2.2_23	0.0968	36	92.3	**MU2.2_25**	26.27	43.38	0.5256	0.00369	1375.6
MU3.1_1	0.1188	38	92.1	**MU3.1_3**	25.69	41.61	0.5207	0.00462	1434.0
MU3.1_8	0.0951	38	89.8	**MU3.1_10**	26.72	41.12	0.5080	0.00356	1371.3
MU3.1_13	0.0953	38	91.8	**MU3.1_16**	22.54	41.19	0.5508	0.00423	1403.5
PAD4_3	0.1023	29	92.5	**PAD4_7**	21.37	49.32	0.6076	0.00479	1420.8
PAD4_5	0.0929	29	91.3	**PAD4_8**	22.34	47.61	0.5884	0.00416	1390.1
PAD5_5_2	0.0988	29	90.6	**PAD5_8**	20.03	47.01	0.6115	0.00493	1427.5
PAD5_3	0.0949	29	92.1	**PAD5_9**	20.90	49.02	0.6114	0.00454	1406.4
PAD5_4	0.1005	29	92.0	**PAD5_10**	21.08	49.06	0.6096	0.00477	1419.3
PAD6_1	0.0924	29	90.2	**PAD6_2**	22.40	44.93	0.5736	0.00412	1391.6
PAD6_8	0.1008	29	90.5	**PAD6_9**	19.55	49.75	0.6306	0.00516	1434.2
PAD6_13	0.044	29	86.2	**PAD6_14**	19.81	49.66	0.6271	0.00222	1239.9
PAD6_15	0.0927	29	87.0	**PAD6_16**	19.56	46.84	0.6163	0.00474	1416.1
APO4_5	0.1074	29	87.8	**APO4_8**	19.19	45.71	0.6150	0.00560	1460.0
APO4_6	0.1002	29	88.0	**APO4_9**	18.35	48.29	0.6384	0.00546	1447.3
APO7_1	0.0959	29	92.6	**APO7_7**	20.53	49.02	0.6156	0.00467	1412.5
APO7_4	0.0992	29	92.6	**APO7_8**	20.07	50.14	0.6263	0.00494	1424.3
DUR6_2	0.0917	29	92.3	**DUR6_3**	21.68	47.87	0.5970	0.00423	1392.2
DUR6_5	0.0519	29	89.6	**DUR6_6**	17.20	41.64	0.6189	0.00302	1307.3
DUR6_7	0.0967	29	90.5	**DUR6_8**	19.56	47.73	0.6208	0.00494	1425.8
DUR8_2	0.0987	29	87.1	**DUR8_3**	19.97	47.65	0.6155	0.00494	1427.1
DUR8_5	0.0617	29	85.5	**DUR8_6**	22.90	41.40	0.5481	0.00269	1297.7
DUR8_7	0.1071	29	89.9	**DUR8_8**	18.47	50.56	0.6474	0.00580	1461.0
138345_1	0.0999	29	92.1	**138345_2**	19.16	49.22	0.6328	0.00521	1436.5
138345_6	0.1063	29	92.8	**138345_7**	19.48	49.62	0.6308	0.00546	1449.1
138345_10	0.0949	29	86.5	**138345_11**	14.36	48.50	0.6937	0.00661	1484.2
340740_1	0.0758	29	89.5	**340740_2**	20.46	44.01	0.5907	0.00371	1361.4
340740_3	0.0921	29	91.2	**340740_4**	22.06	45.14	0.5785	0.00417	1393.4

Table H.1: Al-in-olivine thermometry results

Olivine				**Spinel**					**T (°C)**
Data point	**Al_2O_3 (wt%)**	**± (ppm)**	**Mg#**	**Data point**	**Al_2O_3 (wt%)**	**Cr_2O_3 (wt%)**	**Cr#**	**K_D**	
340740_8	0.0697	29	90.3	**340740_9**	17.25	48.39	0.6531	0.00404	1367.5
340740_11	0.0925	29	91.8	**340740_12**	19.69	49.11	0.6259	0.00470	1411.4
340740_13	0.098	29	91.5	**340740_14**	19.38	48.80	0.6281	0.00506	1429.8
354754_4	0.0673	29	86.2	**354754_5**	15.44	42.11	0.6466	0.00436	1387.5
354754_9	0.0456	29	85.9	**354754_10**	23.55	34.34	0.4945	0.00194	1238.6
362077_1	0.1235	29	90.0	**362077_2**	20.80	49.22	0.6135	0.00594	1476.5
362077_3	0.1015	29	89.5	**362077_4**	20.10	48.23	0.6168	0.00505	1432.3
362077_6	0.1257	29	92.0	**362077_7**	20.45	48.64	0.6148	0.00615	1485.8
362077_10	0.0816	29	90.1	**362077_11**	18.34	45.42	0.6242	0.00445	1398.1
400230_1	0.084	30	87.0	**400230_2**	18.79	45.85	0.6208	0.00447	1400.1
400230_3	0.0959	29	89.1	**400230_4**	19.46	47.86	0.6227	0.00493	1424.6
400230_7	0.0887	29	86.7	**400230_8**	19.09	46.38	0.6198	0.00465	1410.1
400230_10	0.0757	29	85.1	**400230_11**	18.46	44.05	0.6156	0.00410	1380.1
400230_13	0.1054	29	92.0	**400230_14**	26.29	40.85	0.5104	0.00401	1400.1
400230_16	0.089	29	86.8	**400230_17**	17.85	47.75	0.6421	0.00499	1422.5
ED_6	0.0467	38	85.1	**ED_5**	39.71	20.27	0.2551	0.00118	1186.6
ED_13	0.0562	38	85.8	**ED_12**	35.83	24.82	0.3173	0.00157	1231.2
KoP_4	0.0602	38	88.1	**KoP_3**	24.31	40.55	0.5281	0.00248	1283.5
KoP_13	0.0591	38	84.5	**KoP_14**	35.56	23.27	0.3051	0.00166	1245.6
SAU3199_1	0.0469	38	86.1	**SAU3199_4**	27.88	34.59	0.4543	0.00168	1218.1
SAU3199_2	0.051	38	85.9	**SAU3199_3**	28.00	33.55	0.4456	0.00182	1235.9
SAU3199_7	0.0503	38	86.4	**SAU3199_6**	32.10	30.06	0.3858	0.00157	1217.5
SAU3199_12	0.0523	38	86.6	**SAU3199_11**	30.74	32.36	0.4139	0.00170	1228.4
SD_1	0.0509	38	85.5	**SD_2**	29.05	31.68	0.4225	0.00175	1232.6
SD_6	0.0527	38	85.6	**SD_5**	23.62	36.42	0.5084	0.00223	1265.3
SD_10	0.0538	37	85.4	**SD_11**	28.78	30.81	0.4180	0.00187	1246.9
VEY_12	0.0774	38	90.3	**VEY_14**	28.24	40.21	0.4886	0.00274	1314.6
VP1a_10	0.0461	38	86.8	**VP1a_9**	23.27	39.45	0.5321	0.00198	1235.7
VP1a_14	0.0399	38	86.2	**VP1a_12**	24.48	37.68	0.5080	0.00163	1201.5
VP1a_2	0.0396	38	87.7	**VP1b_6**	21.89	42.25	0.5643	0.00181	1211.1
I2_2	0.0804	56	89.7	**I2_3**	29.94	38.33	0.4620	0.00269	1315.9

Table H.1: Al-in-olivine thermometry results

Olivine				**Spinel**					**T (°C)**
Data point	**Al_2O_3 (wt%)**	**± (ppm)**	**Mg#**	**Data point**	**Al_2O_3 (wt%)**	**Cr_2O_3 (wt%)**	**Cr#**	**K_D**	
I2_8	0.0569	57	89.8	**I2_10**	29.06	39.51	0.4770	0.00196	1244.4
I2_20	0.0691	56	89.8	**I2_21**	29.49	37.59	0.4609	0.00234	1285.9
I5_6	0.0678	38	87.3	**I5_5**	22.57	40.28	0.5449	0.00300	1322.8
I5_10	0.0754	37	88.5	**I5_11**	22.40	41.61	0.5548	0.00337	1347.0
I5_23	0.0787	37	88.8	**I5_24**	23.38	40.58	0.5380	0.00337	1350.9
I5_25	0.0677	36	88.4	**I5_26**	23.64	39.46	0.5282	0.00286	1315.7
I5_27	0.0684	37	87.1	**I5_28**	20.27	42.43	0.5841	0.00337	1340.7
I5_30	0.0735	37	89.0	**I5_31**	21.85	42.37	0.5653	0.00336	1344.3
I5_32	0.0872	36	88.5	**I5_33**	23.50	40.40	0.5357	0.00371	1374.9
I5_34	0.0747	37	88.6	**I5_35**	22.49	41.28	0.5518	0.00332	1344.5
I5_39	0.0787	36	89.0	**I5_40**	21.62	43.03	0.5717	0.00364	1361.6
I5_42	0.0699	37	88.6	**I5_43**	23.88	39.57	0.5265	0.00293	1321.1
I5_45	0.0764	36	88.4	**I5_46**	19.88	44.32	0.5993	0.00384	1368.2
I5_8	0.0669	38	89.2	**I5_29**	22.21	41.96	0.5589	0.00301	1320.3
I5_2	0.0578	38	88.7	**I5_36**	23.08	41.06	0.5441	0.00250	1282.5
I5_20	0.0731	37	88.1	**I5_41**	23.20	39.52	0.5333	0.00315	1336.4
I5_13	0.0665	38	88.1	**I5_44**	24.00	39.13	0.5224	0.00277	1309.5
I6_2	0.0669	38	89.7	**I6_4**	22.35	43.13	0.5641	0.00299	1317.7
I9_10	0.0824	38	89.2	**I9_11**	30.27	36.04	0.4440	0.00272	1323.0
I9_3	0.0749	37	90.1	**I9_17**	30.87	34.87	0.4311	0.00243	1300.0
I9_2	0.075	37	88.2	**I9_18**	31.51	33.56	0.4167	0.00238	1298.9
I9_1	0.0674	36	87.5	**I9_19**	31.48	33.73	0.4182	0.00214	1275.5
I9_5	0.102	37	89.5	**I9_20**	32.00	33.21	0.4104	0.00319	1367.9
I9_16	0.0711	36	89.6	**I9_23**	32.03	35.04	0.4232	0.00222	1282.2
I9_24	0.0787	36	88.2	**I9_24**	30.91	34.48	0.4280	0.00255	1311.4
I9_26	0.0851	36	89.8	**I9_27**	32.33	35.43	0.4237	0.00263	1320.0
I9_28	0.0872	37	88.9	**I9_29**	30.98	35.58	0.4352	0.00281	1332.7
I9_30	0.0836	36	88.3	**I9_31**	30.32	35.78	0.4418	0.00276	1326.5
I9_32	0.0419	37	87.7	**I9_33**	30.62	33.97	0.4267	0.00137	1183.2
I9_34	0.0519	37	87.6	**I9_35**	29.98	34.38	0.4348	0.00173	1227.7
I9_36	0.0859	37	88.3	**I9_37**	30.70	34.00	0.4262	0.00280	1333.4

Table H.1: Al-in-olivine thermometry results

Olivine				**Spinel**					**T (°C)**
Data point	**Al_2O_3 (wt%)**	**± (ppm)**	**Mg#**	**Data point**	**Al_2O_3 (wt%)**	**Cr_2O_3 (wt%)**	**Cr#**	**K_D**	
I9_38	0.0701	36	88.8	**I9_39**	30.97	34.98	0.4310	0.00226	1284.7
I9_40	0.0864	37	88.8	**I9_41**	31.31	34.46	0.4247	0.00276	1330.5